Transworld Research Network
37/661 (2), Fort P.O., Trivandrum-695 023, Kerala, India

Recent Res. Devel. Crystal Growth, 5(2009): 141-314 ISBN: 978-81-7895-198-0

5 Imaging convection, concentration and surface micromorphology during crystal growth from solution using optical diagnostics

Sunil Verma[1] **and K. Muralidhar**[2]
[1]Laser Materials Development and Devices Division, Raja Ramanna Center for Advanced Technology, Indore 452013, India; [2]Department of Mechanical Engineering, IIT Kanpur 208016, India

Abstract

Crystals are the workhorses driving the current photonics revolution. Material scientists need to have a detailed understanding of how crystals grow, whereas device engineers need to grow large relatively defect-free crystals that are adequate for the end applications. The process of mass transfer and the convection modes adopted to achieve the desired mass transport rates during growth present a difficult optimization problem. These transport

Correspondence/Reprint request: Dr. K. Muralidhar, Department of Mechanical Engineering, IIT Kanpur 208016, India. E-mail: krishnamurthy.muralidhar@gmail.com

processes affect the growth rate, crystal quality and the surface microstructure over the growing crystal faces. As a result the science of crystal growth is governed by the principles of physico-chemical hydrodynamics during fluid-to-solid phase transition. Therefore, in order to control the process and to ensure growth of large high-quality crystals, it is important to understand the physical phenomena involved during growth.

The present review concerns the study of the process of crystal growth from solution. The change of solution density with temperature (dρ/dT) is negative and that with solute concentration (dρ/dC) is positive. The growth in the gravitational field is often accompanied by a rising buoyant convection current which envelops the crystal, is oscillatory and unstable, and drastically modifies the concentration gradient along the growth interface. As a result the growth history and defect structure of the crystal is a function of the time-dependent spatial distribution of the convection patterns and of the concentration profiles in the surrounding solution. Therefore, mapping of these two parameters during growth is a useful experimental approach to understanding the process of crystal growth and regulating growth conditions to produce crystals of optimal quality. This approach is enhanced by simultaneous measurement of convection and surface micromorphology of the growing crystal faces.

Convection, concentration and surface features during growth of a KDP (Potassium Dihydrogen Phosphate) crystal have been imaged. The relationship of the process parameters to the growth rate, crystal quality and growth mechanism is studied. KDP crystal was chosen as it is an important NLO material and its growth related physico-chemical properties are available in the literature. Optical diagnostics have been employed in the present work as they correspond to photon probes that do not perceptibly affect the process being studied and their response is practically inertia-free. They map the convection and concentration field with a spatial resolution of a micrometer and a temporal resolution of about a millisecond. In addition they are capable of providing a large volume of data of the process under study. The salient results of our work are briefly reported below:

Laser shadowgraph technique has been successfully used for mapping free convection phenomenon during growth in three different geometries. A linearized governing equation of the shadowgraph process has been used to extract information of the refractive index field corresponding to the shadowgraph images. This information is used to trace the optical rays through the growth chamber. It is concluded that the higher order optical effects such as scattering and interference are insignificant during shadowgraph imaging, as the ray deviations are consistently small. The strength of free convection observed through shadowgraph images is

estimated in terms of Grashof number. It is observed that beyond a given supercooling the Grashof number rises exponentially, and the crystal quality becomes sensitive to fluctuation in the concentration field. Inclusions and striations get incorporated beyond this stage of growth. The time-lapsed shadowgraph images are used to quantify the growth rate as a function of supercooling. The shadowgraph images of convective plumes during free convection growth have been used to examine growth mechanisms such as two-dimensional surface growth, and birth and spread mechanism.

A Mach-Zehnder interferometer has been used for imaging concentration field during KDP growth under free and forced convection conditions. Imaging of the concentration field during growth in different geometries has been carried out for various forced convection conditions and quantified in terms of Reynolds number. Results indicate that a uniform concentration is achieved only at an optimized average Reynolds number. Infinite fringe M-Z interferometry is demonstrated to be an extremely sensitive diagnostic tool to detect concentration gradient inside the crystallizer. Wedge and infinite fringe interferograms, and their relative importance for imaging growth in different geometries have been presented. The thickness of the solutal boundary layer (SBL), which is the region of intense solid-fluid interaction, has been imaged and measured precisely (to ~150-300 μm) using shadowgraphy. It has been found to be intricately linked to the growth kinetics. Thinner the boundary layer, faster is the growth kinetics.

The technique of computerized tomography has been used for 3D reconstruction of shadowgraph projection data. Special apparatus have been fabricated for performing the tomography experiments. Convective features as seen in the shadowgraph images have been reconstructed over three planes at different heights above the crystal. Two different algorithms, namely convolution back projection (CBP) and algebraic reconstruction technique (ART) have been employed for the purpose. The effect of the number of views available for reconstruction has been studied using projection data consisting of 18 and 90 views respectively. Additionally, three different data types namely, intensity values, contrast $(I_o\text{-}I_s)/I_s$*, and refractive index corresponding to each shadowgraph image have been used for reconstruction. The influence of the nature of projection data on the reconstructed field is studied. Several cross-checks have been applied to verify the correctness of the obtained reconstruction. Error estimates have been provided for a pair of reconstructed solutions and are found to be small. Tomographic imaging proves to be a useful diagnostic to obtain contours of convection and concentration fields at desired planes of the crystallizer.*

A Michelson interferometer has been set up for measuring minute changes in the solution concentration due to thermal fluctuations. In addition

it has been used for imaging surface micromorphology of prismatic and pyramidal faces of the KDP crystal. Screw dislocation generated growth hillocks have been imaged as concentric fringes of equal thickness.

This article shows that convection patterns and surface features of the crystal can be quantitatively obtained using optical methods.

1. Introduction

The importance of crystals in modern technology can hardly be over-emphasized. They are the workhorses that drive opto-electronic devices of the present photonics era. The quality of crystals needed for optical applications has to be very high. Significant progress in the science and technology of crystal growth has resulted in giant strides in several fields employing devices based on crystals. Today, crystal growth is a multidisciplinary field involving subjects from the basic sciences as well as engineering. Expertise in solid-state physics, chemistry, thermodynamics, fluid mechanics, crystallography, mathematical modeling, optical engineering, and electronics and instrumentation is jointly required. As a result, crystal-growth literature is scattered over several journals and textbooks. This presents a bottleneck for the beginners in the field who wish to carry out interdisciplinary research in the domain of crystal growth.

Crystal growth is a first-order phase transition, and is therefore associated with the liberation of latent heat. An efficient transfer (removal) of this heat from the solid-fluid interface region to the bulk of the solution is a major concern during crystal growth. Additionally, the processes of mass transfer and the convection modes adopted to achieve the desired mass transport rates present a difficult optimization problem. These transport processes of heat and mass significantly affect the compositional homogeneity, surface microstructure and the growth rate of the crystal. Thus crystal growth is governed by the principles of physico-chemical hydrodynamics.

The technology of crystal growth involves designing and developing the necessary apparatus and instrumentation for achieving the controlled phase transition to enable the growth of single-crystalline solids. Therefore, to control the process and to ensure growth of large high-quality crystals, it is important to properly understand the related physical phenomena.

1.1. Physics of crystal growth

1.1.1. Nucleation and growth

Growth of a single crystal is a first-order phase transition that is initiated by the nucleation of a thermodynamically stable crystalline phase. It proceeds by the growth of this phase by attaching (bonding) of appropriate structural

unit from the nutrient medium. For certain materials, there exists a second possibility of converting a polycrystalline phase into single crystal by causing the grain boundaries to sweep through and out of the crystal. We restrict our discussion to the former route of single crystal preparation.

When a crystal is in dynamic equilibrium with its parent nutrient phase, the free energy of such a system is a minimum and no growth takes place. In order to be able to grow the crystal, the equilibrium has to be broken by the application of temperature, pressure, chemical potential or external strain. Therefore, crystal growth occurs under non-equilibrium conditions. It proceeds in two stages: first is nucleation and the second is growth.

The first stage in the process of crystallization is primary nucleation. It is essentially the birth of a new crystal as a result of collisions occurring between atoms, ions or molecules present in the solution. Since it is a statistical phenomenon, the resulting cluster may be stable or unstable and will depend upon the change in the Gibbs free energy accompanying the process. Figure 1.1 shows the change in Gibbs free energy occurring during primary nucleation as a function of cluster or nucleus size. Classical nucleation theory states that the change in this free energy has two components; first, the change in surface free energy and second that in volume free energy. Mathematically it can be written as

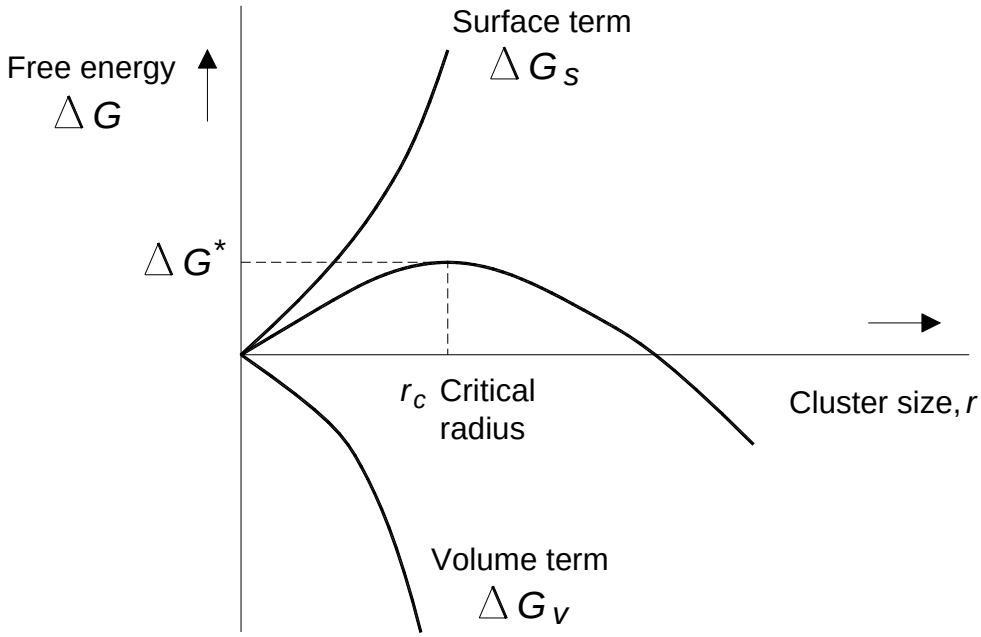

Figure 1.1. Gibbs free energy change as a function of the cluster size during nucleation (Mullin, 2001).

$$\Delta G(r) = \frac{4\pi r^3}{3}\Delta G_v + 4\pi r^2 \Delta G_s$$

where
r = radius of the cluster
ΔG_s = free energy change per unit surface area
ΔG_v = free energy change per unit volume

During the initial stages of cluster formation Figure 1.1 shows that there is a continuous increase in the Gibbs free energy till a critical size is achieved. This results in a barrier for stable growth due to the fact that the surface-to-volume free energy ratio is higher for a smaller cluster than for a larger one. However, once a critical size is achieved, the Gibbs free energy monotonically decreases thereafter. The stable growth of the cluster then leads to a macroscopic crystal. Simply stated, in an experiment, clusters below a critical size are unstable and disintegrate back into the solution, whereas those greater that the critical size are stable and result in growth; cf. Figure 1.2.

Once a stable structure is formed by nucleation, the growth units (atoms, ions, molecules or a group of them) can diffuse from the surrounding supersaturated solution to the surface of the nucleus and get incorporated into the crystal lattice. In general, any crystal growth process proceeds along the following steps:

i) Generation of growth units (or reactants)
ii) Bulk transport of growth units to the growing surface, either by diffusion through the boundary layer or by application of an external driving force
iii) Adsorption and migration on the surface
iv) Deposition (final position on the crystal surface)
v) Growth (advancement) of the crystal surface
vi) Transport of the unwanted products from the solid-liquid interface back to the bulk of the solution.

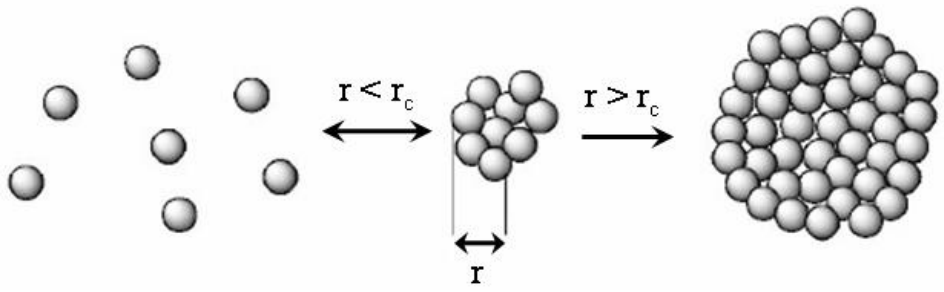

Figure 1.2. The critical size cluster during nucleation.

1.2. Mechanisms of crystal growth

Several models of the growth of a crystal at the macro-scale have been proposed. A few of these are presented below.

1.2.1. Kossel crystal growth mechanism

The importance of surface irregularities acting as sources of crystal growth was first recognized by Kossel, Stranski and Volmer (1939). These authors identified three possible sites for the attachment of a growth unit on an existing crystal surface. These are depicted in Figure 1.3.

The *ledge sites* are available on a flat crystal surface (terrace) and only one intermolecular interaction is possible. The *step sites* are available at the position of a step on the crystal surface and provide the possibility of two intermolecular interactions. The third are *kink sites* which are corner positions on the crystal, making three intermolecular interactions possible. A growth unit with the highest coordination number will be bound most strongly to the crystal, and hence will have least probability of dissolving back into the solution. Considering this fact, the kinks are energetically most favorable sites of growth, followed by steps and ledges. Further, incorporation of a growth unit at a kink position makes available a new kink site. Thus a kink acts as a recurring binding site to the growth process.

1.2.2. Spiral growth mechanism

Until the Burton-Cabrera-Frank (BCF) theory of crystal growth became available (1951), theoretical results predicted that the minimum level of supersaturation required for growth of an ideal crystal ought to be approximately 50%. But this prediction was not in agreement with experimental findings, wherein growth was observed even at supersaturation as low as 2%. This discrepancy in the theoretical and experimental results was

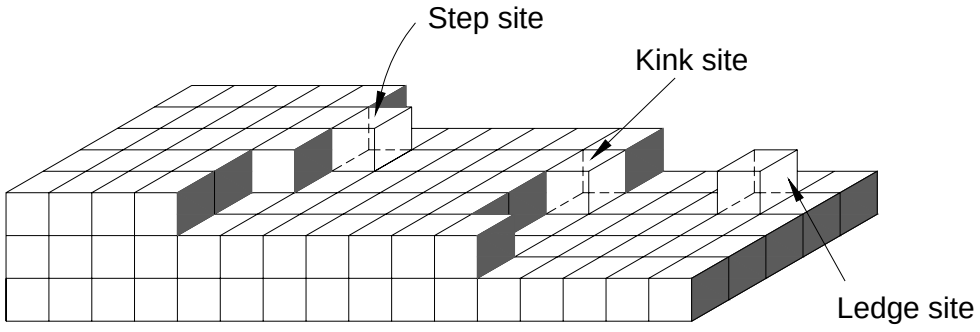

Figure 1.3. Three different sites for attachment of a growth unit in the Kossel, Stranski and Volmer (1939) model.

was solved by the BCF model. It was suggested that growth at low levels of supersaturation is possible provided the crystal being grown has dislocations in it instead of being an ideal defect free crystal. Screw dislocations are spiraling mounds on the crystal surface and provide a continuous source of monomolecular level steps on the crystal surface for uninterrupted growth. The function of these steps is analogous to kinks in the Kossel model of crystal growth. Figure 1.4 depicts a crystal surface growing with the attachment of a growth unit at the step provided by a screw dislocation generated mound.

1.2.3. Two-dimensional growth mechanism

This mechanism of growth is possible only at relatively high levels of supersaturation. For a crystal to grow with this mechanism a two-dimensional nucleus of monomolecular height has to first nucleate on the existing crystal surface (Figure 1.5a). Since the energetics involved in the development of a 2-D monolayer island requires a high driving force, a high level of supersaturation is a necessity. The 2-D island becomes a source of steps and kinks for the newly attaching growth units (Figures 1.5b). The process continues till the plane is completely covered (Figures 1.5c). In order that the crystal continues to grow, a new two-dimensional nucleus has to form on this plane, and the steps described above are then repeated. This mode of growth is also referred to as *birth-and-spread* mechanism, as the nucleation (birth) of a 2-D monomolecular step island is followed by its lateral growth (spread).

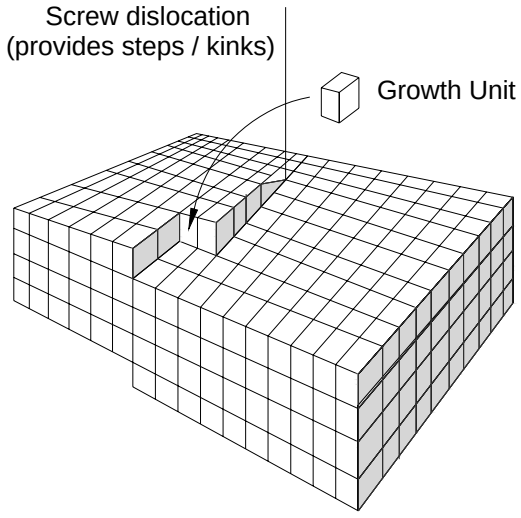

Figure 1.4. Spiral growth mechanism of crystal growth (BCF model).

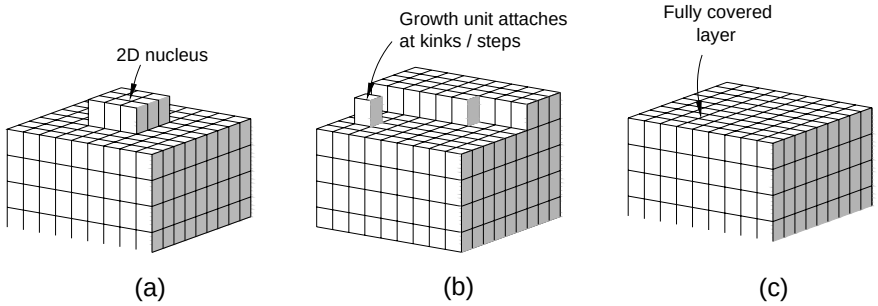

Figure 1.5. Two-dimensional growth mechanism.

1.2.4. Three-dimensional growth mechanism

Growth of this type is possible only at extremely high levels of supersaturation, usually encountered during the rapid-growth method. At such levels of supersaturation, the growth units agglomerate in the solution itself to create stable three-dimensional nuclei. They grow till they are no longer able to remain buoyant in the solution. The heavy nuclei fall on the surface of the crystal underneath, followed by a possible rearrangement over the crystal surface before getting incorporated into the crystal lattice. The processes of clustering and subsequent fall continue resulting in the growth of the crystal. The growth rates achievable by this mechanism are several tens of *mm* per day. It is similar to the *birth-and-spread* growth mechanism except that the nucleus here is three-dimensional.

1.3. Methods of crystal growth

Factors that govern the selection of a technique for crystal growth are listed below.

1. If the required crystalline phase melts *congruently*, i.e. does not decompose at its melting point, or in other words the composition of the solid phase i.e. crystal is same as that in the liquid phase i.e. melt, then melt growth is often preferred. For an *incongruently* melting phase, namely those decomposing before the crystallization temperature, a natural choice is solution or vapor growth.
2. If the material from which the crystal is being prepared dissociates before the growth temperature is reached, then flux growth is a good option.
3. When more than one chemical compound is used for synthesizing the starting material, the stoichiometry of the final crystal often fluctuates from the ideal value. Therefore, when a stoichiometric crystal is needed, one has to adjust the starting compositions of the reacting species.

4. Chemical reactivity of the materials with the growth apparatus is an important factor in choosing the appropriate growth technique.

Thus the choice of a particular type of growth technique is guided by several considerations. The crystal growth from solution is described in detail below, while the other methods of growth are briefly considered.

1.3.1. Solution growth

This is the most widely used method for growing large crystals, several centimeters in size. It is applicable to all classes of materials, including inorganic, organic, metal-organic, complexes and polymers. However, macromolecules (e.g. proteins), that are also grown from solution, achieve a size of only a few millimeters. Solution growth offers the convenience of low operating temperatures, less complicated growth apparatus, and simple instrumentation. However, it demands precise control of the experimental conditions. Unlike melt and flux growth, the method does not allow wide variation from optimum growth conditions. Since the present work concerns solution growth, it is described in some detail in the following sections.

1.3.1.1. Solution, solubility and supersolubility diagrams

A solution is a homogeneous mixture of a solute and a solvent. The choice of the solvent for a given solute is dictated by several parameters, including solubility and its temperature coefficient, viscosity, volatility, toxicity, availability, and cost effectiveness. One of the most commonly used solvents for crystal growth is water.

Solubility of a material in a solvent decides the amount of the material that can be dissolved in it at a particular temperature. If the solubility is too high, it is difficult to grow a large crystal from such a solution. This is because of its sensitivity to thermal fluctuations. At the same time, if the solubility is low, it restricts the growth of large crystals since enough solute is not available for crystallization. The solubility of the material is measured by dissolving it in a continuously stirred solvent; this is done at several temperatures. A relationship so obtained between concentration and temperature fields is referred to as the *solubility diagram*. Figure 1.6 shows a typical solubility diagram. The solubility diagram can be divided into three distinct zones:

i) The *stable zone* of an undersaturated solution where no nucleation or crystal growth is possible. Existing crystals will simply dissolve in the solvent.
ii) The *metastable zone* where growth occurs but spontaneous nucleation does not.
iii) The *labile zone*, where supersaturation is so high that spontaneous nucleation occurs.

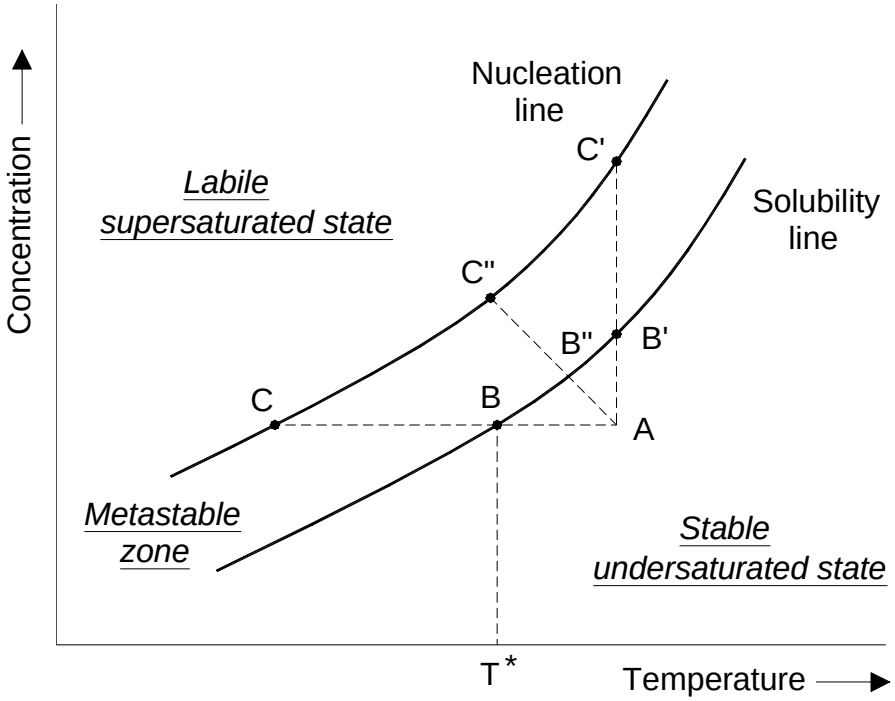

Figure 1.6. A typical solubility-supersolubility diagram (after Mullin, 2001).

1.3.1.2. Driving force for crystal growth

The prerequisite for crystallization to take place is the creation of a suitable driving force for the nucleation to occur. In solution growth, this driving force is referred to as *supersaturation*. It is a state of the solution achieved by manipulating its thermal behavior. It can be achieved in the following three ways:

- **Cooling**: Cooling a saturated solution will result in a supersaturated solution. This corresponds to the horizontal line ABC in Figure 1.6.
- **Evaporation**: Evaporation of the solvent leads to an increase in concentration of the solution, leading to a supersaturated solution. It corresponds to the vertical line AB′C′ in Figure 1.6.
- At times, a combination of cooling and evaporation is adopted. This corresponds to a line like AB″C″ in the above figure.

Technologically, the temperature-reducing technique is the simplest and therefore the commonest. The rate of temperature reduction is chosen carefully, taking into consideration the saturation temperature, the solubility gradient, the volume of the solution, and the dimensions of the crystal available for solute deposition.

1.3.1.3. State of supersaturation

The state of supersaturation can be expressed in terms of any one of the following three quantities:

- **Supercooling:** $\Delta T = T_s - T_g$, where T_s is the saturation temperature and T_g is the growth temperature.
- **Concentration difference**: $\Delta C = C_s - C_g$, *where* C_s is the concentration at saturation temperature and C_g is the actual concentration at the growth temperature. The concentration is expressed in units of x gm of solute per 1000 gm of solvent.
- **Relative supersaturation**: $\sigma = \frac{C_s - C_g}{C_s}$; it is a quantity whose value is usually in the range of ~ 0.05 to 0.5.

1.3.2. Melt growth

Melt growth is used for those solids that can be melted reversibly without chemical decomposition. This usually refers to materials that melt congruently or near congruently, such as a large number of inorganic and semiconductor materials. The growth rate achievable by melt growth is in the range of several millimeters per hour, and is several orders of magnitude greater than solution or vapor growth. Since no foreign molecules are present in the melt, the compositional purity of crystals is high in the case of melt growth when compared with other techniques. A variety of methods are possible for growing crystals from their melt: for example, Bridgman-Stockbarger method, Kyropoulos method, Czochralski method (popularly called the crystal pulling method) and zone melting method. The most widely used is the Czochralski method. The material to be grown (referred to as charge) is melted in a platinum or iridium crucible by employing induction or resistance heating. A seed crystal is then lowered into the molten charge at a temperature just above its melting point such that it just touches the top surface of the melt. By minor adjustment of the temperature, a proper growth interface is achieved between the melt surface and the seed crystal. It is followed by activation of a slow pulling and rotating mechanism to achieve the necking of the crystal. The pull rate is adjusted depending upon the desired crystal diameter. In order to achieve a constant-diameter crystal, several parameters have to be optimized, such as the pulling rate, rate of melt level drop in crucible, heat transfer rates in and out of the system, and the crystal and crucible rotations. Commercially available modern crystal pullers are designed to achieve diameter control. It involves an electronic feedback mechanism to weigh the growing crystal or the melt plus crucible and compare it with the expected rate of increase of the weight of crystal. The

difference is utilized as an error signal to dynamically adjust the pull rate. Alternatively, one can adjust the heater power.

1.3.3. Flux growth

Flux growth can be divided into growth from single component or growth from multi-component mixtures. For single component growth, the nutrient material to be grown alone is melted. For a multi-component charge, the nutrient material is mixed with another chemical before the start of crystallization. Growth from multi-components is performed when the nutrient material melts incongruently, i.e. the material decomposes before melting, so that crystallization by the conventional melt growth technique is not possible. Here, a different phase at the melting temperature is obtained when compared to the one that is required. The secondary component added to the nutrient is called *flux*. It helps in reducing the crystallization temperature so that the desired phase can be crystallized. The nutrient and the flux are placed in a crucible, heated above the liquidus temperature, and allowed to cool. It is expected that one (or may be a few) spontaneously nucleated crystals would grow to a fairly large dimension. Once the growth is complete, the flux is leached or dissolved away to get the grown crystal. This method is also called high temperature solution growth. This method of growth can also be implemented in the following manner: A seed crystal is introduced in the crucible charge and one stable crystal alone is allowed to grow, rather then leaving the crystals to spontaneously nucleate and grow. Homogenization of the melt is achieved by adopting rotation of the seed crystal. This method is called top-seeded solution growth.

1.3.4. Vapor growth

In order to grow crystals from the vapor phase, the solid nutrient phase is vaporized at a temperature above its sublimation temperature. The nutrient and the carrier gas are transported to a second region at a slightly lower temperature, resulting in the supersaturation of the nutrient phase. Supersaturation, when controlled properly, results in crystalline growth of the nutrient material. Any material that can be sublimed without causing its decomposition lends the possibility of its crystalline phase growth by the vapor transport technique. The parameters to be controlled during vapor growth are supersaturation of the nutrient material in the vapor phase, temperature and pressure gradients inside the enclosure, the transfer rate of the vapors from their generation to the region of growth, and the characteristics of a carrier gas, if used. Compared to the other three methods of growth discussed above, the growth rate and the size of the crystal

achievable in vapor growth are small. These limit its usability for growing bulk crystals, though the possibility of growing relatively defect-free crystals is there.

1.4. Optical applications of crystals

Some of the representative crystals grown by the above described techniques, and their optical applications are listed below.

i) Solution growth is used for the following crystals: KDP (potassium dihydrogen phosphate, KH_2PO_4) and its deuterated analogue DKDP (KD_2PO_4) for frequency conversion and electro-optic switching (Q-switches and Pockels cell) respectively; TGS (triglycine sulphate) for laser-energy measuring devices; KAP (potassium acid phthalate) for monochromator applications; $LiIO_3$, ZTS [zinc tris (thiourea) sulphate], and many organic and metal-organic crystals for frequency conversion and other non-linear-optical applications.

ii) Melt growth (by the Czochralski method) is used to grow the following crystals for respective applications: $LiNbO_3$ as a waveguide material for integrated optics, for electro-optic modulation in switching applications and for acousto-optic modulation in SAW devices. Its doped variants such as $MgO:LiNbO_3$ for applications requiring high laser damage thresholds, $Fe:LiNbO_3$ for holographic data storage applications, $Cr:LiNbO_3$ for laser host applications. Ba:PBO (barium doped lead tetraborate, $Ba:PbB_4O_7$) as a high-laser-damage-threshold material; LBO (lithium tetra borate, $Li_2B_4O_7$) for dosimetry applications and for higher order frequency conversion of Nd:YAG fundamental laser line and as an optical parametric oscillator for radiation source in the visible range; Nd:YAG (Nd doped yttrium aluminum garnet) as laser host crystal; $Nd:YVO_4$ (Nd doped yttrium vanadate) for diode pumped solid-state laser applications; $LiTaO_3$ (lithium tantalate) for electro-optic switching and high damage threshold applications; $Ce:BaTiO_3$ (cerium doped barium titanate) and BSO ($Bi_{12}SiO_{20}$) for photorefractive and holographic applications; BGO (bismuth germanate, $Bi_4Ge_3O_{12}$), and PWO (lead tungstate, $PbWO_4$) as good scintillator materials that find wide application in high energy physics, nuclear and space physics applications; and PMO (lead molybdate, $PbMoO_4$) for acousto-optic devices and scintillator applications.

iii) Flux growth is used to grow KTP (potassium titanyl phosphate) for frequency conversion of Nd:YAG laser line, for E-O switching

applications, as an optical parametric source of tunable output from visible to mid-IR, and in integrated optics as waveguide based on ion-exchange on KTP substrate; BBO (β-barium borate, β-BaB_2O_4) for higher-order frequency conversion of Nd:YAG laser line and for optical parametric oscillator and amplifier applications; CLBO (cesium-doped lithium borate, $CsLiB_6O_{10}$) for UV applications and for generating the 4^{th} and 5^{th} harmonics of the Nd:YAG laser line.

1.5. Why emphasize crystal growth from solution?

Since He-Ne laser based optical diagnostics are being used for studying the process of crystal growth, therefore it is essential that the growth medium be transparent to the laser beam. Among the various methods of growth only solution growth satisfies this requirement. It is also the easiest to experiment with because of the near-ambient working temperature. For these reasons, the present work is primarily focused on crystal growth from solution.

1.6. Why map the solution parameters?

Crystal growth is a complex non-equilibrium process, which despite half a century of experiments and theoretical analysis, is still not fully understood. While materials scientists need to have a detailed understanding of how crystals grow, device Engineers need to grow large, relatively defect-free crystals that are optimal for their ultimate applications. The ultimate goal of research on crystal growth is to achieve an in-depth understanding of the process with the aim of improving the microscopic and macroscopic homogeneity of the grown crystals, in addition to increasing their size.

A crystal growing from solution creates thermal and concentration gradients in the surrounding solution by releasing the heat of crystallization and depleting the solute near the growth surface. The resultant temperature and concentration gradients affect the perfection and stability of the crystal grown (Bunn, 1949). The change of solution density with temperature ($d\rho/dT$) is negative and the change of solution density with solute concentration ($d\rho/dC$) is positive. Therefore, crystal growth in the Earth's gravitational field is accompanied by a rising buoyant convection current which envelops the crystal, is often oscillatory and unstable, and therefore drastically modifies the concentration gradient along the growth interface (Chen, 1979A and 1979B). Thus, the growth history and defect structure of the crystal is a function of the time-dependent spatial distribution of the convection patterns, and of the temperature and concentration profiles in the surrounding solution. Therefore, in order to learn how to grow large

defect-free crystals, it is helpful to map the spatial distribution of the solution properties during growth.

Techniques for visualizing the temperature and concentration fields in an aqueous solution have often been used to monitor crystal growth. In addition to these two parameters, a necessary step in growing large inclusion-free crystals is the optimization of convection patterns. This has implications on mechanisms of growth, the onset of morphological instability, and has strong relationship with growth rate and crystal quality. This review paper, discusses mapping of the convection patterns around a crystal growing from solution in different geometries, and their influence on the growth rate and crystal quality.

1.7. Phenomenology of crystal growth from solution

The rate of crystallization is determined by its slowest stage. Two major stages can be identified: (1) supply of crystallization material from the solution to the crystallization surface; (2) incorporation of this material into the crystal structure, i.e. growth of the crystal. If the first stage is the limiting step, the growth is said to proceed in the *diffusion regime*. If the second stage is the limiting step, growth is said to be operating in the *kinetic regime*. Diffusion regime conditions are prevalent during free convection growth, also referred as buoyancy-driven growth. In practice, forced flow conditions are adopted. These conditions bring the process into the kinetic regime of growth and are achieved by employing various modes of stirring. Here the solute is forced to move from the bulk solution towards the crystal surface. There is increased probability of occurrence of defects under irregular or turbulent flow conditions. Under such conditions the growth rate is high. Therefore, the mass transfer and the fluid flow conditions have to be optimized to avoid deleterious effects such as morphological instability, spurious nucleation, and inclusions. Thus, of particular importance in crystal growth from solution are fluid flow, and heat and mass transfer.

1.7.1. Crystal growth from solution in the absence of gravity

Even in the absence of gravity, crystal growth from solution is a complex process, with several potential causes of instability. The basic process - the diffusion of solute from a supersaturated solution to the crystal-solution interface where the solute is incorporated into the crystal - is complicated by several factors. For example, (a) Since the concentration of solute in the solution increases as one moves away from the growth interface, a projecting portion of the growth surface would be expected to grow faster than the rest of the face, (b) Since the crystal grows as a faceted polyhedron rather than a sphere, the concentration gradients in the diffusion zone are not uniform. If interface kinetics is ignored, the corners ought to grow faster than the rest of

the crystal, (c) Transport of solute to the interface does not lead directly to immediate incorporation into the crystal. The intervening steps such as dehydration, adsorption, and surface diffusion to growth sites are grouped under terms such as *growth mechanism* or *interface kinetics*, (d) The processes described in (c) release (or, in some cases, absorb) heat which must be transported away from the interface, either through the crystal or through the solution, (e) In order to maintain supersaturation conditions in the solution for prolonged growth, the solute must be replenished. Methods adopted are forced convection or slow cooling, which creates temperature gradients throughout the solution, (f) Spurious nuclei - unwanted crystals nucleated spontaneously in the supersaturated solution create their own localized depletion zones, which can perturb the growth of the main crystal if they are numerous or grow to be large. These processes make the physics of crystal growth severely complex.

1.7.2. Effect of gravity on solution growth

The principal effect of gravity on crystal growth is to introduce several forms of buoyant convection. For all solutions of interest, the density increases with solute concentration. Therefore, the solute-depleted solution around the crystal tends to rise and converge in a plume above the crystal, while the undepleted solution rises from beneath or around the crystal as shown in Figure 1.7a (Wilcox, 1983; Shlichta, 1985; Verma, 2008A). The heat given off by crystallization also contributes to convection, but to a far smaller degree. A second mode of buoyant convection (Figure 1.7b) occurs when the solution is cooled to maintain supersaturation, since the heat-flow-induced temperature gradients are also density gradients. Other modes of buoyant convection are caused by growth stabilizing techniques such as stirring (Figure 1.7c). Finally, if spurious nuclei occur in a gravitational field and are not suitably removed, they can descend to the bottom of the chamber and act as convection pumps (Figure 1.7d). These modes of convection interact with each other in a complex time-dependent manner that is difficult to completely analyze. Even in the absence of other sources of convection, the solute-depletion convection is spatially irregular because of boundary-layer discontinuities at crystal edges and corners. It is subject to periodic oscillations and unstable responses to small transient accelerations (Wilcox, 1983). These phenomena are described in detail by Chen (1977). For a comprehensive discussion on the importance of transport phenomena in crystal growth from solution, the reader is refereed to a review by Wilcox (1993). Gravity-induced convection can significantly affect crystal growth in several ways. For example, (a) Convection greatly increases the rate of solute transport to the growth interface by replacing the solute diffusion zone with a

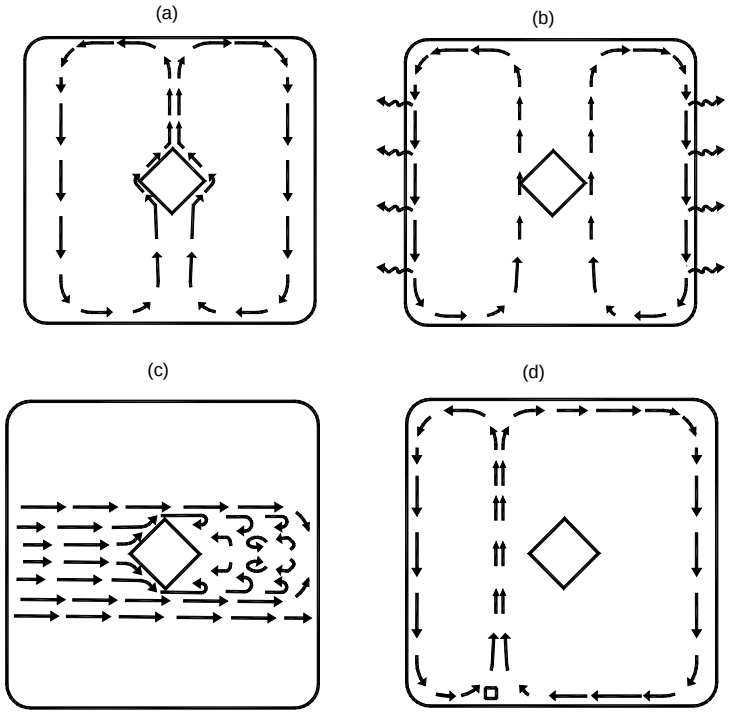

Figure 1.7. (a) Solute depleted solution around the crystal tends to rise and converge in a plume above the crystal; (b) Buoyant convection arises when the solution is cooled to maintain supersaturation; (c) Other modes of buoyant convection are caused by growth-stabilizing techniques such as stirring; (d) Spurious nucleation sites act as convection pumps [Shlichta 1985, Verma, 2008B].

much narrower boundary layer. As a consequence, the crystal growth rate is increased by several orders of magnitude; (b) The relationship between convection and the formation of fluid inclusions is extremely complex. In the absence of all modes of convection, fluid inclusions can be formed either because of the interface instability described in Section 1.7.1, or by the convergence or intersection of layers growing inward from edges and corners, as described in this section. Under uniform laminar convection, whether buoyant or forced, inclusions can form if convection rates are slow enough to allow solute depletion in the boundary layers; this is another reason for the use of forced convection during the growth of large crystals. For moderate buoyant convection, Chen *et al.* (1977) have shown that inclusions tend to occur (i) in stagnation zone such as the center of the bottom face, (ii) in the solute-depleted upper regimes of the side faces, and (iii) at the boundaries of convection cells on the top face (Figure 1.8). Therefore, inclusions share a complex relation with fluid convection; (c) Dislocations are formed by mechanisms similar to those postulated for fluid inclusions, e.g. the convergence or intersection of growth layers and growth

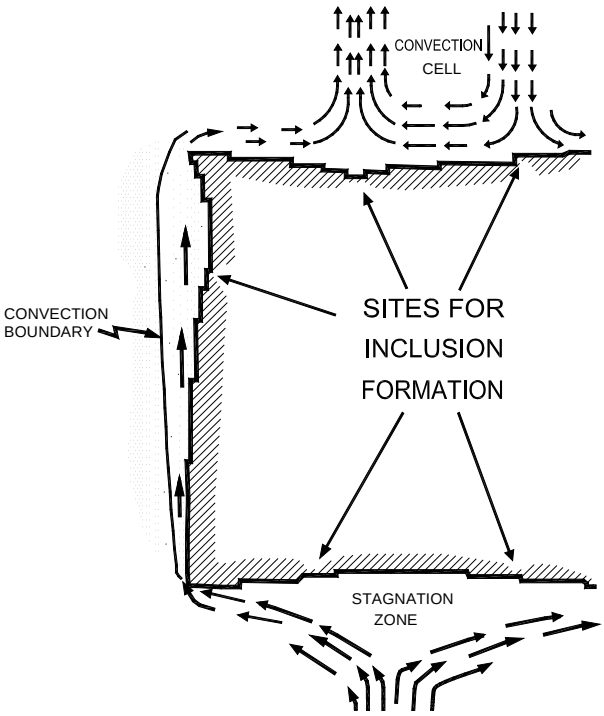

Figure 1.8. Inclusions tend to occur (a) as a result of stagnation zone, (b) on the upper regimes of side faces, and (c) at the boundaries of convection cells [Shlichta 1985, Verma, 2008B].

around a bubble. It may therefore be inferred that dislocation formation is related to convective motion; (d) During the melt growth of semiconductor and oxide crystals, convective oscillations from temperature instabilities result in fluctuation of the doping concentration. These doping inhomogeneities are visible as striated patterns in microscopic pictures of etched crystal surfaces.

1.8. Optical imaging: Why and How?

One could measure solution properties with probes such as thermistors, pH/ion electrodes, and anemometers. The use of probes, however, is always subject to an analog of the quantum-mechanical uncertainty principle in that a few probes provide inadequate data while a high density of probes interact with and distort the system being measured. For example, a single moving probe yields temporally inaccurate data if moved slowly, but stirs the system if moved rapidly. Therefore, probes are useful for providing reference points, but are never a satisfactory method for spatially mapping a system with which they can interact, such as the solution around a growing crystal.

In contrast, optical techniques correspond to the use of *photon probes* that do not perceptibly affect the process being studied. They can map the

properties of the process with a spatial resolution of less than a micrometer and a temporal resolution of less than a millisecond. The response of optical diagnostics is practically inertia-free and has the additional advantage of providing a volume of data of the process under study. Because of these reasons, as well as the availability of fast image acquisition hardware and advanced computers for data reduction, optical diagnostics have seen their revival in the last decade.

1.9. 2D or 3D imaging?

Most optical imaging techniques have a major limitation of providing only a two-dimensional map of the cumulative or average solution property along the viewing direction. This limitation is not serious for many purposes, such as determining the stability and uniformity of convection around a crystal. From an analytical viewpoint, two-dimensional experiments are much simpler to analyze and are generally a useful precursor to a full three-dimensional analysis. For experiments that require three-dimensional mapping, one can consider the use of holography (Hariharan, 1986 and 2002), tomography (three-dimensional reconstruction from a set of angularly differentiated two-dimensional projections) (Herman, 1980; Natterer, 2001), or scanning techniques such as laser-Doppler anemometry (Durst, 1981; Adrian, 1983) and particle velocimetry (Adrian, 1991; Raffel, 1998). The trend in measurements appears to emphasize complex but realistic three-dimensional experiments. In the present work, two-dimensional mapping techniques of shadowgraphy is discussed first, followed by its extension to three-dimensional imaging by tomography.

1.10. Objectives of the present work

The discussion presented in the preceding sections show that fluid convection is an important parameter during crystal growth from an aqueous solution. It strongly influences the growth rate and the quality of the growing crystal. Therefore, the relationship between convection and crystal growth phenomenon has been reviewed in this paper. As a case study, KDP crystal has been chosen because of the availability of data (thermodynamic and optical) related to its growth. In particular, the convection patterns in three different growth geometries have been imaged using shadowgraphy, interferometry and tomography techniques, and its relationship to crystal growth rate and quality presented. The apparatus and instrumentation developed for these experiments is also described in detail. The relationship between free and forced convection during growth with the growth rate and crystal quality is explored. An appropriate quantitative fluid-dynamical criterion is put forth to monitor this relationship. By on-line and *in-situ*

shadowgraph imaging of the growth process under different levels of supercooling (or supersaturation), a safe cooling rate range has been proposed that ensures good quality of the growing crystal with reasonable growth rates. Additionally, the convective features observed in the images are analyzed to infer the growth mechanisms operating at different levels of supersaturation. A comparison between shadowgraphy and Mach-Zehnder interferometry is reported for imaging concentration profiles around a growing crystal. Tomographic reconstruction of shadowgraph projection data is performed for obtaining three-dimensional concentration profiles above a growing crystal.

1.11. Organization of the paper

The paper is organized in the following manner: Section 1 is an introduction to crystal-growth. It covers the basic physics of crystal growth and the different growth mechanisms, followed by a brief description of the different methods of growing crystals. A detailed discussion on the phenomenology of crystal growth from solution is presented next. The salient features of optical techniques and the reasons for performing three-dimensional imaging of crystal growth process are discussed last. Section 2 is a review of the existing literature on the use of optical imaging techniques and computerized tomography for mapping convection during crystal growth from solution. Section 3 describes the apparatus and instrumentation developed and the experimental procedures adopted. Section 4 describes the mathematical formulation of the data analysis procedure for (a) shadowgraph images, (b) Mach-Zehnder interferograms in wedge and infinite setting modes, and (c) algorithms for computerized tomography. Section 5 discusses the shadowgraph imaging of convection for growth in free and forced convection conditions in three different geometries. Section 6 presents interferograms in the wedge and infinite settings Mach-Zehnder interferometer under different convection conditions and growth geometries. Section 7 presents the procedure of three-dimensional reconstruction of the convective field by computerized tomography, using shadowgraph images as the projection data. Section 8 presents conclusions drawn from the present study, followed by a discussion on the scope for future work.

2. Literature survey

In the present section literature in the following areas is surveyed: a) Transport phenomena in crystal growth from solution; b) Optical imaging techniques to map transport processes during crystal growth; (c) Optical imaging of surface microstructure of the growing crystal faces; d) Tomographic imaging in fluids in general and crystal growth in particular.

2.1. Transport phenomena during crystal growth from solution

Wilcox (1983 & 1993) discussed the role of transport phenomena in crystal growth from solution. According to the author, transport processes of fluid motion (convection), heat transfer, and mass transfer strongly influence growth rate, crystal morphology (shape), and formation mechanism of defects such as inclusions. It is suggested that inclusions can be avoided by growing the crystal either very slowly or under well-controlled vigorous convection. The concept of boundary layers, as understood in terms of crystal growth from solution, has been explained. The importance of using various dimensionless numbers in estimating the strength of transport phenomena during crystal growth has been brought out.

Rosmalen *et al.* (1978) investigated the phenomena of inclusion formation by performing flow visualization experiments in a wind tunnel. They observed that at low Reynolds numbers (~ 600) the flow at the rear faces of the crystal results in a closed wake which restricts proper mixing of the solution. This then becomes a cause for inclusions on the KDP faces opposite to the flow direction. At high Reynolds numbers (~ 2500), turbulence causes good mixing of the solution in the wake and hence a better quality of crystal is obtained.

Derby and coworkers (Zhou & Derby, 1997 & Yeckel *et al.* 1998, Vartak *et al.*, 2000 & 2005) performed 3D time-dependent computations to understand the influence of solution hydrodynamics and mass transport processes during KDP and KTP crystal growth. They demonstrated that support structure, crystal geometry, and crystal orientation play important roles in establishing favorable flows during the growth of these two crystals.

2.2. Optical techniques for imaging transport phenomena during crystal growth

In this section a survey of optical techniques for two-dimensional mapping of the solution properties is presented.

Merzkirch's (1987) textbook discusses several optical techniques for the purpose of flow visualization. A more recent compilation of classical and modern optical diagnostics for engineering applications is provided by Mayinger (1994). The volume edited by Goldstein (1996) contains a chapter discussing optical measurement techniques of shadowgraphy, schlieren and Mach-Zehnder interferometry for fluid flow, and heat and mass transfer studies. Settles (2001) provides a comprehensive summary of the applications of shadowgraph and schlieren techniques in all fields of science and engineering. The specific use of optical techniques in crystal growth research is cited below.

Chen (1977) used time-lapse schlieren cinematography to study natural convection patterns around a growing $NaClO_3$ crystal and their relation to crystal defect formation. The author quantified the convective behavior in terms of the *Grashof* number and found that it made a transition from steady laminar to irregular flow when the Grashof number crossed a critical value. In a separate study on the same material, Chen *et al.* (1979A) found that the plume behavior changed from steady-state laminar flow to irregular or oscillatory nature when either the supersaturation or the size of the crystal increased.

Shlichta (1985) used absorption and interferometric techniques to observe small levels of convection in microgravity environment and studied its influence on defect distribution in crystals grown from solution. The main result of their study was that inclusions are related to local variations in convection and interface solute concentration rather than to the overall level of convection in the chamber. It was reported that the crystals grown in high-gravity centrifugal fields show much less inclusions than those grown under normal gravity.

Shlichta (1986) published first review article on the applicability of optical techniques in mapping solution properties during protein crystal growth. The author presented a comparative analysis in the context of protein-crystal growth among schlieren, two-beam interferometry, multiple-beam interferometry, double-exposure holographic interferometry, real-time holographic interferometry, ultra-violet solute absorption, and laser anemometry in terms of sensitivity, real-time motoring capability, ease of setting up experiments, quantitative interpretation, and spatial resolution. The author pointed out that for imaging concentration and convection during protein crystal growth, schlieren and interferometric techniques are only marginally sensitive, while phase contrast schlieren, UV solute-absorption, and laser anemometry are more appropriate. The double-exposure holography and birefringence color mapping (change in the interference color as the crystal dimension increases) were found to be ideal techniques for measuring growth rates of protein crystals.

Bedarida (1986) used single-beam, real-time holographic interferometry to understand the relationship between the growth rate of the individual faces of the growing crystal and the solution concentration near it.

Using schlieren and Mach-Zehnder interferometry, Onuma *et al.* (1988 & 1989B) visualized the diffusion boundary layer and buoyancy-driven convection around growing $Ba(NO_3)_2$ and CdI_2 crystals. The authors found that with increase of supersaturation the plume activity increased.

Since the real driving force for the growth process is surface supersaturation rather than bulk supersaturation, Onuma *et al.* (1989A) used a Mach-Zehnder interferometer to measure the surface supersaturation under

different flow velocities of the solution flowing over the face of a growing K-alum crystal. It was established that a linear relationship does not exist between bulk and surface supersaturation. Onuma *et al.* (1993) used a real-time phase-shifting interferometer to measure concentration over the surface of a $NaClO_3$ crystal under different conditions of convection. The authors showed that the phase-shifting technique is at least 25 times more sensitive than conventional interferometry. Sunagawa and his group have extensively applied optical techniques for studying crystal growth mechanisms, which has been summarized in a review article by Sunagawa *et al.* (1995).

Szurgot (1991) studied the importance of free convection on the surface microtopography and macro-morphology of potassium bichromate crystals growing from an unstirred aqueous solution. They observed that the surface topography was different not only for different faces but also for various parts of the same face. Results showed that the local micromorphology of KBC crystals growing from the unstirred aqueous solution was a result of superposition of solute diffusion and fluid convection.

Yu *et al.* (1994) used holographic interferometry to understand the difference between the diffusion boundary layer and the solute boundary layer near the growing KDP and KTP crystals. The authors observed that the *diffusion boundary layer* is formed due to only diffusion, and was defined as the distance between interface and the point where the tangent of the concentration profile at the surface crosses the bulk concentration profile. On the other hand the *solute boundary layer* had flowing solution and not stagnant, and was defined as the distance between the crystal face and the point where the normal concentration gradient is close to zero. According to the study, the solute boundary layer thickness on different faces of the crystal can be different for a given bulk supersaturation. Moreover, the boundary layer thickness on the faces was observed to vary with position. This indicates that the mass transport within the boundary layer is not merely a diffusion process, but a coupled effect of diffusion and convection. The authors measured holographically the refractive index profile inside the boundary layer and found it to be exponential.

Kim *et al.* (1998A) employed a Mach-Zehnder interferometer to study the rate of change in concentration of the solution at the interface between the crystal and solution as a function of time. Using the interferometer, the authors found values of *dn/dc* for L-Arginine Phosphate (LAP) crystal as 9.4074×10^{-5} [g LAP / liter H_2O]$^{-1}$. Kim *et al.* (1998B) developed a common-path Zeeman interferometer to measure the solution refractive index around the growing crystal to an accuracy of 10^{-8}. This was 100 times better than the resolution of conventional interferometers (Mach-Zehnder and shearing) used for a similar purpose. Using this technique, the authors also developed a

scanning interferometric system that was capable of measuring the refractive index profile in the interface region of the growing crystal.

Duan *et al.* (2001) used a phase-shifting Mach-Zehnder interferometer to map minute buoyancy driven convective features and measure the refractive index distribution around a growing $NaClO_3$ crystal. The authors showed that the convective phenomenon dominates over other parameters in controlling the growth rate.

Kang *et al.* (2001) used particle image velocimetry and phase-sifting Mach-Zehnder interferometry to map the convection and the concentration fields during the growth of $NaClO_3$ crystals. The two-dimensional velocity distributions were found to match the concentration fields, and the coupling of convection with concentration was analyzed.

Chen *et al.* (2002) used a Mach-Zehnder interferometer to visualize the solutal boundary layer and the concentration distribution during the growth and dissolution of $NaClO_3$ crystals. Results indicated that the boundary layer thickness depends on the fluid-dynamic conditions and the position of the crystal face under study.

Srivastava *et al.* (2004) used schlieren, shadowgraph and interferometry technique for visualizing convection around a growing KDP crystal. The aim of the authors was to compare the three techniques with respect to the ease of instrumentation, quality of images, and the scope of quantitative analysis, and settled in favor of schlieren technique.

A state-of-the-art review published recently by Verma & Shlichta (2008B) summarizes optical, electromagnetic, and acoustic imaging techniques that are in use or available for mapping convection, temperature, and solute concentration in the solution around a growing crystal and for measuring the growth rate and the micromorphology of the crystal face itself. The need and value of such mapping, and the comparative value of two- vs. three-dimensional mapping are discussed. They authors report that convection can be mapped by measuring refractive index differences, solute concentration, displacements of particles, or velocity measurements directly. Solution temperature can be mapped either by physical probes, liquid crystal thermography, thermochromism, fluorescence, or interferometric. Solution concentration can be mapped by phase shifting interferometry, electronic speckle pattern interferometry, or optical absorption. Simultaneous measurement of temperature and concentration can be performed using dual-wavelength interferometry or a combination of absorption and interferometry. The measurement of the growth rate and the mapping of facial micromorphology are feasible by optical rotation, cathetometry, by combinations of microscopy and interferometry, and by atomic-level techniques such as atomic force microscopy. Some modes of measurement

can be extended to three-dimensional imaging by holography and optical tomography. This review concludes that although some optical techniques have been extensively used to study crystal growth from solution, many other promising techniques are yet to be explored.

2.3. Optical imaging of surface microstructure of crystal faces

Growth kinetic studies and mapping of surface micromorphology of habit faces of a crystal are indispensable for any comparison of theory with experiment. Due to this reason, the survey of literature on mapping surface microstructure using interferometric techniques is presented in this section.

Chernov *et al.* (1984) and Rashkovich and Shustin (1987) have described several single-beam interferometric techniques such as conoscopy, bilens method, interference of converging light reflected from two parallel faces of the crystal (fringes of equal inclination), and two-beam techniques such as Michelson interferometry for monitoring of the growth rates and other surface-kinetic parameters for crystals growing from solution.

Rashkovich *et al.* (1982) used interference between e- and o- rays, generated inside a birefringent crystal placed between crossed polarizers, for measuring the growth rates of individual faces of crystals. The authors used it in converging beam of light (conoscopy) to study the kinetics of (001) face of TGS crystals growing from a stirred solution. This technique is the easiest to set up and has the advantage that it can be used to record growth rate even in a stirred solution environment. More recently, this technique in parallel mode was used by Sharma *et al.* (2002) for studying the influence of pH and supersaturation on the growth kinetics of prismatic and pyramidal faces of a KDP crystal.

Rashkovich *et al.* (1985) used a Michelson interferometer to study the dependence of normal growth rate (R) and the slope (p) of the dislocation hillock, and the tangential growth rate (V) of the steps on the (100) face of KDP crystal as a function of supersaturation (σ). The main difference between the interference patterns of the hillocks originating from weak (single dislocation) and strong (a group of dislocations) sources is in the slope (steepness), which manifests itself in the form of distance between the concentric fringes. For a given supersaturation, R and p of the strong sources were several times greater than for weak sources.

In studies employing Michelson interferometry (Chernov *et al.*, 1986 & Chernov and Malkin, 1988), the growth kinetics of prismatic (001) and pyramidal (101) face of ADP crystal was investigated at several supersaturation and pH values of the solution. It was found that the growth

and dissolution rates at the location of steps were nearly equal, while at the site of dislocation the dissolution rate was several times that of the growth rate. This observation was attributed to the stress field around a dislocation source. The reason for the large difference in the growth rates of pyramidal and prismatic faces of ADP crystal was attributed to the value of the kinetic coefficient of steps (β) (their rate of incorporation), being two orders of magnitude greater for the pyramidal faces than the prismatic faces.

Rashkovich and Shekunov (1990A, 1990B, 1990C) used the Michelson interferometer to investigate the effect of surface supersaturation and solution flow velocity (hydrodynamics) on the morphological stability of the prismatic faces of ADP and KDP crystals. They found that at low values of σ, the face is covered with a regular-shaped hillock having equispaced steps, while at higher values of σ, the growth velocity of steps on the hillock increases. Thus, either the steps coalesce, leading to the formation of pits, or the edge of the steps loses its stability leading to a macrosteps. The corresponding change in the interference fringes is seen as a shift from equispaced, concentric, elliptic fringes to irregular and jumbled fringes. The velocity and direction of solution flow is also intricately linked to the surface micromorphology through its influence on the supersaturation. Hydrodynamics influences the surface supersaturation over the crystal face, leading to a strong influence over the surface micromorphology. The authors observed that the probability of formation of macrosteps and pits, which result in the loss of morphological stability of the face, is far less at low (1-5 cm/s) as well as at high (75 cm/s) flow rates, as compared to that at moderate fluid speeds (20-30 cm/s). Hence the reason the probability of inclusion formation is higher at intermediate flow rates.

Maiwa *et al.* (1990) used a micro-Michelson interferometer attached to a microscope objective for *in-situ* imaging of the micromorphology of dislocation hillocks on the (111) face of $Ba(NO_3)_2$ crystal. The normal growth rate (R), slope (p), and the tangential velocity (V) of the steps generated from screw and mixed type of dislocations at different flow velocities of the solution were measured. The growth rate, the slope of the hillock, and the step heights were greater for the screw-dislocation-generated hillock than for the mixed type.

Onuma *et al.* (1990, 1991) used a Michelson interferometer for studying the effect of surface supersaturation on the growth and dissolution kinetics of the (111) face of K-alum crystals. The contribution of surface kinetics as compared to diffusion process was smaller for the dissolution process than for growth. Impurities affected growth and dissolution differently at low supersaturations. The real-time phase-shift interferometry developed by Nakadate and Yamaguchi (1990) was incorporated into a Michelson

interferometer by Onuma *et al.* (1994) for measuring surface features as small as 0.92 nm over a growing $Ba(NO_3)_2$ crystal face. This was an order of magnitude improvement over the conventional two-beam interferometry.

In a series of investigations employing Michelson interferometry, Vekilov and coworkers studied various aspects of the growth and dissolution kinetics of the pyramidal (101) face of the ADP crystal. The authors studied the kinetics of dislocation hillocks on the (101) pyramidal face of the ADP crystal in an undersaturated solution (Vekilov *et al.*, 1990). Subsequently different aspects of the growth kinetics, such as the influence of changing dislocation source activity (Vekilov *et al.*, 1992A), the influence of temperature on the movement of steps present on the dislocation hillock (Vekilov *et al.*, 1992B), and the process of step-step interaction (Vekilov *et al.*, 1992C) were studied.

Further, Vekilov and coworkers (Vekilov *et al.* 1993A, 1993B, 1995A) made several interesting investigations on the mechanism of protein crystal growth using Michelson interferometry. Specifically the role of dislocations and two-dimensional nucleation on the growth of lysozyme crystals, and the growth poisoning effect of impurities was studied. For the (101) face of the lysozyme crystal, the authors reported that at very low supersaturation (< 0.4), the impurities poison the steps leading to the cessation of growth. For the intermediate range of supersaturation (between 0.4 to 1.6), a dislocation-source-mediated spiral growth mechanism was observed. Above a certain value, two-dimensional nucleation mechanism took over. In order to increase the resolution of growth rate measurements, Vekilov *et al.* (1995B) developed a methodology of using the phase information contained in the interference intensity distribution. The thickness variation (and hence the growth rate) at any point on the lysozyme crystal surface was measured by detecting the gray value of the pixel corresponding to that point in the Michelson interferogram and recording its sinusoidal variation with time.

Rashkovich and Moldazhanova (1995) used Michelson interferometer to understand the influence of pH on the crystal habit as well as micromorphology of the prismatic and pyramidal faces of the KDP crystal. The kinetic parameters, viz., the free energy and the kinetic coefficient of the steps, were found to be uninfluenced by the solution acidity, while the critical supersaturation (σ^*) at which the tangential growth velocity (V) of the steps increases sharply for the prismatic faces was found to decrease with the deviation of the solution from the stoichiometric pH. The formation of macrosteps on the prismatic faces was observed to be faster under alkaline conditions than under acidic conditions, implying that the prismatic face of the crystal under alkaline solution was much worse than that under acidic environment. In addition, the crystal morphology tended to be isometric as

the solution deviated from stoichiometric pH. In separate studies, Rashkovich and Moldazhanova (1996A) and Rashkovich and Shekunov (1996B) used the Michelson interferometer to study the influence of Cr^{3+}, Fe^{3+} and Al^{3+} impurities on the growth kinetics of the prismatic faces of KDP and ADP crystals. These impurity ions act as growth stoppers and thus decelerate the movements of steps on the prismatic faces, with aluminum being the strongest, followed by iron and chromium.

In order to study the effect of convection on the kinetics of lysozyme growth, a forced flow setup coupled to the interferometer was developed by Vekilov and coworkers. It was found that forced convection decreases the unsteadiness of growth, thus achieving better quality of the final grown crystal. At the same time, the forced flow condition increased the interfacial transport, resulting in accumulation of impurities in the interface region, undermining the growth rate (Vekilov, 1998A, 1998B).

2.4. Optical tomography for fluids and crystal growth

For experiments that involve parameters varying in all three dimensions, quantitatively meaningful results are possible only if the three-dimensional imaging is performed. In order to accomplish 3D imaging one can consider the use of *holography* (Hariharan, 2002), *tomography* (three-dimensional reconstruction from a set of angularly differentiated two-dimensional projections) (Herman, 1980 and Natterer, 2001), or scanning techniques such as *laser Doppler anemometry* (Adrian, 1983) and *particle image velocimetry* (Raffel, 1998). Literature survey related to the use of computerized tomography in three dimensional imaging of fluid parameters is presented here.

Tomography algorithms: The principles and procedures for implementing transform-based reconstruction algorithms are described by Lewitt (1983), whereas the series-expansion based methods are discussed in a tutorial by Censor (1983).

In order to reconstruct a scalar field from its projections, it is essential that full and accurate projection data for all angles be known. However, sometimes due to experimental limitations such measurements are not possible, resulting in incomplete projection data. The effect of data inadequacy on reconstruction has been discussed by Macovski (1983). There are several approaches which have been proposed to handle such an ill-posed problem. An overview of such techniques has been presented by Rangayyan (1985), along with a comprehensive bibliography on the limited-view tomography algorithms.

Common errors in parallel beam CBP based reconstruction, such as the object-centering error, incorrect ray-sum error, detector imbalances, improper filter selection, and limited-data set have been discussed by Schneberk (1990). The artifact resulting from each source of error and possible remedy are suggested.

Subbarao *et al.* (1997) applied 9 different iterative algorithms for reconstruction of a three-dimensional temperature field in natural convection problems. The algorithms tried could be classified into three groups, namely algebraic reconstruction technique (ART), multiplicative algebraic reconstruction technique (MART), and maximization reconstruction technique (MRT). The ART based reconstruction showed systematic convergence with respect to the number of projections; MART produced less error compared to ART; MRT showed intermediate performance compared to ART and MART. The authors also studied the effect of the number of projections and projection angles on the reconstruction accuracy.

Mishra *et al.* (1999A) used interferometric projection data obtained from a Mach-Zehnder interferometer for reconstructing three-dimensional temperature field in a Rayleigh-Benard convection. Limited-view tomography was performed. Only two orthogonal projections were used, employing three different algorithms (ART, MART and Maximum Entropy Optimization Algorithm MAXENT). MART algorithm was found to be most suitable for reconstruction. The correctness of the reconstructed temperature field was tested by a cross-check against the projections from the remaining two view angles. In a subsequent study (Mishra *et al.* 1999B), six different MART-based algorithms were tested by the authors to obtain a robust algorithm which was found to have acceptability over wider range of relaxation factors, convergence, and sensitivity to noise in the projection data. A number of iterative algorithms (ART and MART) have been used by Mishra *et al.* (2004) to access the reconstruction accuracy from varying degrees of incomplete interferometric projection data.

Muralidhar (2001) reviewed different tomographic algorithms for 3D reconstruction of temperature field using interferometric projection data obtained during Rayleigh-Benard natural convection.

Optical tomography in fluids: Sweeney and Vest (1973) reconstructed refractive index field using multi-directional holographic interferograms as the projection data. It was found that for a limited projection data set, an accurate reconstruction could only be obtained if the redundancy of data increased. In a follow-up paper, the authors implemented this technique for reconstructing three-dimensional, asymmetric temperature field inside a fluid encountered during the natural convection process over a heated

horizontal surface (Sweeney and Vest, 1974). Reconstructions were performed under the assumption of straight-line propagation of the rays through the region of interest.

Cha and Vest (1981) presented an iterative scheme for three-dimensional reconstruction of strongly refracting fields using projection data obtained from multi-directional holographic interferometry. The algorithm was applied to the measurement of strongly refracting mass-transfer boundary layers. The bending of rays led to a curved path of the probing rays, resulting in projection data that cannot be handled under the usual straight-line approximation. This is particularly important for optical tomography wherein refraction errors can be significant.

Special numerical methodologies are required for tomographic reconstruction from incomplete or partial projection data arising from either the limited size of the probe beam or an opaque obstacle between the object and the radiation source. Vest and Prikryl (1984) reported a convolution based iterative algorithm for 3D reconstruction of density fields from an incomplete projection data set. An alternate method of reconstruction that can handle sparse projection data has been discussed by Cha and Sun (1990). It is based on iterative reconstruction of the complementary field, the difference between the exact field and its estimate. Through proper choice of the field estimate and use of *a priori* information, the method can compensate for the adverse effects of under-sampling. The methodology requires an initial guess of the object field to be reconstructed. The n^{th} estimate of the object field is updated based on the $(n\text{-}1)^{th}$ iteration values, till a sufficient convergence criterion is satisfied.

Snyder and Hesselink (1984) describe a tomographic procedure based on CBP using Shepp-Logan filter for reconstructing the density field around a helicopter rotor blade tip. The authors investigated, (a) effect of a limited number of view angles (20, 30, 40 and 90), (b) effect of partial projection data of the process field, and (c) ray bending effects on the reconstructed field. The authors obtained good reconstruction using only 40 views over an 80° view-angle (at a spacing of 2°) and for a width of view which was much smaller than the spatial extent of the object. In another study Snyder and Hesselink (1988) developed an optical set up for instantaneous optical tomography of non-stationary fluid flow. The optical set up consisted of an Ar^+ laser that was spread by a cylindrical lens into a fan beam of 220°. The expanded beam fell on 36 focusing mirrors. Each mirror collimated and directed the beam to the center of the object (helium jet), resulting in 36 instantaneous projections spaced along an arc of 180°. The transmitted light was focused by another array of mirrors on to a holographic film. In order to

get the holographic interferogram, a second laser generated a number of reference beams in a similar fashion. The test and the reference beams interfered on the holographic film plane to get the holograms, one with flow and another without flow. These holograms constituted the projection data for the tomographic reconstruction.

Two different forms of optical tomography for reconstructing density can be performed, depending upon whether the imaginary part (absorption) or the real part (phase) of the refractive index is used. Faris and Byer (1986, 1988) attempted both types of tomographic reconstruction of the density field in supersonic jets. In the first study (1986) the authors described an absorption-based tomographic system. It used an arc lamp instead of a laser as the source of radiation. This had the advantage of reducing the noise in the projection data arising due to speckle and interference effects. In addition, this method had the advantage of providing species-selective absorption images and eliminating the errors associated with fringe counting encountered in phase based tomography. The reconstruction was performed with six views using CBP algorithm and the Ram-Lak filter. In order to minimize artifacts due to limited projections, 6 views were suitably interpolated to generate 100 views. In another study by the same authors (1988), phase tomography was attempted using beam deflection measurements. It may be noted that phase tomography can be performed using interferometry, holography, scattering, and beam-deflection measurements. Beam deflection based phase tomography can be performed with either schlieren or shadowgraph imaging techniques. Since beam deflection measurements do not involve fringe counting, error in the projection data is reduced. This type of tomography is ideally suited for those systems wherein large gradients result in too many fringes, creating fringe resolution difficulties.

Optical tomography in crystal growth: Bedarida *et al.* (1983) described the application of multi-directional double-exposure holographic interferometry for obtaining three-dimensional spatial structure of the solution concentration inside the plume and around the crystal. Initially they used transmission holographic interferometry, but subsequently developed a multidirectional holographic interferometry, a method similar to optical tomography, to map the two- and three-dimensional nature of the solution concentration, respectively, around a growing $NaClO_3$ crystal. Solitro *et al.* along with Gatti and Bedarida (1989) developed a fiber-optic based multidirectional holographic interferometer to measure 3D concentration field during crystal growth experiments in space.

Trolinger *et al.* (1991A) used holographic optical elements (HOEs) to facilitate tomographic reconstruction of the solution concentration during

crystal growth in space. In addition, they employed PIV to measure weak convection often encountered during growth in a microgravity environment.

Braslavsky and Lipson (1998B) used multi-directional interferometry along with tomographic reconstruction to obtain three-dimensional maps of the temperature field around growing crystal of heavy water. The apparatus consisted of four Mach-Zehnder interferometers aligned in a manner to simultaneously record the thermal field from four different directions. In order to measure the three-dimensional field of refractive index, the interferograms were analyzed by Fourier fringe analysis followed by application of algebraic reconstruction technique (ART and MART) to process the limited projection data.

Srivastava *et al.* (2005) employed schlieren tomography for imaging the convective and concentration field around a growing KDP crystal. They used four projections between 0 to 180° for reconstruction. The authors adopted a numerical approach to overcome the difficulty of partial projection data. They used CBP algorithms to obtain two-dimensional concentration maps over a few planes at varying heights above a growing KDP crystal.

3. Apparatus and instrumentation

The quality of the apparatus and instrumentation has direct bearing on the data obtained during experiments. This section includes the design features of the apparatus used for experiments. The growth apparatus includes a solution-preparation system, filtration assembly, crystal growth chambers, seed mounting arrangement, crystal rotation system for forced convection experiments, and a temperature controller. Optical instruments configured for the present work are: shadowgraph, Mach-Zehnder interferometer and a Michelson interferometer. Data acquisition instrumentation includes a video camera interfaced to a PC via a frame grabber card.

3.1. Solution preparation apparatus

Careful preparation of a homogeneous saturated solution of KDP in water at an elevated temperature is an important first step for the experiments. The apparatus used and the procedure employed for this purpose is discussed in the following subsections.

3.1.1. Heater-cum-magnetic stirrer

In order to prepare a saturated solution of a solute in water, the temperature of the solution has to be monitored at regular intervals while continuously stirring the solution to achieve homogeneous mixing. This

Figure 3.1. Heater cum magnetic stirrer.

necessitates an appliance that functions both as a heater as well as a stirrer. A commercially available hot plate [*MLH*], the heat input to which is controlled by a thermostat and has a magnet connected to the shaft of the motor under the hot plate, was used for the purpose. The speed of the motor could be varied between 0 to 100 rpm. When a glass beaker containing solute, solvent and a magnetic stirrer (Telfon-coated cylindrical iron piece of dimensions 10 mm diameter and 25 mm length) is placed over such a hot plate, controlled heating as well as homogeneous mixing of the solute and solvent are possible. A thermometer inserted in the solution monitors its temperature. Figure 3.1 shows two such units used for preparing the saturated solution.

3.1.2. Filtration apparatus

Filtration of the saturated solution is the next step of the experimental procedure. An apparatus consisting of a peristaltic pump *[Miclins, Model PP30]* set at a desired flow rate was used to transfer the unfiltered saturated solution to a vacuum filtration assembly *[Pushpak Membrane Filter Assembly]*. The filtration assembly consists of a reservoir at the top for the unfiltered solution and a conical flask at the bottom for collecting the filtered solution. The two chambers are intermediated by a special nylon

membrane filter of 0.2 μm pore size and 47 mm diameter *[Gelman Laboratories, PALL, Model 047100]*. The flask has a port on one side for connecting to a vacuum pump that creates negative pressure inside the flask. The unfiltered solution in the reservoir is consequently sucked through the membrane filter to result in an ultra pure solution in the flask. Figure 3.2 shows the filtration assembly developed and used for the present study.

3.1.3. Thermostated water bath

The filtered solution is kept inside a thermostated water bath (TWB), which maintains the solution at a desired temperature for several days. It consists of a beaker of 20 liter capacity covered with a Plexiglas plate that has ports at suitable location to insert heating elements, a temperature sensor, inlet for distilled water, and a cavity in the middle for placing the beaker with filtered solution. The wattage of the heating elements is governed by the desired rate of increase of temperature of water in the bath. The shape and position of heating elements inside the bath is such so as to achieve uniform heating of the solution. A resistance type thermometer, PT-100, is the temperature sensor which is connected to a temperature control circuitry.

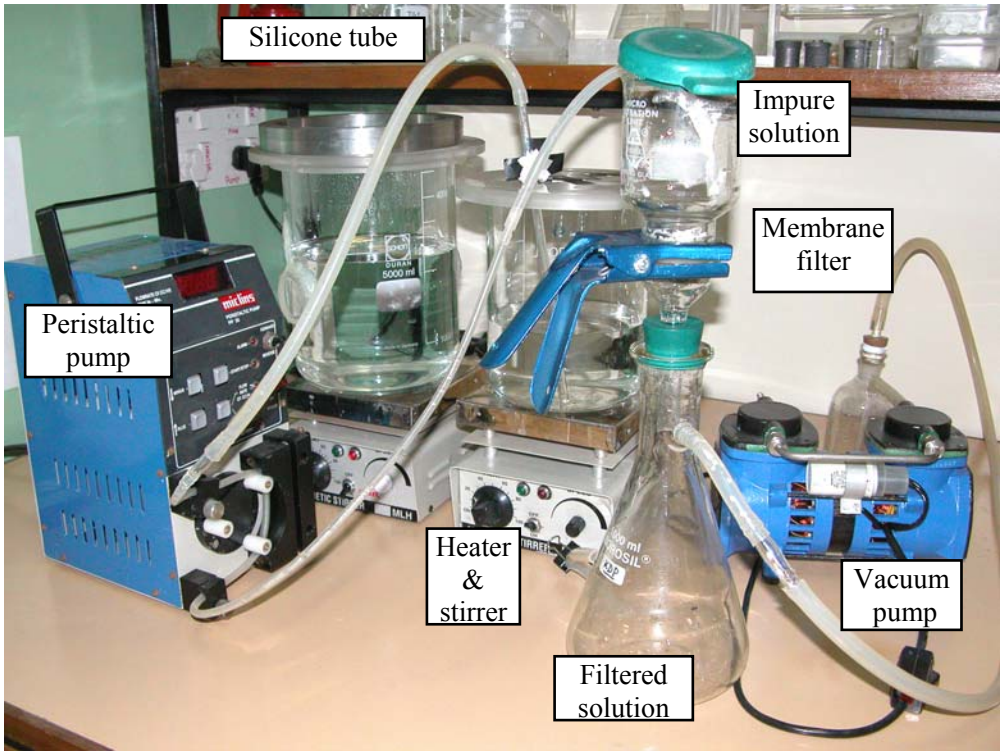

Figure 3.2. Filtration assembly consisting of the peristaltic pump, silicone tubes, impure solution reservoir, membrane filter, conical flask and vacuum pump.

3.1.4. Temperature control instrumentation

Thermal stability of the aqueous solution is crucial to conduct repeatable experiments and to avoid the problem of spurious nucleation and inclusions. The design of the crystal growth cell and the thermostated water bath are mainly driven by this consideration. The power to the heater immersed in the bath is fed through a thyrister (*Eurotherm Model 425*) that gets fired as per the signal received from a PID-based programmable temperature controller (*Eurotherm Model 902P*), which in turn receives signal from a temperature sensor (PT-100). The control signal from the temperature controller is dependent on a comparator output, which continuously examines the set-point temperature against the actual process temperature. This instrumentation helps in achieving the temperature stability within ±0.01°C of the set point value in the range 30-70°C. The thermostated water bath along with the control circuitry is shown in Figure 3.3.

3.2. Crystal growth apparatus

Two different crystal growth cells are designed and fabricated for performing the experiments. The design details of both the cells are described below.

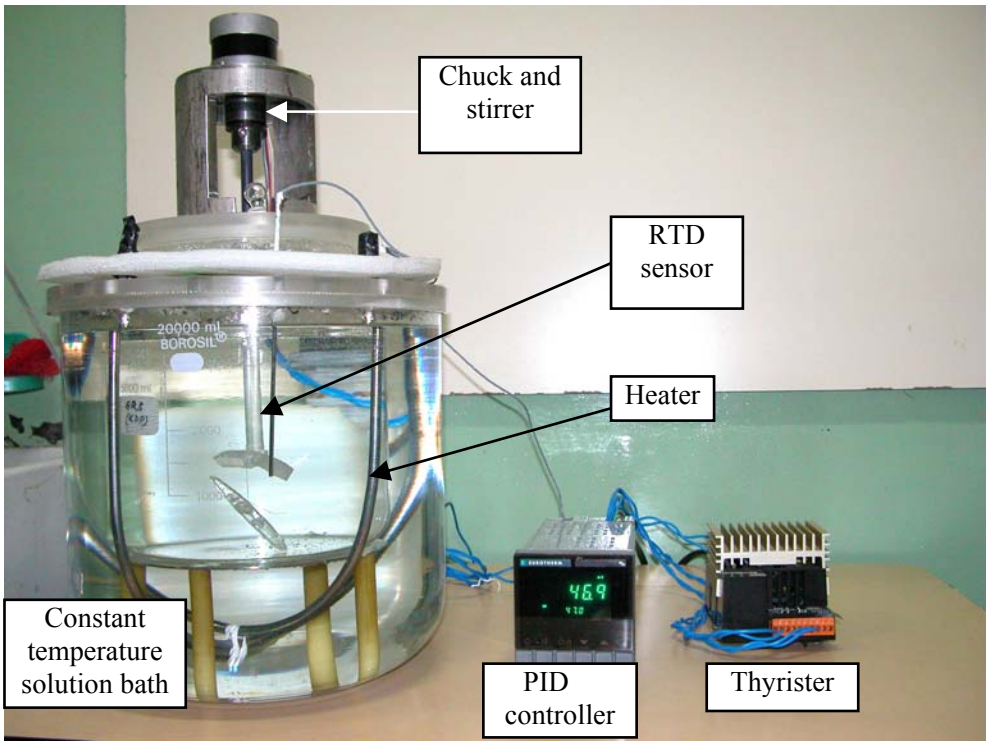

Figure 3.3. Constant-temperature bath with temperature controlling instrumentation.

3.2.1. Growth cell with a cylindrical geometry

A double-walled growth cell of glass has been designed and fabricated for performing the crystal growth experiments. It has a cylindrical geometry with the cavity between the two concentric cylinders filled with thermostated water. The PID based programmable temperature controller *(Eurotherm)* described above is employed for maintaining the solution temperature within ±0.01°C. In order to facilitate unhindered passage of the laser beam through the growth cell, quartz optical windows are provided on both sides of the cell. Two ports are provided for inserting a temperature sensor and a crystal seed into the growth chamber. Figure 3.4 shows the schematic drawing of the cylindrical growth cell.

3.2.2. Growth cell with beaker geometry

In order to perform laboratory-scale experiments in a growth geometry similar to that used in full scale growth systems, a cell having axisymmetric geometry has been fabricated. For this purpose, two beakers, one inside the other, having through ports for the passage of laser beam, are joined together by a glass tube around the ports. The through-ports are covered with optical windows which are coplanar as well as collinear to avoid refraction errors. The intermediating space between the two beakers is filled with thermostated water.

3.2.3. Multiple-window crystal growth chamber for tomography experiments

A special growth chamber has been fabricated to perform shadowgraph and interferometric tomography of crystal growth from solution (Verma, 2005A). The chamber has several novel features. In addition to leaving the crystal undisturbed during the process of recording the projection images, the chamber maintains an extremely high level of precision required in interferometric tomography experiments. The growth chamber has a double-walled geometry, with the inner cell acting as the growth cell and gap between the inner and the outer cells filled by thermostated water at the desired temperature. The inner cell is an octagonal shaped glass vessel having one port on each side of the octagon for the light beam. The ports are covered with quartz optical windows of 35 mm diameter for the passage of the laser beam. The octagonal cell is placed inside a cylindrical glass vessel that has eight ports covered with quartz windows. The passage of the laser beam from the outer cell to the inner cell is isolated from the intervening thermostated water by aluminum tunnels connecting the two cells. The four windows along a given direction have to be collinear and parallel to each other. This is ensured using an auto-collimator during fabrication. In addition, the centers

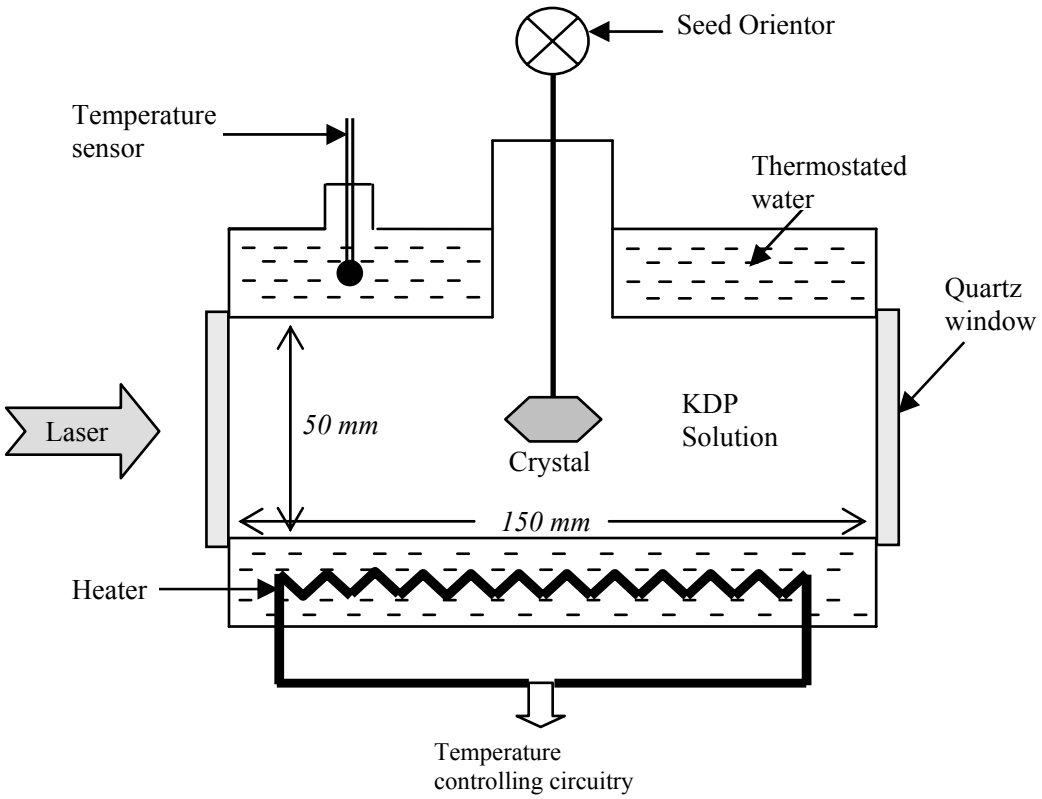

Figure 3.4. Schematic drawing of the double-walled cylindrical crystal-growth cell.

of all the sixteen windows along the four directions lie over a horizontal plane. Wedge compensators, one for each port, are used to correct for any residual wedge between pairs of windows on the inner and the outer cells. These are particularly necessary for the interferometric tomography experiments, wherein the alignment of the interferometer has to be maintained in the wedge setting and in the infinite setting modes for the entire duration of the experiment. The eight wedge compensators (four pairs) are carefully aligned at the start of the experiment to ensure that the four interferograms correspond exactly either to the wedge or an infinite fringe setting. Figures 3.5(a-b) show the eight-window growth chamber and a seed crystal mounted on a seed rod as seen from one of the windows.

3.3. Apparatus for forced-convection experiments

In order to conduct experiments under forced convection conditions, several apparatus have been fabricated. The details of each are given below.

3.3.1. Crystal rotation assembly

The crystal growth experiments were performed under free as well as forced convection. In order to achieve forced convection conditions, the crystal was

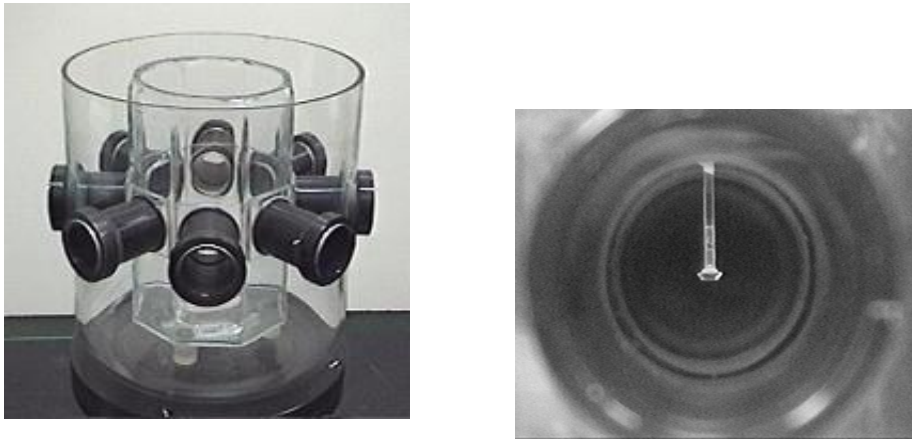

(a) (b)

Figure 3.5. (a) Wedge compensator mounted side-view of the chamber, (b) Seed crystal hanging from a glass rod as seen from one of windows of the growth cell.

rotated at various RPMs using a stepper motor. Wobbling of the crystal growth apparatus during rotation is not desirable as it results in irregular flow in the growth cell. Also, any deviation between the axis of the crystal hanging apparatus and the symmetry axis of the growth cell during rotation is detrimental to the quality of the projection data that is used for tomographic reconstruction. For these two reasons, a special apparatus has been designed and fabricated for the forced convection experiments. A stainless steel tube of 10 mm wall thickness and 120 mm inner diameter is precisely machined at both the ends to achieve the desired parallelism. A steel plate of 140 mm diameter is fixed to the top end of the pipe section in order to fit a stepper motor over it. A mechanical chuck is press-fitted to the shaft of the stepper motor. A Plexiglass platform hanging from a circular rod of the same material is tightened into the chuck. The tube section is provided with sufficient space to allow easy access for tightening and releasing of the Plexiglas rod. The final assembly results in a wobble free rotation of the platform, which is shown in Figure 3.6(a).

3.3.2. Slow-rotation platform

To capture the projection data along different view angles, the growth chamber needs to be turned. In order that the growth process remains undisturbed and no wedge is introduced between the interfering wavefronts due to the rotation, a high-precision wobble-free motorized slow-rotating platform has been fabricated. The multiple-window growth apparatus is placed on the motorized rotation assembly for collecting the projection data. Figure 3.6(b) shows the wobble-free motorized slow- rotation platform used for turning the growth chamber.

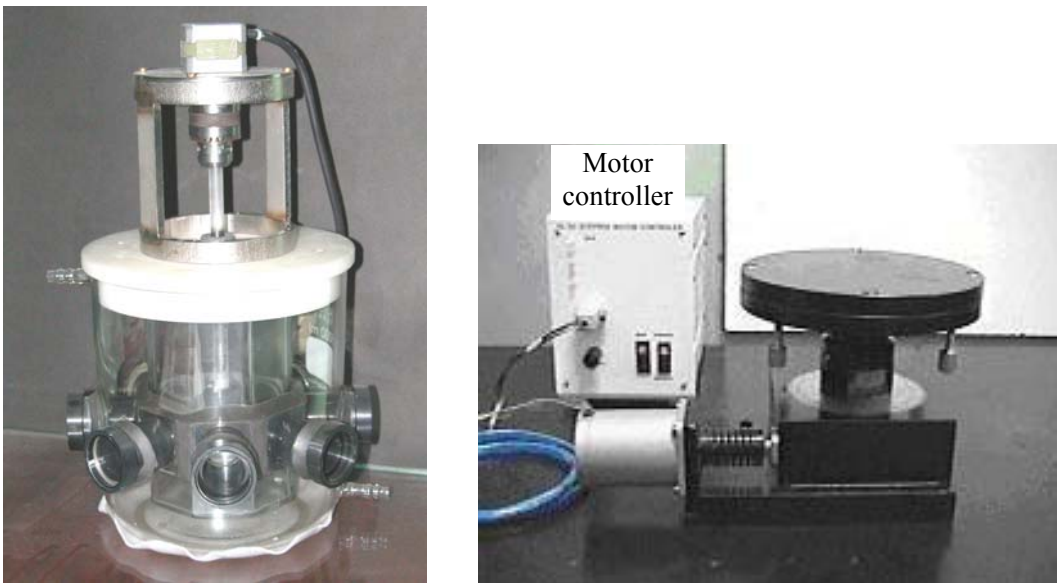

(a) (b)

Figure 3.6. (a) Wobble-free forced convection apparatus, (b) slow rotation platform.

3.4. Thermostatic water recirculation system

The stability of temperature of the aqueous solution is crucial for growing good quality crystals. Hence it is necessary to perform the experiments in a controlled thermal environment. It is essential that the fluctuations in the ambient environment do not affect the temperature of the process under study. For this purpose a thermostatic water reservoir was fabricated in which the temperature was precisely controlled. A PID-based programmable temperature controller *(Eurotherm)* with an accuracy of ± 0.01°C was used. Thermostated water was pumped up to the cavity inside the double walled growth cell with the help of a centrifugal pump-and-valve system *(Suzuki* pump*, Legris* valves*)* fabricated specifically for the purpose. Two pumps and four valves were used in the system. By alternately switching the operation of one pump to other every 12 hours, the system was operated uninterrupted for the entire duration of the experiment lasting several days The photograph of the pump and valves system is shown in Figure 3.7. The temperature sensor connected to the controller circuitry was placed inside the growth chamber to allow careful control of the solution supersaturation during the experiment.

3.5. Optical instrumentation

The laser based diagnostics used for imaging convection, concentration and surface features during crystal growth are discussed in the following sections.

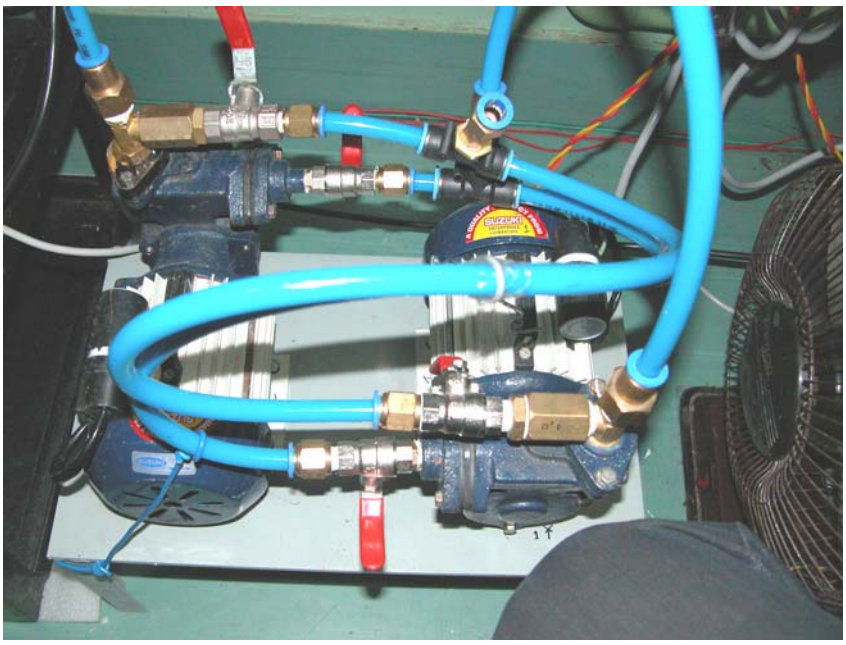

Figure 3.7. Pump-and-valve system for recirculating thermostated water through the cell.

3.5.1. Shadowgraph set-up

Shadowgraphy has been extensively used in experimental fluid mechanics research for fluid flow visualization. It employs an expanded collimated beam of light from a laser source that traverses through the field of disturbance. If the disturbance is a field of varying refractive index, the individual light rays passing through the field are refracted and bent out of their original path. This causes a spatial modulation of the light-intensity distribution with respect to the original intensity on the screen. The resulting pattern is a shadow of the refractive-index field in the region of the disturbance. Figure 3.8 shows the experimental set up of the shadowgraph technique. A He-Ne laser of 25 mW power is expanded and collimated to a diameter of 30 mm by a beam expander. The collimated beam passes through the growth chamber in which the KDP crystal is grown. The beam emerging at the exit window of the growth cell falls on a screen resulting in the shadowgraph image. The images are continuously recorded using a video camera (*Sony Handycam* 360X) interfaced to a computer through a 1024 × 1024, 25 Hz frame grabber card (*Coreco Imaging*).

3.5.2. Mach-Zehnder interferometry

A Mach-Zehnder interferometer comprises of four independent components, two beam-splitters and two mirrors, arranged diagonally on the four corners of a square (or rectangle). The four components have to be exactly at 45˚ to the input beam direction, and the proper functioning of the

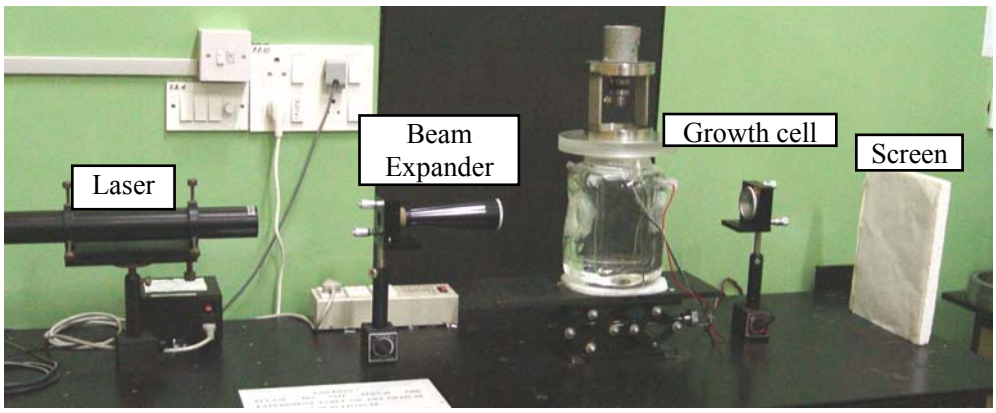

Figure 3.8. Experimental setup of the laser shadowgraphy technique.

interferometer is critically dependent on the alignment of all the four components with respect to the angle specified. Such a four-component-based Mach-Zehnder interferometer is susceptible to frequent misalignments, owing either to the mechanical disturbances/vibrations in the surroundings or the fluctuations in environmental parameters inside the laboratory. Both factors are detrimental to the quality of the experimental data. In order to overcome this difficulty, a novel interferometer was designed and developed (Verma, 2005A).

3.5.2.1. Rigid-type Mach-Zehnder interferometer

It is a two-component rigid-type Mach-Zehnder interferometer. It consists of two rhomboid prisms, constituting the two arms of the interferometer, with a beam splitter and a mirror at the ends of each prism. The axial separation between the beam splitter and the mirror on the rhomboids is 300 mm, while the incident face has a dimension that facilitates passage of a beam of 50 mm diameter. Since the dimension of the interferometer is large, hollow rhomboids are preferred in order to keep the weight of the interferometer to minimum possible. The material chosen for fabricating the prisms is optical quality glass having low thermal expansion coefficient, so that once the alignment is finalized the fluctuations in the environment do not disturb the interferometer. The parallelism between the beam splitter and the mirror on each arm of the interferometer is ensured during the fabrication of the rhomboids. The flatness of all the components on the two rhomboids is such that the overall wavefront distortion is better than $\lambda/4$. Since the two arms of the interferometers are completely independent, a test object of any dimension can be accommodated within the interferometer. As the rhomboids are constant-deviation prisms, this property translates into the main advantage: Immunity to mechanical disturbances as well as environmental fluctuations. It helps in easy and quick alignment of the interferometer, either in the wedge-fringe setting or in the infinite-fringe setting. The rigid-type M-Z interferometer is shown in Figures 3.9.

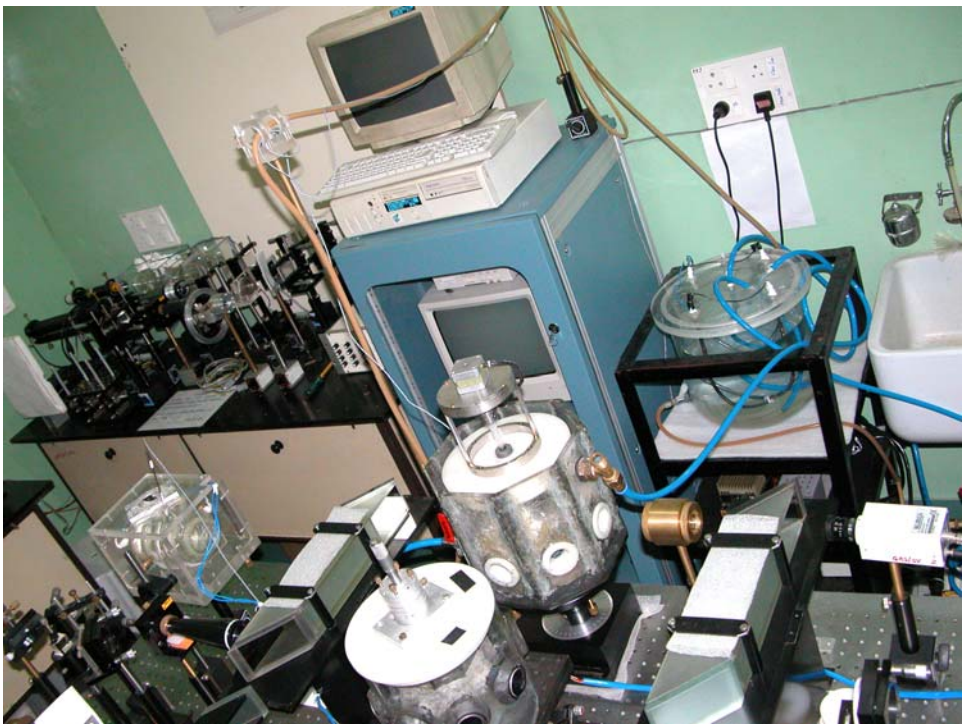

Figure 3.9. Full view of the experimental set up involving the interferometer, growth cells, thermostated water recirculation system and camera.

In order to benchmark the rigid-type Mach-Zehnder interferometer, it was aligned in the wedge- as well as the infinite-fringe setting modes without any disturbance in the beam path. The two types of fringe patterns are shown in Figures 3.10(a-d). It was found that the effort required in setting up the present Mach-Zehnder interferometer is much less than that required for an interferometer with four independent components. It was easy to switch between the infinite and wedge fringe modes. Both the wedge- as well as the infinite-fringe setting modes have been used to image crystal growth experiments.

3.5.2.2. Compensation chamber

To be able to quantify the growth parameters such as concentration and fluid flow around the growing crystal, we have to ensure that the origin of the interferometric fringe patterns is the optical path difference arising from the changes in the growth parameters alone. This can be ensured only if the optical path of the two interfering beams is made equal before the growth phenomenon is initiated. The interferograms can then be unambiguously attributed to solute movement during the growth process. At the experimental level, this points towards the importance of having a *compensation chamber* identical to the growth chamber, but without any crystal growth activity inside. This is necessary to compensate for the phase difference arising from

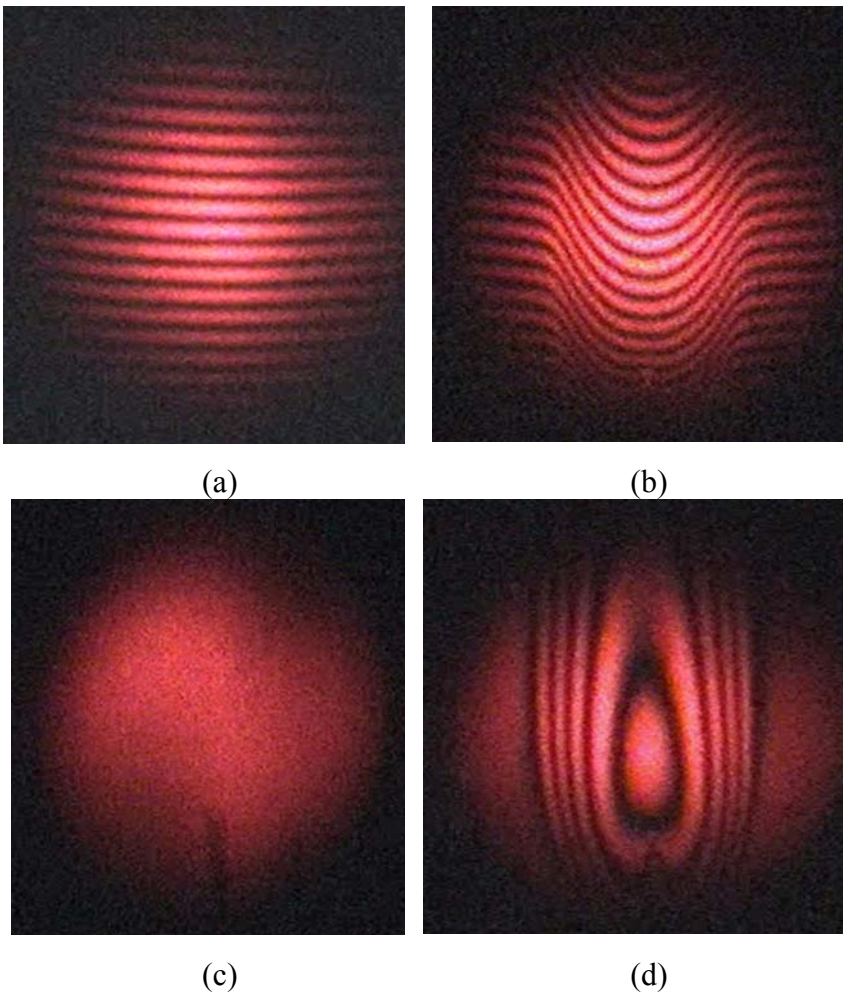

Figure 3.10. Mach-Zehnder interferograms. (a) Wedge fringes, (b) Candle flame in the wedge fringes, (c) Infinite fringe, and (d) Candle flame in the infinite fringe.

the passage of laser beam through the growth chamber containing the solution. The compensating chamber has a solution of similar concentration (hence density) in it. It ensures that changes in the fringes observed during growth are only due to refractive-index variations as a result of crystal growth.

3.5.2.3. Wedge compensator

Keeping in view the high level of instrumental precision required in interferometric tomography experiments, the Mach-Zehnder interferometer has been developed with precautions so as to eliminate possible sources of errors. The *wedge compensator* is one such piece of optical hardware which is used to correct for any residual wedge between the interfering wavefronts arising due to imperfections in the optical components. The parallelism of the four pairs of windows on the inner as well as the outer chamber of the

double-walled growth cell is ensured using an auto-collimator. Residual wedge, if any, between the pair of windows is compensated by using wedge-compensators, one each for the eight beam ports. This requires that at the start of the experiment, all the eight wedge compensators (four pairs of wedge-compensators) are carefully aligned. The four interferograms then correspond exactly to either the wedge fringe setting or an infinite setting. A pair of compensating wedges is used to control the angle between the interfering wavefronts. In addition, by introducing an additional wedge compensator, the interferometer can be operated simultaneously in the infinite-setting and the wedge-setting modes.

3.5.2.4. Pneumatic vibration isolation optical table

Interferometric imaging being extremely sensitive to vibrations and fluctuations in the environmental parameters, additional devices are required to isolate the experimental set up. The complete experimental apparatus including the interferometer and the crystal growth apparatus was placed on an optical table with pneumatic vibration isolation legs (*Standa Opto-Mechanical Instruments*). The pneumatic legs help in eliminating floor vibrations from getting transmitted to the aqueous solution around the crystal and to the interferometer.

3.5.3. Michelson interferometer

A Michelson interferometer has been set up for on-line monitoring of microtopography of a growing crystal face. In this interferometer, a laser beam is split into two beams at right angles to each other by a 50:50 beam splitter. One of the beams traverses towards a mirror and gets reflected back to the beam splitter (reference beam), while the second beam is reflected from the surface of the growing crystal (test beam). These two reflected beams recombine at the beam splitter to produce an interference pattern. The image is then grabbed by the image acquisition hardware. In order to get an interference pattern with good contrast, the intensity of the reference beam is reduced and made equal to that of the test beam by a neutral density filter. Figures 3.11 shows the photograph of the Michelson interferometer.

The Michelson interferometer can be aligned in two different modes.

i) **Fringes of equal thickness**: When a slight wedge is introduced between the two interfering beams by deliberately tilting one of the mirrors of the interferometer, fringes of equal thickness are obtained. These fringes, also called *Fizeau fringes*, are parallel and equidistant straight lines (Figure 3.12a).

ii) **Fringes of equal inclination**: When the input laser beam is expanded to get a source of large angular size and the interfering wavefronts obtained from it are exactly parallel to each other, we observe rings in the interference pattern (Figure 3.12b) due to an air gap of constant thickness between them. These fringes are formed at infinity, and a suitable lens can be used to receive them on its focal plane. If the parallel gap is that of air, we have a simple relation

$$2t\cos\theta = n\lambda$$

We can easily see that, for constant value of t, we obtain fringes of equal inclination, namely circles. These fringes are also referred to as *Haidinger fringes*. By moving one of the mirrors parallel to itself, the diameter of the rings is increased. If the alignment of the beam splitter is exactly 45° to the incident beam, we get perfectly circular fringes. If the inclination shifts from 45°, the fringes first become elliptical and with further misalignment turn into hyperbolas.

Michelson interferograms provide a geographical description of the surface features of the growing face. This information can be used to deduce various growth kinetic parameters. The interferograms provide direct visual evidence of the mechanism of growth, e.g. spiral growth, two-dimensional nucleation, or birth-and-spread mechanism. Initially the interferometer is aligned to get fringes of equal thickness (*Fizeau fringes*), which are then separated to yield only one fringes in the filed of view (i.e. infinite fringe interferogram). After this stage, the interferograms that appear in the field of view are due to the micro-morphological features of the growing crystal face, and carry information of the growth mechanism.

3.6. Image acquisition and data processing instrumentation

The experimental results are recorded in the form of movies on video cassettes (*SONY Hi8*) by a video camera (*SONY Handycam Vision, Model - CCD TRV67E Hi8*). The camera is interfaced to a personal computer (*HP Vectra, Pentium-IV, 1.7 GHz processor, 1 GB RAM, 80 GB HDD*) through a 1024 × 1024, 25 Hz frame grabber card (*PC-COMP*) to capture specific image frames from the movies. In order to extract the relevant portion of the experiment from video movies, the camera is interfaced to a specialized movie-making hardware (*MovieBOX DV, Pinnacle Systems*) through an *IEEE-1394* interface card and cable (*Firewire*). The software used for the purpose is *Pinnacle Studio Version-8*. The image processing and quantitative analysis of the experimental results is performed on the PC. The photograph of the image acquisition and data processing workstation is shown in Figure 3.13.

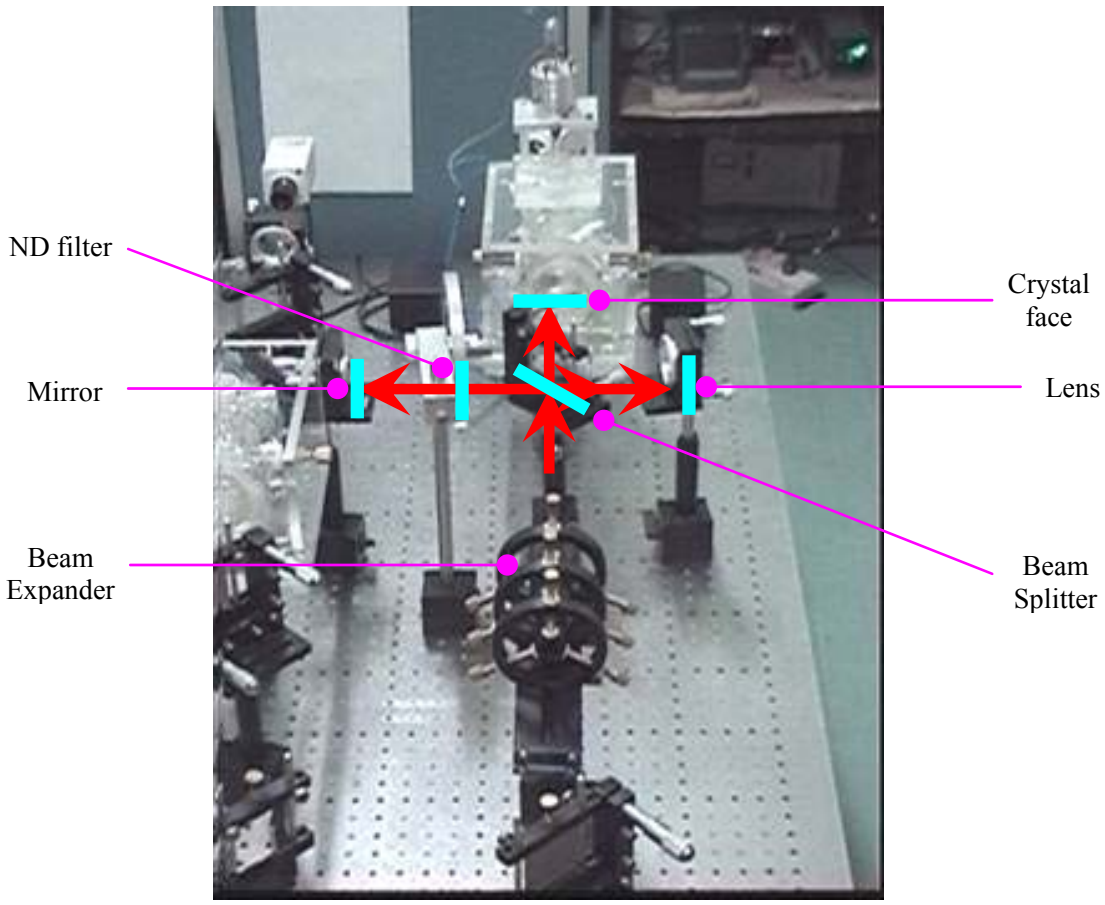

Figure 3.11. Michelson interferometer.

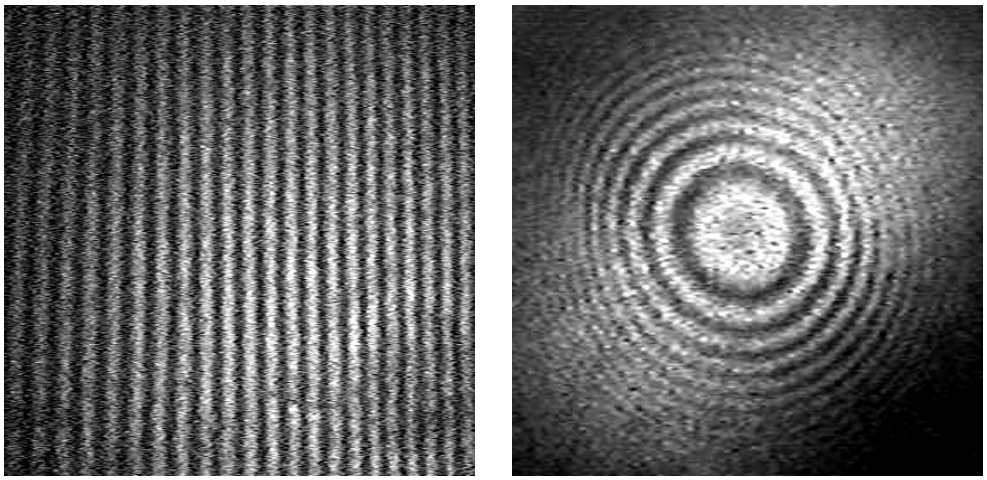

(a) (b)

Figure 3.12. Michelson interferograms. (a) *Fizeau* fringes (fringes of equal thickness), (b) *Haidinger* fringes (fringes of equal inclination).

Figure 3.13. Image acquisition and data processing workstation.

3.7. Experimental methodology

The procedure used for crystal growth experiments is presented in the following sections.

3.7.1. Preparation of the supersaturated solution

It would be perfectly appropriate to say that the quality of the crystal grown will be as good as the purity of the water and the chemicals used for preparation of the solution. It is desirable to use double-distilled water having resistivity of 18 MΩ-cm and chemicals with purity of 99.9%. The preparation of the supersaturated solution of the material is guided by the solubility data of the material for the given solvent. It is known that at a given temperature T_1 a particular solvent has a maximum limit up to which a particular solute can be dissolved in it. Any extra amount of salt added to this solution will result in the solute settling at the bottom of the container. Such a solution is said to be *saturated* at temperature T_1. If a seed crystal of the same composition is immersed in the saturated solution and the temperature is kept fixed at T_1, the crystal neither grows nor dissolves. In order to be able to grow this seed crystal we must increase the solute content in the solution. This is achieved by overheating the solution to temperature T_2. It amounts to increasing the solubility limit of the solvent and hence an extra amount of solute can be dissolved in it. Once this extra solute has been dissolved, the

resulting solution is slowly cooled to its original starting temperature T_1. The solution is now supersaturated at the temperature T_1 and in the presence of the seed crystal the excess salt will preferentially get deposited on it.

3.7.2. Solution filtration

Filtration of the solution is an extremely important step in the growth of large, good quality crystals. It is necessary to filter suspended particles from the solution which otherwise act as sources of secondary nucleation. Before starting the filtration, the solution is first overheated 5 degrees above its saturation temperature. As a result the solution becomes under-saturated and the probability of formation of nucleation during filtration is reduced. It may be noted that the process of filtration leads to loss of small fraction of solvent and solute, which results in slight shift of the saturation temperature.

3.7.3. Overheating the prepared solution

The supersaturated solution is highly unstable and even a slight physical disturbance leads to instant nucleation of extra solute at the bottom of the container. Thus supersaturated solutions ought to be handled carefully. While filtering a supersaturated solution spontaneous nucleation occurs over the membrane filter and the transferring tubes itself by heterogeneous nucleation mechanism. The problem can be circumvented by overheating of the solution to about 15 degree above its saturation temperature for about 5 hours. It results in the dissolution of microclusters and also eliminates any microbial activity. In addition, filtration through membrane filter (0.02 μm pore size), removal of rough surfaces/edges inside the crystallizer, and the prevention of cavitations by stirring the solution, also help in reducing the homogeneous and heterogeneous nucleation. Figure 3.14 shows the experimental table for solution preparation, filtration and subsequent overheat treatment.

3.7.4. Preparation of seed crystal

Growth starting from a spontaneous nucleation is undesirable because of its uncontrollable nature. It is therefore required that a small crystal (of the same material) of high physical, mechanical and optical quality with no residual stresses be introduced into the supersaturated solution. This would result in preferential crystallization on it rather than at any other location in the crystallizer (because of the lower activation barrier). This small crystal is called a seed crystal. The necessity of using a seed crystal can be further understood for those device applications wherein morphology of the crystal required is different from its natural habit of growth. In such situations, by using a seed of desired shape, along with optimization of the growth parameters, one can obtain the desired crystal shape (within limits). Seed crystals are generally

Figure 3.14. Experimental platform for solution preparation, filtration and overheating.

prepared either from spontaneous nucleation (if as-grown morphology is desired in the bigger crystal) or by cutting a smaller portion of desired shape from a larger crystal. The mechanical handing during the cutting of the crystal is crucial because it introduces stresses into the crystal that act as sources of dislocations in the grown crystal. Special care ought to be taken to place the seed crystal such that when a crystal grows, no external pressure is imposed, which causes stress inside the material. Secondary nuclei often accompany the appearance of fractures and solution inclusions in a crystal.

3.7.5. Determining the saturation temperature

At the saturation temperature the seed crystal neither grows nor dissolves. Below this temperature, it starts to grow, whereas above it, the crystal dissolves. Experimentally, it is easy to detect when the crystal just stops dissolving rather than when it just starts to grow. In order to find the point of stopping of the dissolution (in other words, start of the growth) the temperature of the solution is raised to a value such that the crystal starts to dissolve. The solution temperature is then allowed to steadily decrease. Cooling the solution slowly in a controlled manner through the programmable temperature controller allows determination of the saturation temperature. All through the cooling process, the dissolution of the crystal is

monitored. Initially it is monitored visually by observing the size of the crystal. When it appears that the crystal size is neither increasing nor decreasing then a second method based on shadowgraph optical technique is used for precise determination of this temperature. Shadowgraphy is used to image the feeble convection plume rising above the crystal when it is in the growth mode. A descending plume is visible in the shadowgraph image when the crystal dissolves. We have adopted this method of determining saturation temperature in all our experiments. Using this technique, the saturation temperature was determined to an accuracy of ±0.1°C. Precise determination of the saturation temperature is necessary because the post-experiment data analysis requires it to be known exactly.

3.7.6. Crystal mounting geometries

The plume orientation around a growing crystal depends on the manner in which it is mounted and the faces that are allowed to grow. Experiments have been performed in three different growth geometries in order to understand their influence on the growth rate and the crystal quality.

3.7.6.1. Crystal orientation for shadowgraph and Mach-Zehnder imaging

Figure 3.15 shows the photographs of the three different geometries. These are:

(a) Crystal hanging from a glass rod.
(b) Crystal placed on a platform.
(c) Crystal perched on top of a glass rod.

Seed crystals should be mounted on a smooth surface. The use of a rough support can provide many centers of spurious nucleation. These interfere with the growth of the original crystal. Hence, such platforms have been fabricated from Plexiglas.

3.7.6.2. Crystal orientation for Michelson interferometry

The crystal mounting geometry in the case of the Michelson interferometer is different from those of the shadowgraph and the Mach-Zehnder interferometer. This is because, in the former, one is interested in imaging the crystal surface phenomena as a function of the growth environment. In other experiments the interest is in correlating the solution characteristics prevalent around the crystal with parameters such as growth rate, morphology, and quality. As a result, in Michelson interferometry, imaging is in the reflection mode where one of the interfering beams gets reflected from a designated crystal surface and carries with it the geographical description of the surface features developing on it. In Mach-Zehnder interferometry, one of the interfering

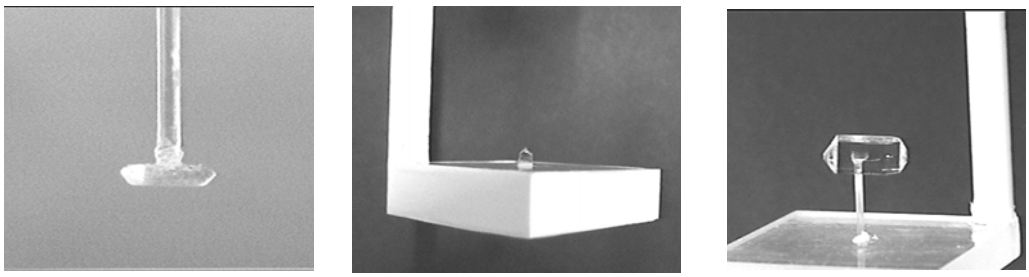

Figure 3.15. Three different growth geometries.

beams is transmitted through the crystal and the surrounding solution, thus carrying information about the bulk growth rate, quality, and the solution parameters around the crystal.

3.7.6.3. Crystal plate preparation and mounting for Michelson interferometry

In order to study the surface microstructure developing over prismatic {100} and pyramidal {101} faces, crystallographic plates parallel to the respective face were cut from an already available KDP crystal by a crystal cutting machine using a diamond blade *(Buehler make, Germany).* The surface of the crystal plate is made flat using a silicon carbide emery paper, followed by polishing using alumina (Al_2O_3) powder and glycol over a felt cloth. Two such prismatic plates cut parallel to (100) and (010) faces, and two pyramidal plates cut parallel to $(0\bar{1}1)$ and $(\bar{1}01)$, are shown in Figures 3.16(a-b) respectively. The polished crystal plate is then fixed on a fine machined Plexiglas base with a suitable adhesive. Except the face to be studied, the other faces are covered by a Teflon tape.

3.7.6.4. Crystal face orientation mechanism

The orientation of the crystal face with respect to the incoming laser beam is crucial to get the necessary fringe patterns in the Michelson interferometry. This is because of the two reasons:

i) The input laser beam has to be incident perpendicular to the crystal face so that the reflection from the surface traverses back and interferes with the reference beam.

ii) The reflectivity of the crystal surface is so poor (0.1% of the reference mirror) that it requires a trained eye to spot the reflected beam spot. This problem is further aggravated by the presence of multiple optical surfaces (such as windows of the growth cell, optical components of the

interferometer) whose reflectivity is greater than the crystal surface. Due to this several spots of reflected light are obtained, which make it extremely difficult to properly align the crystal plate. These difficulties necessitated the development of an instrument that could provide the necessary degree of freedom for easy alignment of the crystal face. These were as follows:

(a) Rotation (0-180°) about the *z*-axis while the crystal plate is oriented along $x = k$ $(or\ y = k)$ plane. For the (100) crystal face, the *z*-axis lies inside the crystal plate such that the <100> crystal direction lies either along the *x*- or the *y*- axes.
(b) Tilts (0-30°) of the crystal plate about the remaining two orthogonal planes, i.e. $y = m$ $or\ z = n$ planes, i.e. rotation about *x*- and *y*- axes.

3.7.7. Initiation of the crystal growth

Depending upon the geometry chosen for growth, a small (2-3 mm) and transparent seed crystal of KDP of appropriate morphology is immersed in the solution. While immersing the seed crystal, the solution temperature is kept 0.5 degrees above its saturation value so as to dissolve a few surface layers of the crystal. The dissolution helps in the elimination of the physical imperfections on the crystal faces, and also of any surface contamination introduced during crystal processing. After dissolving the crystal for a few minutes, the solution is cooled to its saturation point. A programmed cooling of the solution with an appropriate cooling rate is given from this point onwards to continue growth.

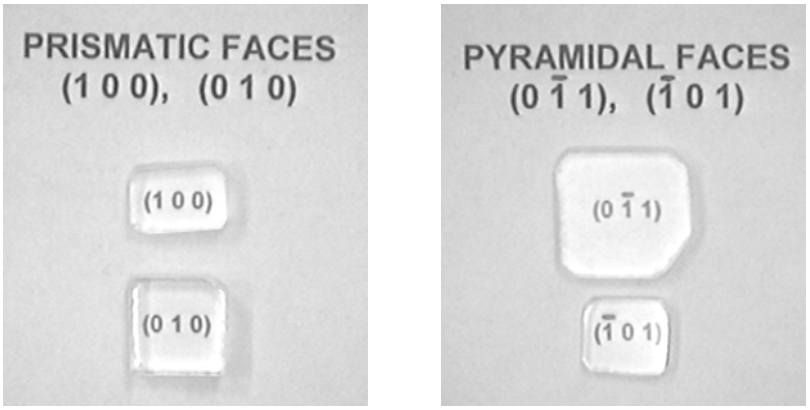

(a) (b)

Figure 3.16. (a) Cut and polished prismatic faces, (b) Cut and polished pyramidal faces.

3.7.8. Removing the crystal after growth for *ex-situ* characterization

Once the growth experiment is completed, the crystal is removed from the growth cell to perform ex-situ characterization. These studies include growth rate calculations in different directions, and inspecting the crystal quality for defects such as inclusions, voids, striations and cracks. The characterization results are then correlated with the growth parameters of the experiment. In order to be able to perform the above tests on the grown crystal, precautions are taken to keep the crystal and its surface in the as-grown conditions. This necessitates protecting the crystal from getting exposed to ambient temperature during removal from the growth cell. Sudden temperature differences can lead to cracking due the anisotropic thermal contraction. In addition, the solution layer that is in contact with the crystal is removed instantly to avoid development of spurious surface microstructure. The approach followed was to add an immiscible organic solvent such as n-hexane to the solution. The solvent forms a thick layer at the top of the solution. During extraction, a protective layer envelops all the crystal faces and keeps the surface features intact. The immiscible solvent prevents evaporation of the solution and hence, continuous changes in the solution supersaturation.

4. Data analysis

The present section has discussions on how shadowgraph images and interferograms can be quantitatively analyzed to retrieve information about the concentration field.

4.1. Shadowgraphy

It employs an expanded and collimated beam of laser light. The light beam traverses through the region of interest, which, in the present application, is an aqueous solution of KDP material. During crystal growth, the KDP solution is a field of varying refractive index and the individual light rays passing through the field are refracted and bent out of their original path. This causes a spatial modulation of the light intensity distribution. The resulting pattern is, in effect, a shadow of the refractive-index field in the region of the disturbance.

4.1.1. Governing equation and approximations

Consider a medium with refractive index n that depends on all the three space coordinates, namely $n = n(x, y, z)$. We are interested in tracing the path of light rays as they pass through this medium. Starting with the knowledge of the angle and the point of incidence of the ray at the entrance plane, we

would like to know the location of the exit point on the exit window, and the curvature of the emergent ray (Born, 1980; Schopf, 1996, Verma, 2005C).

Let the ray be incident at point $P_i(x_i, y_i, z_i)$ and the exit point be $P_e(x_e, y_e, z_e)$. According to Fermat's principle the optical path length traversed by the light beam between these two points has to be an extremum. If the geometric path length is L, then the optical path length is the product of the geometric path length with the refractive index of the medium. Thus

$$\delta\left(\int_{P_i}^{P_e} n(x,y,z)ds\right) = 0 \tag{4.1}$$

Parameterizing the light path by a coordinate z, the above condition can be represented in terms of two functions $x(z)$ and $y(z)$, and the equation can be rewritten as

$$\delta\left(\int_{z_i}^{z_e} n(x,y,z)\ \sqrt{x'^2+y'^2+1}\ dz\right) = 0 \tag{4.2}$$

where primes denote differentiation with respect to z. Application of the variational principle to the above equation yields two coupled Euler-Lagrange equations, that can be written in the form of the following differential equations for $x(z)$ and $y(z)$:

$$x''(z) = \frac{1}{n}\left(1+x'^2+y'^2\right)\left(\frac{\partial n}{\partial x} - x'\frac{\partial n}{\partial z}\right) \tag{4.3}$$

$$y''(z) = \frac{1}{n}\left(1+x'^2+y'^2\right)\left(\frac{\partial n}{\partial y} - y'\frac{\partial n}{\partial z}\right) \tag{4.4}$$

The four constants of integration required to solve these equations come from the boundary conditions at the entry plane of the chamber. These are the co-ordinates $x_i = x(z_i),\ y_i = y(z_i)$ of the entry point z_i and the local derivatives $x_i' = x'(z_i),\ y_i' = y'(z_i)$. The solution of the above equation yields the two orthogonal components of the deflection of the ray at the exit plane, and also its slope.

In the experiments performed, the solution is confined between parallel planes and the illumination is via a parallel beam perpendicular to the entry plane. The length of the growth chamber containing the fluid is D and the

screen is at a distance L behind the growth chamber. The z -coordinates at entry, exit and on the screen are given by z_i, z_e and z_s respectively. Since the incident beam is normal to the entrance plane, there is no refraction at the optical window. Hence the derivatives of all the incoming light rays at the entry plane are zero: $x_i' = y_i' = 0$. The displacements $(x_s - x_i)$ and $(y_s - y_i)$ of a light ray on the screen (x_s, y_s) with respect to its entry position (x_i, y_i) are

$$x_s - x_i = (x_e - x_i) + L\,x'(z_e) \tag{4.5}$$

$$y_s - y_i = (y_e - y_i) + L\,y'(z_e) \tag{4.6}$$

where x_e, y_e, and $x'(z_e), y'(z_e)$ are given by the solutions of Equations (4.3) and (4.4), and the refraction at z_e, respectively.

The above formulation can be further simplified with the following assumptions.

Assumption 1. Assume that the light rays incident normally at the entrance plane undergo only infinitesimal deviations inside the inhomogeneous field, but have a finite curvature on exiting the chamber. The derivatives $x'(z_i)$ and $y'(z_i)$ are therefore zero, whereas $x'(z_e)$ and $y'(z_e)$ at the exit plane have finite values. The assumption is justifiable because of the smoothly varying refractive index of the KDP solution. Under this assumption, Equations 4.3 to 4.6 become

$$x''(z) = \frac{1}{n}\left(\frac{\partial n}{\partial x}\right) \tag{4.7}$$

$$y''(z) = \frac{1}{n}\left(\frac{\partial n}{\partial y}\right) \tag{4.8}$$

$$x_s - x_i = L\,x'(z_e) \tag{4.9}$$

$$y_s - y_i = L\,y'(z_e) \tag{4.10}$$

Rewriting Equations 4.9 and 4.10 as

$$x_s - x_i = L\int_{z_i}^{z_e} x''(z)\,dz \tag{4.11}$$

$$y_s - y_i = L\int_{z_i}^{z_e} y''(z)\,dz \tag{4.12}$$

and using Equations 4.7 and 4.8, Equations 4.11 and 4.12 become

$$x_s - x_i = L\int_{z_i}^{z_e} \frac{\partial(\log n)}{\partial x}\,dz \tag{4.13}$$

$$y_s - y_i = L\int_{z_i}^{z_e} \frac{\partial(\log n)}{\partial y}\,dz \tag{4.14}$$

Assumption 2. The assumption of the infinitesimal displacement inside the growth chamber can be extended and taken to be valid even for the region falling between the screen and the exit plane of the chamber. As a result, the coordinates of the ray on the screen can be written as

$$x_s = x_i + \delta_x(x_i, y_i) \tag{4.15}$$

$$y_s = y_i + \delta_y(x_i, y_i) \tag{4.16}$$

The deviation of the rays from their original paths in passing through the inhomogeneous medium results in the change of intensity distribution on the screen as compared to the original distribution when the disturbance is not present in the beam path. The shadowgraph method measures this change in the intensity distribution. The intensity at point (x_s, y_s) on the screen is a result of several beams moving from locations (x_i, y_i) and getting mapped on to the point (x_s, y_s) on the screen. Considering the fact that the area of the initial spread of the light beam gets deformed on passing through the refractive medium, the intensity at point (x_s, y_s) is

$$I_s(x_s, y_s) = \sum_{(x_i, y_i)} \frac{I_o(x_i, y_i)}{\left|\dfrac{\partial(x_s, y_s)}{\partial(x_i, y_i)}\right|} \tag{4.17}$$

where I_s is the intensity on the screen in the presence of the inhomogeneous refractive index field, and I_o is the original undisturbed intensity distribution. The denominator in the above equation is the Jacobian $J(x_i, y_i; x_s, y_s)$ of the mapping function of (x_i, y_i) on to (x_s, y_s), as shown in Figure 4.1 below.

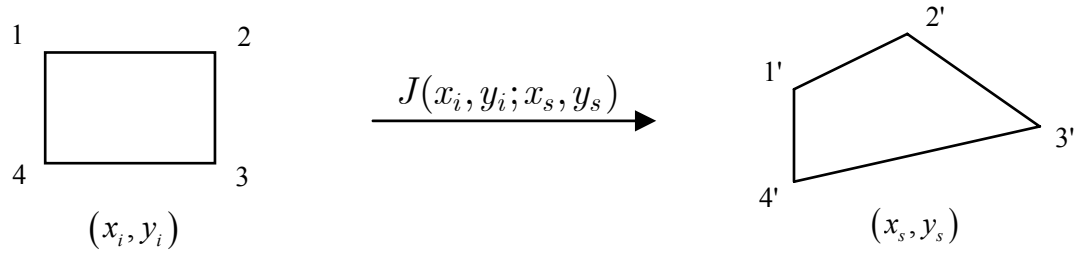

Figure 4.1. Jacobian $J(x_i, y_i; x_s, y_s)$ of the mapping function of (x_i, y_i) onto (x_s, y_s).

Geometrically it represents the ratio of the area enclosed by four adjacent rays after and before passing through the inhomogeneous medium around the growing crystal. In the absence of the inhomogeneous field, such an area is a regular quadrilateral. It transforms to a deformed quadrilateral when imaged on to a screen in the presence of the inhomogeneous field. The summation in the above equation extends over all the rays passing through points (x_i, y_i) at the entry of the test section that are mapped onto the small quadrilateral (x_s, y_s) on the screen and contribute to the resulting light intensity within.

Assumption 3. Under the assumption of infinitesimal displacements, the deflections δ_x and δ_y are small. Therefore the Jacobian can be assumed to be linearly dependent on them by neglecting the higher powers of δ_x and δ_y, and also their product. Therefore, the Jacobian can be expressed as

$$\left|\frac{\partial(x_s, y_s)}{\partial(x_i, y_i)}\right| \approx 1 + \frac{\partial(x_s - x_i)}{\partial x} + \frac{\partial(y_s - y_i)}{\partial y} \tag{4.18}$$

Substituting this form in Equation 4.17, we get

$$I_s(x_s, y_s)\left[1 + \frac{\partial(x_s - x_i)}{\partial x} + \frac{\partial(y_s - y_i)}{\partial y}\right] = \sum_{(x_i, y_i)} I_o(x_i, y_i) \tag{4.19}$$

Simplifying further we get

$$\frac{I_o(x_i, y_i) - I_s(x_s, y_s)}{I_s(x_s, y_s)} = \frac{\partial(x_s - x_i)}{\partial x} + \frac{\partial(y_s - y_i)}{\partial y} \tag{4.20}$$

Using Equations 4.13 and 4.14 for $(x_s - x_i)$ and $(y_s - y_i)$, and integrating over the dimensions of the growth chamber, we get

$$\frac{I_o(x_i, y_i) - I_s(x_s, y_s)}{I_s(x_s, y_s)} = (L \times D)\left(\frac{\partial^2}{\partial x^2} + \frac{\partial^2}{\partial y^2}\right)\{\log n(x, y)\} \tag{4.21}$$

Equation 4.21 is the governing equation of the shadowgraph process under the set of linearizing approximations 1-3. In concise form the above equation can be written as

$$\frac{I_o - I_s}{I_s} = (L \times D)\,\nabla^2\{\log n(x, y)\} \tag{4.22}$$

4.1.2. Numerical solution of the Poisson equation

The governing differential equation of the shadowgraph process (Equation 4.22) relates the intensity variation in the shadowgraph image to the refractive index field of the inhomogeneous medium. In order to solve the equation to obtain the refractive index, the following numerical procedure is adopted (Verma, 2006). First, the Poisson equation is discretized over the physical domain of interest by a finite-difference method. The resulting system of algebraic equations is solved for the image under consideration to yield a depth-averaged refractive index value for each node point of the grid. A mix of Dirichlet and Neumann boundary conditions are used for the purpose. The refractive index conditions used on the boundaries are shown in Figure 4.2. A computer code has been written for solving the Poisson equation, and it has been validated against analytical examples. The experimental input to the code is the matrix of gray values of pixels in the shadowgraph image. The output generated by the Poisson solver is a matrix containing the averaged refractive index at each node of the grid. The relationship between the refractive index and the concentration of the KDP saturated solution is used (Rashkovich, 1991) to obtain the concentration field in each shadowgraph image.

4.1.3. Ray tracing through the KDP solution: Importance of the higher-order effects

In order to assess the importance of higher-order optical effects such as scattering and interference in shadowgraph imaging, the extent of the bending of rays is estimated by tracing the passage of rays through the KDP solution. In order to accomplish this step, the shadowgraph images of the growth process recorded at different stages of growth are analyzed as follows: The Poisson equation governing the shadowgraph process is solved numerically to yield a depth-averaged refractive index value for each node point of the grid (Section 4.1.2). The refractive index information is then used to determine the

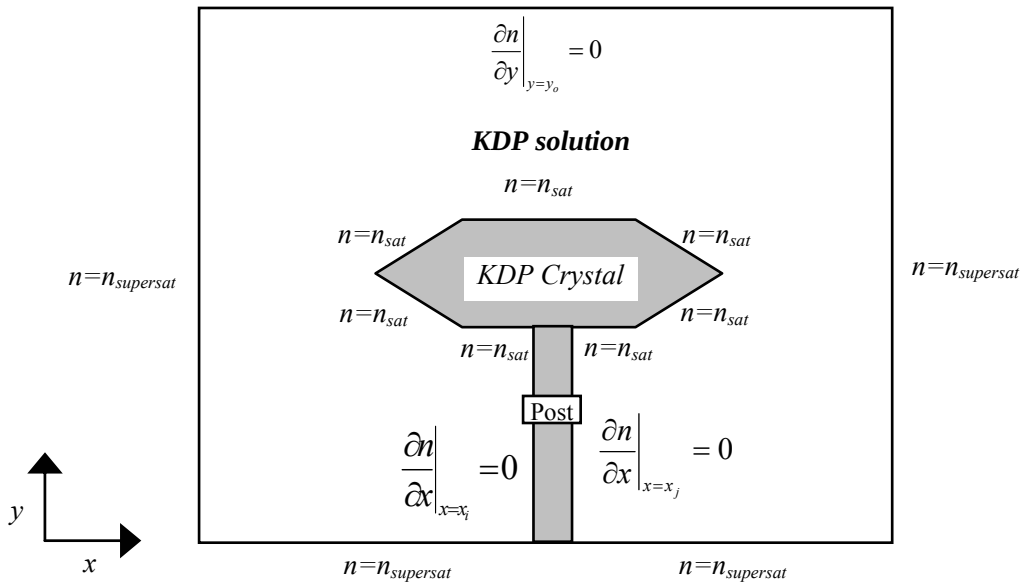

Figure 4.2. Refractive index specification on the boundaries.

deflection of the ray at the exit plane of the growth chamber by solving the coupled ordinary differential equations (ODEs) governing the passage of light ray through the region of disturbance (Equations 4.3 and 4.4, Section 4.1.1). The solution of these equation yields the two orthogonal components of the deflection of the ray and its gradient at the exit plane of the test cell. For the Poisson equation to be applicable for shadowgraph analysis, the ray deflections should be small. The small deflection approximation can be assessed with this approach. A computer code for solving the coupled ODEs uses the fourth order Runge-Kutta method. It has been written and validated against analytical examples.

4.1.4. Correction factor for refraction at the glass-air interface

During the process of crystal growth the KDP solution is a medium of varying refractive index, leading to the bending of the rays as the laser beam traverses through the solution. At the exit from the growth chamber, the light ray encounters two different interfaces, namely solution and glass, followed by glass and air. Thus, the light ray emerges at an angle different from the angle at which it is incident on the solution and glass interface. The refractive indices of the KDP solution, the quartz window, and the air result in a scale factor which must be taken into account to get the correct emergent angle of the ray. The optical path of the light ray through the two interfaces is shown in Figure 4.3 below. The mathematical expression of the scale factor used in calculations is derived below.

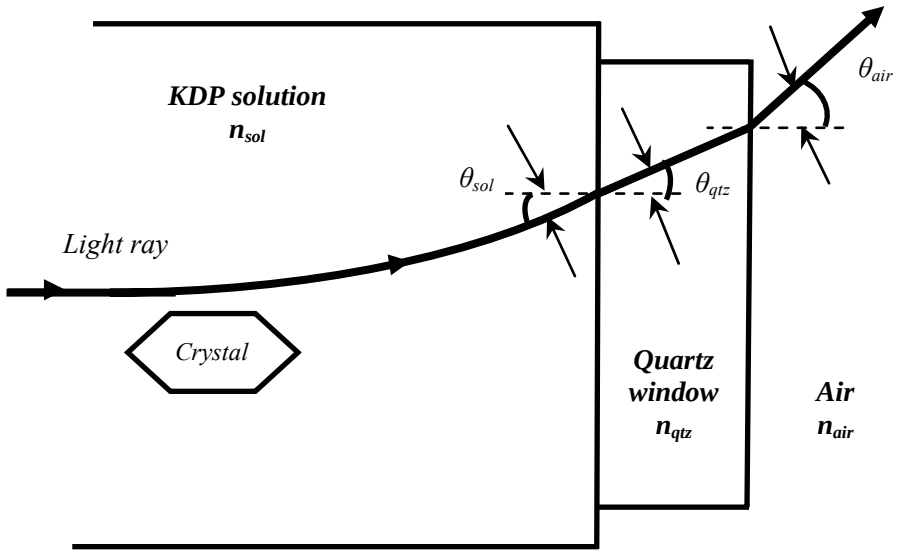

Figure 4.3. Optical path of the light ray passing from the growth chamber into the air.

Applying Snell's law for refraction of the light ray passing from the solution into the quartz optical window, we get

$$\frac{\sin\theta_{sol}}{\sin\theta_{qtz}} = \frac{n_{qtz}}{n_{sol}} \tag{4.23}$$

where $\theta_{sol}, \theta_{qtz}, n_{sol}$ and n_{qtz} are the angles of incidence of the light at the quartz window, the angle of refraction of the light ray into the quartz window, the refractive index of the KDP solution, and the refractive index of the quartz window respectively. Applying Snell's law again for the ray passing from the quartz optical window to the surrounding air, we get

$$\frac{\sin\theta_{qtz}}{\sin\theta_{air}} = \frac{n_{air}}{n_{qtz}} \tag{4.24}$$

where $\theta_{qtz}, \theta_{air}, n_{qtz}$ and n_{air} are the angles of refraction of the light ray into the quartz window, the angle of refraction of the light ray in the air, the refractive index of the quartz window, and the refractive index of air respectively. Substituting the expression for $\sin\theta_{qtz}$ from Equation (4.23) into Equation (4.24), we get

$$\frac{\sin\theta_{sol}}{\sin\theta_{air}} = \frac{n_{air}}{n_{sol}}$$

Under the small-angle approximation $\sin\theta \approx \theta$ and therefore

$$\frac{\theta_{sol}}{\theta_{air}} \approx \frac{n_{air}}{n_{sol}}$$

$$\theta_{air} \approx \frac{n_{sol}}{n_{air}}\theta_{sol} \quad . \tag{4.25}$$

Thus the correction factor for additional refraction at the optical window is $\frac{n_{sol}}{n_{air}}$.

4.1.5. Methodology for determining the supersaturation at each stage of the experiment

The technique of slow cooling is adopted for the growth of the KDP crystal. As a result the experiment proceeds through different stages of supersaturation depending upon the amount of supercooling given to the solution from its saturation temperature. The equation for determining the concentration of KDP solute in water for temperatures in the range 29 – 50°C is (Rashkovich, 1991; p. 19)

$$C = (10.9 \pm 0.2) + 0.3616\ T \pm 0.04 \text{ g KDP/100g water}$$

This expression is used to compute the saturation concentration of the KDP solution at any desired temperature. The difference in the concentration at saturation temperature and the temperature at which the experiment is performed gives us the extent of supersaturation of the solution. This is the driving force for the growth process and is computed at each stage of imaging experiment.

4.1.6. Dimensionless numbers in crystal growth

In principle, for a quantitative estimate of the influence of the fluid-dynamical conditions on any physical process one needs to solve the Navier-Stokes equations. For qualitative analysis, it is sufficient to obtain an order-of-magnitude estimate through various dimensionless numbers formulated for the purpose (Gebhart, 1988). Since formulating and solving full Navier-Stokes equation for understanding the influence of transport conditions on the solution growth process is beyond the scope of the present review, a concise

discussion on *Grashof*, *Reynolds* and *Schmidt* numbers, the three important dimensionless numbers relevant during crystal growth from solution is presented below.

Grashof number (Gr): It measures the importance of buoyancy-driven convection in the physical process under study. It is defined as the ratio of buoyancy forces in the liquid to viscous forces. In the physical process of interest, buoyant convection could arise either due to thermal differences or due to density differences in different regions of the fluid. In crystal growth from solution, buoyant convection develops due to difference in the density of the solution near and far away from the crystal. Mathematically, it is represented as

$$Gr = \rho \frac{\partial \rho}{\partial C} \frac{(C_o - C_i)}{\mu^2} g L^3 \cdot \tag{4.26}$$

Here $\rho, \partial\rho/\partial C, C_o, C_i, g, L$ and μ are the density of the solution at a certain temperature in *kg/m*^{3}, gradient of density with concentration, bulk solute concentration in *mole/m*^{3}, interface concentration near to the crystal, acceleration due to gravity in *m/s*^{2}, characteristic length in *meters*, and the dynamic viscosity of the solution in *kg/m-s* respectively. The characteristic length is defined in a manner so as to take into account the influence of overall dimensions of crystal on the flow behavior. Density and viscosity of the KDP solution are functions of concentration of solute present in the solution and its temperature. These physico-chemical properties of the solution are available in the literature (Rashkovich, 1991).

Reynolds number (Re): Reynolds number measures the overall intensity of the flow during growth. It is used to determine whether a given flow field will be laminar or turbulent. It is defined as the ratio of inertial forces to viscous forces, and is mathematically given as

$$\mathrm{Re} = \frac{\omega L^2}{\nu} \tag{4.27}$$

where ω is the rotation velocity in *rad / s*, L is the characteristic length in *meters* and ν is the kinematic viscosity in *m*^{2}*/s*. The kinematic viscosity (ν) is related to density as μ / ρ, where μ is the dynamic viscosity in *kg/m-s* and ρ is the density of the fluid in *kg/m*^{3}. Laminar flow occurs at low Reynolds numbers where viscous forces are dominant. It is characterized by smooth

and continuous fluid motion. Turbulent flow occurs at high Reynolds numbers where inertial forces dominate. It is characterized by the appearance of eddies, vortices and flow fluctuations. The transition between laminar and turbulent flow is often indicated by a *critical* Reynolds number.

Three different crystal growth geometries are used in the present work, namely (i) growth of crystal placed on a platform, (ii) growth of a crystal held on top of a glass rod fixed to a platform, and (iii) crystal hanging from a glass rod. The characteristic lengths used for computing the Reynolds number for the three geometries have to be carefully selected.

Schmidt number (Sc): It is defined as the ratio of momentum diffusivity to species diffusivity, and is a fluid property. It is a measure of the ratio of the hydrodynamic and diffusion boundary layer thicknesses. Mathematically it is represented as

$$Sc = \frac{\mu}{\rho D} \tag{4.28}$$

Here symbols μ, ρ and D are dynamic viscosity in *kg/m-s*, density in kg/m^3 and diffusion coefficient of solute in the solution in m^2/s, respectively.

4.1.7. Relationship between density and refractive index: Gladstone-Dale equation

A one-to-one correspondence between the refractive index of the medium and the density (or concentration) is established as follows. The index of refraction of a homogeneous medium is a function of density given by the Lorentz-Lorenz relationship (Goldstein, 1996)

$$\frac{n^2 - 1}{\rho\ (n^2 + 2)} = \text{ constant } (k) \tag{4.29}$$

where n is the refractive index and ρ is the density of the medium. Rearranging the above equation we get

$$n^2 - 1 = \rho k (n^2 + 2).$$

Differentiating both sides with respect to density we get

$$2n \frac{dn}{d\rho} = \rho k \left(2n \frac{dn}{d\rho} \right) + k \left(n^2 + 2 \right).$$

Rearranging the above equation results in the gradient of refractive index with density

$$\frac{dn}{d\rho} = \frac{k\left(n^2+2\right)}{2n(1-\rho k)}.$$

When $n \cong 1$ (for gases) the Lorentz-Lorenz relationship reduces to the Gladstone-Dale equation

$$\frac{n-1}{\rho} = k \cdot$$

The constant *k* is called Gladstone-Dale constant. It is a material property and varies slightly with wavelength. Usually the constant *k* is replaced by the value of refractive index of the medium at some standard condition i.e. $k = \frac{n_o - 1}{\rho_o}$, resulting in the following expression for the Gladstone-Dale equation

$$\rho = \rho_o \left(\frac{n-1}{n+2}\right) \tag{4.30}$$

For small changes in concentration, and nearly uniform bulk pressure, fluid density is a linear function of concentration:

$$\rho = \rho_o \left\{1 - \gamma\left(C - C_o\right)\right\}$$

Here dependence of density on pressure has been taken to be of secondary importance. Since liquids are practically incompressible, their density varies only with concentration of solute. Within limits, the variation is taken to be linear. Since dn/dC is a material property, it is a constant. In summary, changes in concentration are associated simultaneously with changes in refractive index of the fluid medium. Because of principles of wave optics, it results in a phase change of the light wave traversing the medium during a measurement. Phase change is the origin of fringe formation in the interferometric images.

If the pressure variation within the fluid region is negligible, the fluid density is uniquely related to the refractive index, and hence to the solute concentration. The relationship between the refractive index and the

concentration is linear for most of the physical processes of interest here. Since the process of crystal growth from solution is mediated by slow cooling of the solution, it is natural to perceive that the temperature and the concentration changes accompany it. However the cooling rates employed during growth are negligibly small with respect to the time frame of imaging. Hence the solution is assumed to be isothermal for the short durations during which imaging is performed. Crystal growth from solution is primarily a mass transfer process driven by the concentration difference between regions near the crystal boundaries and far away from it. The physical property that governs the measurement process during growth is dn/dC of the solution under study.

4.2. Interferometry

Different types of optical techniques have been used for mapping of fluid flow, temperature and concentration. These include, (a) flow marker techniques using dye, bubbles and neutrally buoyant seeds that enable direct visualization of the fluid motion; (b) techniques in which the frequency of the incident radiation gets Doppler-shifted after getting scattered from the particles moving with the flow, for example laser Doppler velocimetry; and (c) techniques which measure the index of refraction of the medium through which the light beam propagates. The third category includes interferometry, shadowgraphy and schlieren. In the present work we are mainly concerned with these latter techniques.

The sensitivities of the three refractive-index based methods are quite different. Interferometry is used when the expected changes in the refractive index are small, whereas shadowgraphy and schlieren are used when the changes in the refractive index are large. Principally, the three techniques measure the physical property in an integrated manner, i.e. the output is an integration of the physical quantity of interest along the path of the beam through the process chamber. Therefore, ideally these should be applied for measurements in two-dimensions, where the approximation of negligible variation of the physical quantity in the third dimension can be assumed to be valid. In case this assumption is not applicable, the variation in the third dimension has to be obtained by applying analytical techniques, such as computerized tomography.

Interferometers are usually employed for quantitative data analysis. The physics behind the generation of interferograms is fundamentally different from that of the formation of shadowgraph and schlieren images. The latter are formed due to deflection of the light beam while traversing through the region of disturbance. As a result the intensity pattern on the screen gets altered when compared to the reference intensity pattern. In the case of

interferometry, it is the phase change of the test beam with respect to the reference beam which is at the origin of the formation of interferograms. The refraction of the light is a second-order optical effect and is an undesirable phenomenon in interferometry. It introduces an error in the equations governing the formation of interferograms. Similarly, scattering of the light beam is also a higher-order optical effect and is not desirable during interferometry. In order to understand interferometric measurements the wave nature of light is invoked. As mentioned above, interferometry is used when the expected changes in temperature or concentration are small. If the thermal or solutal changes in the region of interest are large, they limit the usefulness of interferometry in process monitoring for the following reasons: (i) the linearity between density (through temperature or concentration) and refractive index breaks down; and (ii) large gradients in the temperature and concentration fields result in sharp bending of rays. Both these effects complicate interferometric data analysis.

The most common form of interferometer used in fluid dynamics research is the Mach-Zehnder interferometer. It is used for mapping concentration in those processes where changes in temperature can be neglected. The interferograms provide direct visual evidence of the solutal field prevailing inside the process chamber. The quantitative methodology of extracting concentration change per fringe shift from the wedge and infinite fringe settings is described below.

Let *n(x,y,z)* and *C(x,y,z)* be the refractive index and concentration fields respectively in the physical domain of interest. With reference to our test cell, coordinates *x* and *y* form the vertical plane, which is perpendicular to the beam propagation direction, and the *z-axis* is the horizontal line along the length of the growth chamber. The light beam propagates parallel to the *z-axis*. Let n_o and C_o be the reference values, as encountered by the reference beam passing through a compensating chamber. The interferogram is a fringe pattern arising from the optical path difference

$$\Delta PL(x,y,z) = \int_0^S \left[n(x,y,z) - n_o \right] ds \tag{4.31}$$

which in terms of concentration is

$$\Delta PL(x,y,z) = \frac{dn}{dC} \int_0^S \left[C(x,y,z) - C_o \right] ds \cdot \tag{4.32}$$

The above integral is evaluated along the path of the light ray given by the coordinate *s*. If we neglect higher order optical effects such as refraction and

scattering, the path of the light ray will be straight along the length of the growth chamber, and the integral evaluation is greatly simplified. Since the interference fringes are loci of constant phase or constant phase difference, the optical path difference ΔPL is constant on a given fringe.
Therefore

$$\int_0^L \left[C(x,y,z) - C_o\right] dz = \frac{\Delta PL(x,y,z)}{dn/dC} = \text{constant} \tag{4.33}$$

and it follows that

$$\int_0^L C(x,y,z)dz \; - \; C_o L = \text{constant} \tag{4.34}$$

for a given fringe.

The integral $\int_0^L C(x,y,z)dz$ is equal to $\overline{C}L$, where $\overline{C}$ is the average value of the variable *C(x,y,z)* along the length L traversed by the laser beam inside the growth cell. Under the approximation of negligible refraction, the above integral reduces to a line integral of the function *C(x,y,z)* along the *z-axis*. Hence, we get

$$(\overline{C} - C_o)\, L = \text{constant} = \frac{\Delta PL}{dn/dC} \cdot \tag{4.35}$$

This equation holds for all the fringes in the case of the infinite-fringe setting interferogram. When refraction effects are neglected, light rays travel in straight lines and the path traveled by all the rays is constant, equal to the length L of the test cell. In such a situation, Equation 4.35 implies that $\overline{C}$ is also a constant over the fringe. Hence, each fringe of the interferogram represents a locus of points over which the average of the concentration field evaluated along the length of the test cell is constant; i.e. the fringes are isoconcentration contours. In case of processes governed predominantly by thermal changes, fringes correspond to isotherms.

For a change in path length by one wavelength, one fringe shift occurs. Since this change in path length per fringe shift is constant, the change in concentration per fringe shift is also a constant. Defining the function $(\overline{C} - C_o)\, L$ in Equation (4.35) as $f(\overline{C}, L)$, the concentration at two successive fringes for a given value of L can be obtained as

fringe 1: $$f_1(\overline{C_1}, L) = \frac{\Delta PL}{dn/dC}$$

fringe 2: $$f_2(\overline{C_2}, L) = \frac{(\lambda + \Delta PL)}{dn/dC}$$

where λ is the wavelength of the laser. From these two equations the concentration change per fringe shift can be calculated as

$$\Delta C_E = \frac{1}{L}\left\{f_2(\overline{C_2}, L) - f_1(\overline{C_1}, L)\right\} = \frac{\lambda / L}{dn/dC}. \tag{4.36}$$

The number of fringes expected in a projection can be estimated from the relation

$$\text{Number of fringes} = \frac{C_2 - C_1}{\Delta C_E} \tag{4.37}$$

This relation is valid when (a) the refraction effects are negligible and (b) the test beam is traversing through a single fluid. The value of ΔC_E is a constant for a particular fluid and the experimental parameters, i.e. length of the test cell and the wavelength of the laser.

Now consider the situation wherein concentration gradients are large and the ray traverses a different distance through the cell. Let the two light rays traverse paths L_1 and L_2 respectively inside the test cell, and the corresponding line integrals of the concentration field $C(x,y,z)$ resulting in the average concentrations be $\overline{C_1}$ and $\overline{C_2}$ respectively. Using Equation (4.35) we can write

$$(\overline{C_2} - C_o)\, L_2 = (\overline{C_1} - C_o)\, L_1 .$$

Thus, the line integral value $\overline{C_2}$ at a location on the fringe which corresponds to the length L_2 can be expressed in terms of the line integral value $\overline{C_1}$ at some other location corresponding to the ray length L_1 as

$$\overline{C_2} = C_o + \frac{L_1}{L_2}\left(\overline{C_1} - C_o\right). \tag{4.38}$$

4.2.1. Refraction effects

The presence of strongly refracting fields can modify Equation (4.36) for the concentration difference per fringe shift. In the present context, a strongly refracting field will arise when there is large concentration difference in the vertical direction inside the test cell. Hence, the light ray will not travel in a horizontal plane; instead it will bend in the vertical direction, the extent of which depends on the magnitude of the concentration gradient. Therefore refraction will introduce an additional path length for the test beam. It is worth pointing out that the choice of the algorithm for reconstruction of the concentration field from the interferometric projection data depends upon whether the rays passing through the test cell move in a straight line or along curved path. In case of straight line propagation, a plane-by-plane reconstruction of the concentration field is possible by conventional tomographic reconstruction algorithm. Refraction effects result in distortion of the interferometric fringe pattern such that the fringes cannot be assigned specific concentration values. Therefore it necessitates development of specific algorithms that enable extraction of concentration values from the complex interferograms, followed by a whole-field reconstruction methodology. The refraction errors in the present application are indeed negligible, which is justifiably so, since the KDP solution refractive index is a very slowly varying function of concentration and temperature. For the sake of completeness of the discussion on interferometric imaging, we present below the derivation of the formula for calculating the change in concentration per fringe shift under the presence of strongly refracting fields.

Consider the path of the light ray AB through a test cell (Figure 4.4) when it is affected by refraction effects. Let α be the bending angle at a location P of the test cell. The optical path length from A to B is given by

$$AB = \int_A^B n(x,y,z)\, ds$$

$$= \int_0^L n(x,y,z)\, \frac{dz}{\cos\alpha}.$$

Here y is a coordinate parallel to the gravity vector and z is parallel to the direction of propagation of light. The length of the test section in the z-direction is indicated as L.

Assuming α to be small, $\cos(\alpha)$ can be expressed as

$$\cos\alpha = (1-\alpha^2)^{1/2}$$

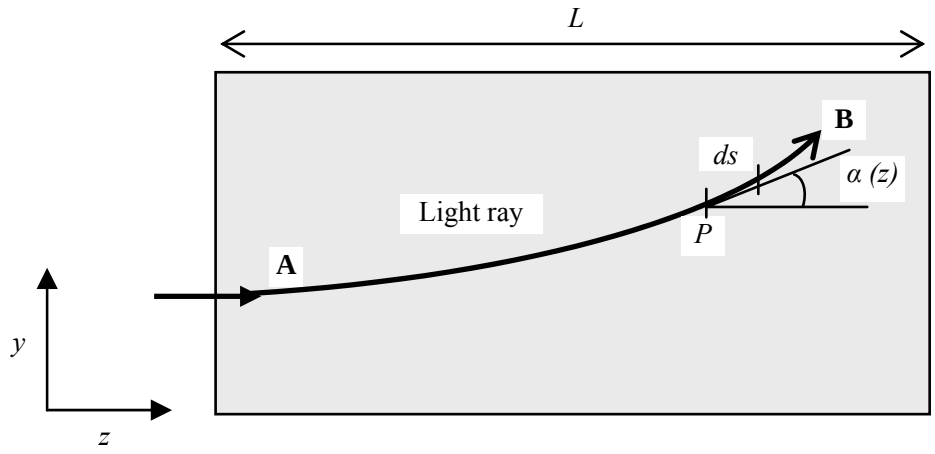

Figure 4.4. Bending of the light ray due to refraction effects.

Using the first two terms of the binomial expansion, one can approximate

$$\cos\alpha \sim 1 - \frac{\alpha^2}{2}$$

Hence the optical path length is given by

$$AB = \int_0^L n(x,y,z)\left(1-\frac{\alpha^2}{2}\right)^{-1} dz$$
$$= \int_0^L n(x,y,z)\left(1+\frac{\alpha^2}{2}\right) dz \qquad (4.39)$$

The cumulative bending angle *α(z)* at any location along the *z* axis can be easily calculated. It can be shown that the expression for the bending angle *α(z)* is (Goldstein, 1996)

$$\alpha(z) = \frac{1}{\overline{n}(x,y)}\frac{\partial \overline{n}(x,y)}{\partial y} z \qquad (4.40)$$

where $\overline{n}(x,y)$ is the average line integral of $n(x,y)$ over the test cell dimension *L*. Similarly the expression $\partial\overline{n}(x,y)/\partial y$ represents the average line integral of the transverse derivative of $n(x,y)$ over the length *L*.

Substituting the expression for *α(z)* from Equation (4.40) in Equation (4.39) we get

$$AB = \int_0^L n(x,y,z)\left(1 + \frac{1}{2}\frac{1}{\overline{n}^2}\left(\frac{\partial \overline{n}}{\partial y}\right)^2 z^2\right)dz$$

$$= \overline{n}(x,y)L + \frac{1}{6\,\overline{n}}\left(\frac{\partial \overline{n}}{\partial y}\right)^2 L^3 \tag{4.41}$$

The optical path of the reference beam is

$$AB = \int_0^L n_o dz$$

$$= n_o\, L \tag{4.42}$$

Hence the difference in the optical path lengths of the test and reference beams in the presence of refraction effects is

$$\Delta PL = \overline{n}(x,y)L + \frac{1}{6\,\overline{n}}\left(\frac{\partial \overline{n}}{\partial y}\right)^2 L^3 - n_o L$$

$$= \left(\overline{n}(x,y) - n_o\right)L + \frac{1}{6\,\overline{n}}\left(\frac{\partial \overline{n}}{\partial y}\right)^2 L^3$$

$$= \left(\overline{C}_1(x,y) - C_o\right)L\frac{dn}{dC} + \frac{1}{6\,\overline{n}}\left(\frac{\partial \overline{n}}{\partial y}\right)^2 L^3 \tag{4.43}$$

where $\overline{C}_1(x,y)$ represents the average line integral of the temperature field along the direction of the ray at a given point on the fringe. The corresponding ray over the next fringe corresponds to an additional path of λ and can be written as

$$\Delta PL + \lambda = \left(\overline{C}_2(x,y) - C_o\right)L\frac{dn}{dC} + \frac{1}{6\,\overline{n}}\left(\frac{\partial \overline{n}}{\partial y}\right)^2 L^3 \tag{4.44}$$

where $\overline{C}_2(x,y)$ represents the average line integral of the temperature field along the direction of the ray at a point on the next fringe. The successive temperature difference between the two fringes is

$$\lambda = \left(\overline{C}_2(x,y) - \overline{C}_1(x,y)\right) L \frac{dn}{dC} + \frac{1}{6\,\overline{n}} \left(\frac{d\overline{n}}{dC}\right)^2 \left(\left(\frac{\partial C}{\partial y}\bigg|_2\right)^2 - \left(\frac{\partial C}{\partial y}\bigg|_1\right)^2 \right) L^3 \tag{4.45}$$

and the concentration change per fringe shift is

$$\Delta C_E = \frac{\lambda - \left(\frac{1}{6\overline{n}(x,y)}\right)\left(\frac{d\overline{n}}{dC}\right)^2 \left(\left(\frac{\partial C}{\partial y}\bigg|_2\right)^2 - \left(\frac{\partial C}{\partial y}\bigg|_1\right)^2 \right) L^3}{L\left(\frac{dn}{dC}\right)}. \tag{4.46}$$

Since the gradient in the concentration field is not known before the calculation of the fringe concentration, the factor $\left(\frac{\partial C}{\partial y}\big|_2\right)^2 - \left(\frac{\partial C}{\partial y}\big|_1\right)^2$ must be calculated from a guessed concentration field. Thus the final calculation of ΔC_E relies on a series of iterative steps with improved estimates of the concentration gradients. As an estimate, the concentration gradient can be replaced by its largest value, namely at the wall. It can be readily calculated using correlations for *Schmidt* number (mass transfer) and *Nusselt* number (heat transfer). A realistic estimate is obtained by employing the average concentration gradient for locations 1 and 2.

4.2.2. Evaluation of interferograms

The thinned fringes carry the essential information of the process parameter rather than the thick fringe bands. Hence, in order to extract quantitative data from the Mach-Zehnder interferograms, we have to obtain the fringe skeleton. For our process, the thinned fringes contain the information about the path-integrated concentration field. In the sub-sections below we discuss the methodology for calculating the concentration field from interferograms recorded in the infinite- and wedge-fringe settings.

4.2.2.1. Infinite fringe interferograms

Let us consider an infinite fringe interferogram as shown in Figure 4.5. The aim is to find the absolute concentration corresponding to each fringe curve. We know that the change in concentration per fringe shift is given by

$$\Delta C_E = \frac{\lambda / L}{dn/dC} \text{ and } C_2 - C_1 = \frac{\lambda / L}{dn/dC} \tag{4.47}$$

At the top boundary the concentration is equal to the saturation concentration, C_{sat}, whereas the bottom, the left and the right boundaries are at concentrations equal to the supersaturation value, $C_{supersat}$. If the crystal is present in the field of view, then the concentration at the crystal boundaries is equal to the saturation value, C_{sat}. Our aim is to find the concentrations C_1, C_2 and C_3 at the fringes 1, 2 and 3 respectively in the interferogram (Figure 4.5) with the given boundary conditions. Although the concentration values at the lower and the upper boundaries are known, assigning concentration to the first fringe appearing near the boundary is not straightforward. This is because the concentration gradients near the boundary result in several fine fringes that are lost because of the finite resolution of the CCD/video camera. Also, the first fringe may be distorted during the image processing operations. Hence it becomes necessary to assign concentration to the first visible fringe by an appropriate analytical procedure. The methodology of finding the concentration values at the first and the subsequent fringes is presented below.

Step-1: First identify that region of the interferogram where the fringes are closely packed. The fringes 1, 2, and 3 are three such fringes in the above interferogram (Figure 4.5).

Step-2: Fitting a second-order polynomial of the type $C(y) = \alpha + \beta y + \gamma y^2$ to the three fringes, we get

$$C_1 = \alpha + \beta y_1 + \gamma {y_1}^2$$

$$C_2 = \alpha + \beta y_2 + \gamma {y_2}^2$$

$$C_3 = \alpha + \beta y_3 + \gamma {y_3}^2$$

where y is the vertical coordinate measured from the lower boundary. An exploded view of the three fringes and the coordinate axis is shown in Figure 4.6. Using above equations we obtain two simultaneous equations for the two unknowns β and γ:

$$\Delta C_E = C_1 - C_2 = \beta (y_1 - y_2) + \gamma ({y_1}^2 - {y_2}^2)$$

$$\Delta C_E = C_2 - C_3 = \beta (y_2 - y_3) + \gamma ({y_2}^2 - {y_3}^2)$$

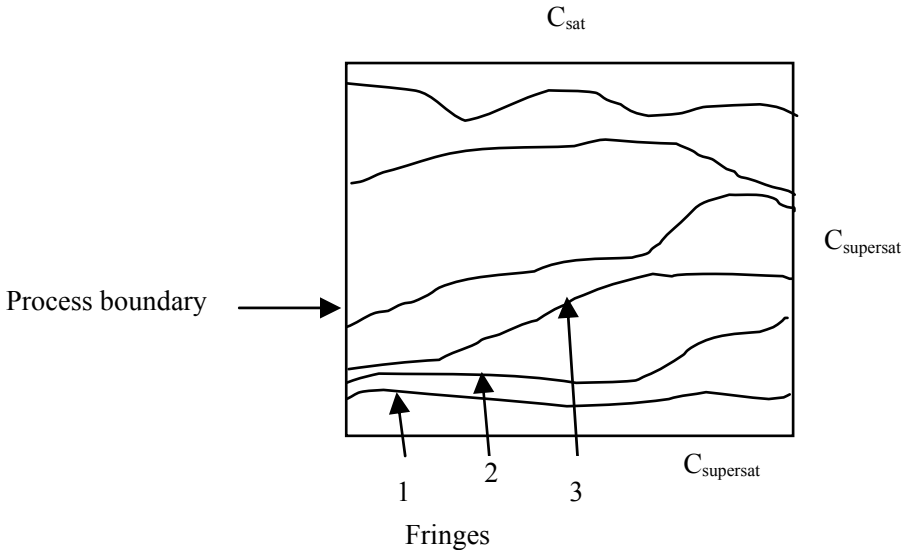

Figure 4.5. Infinite fringe interferogram of the concentration field. The boundary conditions shown in the above figure refers to the growth mode shown in Figure 4.2 wherein the crystal is in the middle of the image. The crystal and post have been omitted in the above figure to keep out the details not relevant to the discussion.

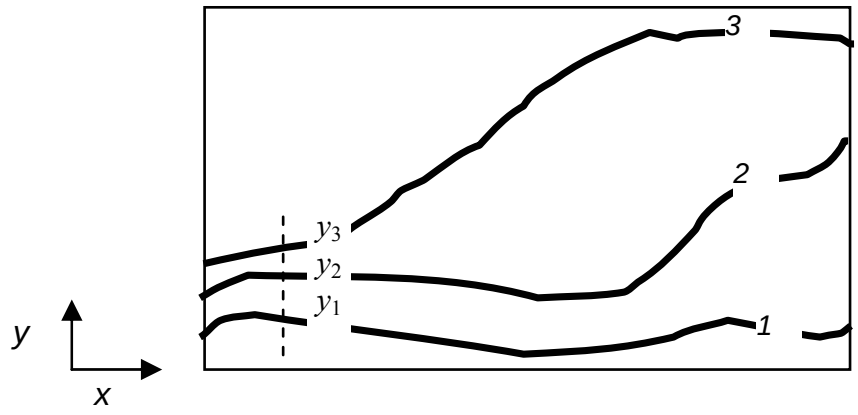

Figure 4.6. Exploded view of the fringes 1, 2 and 3 along with the coordinate system used.

These are solved to obtain the constants β and γ. Here, ΔC_E is the concentration change per fringe shift in the fluid.

Step-3: The next step in the analysis procedure is to compute the concentration gradient near the boundary close to the fringes. In the interferogram shown in Figure 4.6, we would be interested in finding the concentration near to the lower boundary. In our experimental conditions, this boundary is either a Plexiglas base of the platform structure on which the crystal is growing, or a relatively far-away location from a crystal growing in

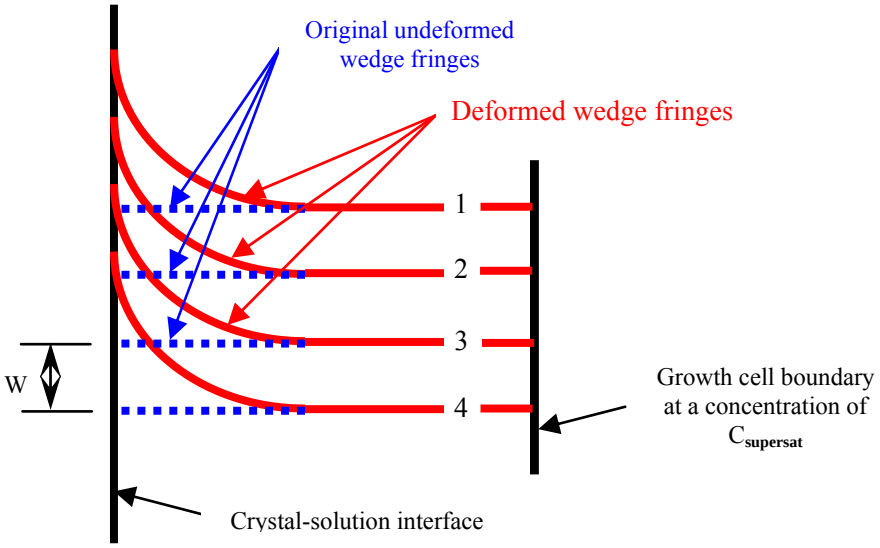

Figure 4.7. Wedge fringe pattern with and without the field of disturbance.

hanging geometry. In both experiments, the concentration gradient at the boundary is expected to be locally constant. However, it may be noted that depending upon the growth conditions employed, this situation may change. For example, in case of growth under free convection we have observed a vertical concentration gradient inside the growth chamber. It becomes steep with the progress of growth due to accumulation of low-density solution at the top under the influence of gravity.
The concentration gradient at the boundary can be given as

$$\left.\frac{\partial C}{\partial y}\right|_{y=y_o} = \beta + 2\gamma y_o \quad . \tag{4.48}$$

Step-4: Once the concentration and the concentration gradient at the boundary are known, the concentration at fringe 1 near the lower boundary can be obtained as

$$C_1 = C_{boundary} + \left.\frac{\partial C}{\partial y}\right|_{boundary} (y_1 - y_o) \tag{4.49}$$

and so

$$C_1 = C_{\text{supersat}} + (\beta + 2\gamma y_1)(y_1 - y_o)$$

Step-5: ΔC_E is the quantum of concentration change per fringe shift; thus concentration at subsequent fringes 2, 3 and others can be computed by adding it to the concentration of the previous fringe. However, if the concentration gradient is negative in the counting direction, subtraction is to be performed.

Step-6: Since the interferogram is digitized and stored in a computer in the form of a matrix of integers, the above procedure of computing concentration can be implemented for any element of the matrix. In our experiment the concentration is a smoothly varying function, and it is expected that the concentration difference between adjacent rows of the matrix will be small. Hence the evaluation procedure is applied to the rows coinciding with the fringe locations but not in the gap between them.

4.2.2.2. Wedge fringe interferograms

The Mach-Zehnder interferometer is not always used with the two interfering wavefronts parallel to each other, as in the infinite-fringe setting discussed above. There is a second mode in which the two interfering wavefronts have a small angle θ between them, introduced deliberately during alignment. Upon interference they produce an image consisting of bright and dark fringes, representing the loci of constructive and destructive interference respectively. These parallel and equally spaced fringes are referred to as wedge fringes. The spacing between the wedge fringes is a function of the tilt angle and the wavelength of the laser light used, and is given by

$$d = \frac{\lambda/2}{\sin(\theta/2)} . \tag{4.50}$$

For small tilt angles, the above expression becomes

$$d \sim \frac{\lambda}{\theta} . \tag{4.51}$$

As θ is decreased to zero, the wedge fringes get farther apart, approaching the infinite-fringe pattern.

When a thermal or concentration field is introduced in the path of the test beam, the phase of the test wavefront gets distorted. Upon interference with the reference wavefront, it manifests itself as a change from straight and parallel fringes to curved fringes. The two interference patterns are shown schematically in Figure 4.7 and as an exploded view in Figure 4.8.

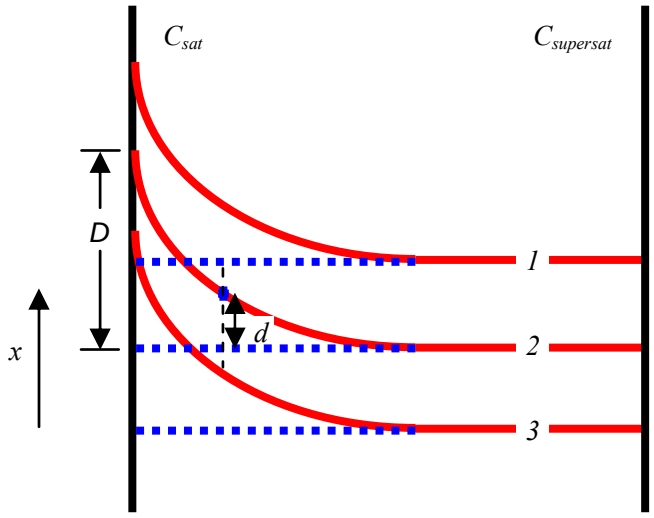

Figure 4.8. Computing concentration in the presence of the wedge fringes.

Let us find concentration at a point x in the interferogram. The deviation of fringe 2 near the crystal-solution interface is D, while at point x is d. Thus it can be written as (Goldstein, 1996)

$$\frac{C(x) - C_{\text{sat}}}{C_{\text{supersat}} - C_{\text{sat}}} = \frac{d}{D} \tag{4.52}$$

Since all other parameters except $C(x)$ are known, the local concentration can be easily calculated. The concentration gradient dC/dx is obtained from the slope of the fringes at a point x. The above methodology is used for calculating the concentration at points which lie on the wedge fringes. However, if one were to find concentration at a point lying between two wedge fringes, instead of on them, then one has to locate four nearby points on the wedge fringes and compute their respective concentrations. It is followed by a suitable interpolation technique to find the concentration at the desired point.

4.2.3. Concentration data over a uniform grid

Once the absolute concentration field corresponding to the fringes (in the wedge as well as infinite fringe setting) has been computed, the irregularly spaced concentration data must be transferred to a two-dimensional uniform grid over the fluid region. This is necessary to enable application of the tomographic algorithms for reconstruction of the three-dimensional concentration field. For this purpose, a two-dimensional linear interpolation

procedure is used by superimposing a 2D grid over the thinned interferograms. After completing the interpolation procedure, the equi-concentration contours are plotted. These contours should closely follow the originally recorded fringe pattern. It works as a cross-check for the data obtained after interpolation and provides an estimate of the interpolation errors.

4.3. Image processing

The shadowgraph images and the Mach-Zehnder interferograms are processed quantitatively to extract the concentration and convection field parameters. In case of shadowgraphy, the absolute value of the light intensity (gray value) at each pixel carries the information of the process parameter. Since this value gets altered by the image processing operations, raw experimental images are used for data analysis of concentration, followed by tomographic reconstruction. However, to compute the growth rate of the crystal, the information about the external shape of crystal at regular intervals of time is required. Since the absolute value of light intensity is not used for these computations, we use *edge detection* to get the edges of the crystal at different stages of the experiment. In the case of Mach-Zehnder interferograms, the absolute value of the intensity at each pixel is not important and the interferograms were processed for improving the image quality by the following operations (Jain, 2001):

(i) **Edge detection**: To extract the edges of the crystal in the shadowgraph images.
(ii) **Filtering**: To remove localized intensity maxima.
(iii) **Image enhancement**: For improving the contrast of the interferogram.
(iv) **Fringe thinning**: To extract the skeleton of the interference fringes.

4.4. Computerized tomography

Computerized tomography (CT) is defined as the process of producing a two-dimensional distribution of a function from its one-dimensional line-integrals obtained along a finite number of lines at known locations [Herman, 1980]. This definition could be extended to include three-dimensional reconstruction of a function from its two-dimensional projections taken along a fixed number of known directions. In the context of the present study, the projection data is the line integrals of refractive index field taken along different angular directions. The line integrals manifest as intensity values in the shadowgraph images or Mach-Zehnder interferograms. The procedure of extracting the refractive-index field (or concentration field) from the shadowgraph images is discussed in Section 4.1.2. Similarly, the procedure for obtaining refractive-index (or concentration) field from the Mach-Zehnder

interferograms is discussed in Section 4.2.3. A set of such line integrals taken along different directions represents the projection data of the concentration field. If the original field is two-dimensional, its projection data are one-dimensional line integrals. Several such line integrals taken at different angles are used to reconstruct the two-dimensional concentration field, using principles of computerized tomography. If the field is three-dimensional, its projection data are two-dimensional images. Several such images taken at different directions are used for true three-dimensional reconstruction of the concentration field. We shall now discuss the procedure for computing the three-dimensional concentration field from two-dimensional shadowgraph images and Mach-Zehnder interferograms recorded along different directions.

Tomography is essentially a two-step process: first, collection of the projection data and, second, reconstructing the field parameter using numerical algorithms. Reconstruction algorithms referred to as *convolution back projection (CBP)* and *algebraic reconstruction technique (ART)* are briefly reviewed below.

4.4.1. Convolution back projection algorithm

Consider reconstruction of a function $f(r,\phi)$, which in general represents physical quantities such as density, refractive index, and void fraction, from its line integrals taken along a few directions. Figure 4.9 shows the schematic drawing of the data collection geometry for a parallel beam CT scanner. Here, a unit circle represents the object, and the chord SD represents one data ray. The ray indices are s and θ, where s is the perpendicular distance of the ray from the object centre and θ is the angle made by the viewing direction.

The *Radon transform* defines the projection data as

$$p(s,\theta) = \int_{SD} f(r,\phi)dz \tag{4.53}$$

Implementing the *projection slice theorem*, namely the equivalence of 2-D Fourier transform of the object function $f(r,\phi)$ and 1-D Fourier transform of projection data $p(s;\theta)$, we get

$$\hat{p}(R,\theta) = \hat{f}(R\cos\theta, R\sin\theta) \tag{4.54}$$

Taking the 2D inverse Fourier transform of the above function results in the tomographic inversion formula

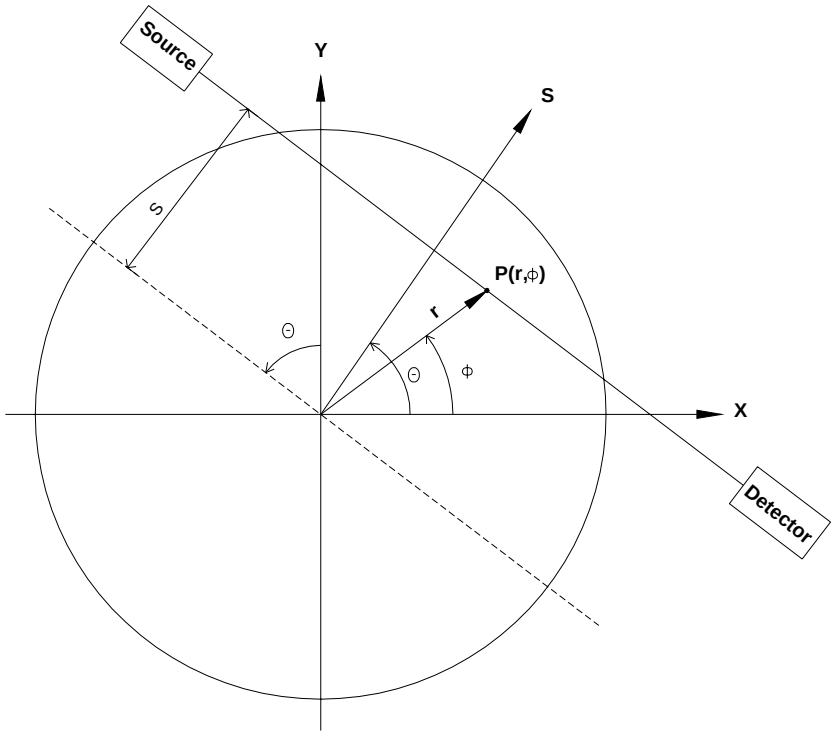

Figure 4.9. Parallel-beam data collection geometry.

$$f(r,\phi) = \int_0^{\pi} \int_{-\infty}^{\infty} \hat{p}(R,\theta)\, e^{i2\pi Rr\cos(\theta-\phi)}\, |R|\, dR\, d\theta \tag{4.55}$$

where

$$\hat{p}(R,\theta) = \int_{-\infty}^{\infty} \hat{p}(s,\theta)\, e^{-i2\pi Rs}\, ds \tag{4.56}$$

In the above equation for $f(r,\phi)$, the inner integral is divergent. Hence, for practical implementation of the above formula a filter function has to be used. The filter introduces frequency band-limitation in the reconstruction. After introduction of the filter function the approximate form of $f(r,\phi)$ is

$$\tilde{f}(r,\phi) \approx \int_0^{\pi} \int_{-\infty}^{\infty} \hat{p}(R,\theta)\, e^{i2\pi Rr\cos(\theta-\phi)}\, |R|\, W(r)\, dR\, d\theta \tag{4.57}$$

where

$$W(R) = 1, \quad |R| \le R_c$$
$$= 0, \quad |R| > R_c$$

Using the convolution theorem for Fourier transforms, we get

$$\tilde{f}(r,\phi) \approx \int_0^{\pi} \int_{-\infty}^{\infty} p(s,\theta)\, q(s' - s)\, ds\, d\theta \tag{4.58}$$

where

$$q(s) = \int_{-\infty}^{\infty} |R|\; W(R)\, e^{i2\pi Rs}\, dR \tag{4.59}$$

with

$p(s;\theta)$, the projection data;

s', the s value of the data ray passing through the point (r,ϕ) being reconstructed;

θ, the source position;

R, R_c, the Fourier frequency and the Fourier cut-off frequency respectively;

$q(s)$, the convolving function; and

$W(R)$ the filter function.

The inner integral in the final equation is a one-dimensional convolution, and the outer integral, corresponding to the averaging operation (over θ), is termed as the back projection, and hence the name *convolution back projection* for this reconstruction algorithm.

4.4.2. Algebraic reconstruction technique

The algebraic reconstruction technique (Censor, 1983; Muralidhar, 2001) is fundamentally different from the transform technique in the sense that the discretization of the problem is carried out at the very beginning. In the transform methodology of Section 4.4.1, the continuous problem is analytically treated until the very end, when the final formulae are discretized for computational implementation. Figure 4.10 shows the discretization of the region of interest. Collection of the projection data results in a matrix equation

$$\{\Phi_i\} = [w_{ij}]\{f_j\} \tag{4.60}$$

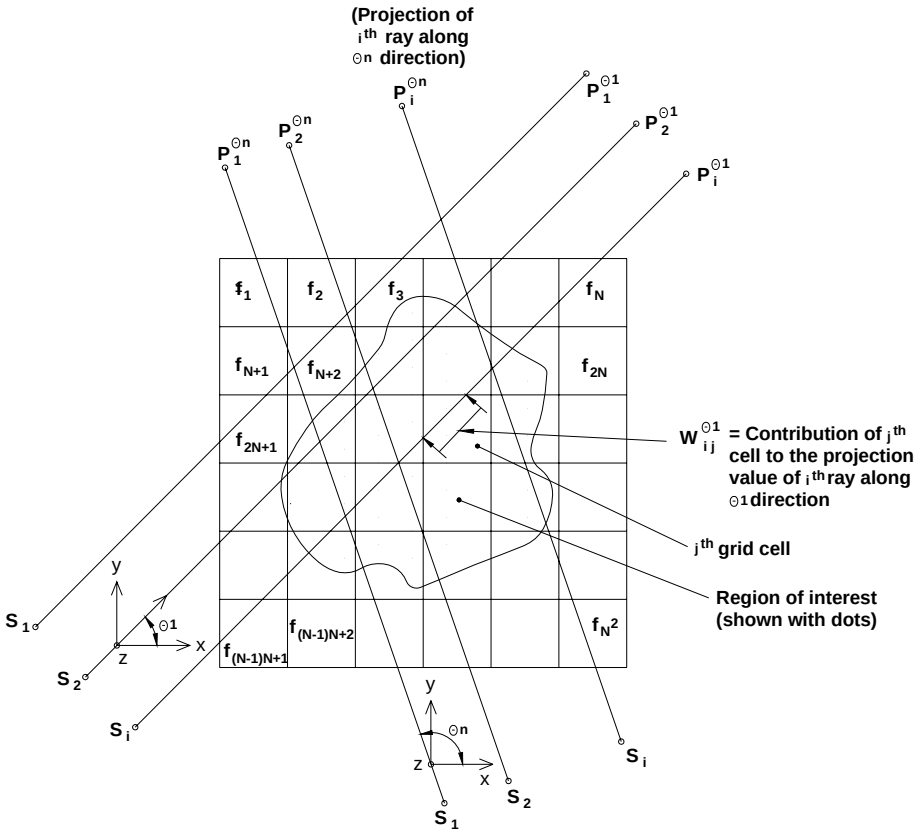

Figure 4.10. Discretization of the region of interest.

where *j=1...N, i=1...M (> N),* with *f* representing the basic unknowns of the grid, Φ the projection data, and $[w_{ij}]$ the weight factor. The above problem reduces to the problem of finding a generalized inverse of the matrix $[w_{ij}]$. The steps involved in the algebraic reconstruction algorithm are:

1. Initial assumption of the field to be reconstructed over a grid.
2. Calculation of the projection data with the initial guess.
3. Computation of the correction factor.
4. Distribution of the correction factor suitably among all the cells.
5. Test for convergence.

4.4.3. Reconstruction using *convolution back projection* (CBP) algorithm

Implementation of the CBP algorithm requires continuous projection data between 0-180°. The experimental set up used in the present work allowed only 18 projection images between 0-180°. Therefore, in order to implement CBP, a linear interpolation scheme was used for increasing the size of the projection data set.

4.4.3.1. Partial projection data

In tomography, the projection data required for reconstruction should be available for the full width of the flow field from each view angle rather than the partial width. The experimental apparatus used in the present work was such that only 20% of the flow field could be covered in each view angle, owing to the size of the laser beam (30mm) being less than the diameter of the process chamber (150mm). It resulted in a partial projection data set. This limitation was overcome by following a suitable extrapolation scheme to obtain projection values for points lying outside the volume included by the source-detector configuration. The extrapolation procedure adopted in the present work assumes that the concentration field is spatially uniform outside the central core of 20%. This is a justifiable assumption as the solution concentration is practically homogeneous away from the crystal-solution interface. However the variations in the chord length of the rays as they pass through different regions of the growth chamber have to be taken into account. The implementation of the interpolation step followed by extrapolation of the experimental information results in *complete* projection data, an essential requirement for the CBP algorithm. The projection data for each view angle should be consistent in terms of the average solution concentration over a given plane of the fluid layer. In other words, the average concentration should be constant for a given plane irrespective of the view angle. This mass-balance consistency check was performed for all data sets before applying the reconstruction algorithms.

4.4.4. Reconstruction using *algebraic reconstruction technique* (ART)

The discussion on the need for a consistent data set is applicable to ART family of algorithms as well. However, these algorithms can work with partial data. The solution obtained by this approach is expected to capture the global trends in the numerical solution, with finer features appearing in the reconstruction, when more complete projections become available.

Implementation of the ART family of algorithms requires an initial guess for the refractive index field to start the iterations. Convergence is known to be strongly sensitive to the starting guess. One of the purposes of using CBP in the present work, in spite of the recommendation against its use in situations involving incomplete and partial projection data, was to use this solution as the starting guess for the reconstruction based on ART. The ART family of algorithms has the advantage that it facilitates a crosscheck on the correctness of the converged solution. The procedure for the crosschecks has been discussed in detail by Mishra *et al*. [1998].

4.4.5. Sources of error

The tomographic reconstruction could have several sources of error arising out of experimental and computational factors. Some of these are:

- the limited number of view angles (incomplete data) available for reconstruction;
- partial projection data due to constraints of experimental apparatus or an opaque object blocking the source-detector path;
- bending of rays due to strongly refracting media;
- poly-chromaticity of radiation (beam hardening effects)[1];
- statistical nature of the radiation emission process[1];
- the issue of frequency-band limitation[2]
- there are a few other common type of errors in parallel beam CBP based reconstruction, such as the object centering error, incorrect ray sum error, detector imbalances and improper filter selection.

4.5. Michelson interferometry

A Michelson interferometer has been set up for on-line monitoring the growing face of a crystal. In this interferometry, one of the interfering beams is reflected from the surface of a growing crystal to get the microtopographic details of the growing surface. Since interferometry through the solution requires reflection of the light beam from the solution-crystal interface, it is a difficult task. Clear fringes can be recorded when the difference in refractive index between the solution and the crystal is sufficiently large. In spite of the inherent difficulties in working with this technique, it has been used for studies in growth kinetics.

The basic principle of the Michelson interferometry is that the phase variation due to growth or dissolution of the crystal surface manifests itself in the form of change in the fringe pattern. For example, if a crystal face has a growth hillock originating from a screw dislocation, the corresponding interference pattern consists of concentric fringes of equal thickness. Figure 4.11 shows

---

[1] *Poly-chromaticity and statistical nature of emitted radiations are important in case of x-ray tomography. This is because the x-ray sources are not strictly monochromatic (unlike a laser) and the x-ray emission follows Poisson statistics in time. Due to these two factors, the photon energy and the number of counts of detector (projection value) are marred by errors.*

[2] *A space-limited object has infinite spread in terms of frequency. However for computational purpose, the infinite frequency band is truncated by using suitable filters. This forceful truncation of frequency band introduces errors in the reconstructed field.*

schematically the process of fringe formation from a surface having a hillock generated from a dislocation.

With every change in the crystal thickness by $\lambda/2n$, one fringe shift takes place. Here λ is the wavelength of the laser used and n is the refractive index of the solution. From such an interferogram the geographical description of the crystal face is obtained. Quantitative analysis of the interferogram yields the growth-kinetic parameters such as normal growth rate R, slope of the dislocation growth hillock p, and tangential growth velocity V of the steps. These are computed as follows:

The difference of heights between two points on adjacent fringes of an interferogram corresponding to a growth hillock or dissolution valley is given by

$$d = \frac{\lambda}{2n} \tag{4.61}$$

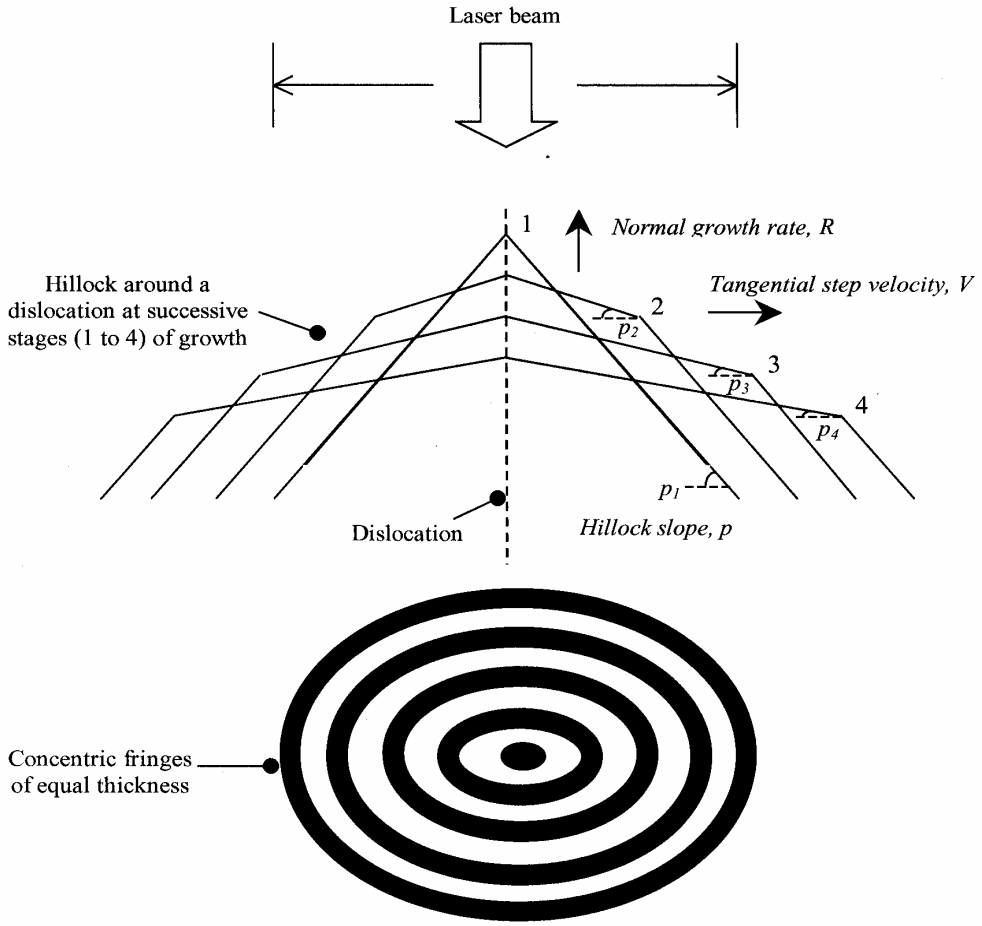

Figure 4.11. Schematic drawing of the Michelson fringe formation from a crystal face having a hillock generated from a dislocation.

If the total variation in the crystal thickness normal to the crystal face is Δh in time Δt, the normal average growth rate is given by

$$R = \frac{\Delta h}{\Delta t} \tag{4.62}$$

Here $\Delta h = N \times d$ and N is the total number of fringes that have crossed the point of observation on the interferogram. Thus the normal average growth rate becomes

$$R = \frac{N \times \lambda}{2 \times n \times \Delta t} \tag{4.63}$$

If D is the physical distance between the two points lying on adjacent fringes, the slope p of the hillock is given by

$$p = \tan\theta = \frac{d}{D} \tag{4.64}$$

The normal growth rate and the slope of the dislocation hillock are related to the tangential step velocity V as follows:

$$R = p \times V \tag{4.65}$$

Thus, by calculating R and p, the tangential step velocity V is obtained.

5. Shadowgraph imaging of crystal growth from solution

Since the crystal is growing from the liquid phase, therefore the flow conditions prevalent inside the crystallizer are expected to influence the crystal quality and the growth rate. The three aims of the shadowgraph imaging are (a) to observe the initiation and subsequent buildup of buoyancy driven as well as forced convective phenomena during crystal growth from solution, (b) to find an optimum cooling rate of the solution under free convection conditions that results in high growth rate as well as good quality, and (c) to establish a relationship between the convective features and the growth rate and crystal quality. For each convection mode, growth in three different geometries have been imaged, namely (i) crystal hanging from a glass rod, (ii) crystal perched on top of a glass rod, and (iii) crystal placed on a platform. The growth has been quantified in terms of the average growth

rates along <100> and <001> crystallographic directions of the KDP crystal. A discussion about the quality of the crystal in terms of the transparency and the visible defects such as inclusions, voids, cracks, and striations is presented along with the possible cause of their incorporation.

5.1. Crystal growth under free convection

The experiments done under buoyancy driven convective conditions in three different geometries are described below. The strength of free convection has been studied as a function of supercooling and crystal size, and its influence on growth rate and crystal quality has been discussed.

5.1.1. Crystal growth in top hanging geometry

A KDP crystal of dimensions 2×2×2 mm^3 having natural bi-pyramidal morphology with c-axis in horizontal direction is glued to one end of a glass rod (1.5 mm diameter) and hung inside the crystallizer (Figure 5.1). The KDP solution has a saturation temperature of 58°C and stoichiometric pH (4.3). The impurities in the solution are as-present in a commercially available KDP chemical (99.5% pure, GR-grade, *Merck* India). A cooling rate of 0.2°C/hr has been used. The growth has been performed for 27 hours and the total supercooling provided to the solution is 5 degrees.

It has been observed that even when the crystal is not subjected to any external mode of convection, the gravity induces convection due to buoyancy effect, which increases with the size of crystal and the degree of supercooling (or supersaturation). With time this convection activity becomes vigorous in strength, irregular, unstable, and three dimensional in character. Such a nature of convection leads to uncontrolled and fast growth of all the faces of KDP crystal, becoming a cause of several types of defects, inclusions being the most serious of them. Thus a properly controlled free convection is required to achieve the desired growth rate and quality. One of the ways to achieve it is through the application of an optimum cooling rate so as to achieve the desired levels of supersaturation.

The representative shadowgraph images of convective plumes at the final stages of the experiment are shown in Figures 5.2(a-c). The crystal grows to dimensions of *13×10×23* mm^3 ($a \times b \times c$ mm^3) at the end of the experiment. The average growth rate of the KDP crystal along <100> and <001> directions are 9.6 and 18.5 mm/day respectively. For free convection conditions these are considered very high, which are attributed to the high cooling rates employed. The growth rates achieved in the experiment are high, but the crystal quality is not good (Figure 5.3). The reason for the deterioration of the crystal quality is generation of defects, namely inclusions due to entrapment of the solution between the fast growing steps and edges of

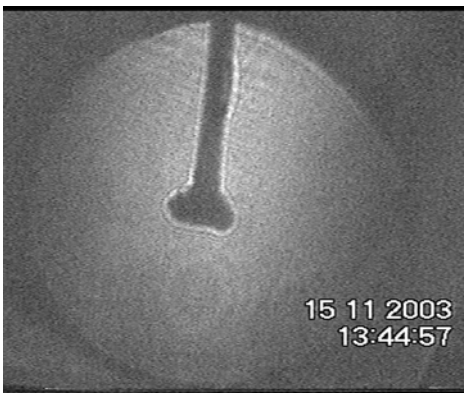

Figure 5.1. Seed hanging from a glass rod.

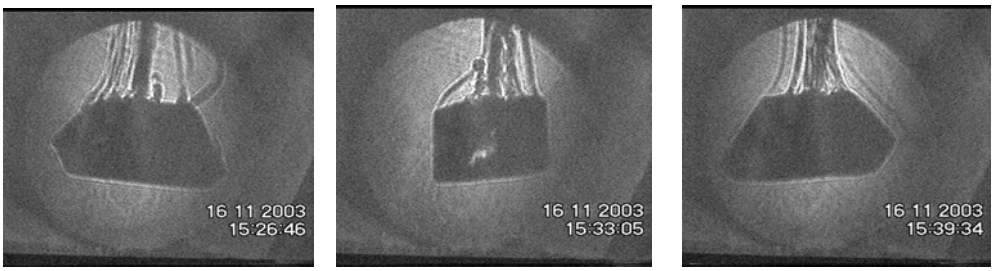

(a) (b) (c)

Figure 5.2 (a-c). Shadowgraph images from 3 different directions (0, 80 & 160°).

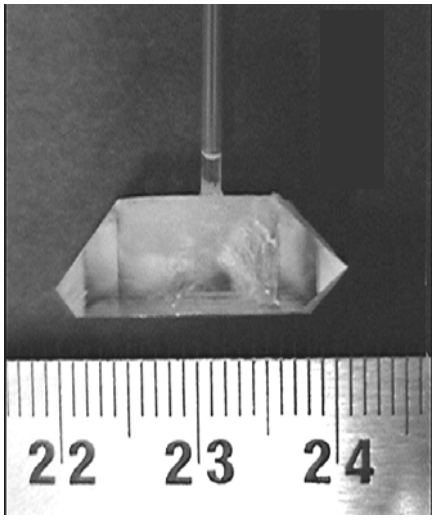

Figure 5.3. The size and the quality of the crystal.

the crystal. This is augmented by the free convection conditions which did not allow quick replenishment of the solute depleted solution. As a result it accumulates near the crystal surface and gets trapped between the edges of

the growing crystal. This suggests that cooling rates ~ 0.2°C/hr under free convection conditions are not advisable for growing a good quality crystal.

5.1.1.1. Importance of higher order optical effects during shadowgraph imaging

Optical rays are traced through the KDP solution around the growing crystal at different times of growth to get an estimate of the higher order optical effects such as scattering and interference during shadowgraph imaging. Figures 5.4(a-c) show paths of rays passing through node point (150,75), out of the 240 × 240 grid. These are drawn using the refractive index field obtained at the end of 1, 2.5 and 6 hours respectively. The deflections of the rays passing through (150, 75) node point has the maximum deflection of ~ 0.4 cm after 6 hours. From the results of the ray tracing calculations it is found that the deflections at the exit plane of the growth cell lie in the range of 0.06 - 0.4 cm. These are insignificant in comparison to the extent of the inhomogeneous field (15 cm). It points to the fact that the higher order optical effects are negligible during shadowgraph imaging. They justify the assumption of negligible deflection made in linearizing the governing equation for the shadowgraph process (Section 4). Additionally, the deflection is greater in the vertical direction as compared to the horizontal direction. It suggests that the concentration gradient is predominantly in the vertical direction. This is expected in case of gravity driven convection.

5.1.2. Growth of a crystal held on top of a glass rod

In this section convective activity during growth of a crystal placed on top of a glass rod is imaged (Figure 5.5). A relatively low cooling rate of 0.02°C/hr was used for growth as the previous rate of 0.2°C/hr proved too high, resulting in poor crystal quality. The modified growth geometry is expected to help in unhindered visualization of the convective process over the top face of the growing crystal. A KDP crystal of dimensions $2\times1\times2$ mm^3 having natural morphology is used as a seed. The solution has a saturation temperature of 55.2°C and the cooling rate adopted during the growth was 0.02°C/hr. The pH and chemical purity used for preparing the solution are same as in the previous experiment.

Figures 5.6(a-c) show the shadowgraph images of the convection patterns taken at regular intervals during the 150 hours of the growth process. It is observed that the plume activity gradually builds up as the supercooling increases. Initially the plumes are weak in intensity, but stable and laminar (Figure 5.6a). After about 60 hours of growth the crystal dimension increases and the plumes become strong. The plumes are seen to rise only from the edges

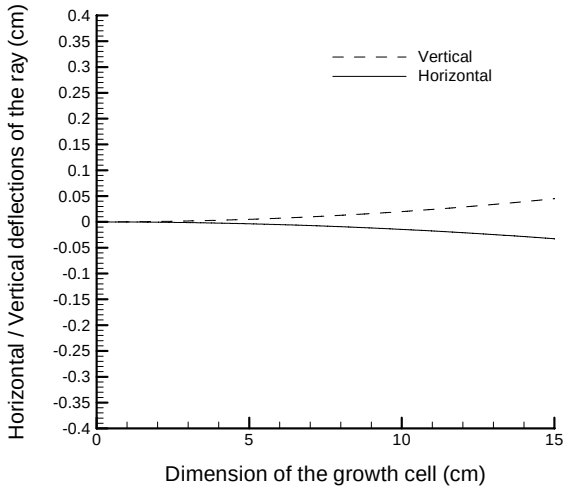

(a)

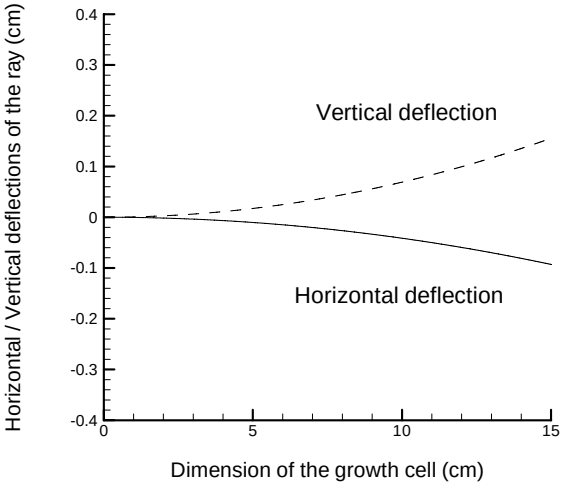

(b)

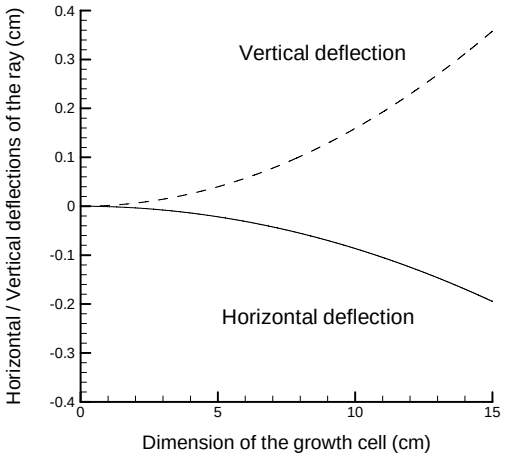

(c)

Figure 5.4(a-c). Path of a light ray as it passes through the KDP solution after 1, 2.5 and 6 hours of the start of the second experiment respectively.

of the crystal. This is because the depleted solution creeps along the crystal surface, and at the edges, it rises under the action of buoyant force in the form of two streaks of lower density solution. The laminar behavior of plumes is maintained at this stage as well (Fig. 5.6b). After about 100 hours of growth, plumes are seen to emerge from several spots on the crystal top surface. At this stage the plume behavior breaks down from the laminar state and becomes irregular (Fig. 5.6c). At the end of the experiment, the buoyancy driven convective activity becomes chaotic. This is the final state of convection observed in the experiment. The shadowgraph images (Fig. 5.7 (a-b)) recorded at 20 and 80 degrees shown that the free convective activity is truly three-dimensional.

The shadowgraph images are analyzed numerically as per the procedure described in Section 4 to obtain the refractive index field averaged along the viewing direction. Figures 5.8(a-b) are the refractive index contours plot corresponding to the shadowgraph images of Figures 5.7(a-b) respectively. A row in the refractive index matrix corresponds to a 2D plane through the growth chamber. The entries in a row are the averaged line integral values of the refractive index field along the direction of the laser beam. It is observed that the refractive index field does not represent the asymmetry as observed in the contrast of the shadowgraph image. The reason for this is extremely small variation in the refractive index ($\sim 10^{-5} - 10^{-6}$) corresponding to the

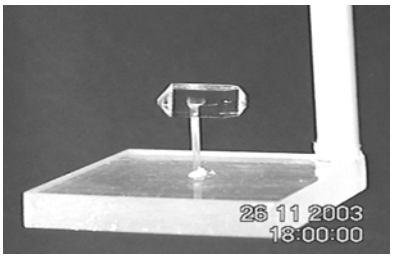

Figure 5.5. Schematic drawing and the photograph of the growth geometry.

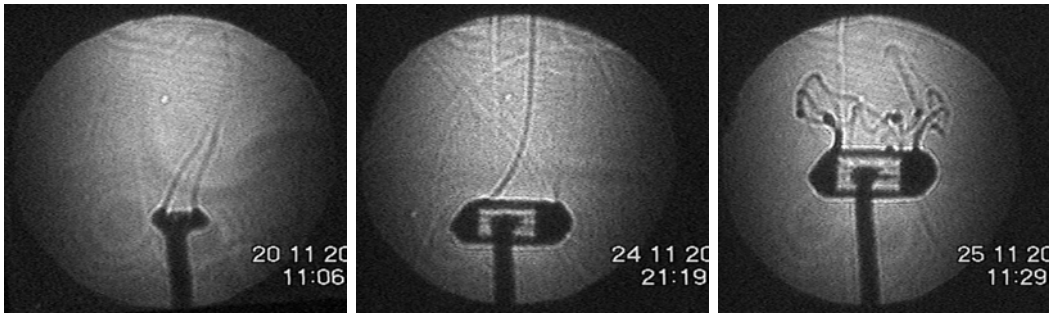

(a) 0.5°C (b) 3°C (c) 3.5°C

Figure 5.6 (a-c). Buoyancy driven flow transition sequence as observed during growth.

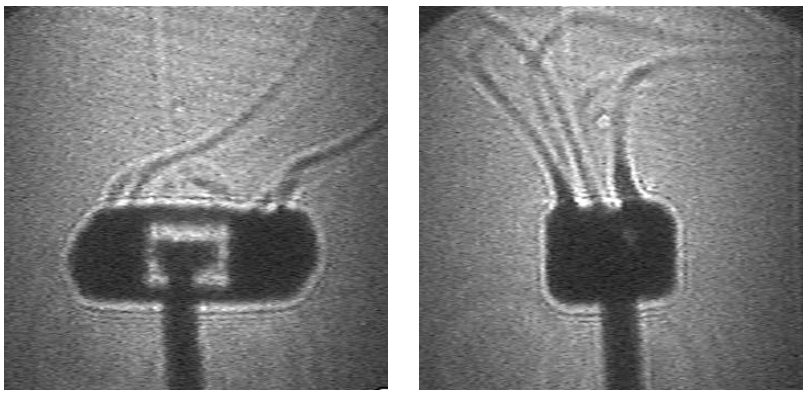

(a) (b)

Figure 5.7 (a-b). Shadowgraph images recorded along 20 and 80° angles showing the three-dimensional character of flow field.

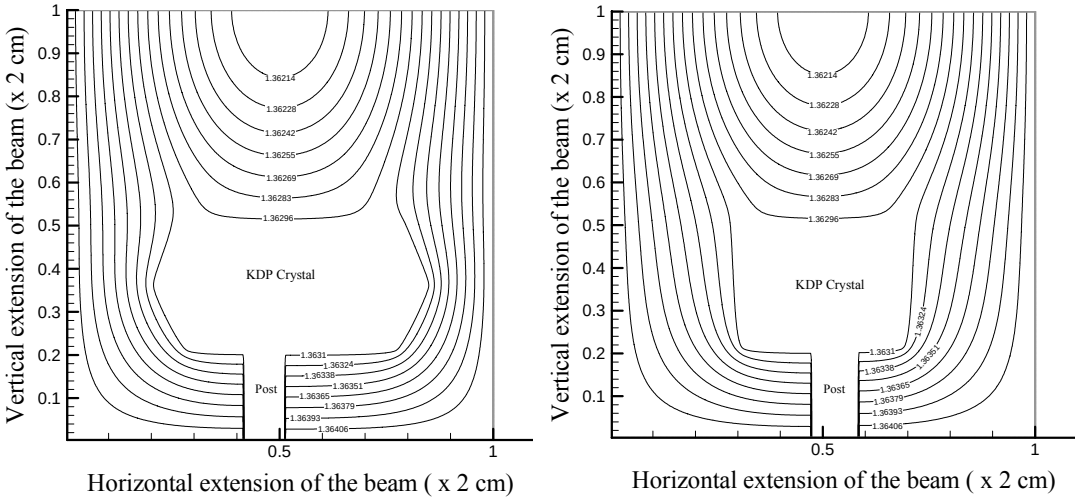

(a) (b)

Figure 5.8 (a-b). Refractive index contours corresponding to the shadowgraph images shown in Figures 5.7(a-b) respectively. They are obtained by solving the Poisson equation governing the shadowgraph process.

sharp contrast features in the images. These are very small to be visible in the contour plots of the refractive index. However, shadowgraph imaging has the potential in showing up minute variations in the refractive index field as sharp contrast changes in the shadowgraph images.

The strength of free convection is measured as a function of supercooling of the solution and characteristic length of the growing crystal by computing the Grashof number. The values are given in Table 5.1. It is observed that *Gr* number increases slowly up to supercooling of 2.5°C, beyond which it shows an exponential behavior. The exponential rise in *Gr* number is associated with strong free convection around the crystal. At this stage it makes transition from

laminar nature to irregular and chaotic. It is observed that crystal grows fast under such conditions and is prone to defects generation. It is therefore necessary to have a precise control of supercooling during this stage to achieve the desired crystal quality while maintaining high growth rate.

The crystal grew from $2 \times 1 \times 2$ mm^3 to $8 \times 7 \times 17$ mm^3. This corresponds to average growth rates of 2.4 and 0.96 mm/day along <*001*> and <*100*> directions of the KDP crystal respectively. It is observed that growth along <*001*> is several times that along <*100*> up to an intermediate value of supercooling (< 2°C). This interchanges at high values of supercooling, when a concurrent increase in the free convection is observed. The growth under free convection is primarily occurring under diffusion and a sudden increase of supercooling is detrimental to the crystal quality.

Figure 5.9 shows the quality of the grown crystal which is very good. It implies that the cooling rate of 0.02ºC/hr is optimum for growing good quality crystal under free convection conditions in a conventional growth geometry. The crystal was clear of any visible defects such as inclusions, bubbles and streaks except those present in the seed crystal. The percentage transmission in the visible region was measured using a spectrophotometer and was found to be over 80 percent (with correction for *Fresnel* losses) revealing good optical quality of the grown crystal.

Table 5.1. Grashof number as a function of supercooling of the solution and the characteristic length of the KDP crystal. The crystal is placed on top of a glass rod fixed to a platform, and grown under free convection conditions.

Supercooling (°C)	***Characteristic Length (mm)***	***Grashof number (Gr)***
0	1.3269	0
0.5	1.578	0.798
2	2.1368	7.76
2.5	2.7021	19.3
3	3.4664	48.2
3.5	3.8935	78.6

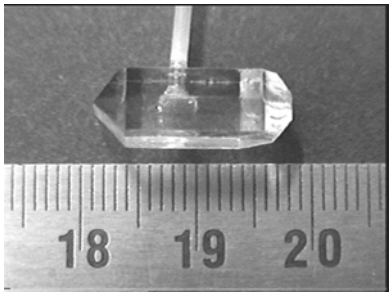

Figure 5.9. The size and quality of the crystal grown during the experiment.

5.1.3. Growth of a crystal placed on a platform

There is a third geometry for growing crystals in which the crystal is placed on top of a platform. A seed crystal of dimensions 2×2×4 mm^3 having c-axis vertically upwards is used (Figures 5.10). The pH of the solution is 4.3 and the chemicals used for preparing the solution have purity of 99.5%. The solution has a saturation temperature of 60°C and the average cooling rate adopted during the growth is 0.02°C/hr. The experiment is performed for 200 hours and the total supercooling provided to the solution is 5 °C.

The shadowgraph images recorded at successive stages of the growth are shown in Figures 5.11(a-c). In the initial stages of the growth, a weak and unstable plume is observed originating from the crystal tip. With the increase of supercooling, the plume strength, width at the base and their number increases. This is a clear signature of the increase in the growth related convective phenomena around the crystal. It is observed that for low supercooling (< 2.5°C), the growth along <001> direction is predominant, resulting in the elongation of the crystal. However, with the increase of supercooling beyond this value, the growth rates along <100> and <001> directions get reversed resulting in an increase of the crystal cross-section. It suggests that a controlled cooling rate of ~ 0.02°C/hr helps in increasing the crystal cross-section which is desired for device fabrication, while maintaining the crystal quality. At the end of the experiment, we observe that the laminar character of convective plumes changes intermittently to irregular, followed by chaotic, and finally turbulent (Figures 5.12(a-d)). This cycle is observed to repeat itself after regular intervals of a few minutes. This is the transition sequence of the free convective activity expected when the crystal has grown to a relatively larger size.

The strength of free convection at different stages of the experiment has been quantified in terms of the Grashof number (Table 5.2). Since in this experiment the cooling was provided to solution in a highly controlled manner, it has its bearing on the convective behavior, which is reflected in the values of Grashof number. It is observed that up to a supercooling of 4.5°C,

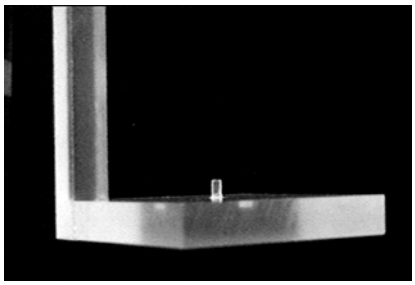

Figure 5.10. Crystal placed on a platform under free convection conditions.

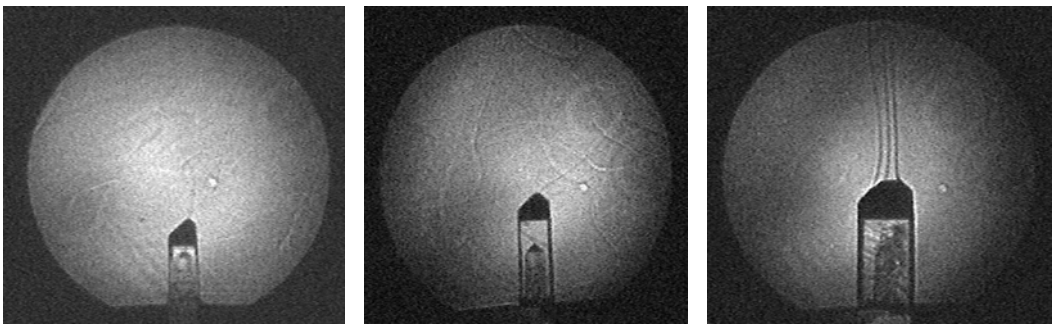

(a) 1°C (b) 3.5°C (c) 5°C

Figure 5.11(a-c). Plume activity and the growing crystal at different stages of supercooling.

the Grashof number increases gradually up to 60. This corresponds to laminar nature of the convection. Beyond this stage when the plume behavior is observed to turn irregular and chaotic, the Grashof number value rises exponentially. Thus there is a critical *Gr* number that lies beyond 60.

The average growth rate of the crystal after the completion of the experiment was found to be 0.5 and 1.35 mm/day along <100> and <001> respectively. Comparing the growth rate along the two directions at a given supercooling with the values of Grashof number recorded at the same supercooling, it is observed that growth rate of <001> decreases and that of <100> increases at the point where there is a transition in the convective behavior. Thus there is a direct linkage between the free convection behavior around the crystal and the growth rate of the crystal faces. Beyond a given value, referred to as *critical Grashof number*, which is found to be just above 60 in the present experiment, a transition of the plume behavior is observed from laminar to irregular. Simultaneously, a morphological transition is observed from elongated form to isometric shape.

The optical quality of crystal (namely, transparency) is good (Figure 5.13), which is attributable to the controlled cooling rate of 0.02°C/hr and laminar free convection till the end of the experiment. The experiment is stopped as soon as the flow made transition to irregular and chaotic behavior.

5.2. Crystal growth under forced convection

The primary objective of the experiments reported in Section 5.1 has been to map free convection around crystal growing in three different geometries, and to establish a relationship between the convective flow patterns and the growth rate and the crystal quality. The platform geometry has been found to be a favored choice for growth, although comparable growth rate and crystal quality are obtained in case of crystal growing in perched on top geometry as

well. However, due to practical difficulties in growing large size crystals by perching them on top of a glass rod, it may not be preferable over the platform geometry. The second aim of the experiments was to find an optimum cooling rate that results in high growth rate and desired crystal quality. The optimum cooling rate obtained in free convection experiments is 0.02°C/hr.

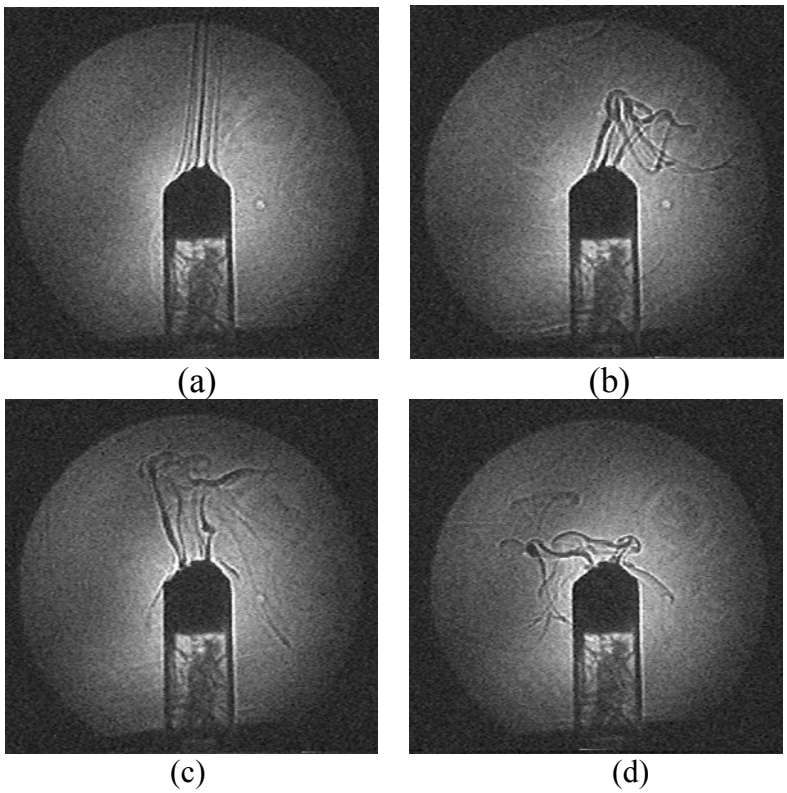

Figure 5.12. (a) Laminar nature of plumes followed by irregular (b), chaotic (c), and finally turbulent (d).

Table 5.2. Grashof number during successive stages of growth. The growth was performed on a platform and under free convection conditions.

Supercooling (°C)	***Characteristic length (mm)***	***Grashof number (Gr)***
0	1.71024	0
0.3	1.78157	0.748
0.6	2.0989	2.4
1	2.17817	4.5
2	2.39175	11.8
3.5	2.69334	29.05
4	2.91615	41.8
4.5	3.21485	62.6
5	3.95057	127.6

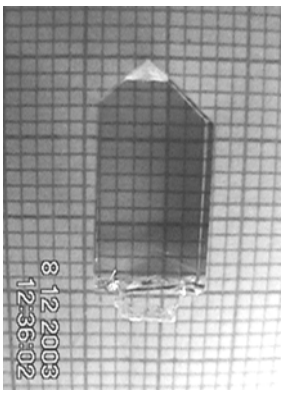

Figure 5.13. The size and the quality of the crystal grown in platform geometry during free convection experiment.

In order to perform a comparison with the results of growth under free convection conditions, a series of experiments under forced flow conditions have been performed. The results are also expected to provide information about the importance of forced flow condition in achieving high growth rate. Forced convection conditions are achieved by adopting *accelerated crucible rotation technique* (ACRT) type of rotation, where the crystal is rotated in an accelerated manner in either clockwise or anticlockwise direction starting from a state of rest to a maximum rotation rate. It is then allowed to rotate at that maximum RPM for fixed time duration, after which it decelerates slowly to rest. The same cycle of acceleration, steady rotation and deceleration is repeated in the reverse direction. The clockwise and anticlockwise rotations taken together constitute one cycle of the ACRT (Figure 5.14). The time durations (in seconds) of the respective phases of the ACRT cycle are as follows:

Acceleration time (Spin up)	:	40 s
Steady rotation time	:	40 s
Deceleration time (Spin down)	:	40 s
Stationary time	:	40 s
Maximum rotation rate during steady phase	:	32 RPM

These parameters were obtained by studying the influence of the time durations and the rotation rates of the ACRT cycle on the uniformity of the concentration field during growth.

5.2.1. Growth in platform geometry

The crystal is placed on a Plexiglas platform (Figure 5.15) which is rotated using ACRT mode of forced convection. The seed crystal dimensions

are 2×2×3 mm^3. The saturation temperature of the solution is 59°C; the cooling rate during the experiment is increased from 0.01°C/hr for the first 100 hours of the experiment, to 0.02, 0.04 and 0.05°C/hr for the subsequent 50, 25 and 20 hours of the experiment respectively. The duration of the experiment is 195 hours and the total supercooling provided is 4°C.

When the rotation is started, a strong fluid flow is experienced within the crystallizer. The flow inside the crystallizer is highly non-uniform in the beginning, resulting in a complex concentration field. The shadowgraph image generated when a laser beam passes through such a fluid flow and concentration field has sharp contrast variations at every few millimeters spatial region of the beam dimension (Figure 5.16a). After a few minutes of rotation the fluid flow becomes regular and the concentration field attains uniformity, resulting in a shadowgraph image that has no sharp contrast variations (Figure 5.16b).

The shadowgraph images are recorded in two different modes during the experiment: (a) during the steady rotation (32 RPM) and (b) during the

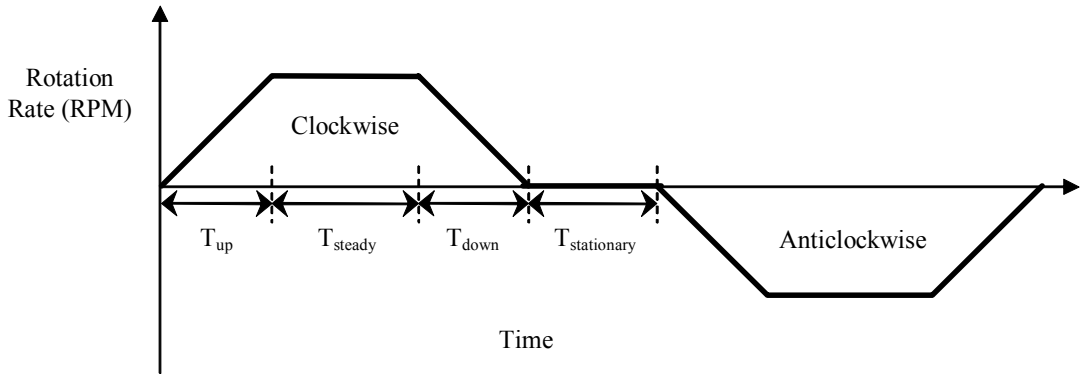

Figure 5.14. Single ACRT cycle consists of spin up (acceleration), steady rotation, spin down (deceleration) in clockwise direction, followed by a stationary phase, and repeat of the three steps in an anticlockwise direction.

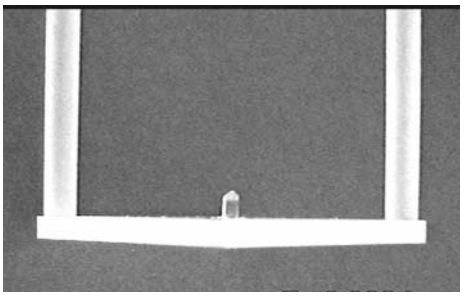

Figure 5.15. The seed crystal placed on a platform under forced convection conditions.

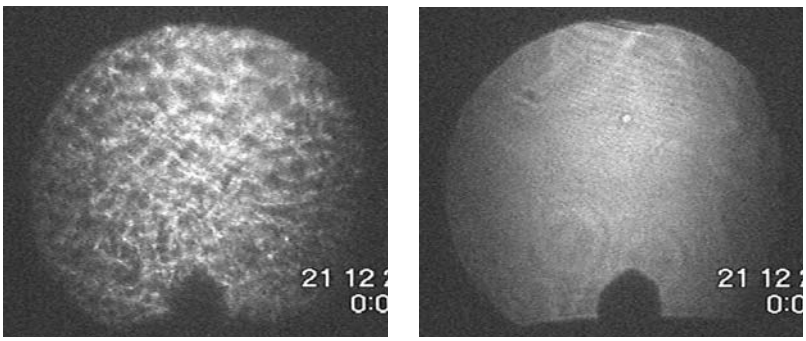

(a) (b)

Figure 5.16. (a) The convective and concentration fields at the start and (b) a few minutes after rotation, respectively.

stationary phase of the ACRT cycle. Figures 5.17(a-c) and Figures 5.18(a-c) are the images captured during the steady rotation and stop phases of the ACRT cycle respectively. During the steady rotation phase no convective plumes are observed. However within a few seconds of the stopping of the rotation, free convection plumes appear. These are weak and feeble in the beginning but become strong, stable, and laminar with a broad width at the end. No irregular or chaotic plumes are observed during the stop phase of the ACRT cycle. It can be attributed to a controlled cooling rate adopted during the experiment, augmented further by forced convection that results in uniform concentration of the solution within the crystallizer. This results in a uniform driving potential for mass transfer from all direction around the crystal. It contributes to laminar convective behavior during the stop phase of the ACRT cycle. On the other hand, during growth under free convection, the gravity force is acting vertically downwards, which results in a buoyant force that acts in a manner which makes the plume behavior progress from being irregular to chaotic and finally turbulent with the growth of the crystal at higher levels of supercooling. Such plume behavior has been found to result in an undesirable flow characteristic that lead to deterioration of the crystal quality. However, under controlled forced convection no such fluid flow is observed at the same levels of supercooling. This has been found to lead to good crystal quality at the end. The forced convection during the experiment is characterized in terms of Reynolds number. The values at different growth temperatures during the experiment are given in Table 5.3. The average Reynolds number during this experiment is close to 8315.

Although the crystal is grown under forced convection conditions, but during the stop phase of the ACRT cycle, the free convection plumes are seen to emerge from the crystal {Figures 5.18(a-c)}. The finally grown crystal is shown in Figure 5.19, and has a small inclusion at the left side of the bottom of

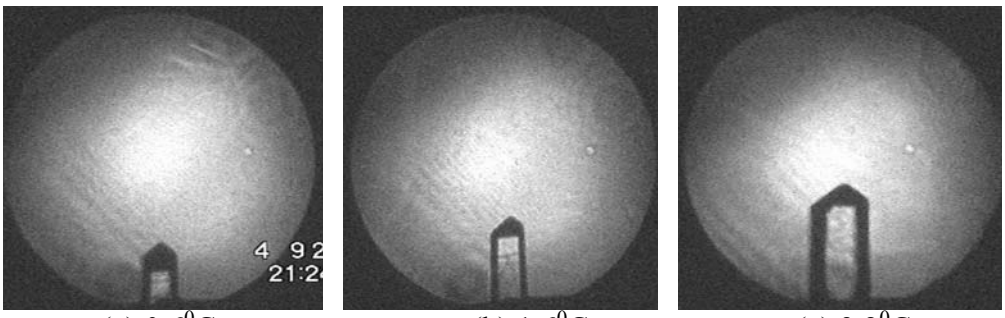

(a) 0.6^0C (b) 1.6^0C (c) 3.2^0C

Figure 5.17(a-c). The shadowgraph images captured during the steady rotation phase of the ACRT cycle. No free convection plumes are observed in these images.

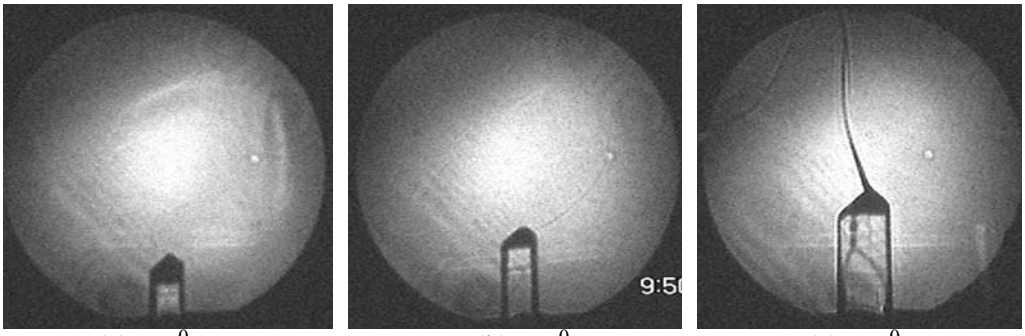

(a) 0.6^0C (b) 1.6^0C (c) 3.2^0C

Figure 5.18 (a-c). The free convection plumes seen in the shadowgraph images captured during the stationary phase of the ACRT cycle.

the crystal. Therefore, it is concluded that although it is possible to apply relatively higher level of supercooling under forced convection conditions, but there is a critical value beyond which the crystal quality is a sensitive function of supercooling.

The final dimension of the crystal is $10\times7\times13$ mm^3. The average growth rate at the end of the experiment is found to be 1.2 and 0.84 mm/day along <001> and <100> directions respectively. At low supercooling, crystal grows primarily along <001> direction and the growth rate steadily increase up to a given supercooling (0.8 °C). Beyond this value there is a drop in the growth along <001> direction whereas that along <100> picks up. However with further increase of supercooling the growth rate of the crystal along both the directions increase. Additionally we observe that the growth in <100> direction is very less at small supercooling as compared to that at high supercooling. This is seen in the shadowgraph images (Figures 5.17(a-c)) where the crystal is observed to increase primarily along <001> direction up to a supercooling of 1.6°C. Up to this value the growth rates along <001> is

Table 5.3. Reynolds number at different stages of growth of a KDP crystal grown in platform geometry under forced convection achieved by ACRT.

Growth Temperature (C)	*Reynolds number (Re)*
59	8390.8
58.4	8370.7
58.3	8367.2
58.2	8363.7
58.1	8360.2
57.4	8334.9
56.2	8288.5
55.8	8272.2
55	8238.4

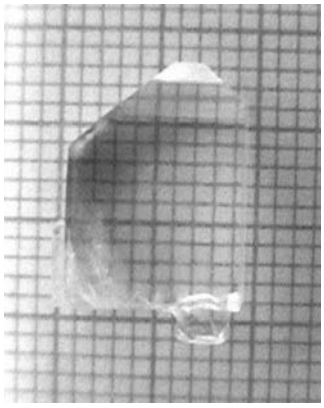

Figure 5.19. The size and the quality of the crystal grown in platform geometry during the ACRT mode forced convection experiment.

15-20 times higher than that along <100> direction. This ratio decreases beyond 1.6°C supercooling and approaches a value ~ 1.5 to 2.0. As a result the crystal approaches isotropic morphology, which is desired for the device applications. It may be noted that during the entire experiment the growth rate along <001> direction is maintained above <100> direction. This is different from the free convection experiment where an interchange between the growth rates along the two directions is observed at higher value of supercooling.

5.2.2. Growth of a crystal hanging from a glass rod

In order to compare growth under free and forced convection conditions for top hanging geometry, an experiment was performed in forced convection conditions achieved by ACRT. The saturation temperature of the solution was 56°C and the cooling rate was 0.02°C/hr. The experiment has been

performed for 75 hours and the total supercooling provided to the solution was 1.5°C. The solution has stoichiometric pH and the purity of the chemical used for preparing the solution is 99.5%. A KDP seed crystal of dimensions 1.5×3×3 mm^3 having bipyramidal morphology and c-axis in horizontal direction is glued to a glass rod and hung inside the crystallizer (Figure 5.20).

The shadowgraph images recorded during steady rotation phase of the ACRT cycle are shown in Figures 5.21(a-c). Free convection plumes are not observed under forced conditions. During the stationary phase of the ACRT cycle, gravitational forces influence the flow in the solution. It results in the appearance of free convection plumes from the crystal edges (Figures 5.22(a-c)). The plumes are laminar from start till the end of the experiment. This flow behavior is attributed to the usage of optimum cooling rate of ~ 0.02°C/hr, and the total supercooling provided to the solution is relatively small (1.5 degrees). It is much smaller then 2.5°C that is found necessary for the crystal to grow along <100> and <010> directions, i.e. for the prismatic faces to grow.

The results of the current and previous experiments suggest that for supercooling less than 2.5°C, the crystal grows predominantly along the c-axis. For the growth of prismatic faces to occur, a sufficiently high value of supercooling is required. This observation has been found to have a visual signature as well in the form of the location of the plume on the crystal surface. If the crystal grows predominantly along the <001> direction, the free convection plumes arising during the stop phase of the ACRT rotation cycle originate from the ends of the crystal. This is because the crystal is mainly increasing in length and the growth units attach on the pyramidal facets. Thus the depleted solution rises only from the crystal ends. The origin of the plume is thus a clear indicator of the growing faces of the crystal. Shadowgraph snap shots recorded during the steady rotation phase of the ACRT cycle provide the proof of the presence of strong centrifugal forces during forced convection (Figures 5.23(a-b)). As a result, the solute depleted solution present near the crystal-solution interface gets thrown outwards into the bulk solution. Thus the rotation of the crystal in top hanging geometry fulfills two purposes: first, it helps in the uniform mixing of the solution, and second, the depleted solution does not stay near the crystal interface for too long. The latter has two beneficial effects: (i) no drop in the growth rate is observed, which could happen if the depleted solution is allowed to accumulate around the crystal and (ii) the quick removal of the growth debris from near the crystal faces reduces the probability of the inclusion formation due to entrapment of the solution under high supersaturation conditions.

The strength of forced convection during different stages of the experiment is measured in terms of Reynolds number. It is given in Table 5.4

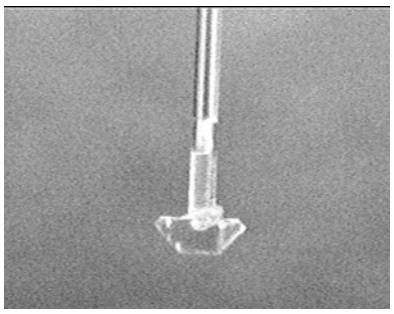

Figure 5.20. The seed crystal hanging from a glass rod.

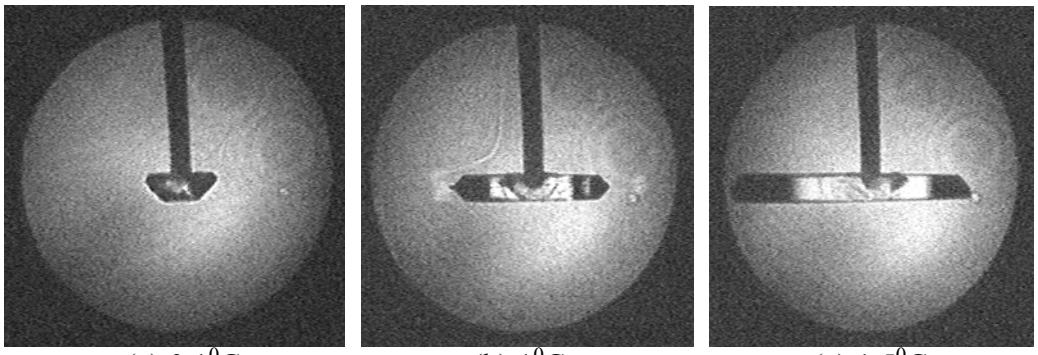

(a) 0.1^0C (b) 1^0C (c) 1.5^0C

Figure 5.21(a-c). The shadowgraph images at different stages of growth under forced convection using ACRT type flow.

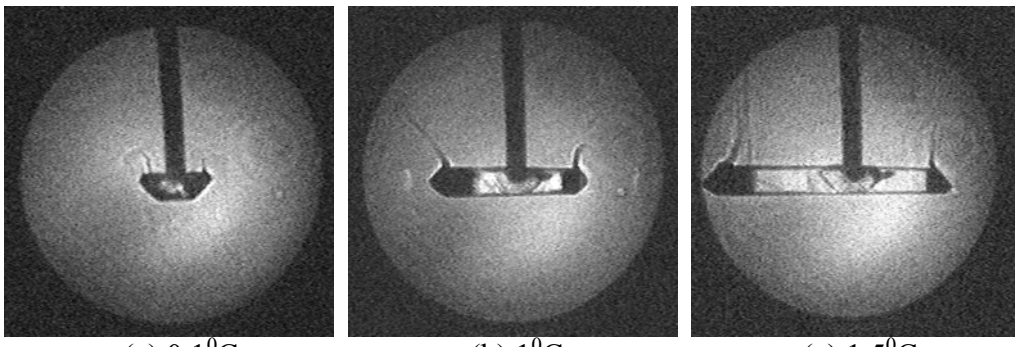

(a) 0.1^0C (b) 1^0C (c) 1.5^0C

Figure 5.22(a-c). The free convection plumes observed at different stages of growth during the stationary phase of the ACRT cycle. The value of supercooling at which the image was recorded is given under the each image.

as a function of growth temperature. Comparing the Reynolds number for growth in top hanging geometry with that under platform growth geometry (Table 5.3), the values are less by an order of magnitude. This implies that the forced convection inside the growth chamber is much weaker in case of top

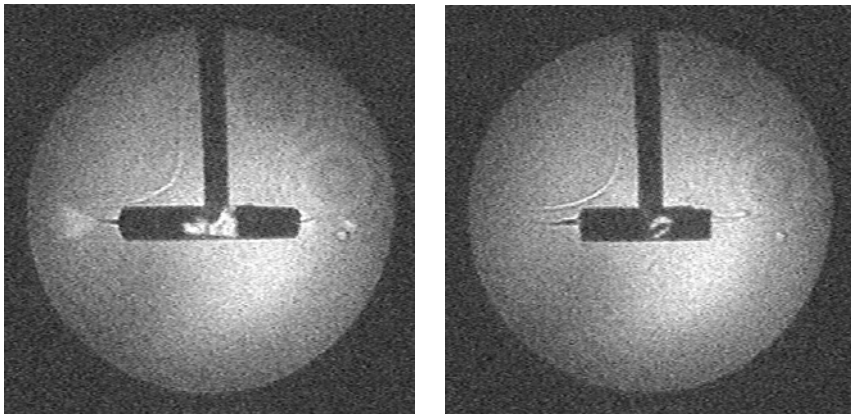

(a) (b)

Figure 5.23(a-b). Two snap shots during the crystal rotation. The outward movement of the depleted solution under the action of centrifugal force due to crystal rotation.

top hanging geometry as compared to that in platform growth. It is justified considering the structure driving the forced convection in the two cases. This aspect has been incorporated in the definition of characteristic length of the crystal for the two geometries. In case of platform growth, dimensions of platform have been taken as characteristic length whereas for growth in top hanging geometry it is the length of the crystal along c-axis. Since the platform dimensions are constant throughout the experiment, the Reynolds number has an average value of 7600 in constant RPM mode and 8615 in the ACRT mode. The Reynolds number value decreases by 2% from the start to the end of the experiment. The minor decrease is attributable to the increase of viscosity due to cooling of the solution that dampens the forced convection. On the other hand, the Reynolds number and its trend in case of top hanging geometry is different in following respects: (a) the absolute values are an order of magnitude lower, (b) the values show an increasing trend and, (c) the percentage increase is 200%. The reasons for these results are as follows: The smaller values are attributed to a much smaller characteristic length in case of top hanging geometry. A 200% increase is due to sharp increase of the crystal dimension during the experiment. This results in several fold increase of the Reynolds from its starting value. This increase offsets the minor decrease due to solution viscosity. In relative sense this increase appears very large, but in absolute sense the values are still several times smaller than those for the platform growth. Thus the forced convection in platform growth is much stronger than that in top hanging geometry. This has its effect over the growth process as well. The crystal in top hanging geometry does not grow along <100> and <010> direction, and as a result develops in to an elongated morphology.

The crystal dimensions at the end of the experiment are 1.5×6×17 mm^3. The average growth rate along <001> and <010> directions are 4.48 and 0.96 mm/day respectively, whereas practically the crystal does not grow at all along <100> direction. As a result crystal morphology developed in to an elongated form. No increase in crystal cross-section takes place. This is an undesired phenomenon and thus such growth geometry is not favorable for growing isometric morphology KDP crystals. The final size and the quality of the crystal at the end of the experiment are seen in Figure 5.24.

Table 5.4. Reynolds number at different stages of growth of a KDP crystal grown in hanging geometry under forced convection achieved by ACRT.

Growth temperature (°C)	***Reynolds number (Re)***
56	52.9
55.9	82.7
55.5	143.9
55.2	249.6
55	391.5
54.7	682.2
54.5	983.6

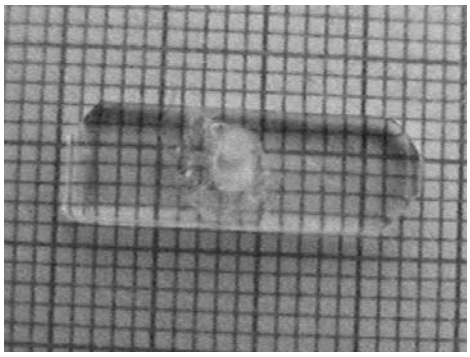

Figure 5.24. The size and the quality of the crystal grown under forced convection in top hanging geometry.

5.2.3. Growth of a crystal perched on top of a glass rod

There is a third geometry of growth in which the crystal is perched on top of a glass rod. In order to compare its growth under free convection, an experiment under forced convection has been done. The saturation temperature of the solution was 46°C and the cooling rate provided was 0.02°C/hr for the first 50 hours, which was increased to 0.03°C/hr for the next 32 hours, and finally to 0.04°C/hr for the last 24 hours. The experiment has been performed

for 106 hours and the total supercooling provided to the solution was 2.9°C. A seed crystal of dimensions 1.5×3×3 mm^3 having natural morphology was glued to a glass rod and placed upright on a platform (Figure 5.25).

The convective field observed during steady rotation phase of the ACRT cycle is shown in Figures 5.26(a-c). The solute depleted solution does not rise up in the form of a plume as the centrifugal force due to forced convection is much stronger than the gravitational force under free convection. It is observed that the crystal grows only along *c-axis* up to a supercooling of 1.6°C, and starts to grow along *a-b* directions at relatively higher supercooling. The shadowgraph images recorded during the stationary phase of the ACRT cycle are shown in Figures 5.27(a-c). Different types of plumes are observed at different stages of the growth, which are signatures of different growth mechanisms. The nature of these plumes and the growth mechanism that they represent are discussed below.

Edge plumes: Figure 5.28(a) shows growth wherein the plumes originate from the edges. These plumes are signatures of the growth of the pyramidal faces of the crystal, and hence the elongation of the crystal along the c-axis. It is concluded that at low levels of supercooling (< 1.5 – 2°C), only growth of pyramidal faces occur. Prismatic faces grow at a relatively higher supercooling. It suggests that the *induction period* (time taken for the growth to start) is smaller for pyramidal faces as compared to the prismatic faces.

Surface plumes: The edge plumes are gradually replaced by surface (or layer-by-layer) plumes (Figure 5.28b). With increase in supercooling beyond 1.6°C, the frequency of edge plumes decreases and that of surface plumes steadily increases. The surface plumes are signatures of *layer-by-layer growth* of the prismatic faces which results in increase in the crystal dimension in the *a-b* direction. During this stage crystal grows by a *two-dimensional nucleation mechanism*.

Edge and Surface plumes: At low supercooling only edge plumes were observed, which are followed by surface plumes at intermediate level of supercooling (>2.0°C). However, the transition is so gradual that for some time, both types of plumes are observed simultaneously (Figures 5.28c). At this stage of growth, pyramidal as well as prismatic faces grow at competing growth rates.

Birth & Spread plumes: When the supercooling approaches 3°C, the surface plumes that are signature of the two-dimensional growth mechanism give way to a third type, named *umbrella* plumes. These are signature of *birth and spread growth mechanism*. This mechanism is a three-dimensional mode of

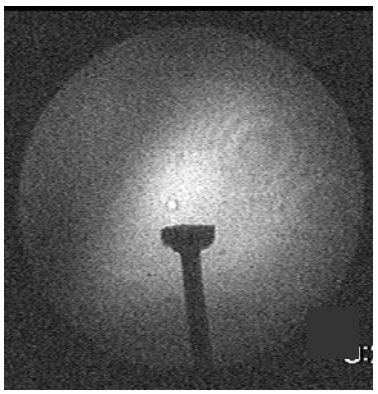

Figures 5.25. Seed crystal perched ontop of a glass rod.

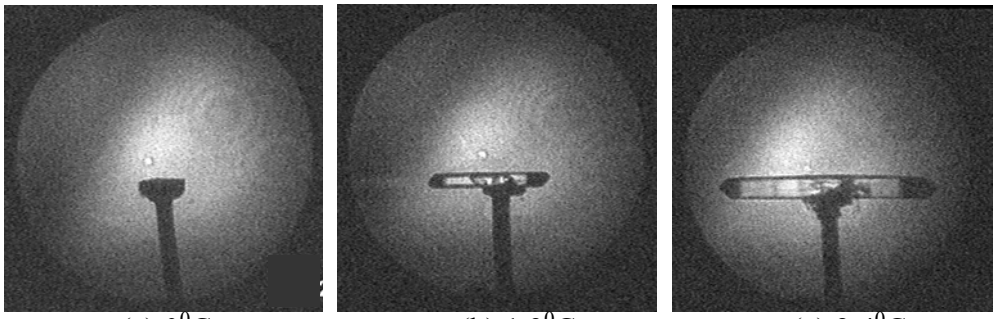

(a) 0^0C (b) 1.3^0C (c) 2.4^0C

Figures 5.26 (a-c). Shadowgraph images under forced convection conditions for a crystal placed on top of a glass rod.

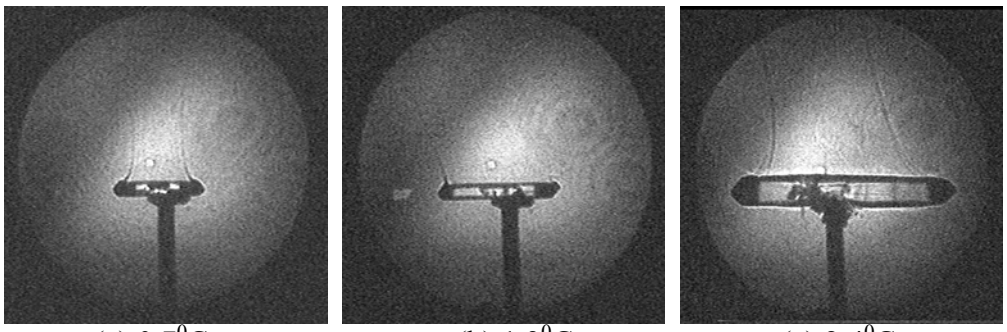

(a) 0.7^0C (b) 1.3^0C (c) 2.4^0C

Figures 5.27 (a-c). Shadowgraph images of the growth under stationary phase of the ACRT cycle. The free convection plumes are visible in the images.

growth that operates at relatively higher levels of supercooling (> 3°C). Here microscopic cluster of growth units is first formed (birth) inside the solution, which then falls on to the crystal surface under its own weight and rearranges (spread) itself on the crystal surface before the constituent atomic units get

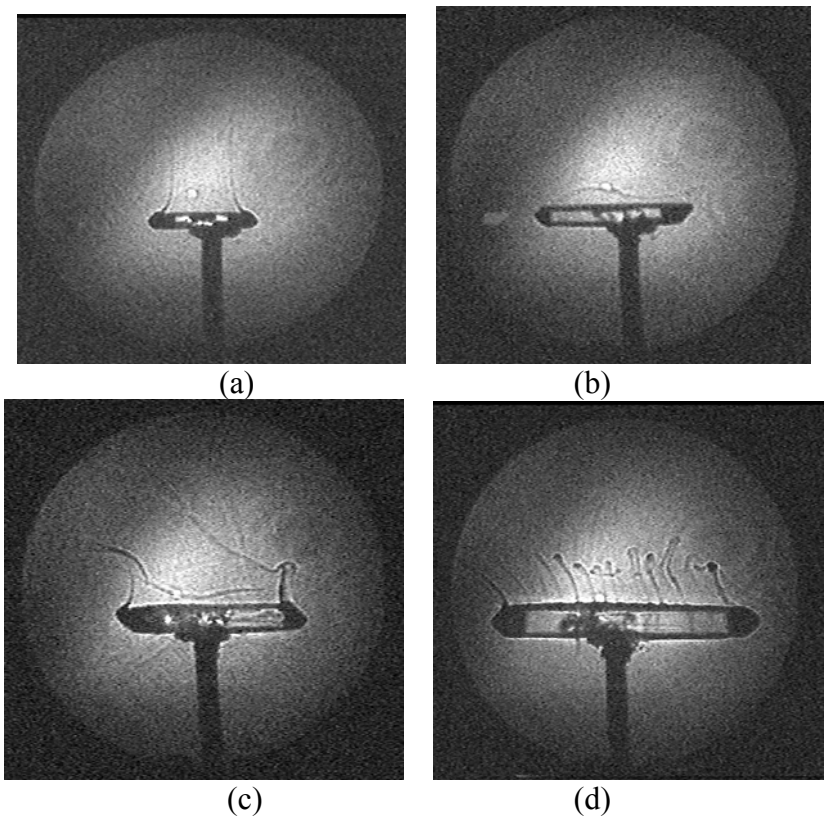

Figure 5.28. Different types of plumes observed during growth. (a) Edge plume, (b) Surface plume, (c) Edge & Surface plume, and (d) Birth and Spread plume.

incorporated into the crystal lattice. After a few hours of growth the frequency of surface plume decreases and that of the birth and spread plumes increases (Figure 5.28d).

The strength of forced convection during the experiment is measured in terms of the Reynolds number (Table 5.5). It decreases by 2.5% from its starting value, which is almost of the same order as observed in the platform growth. It has an average value of ~ 7660 during the experiment.

The size of the crystal at the end of the experiment is $4\times4\times20$ mm^3. The average growth rates of the crystal along <001> and <100> direction are 4 and 1.6 mm/day respectively. Since the crystal grows along <100> direction only in the last 36 hours of the experiment, this time period is taken for computing the growth rate along this direction. The disparity in the growth rate along two directions is very large. As a result, crystal grows into an elongated form, which is undesirable from device point of view. This peculiar growth rate behavior is observed in case of crystal growth in hanging geometry as well. The size and the quality of the crystal grown are shown in Figures 5.29.

Table 5.5. Reynolds number at different stages of growth of a KDP crystal grown in hanging geometry under forced convection achieved by ACRT.

Temperature of KDP solution **(°C)**	***Reynolds number*** **(Re)**
46	7756.8
45.7	7737.9
45.3	7712.5
44.7	7673.9
44.4	7654.4
44	7628.1
43.1	7568.2

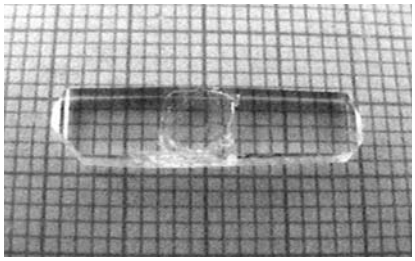

Figure 5.29. The size and the quality of the crystal growth under forced convection conditions for a crystal perched on top of a glass rod placed on a platform.

5.3. Closure

Laser shadowgraph technique has been successfully used for mapping free convection phenomenon during crystal growth in different geometries. It has been found to be a highly sensitive imaging tool for mapping minute changes in the refractive index field, which appear as high contrast features in the images. The evolution of the averaged refractive index (concentration) field along the line-of-sight is obtained by solving a linearized governing equation of the shadowgraph process at different stages of growth (Verma, 2005C). In the initial stages of growth, the crystal dimension is small and the growth chamber has isolated regions of high and low concentration that do not mix with each other. With the growth of the crystal, free convection is established. It helps in breaking regional non-uniformity in the concentration field (Verma, 2005D). Once a plume is established, concentration gradients are higher in the vicinity of the crystal as compared to in the bulk of the chamber. This is favorable for fast growth kinetics because high gradients signify high mass fluxes of solute towards the crystal faces. Plume formation also explains preferential growth of one face with respect to the other.

There is a tradeoff between growth rate and the quality of the crystal. Only at optimum values of process parameters, such as cooling rates and

convection strength, are best results obtained. The strength of free convection is quantified in terms of Grashof number. Beyond a certain supercooling, the Grashof number rises exponentially, and the crystal quality becomes sensitive to temporal fluctuations in the concentration field (Verma, 2007). Inclusions and striations get incorporated beyond this stage of growth. The critical Grashof (Rayleigh) number in the present set of experiments falls in the range of 60 to 85 ($\sim 3\times10^4$).

Time-lapsed shadowgraph images are used to quantify the growth rate as a function of supercooling. Based on growth rate results and convection imaging, a cooling rate in the range 0.02 - 0.03°C/hr is found to be optimum to grow crystals with high growth rate and good quality (Verma, 2008A).

The nature of free convection plumes in the shadowgraph images are correlated with the growth mechanism. Signatures of two-dimensional nucleation and birth and spread mechanism have been observed (Verma, 2008A).

6. Interferometric imaging of crystal growth from solution

In the preceding section, shadowgraphy has been used to image the process of crystal growth from solution. The results of the shadowgraph imaging established that the flow conditions prevalent during the crystal growth process are important in deciding the growth rate and the quality of the grown crystal. In the present section, the results of Mach-Zehnder interferometric imaging to measure concentration field and solutal boundary layer during growth are reported. The design details of the Mach-Zehnder interferometer, the multi-window double-walled crystal growth apparatus, the temperature controlling instrumentation, and the image acquisition hardware used for the experiments have been explained in Section 3. The growth process is performed in the following two geometries: (a) the conventional hanging geometry, in which the crystal is hung from a glass rod, and (b) the platform geometry, in which the crystal is placed on a Plexiglas platform. For each geometry, the growth process is monitored under free as well as forced convection conditions. In all the experiments reported in this chapter, the pH of the KDP solution is the stoichiometric value of 4.3. The impurities in the solution are as present in the commercially available KDP chemical (99.5 % pure, GR-grade, *Merck* India).

6.1. Crystal growth under free convection

It has been observed in section 5 that flow conditions and the growth geometry adopted during growth are important parameters for achieving desired growth rate and crystal quality. Therefore to understand this linkage

better, growth experiments have been performed under free convection conditions in two different growth geometries. Mach-Zehnder interferometry in infinite and wedge fringe settings has been used for the purpose. The shadowgraph images are also presented at a few places.

6.1.1. Crystal growth in hanging geometry imaged in wedge fringe setting

A KDP seed crystal of dimensions 2×4×4 mm^3 having bi-pyramidal morphology and *c*-axis horizontal is glued to one end of a thin glass rod (1.5 mm diameter) and hung inside the crystallizer (Figures 6.1). The saturation temperature of the solution is 41°C. The solution cooling rate is steadily increased during the experiment from 0.01°C/hr for first 10 hours to 0.02, 0.04 and 0.05°C/hr for the next 36, 72 and 36 hours respectively. The temperature at the end of the experiment is 36.5°C resulting in a total supercooling of 4.5°C in 155 hours. As a result an average cooling rate of 0.03°C/hr is achieved during the experiment.

The wedge interferograms recorded at different stages of the experiment are shown in Figures 6.2(a-c), and the corresponding shadowgraph images shown in Figures 6.3(a-c). The development of buoyancy driven convection activity and the *solutal boundary layer* (SBL) at different stages of the growth is observed. In literature the region of intense solid-fluid interaction near to crystal boundaries is often referred to as *diffusion boundary layer* (DBL). The term DBL has its origin in the fluid mechanics literature where it refers to a region of almost stagnant fluid film over a surface having flowing fluid. In the context of crystal growth, this is not true. The boundary layer region near to the crystal edges is where all the dynamics of crystal growth is occurring, and is different from the stagnant film model of fluid mechanics. Thus in order to differentiate between the two, here it is named *solutal boundary* layer. The extent of the solutal boundary layer is taken up to the point where the interface concentration (saturation value) approaches the bulk concentration (supersaturation value). In the beginning, the solution supersaturation is low, resulting in weak driving force. As a result the incorporation of the growth units moving randomly in the fluid phase into an ordered crystalline phase is slow. Thus the increase of concentration from the interface value to the bulk value is very gradual. This dynamics is reflected in the thickness of the solutal boundary layer. At this stage a thick boundary layer is observed around the crystal facets. As the supersaturation increases on cooling the solution, the driving force increases. This results in increased dynamics in the interface region. The movement of growth units from the bulk solution towards the interface region and movement of the growth - debris

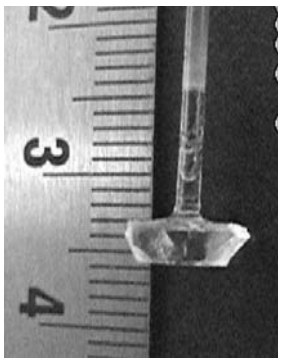

Figure 6.1. Seed crystal hanging from a glass rod.

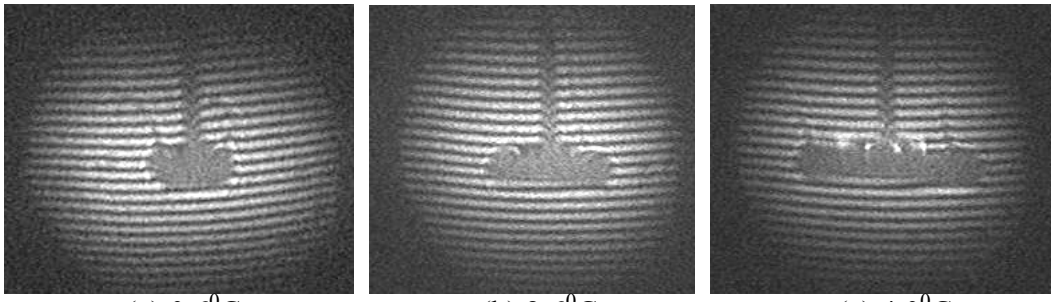

(a) 0.6^0C (b) 2.6^0C (c) 4.0^0C

Figure 6.2(a-c). Wedge interferograms of the crystal growing under free convection conditions in top hanging geometry. The images show the edge plumes at different stages of the growth. The supercooling at which the image is recorded is given under the image.

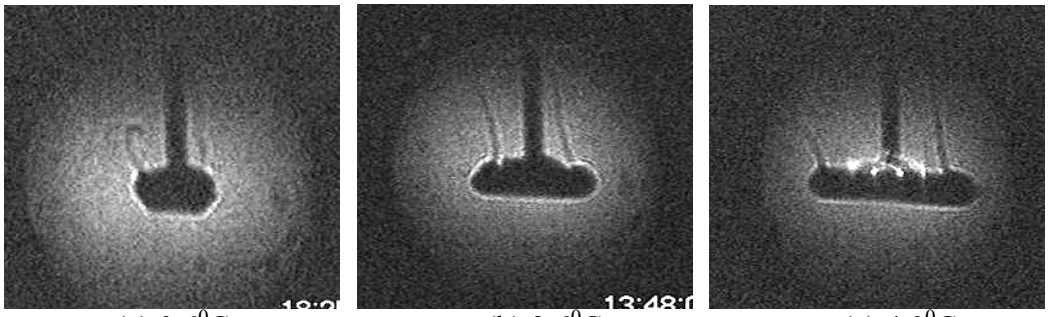

(a) 0.6^0C (b) 2.6^0C (c) 4.0^0C

Figure 6.3(a-c). Shadowgraph images of the crystal growing under free convection conditions in top hanging geometry. These images have one-to-one correspondence with the wedge interferograms shown in Figures 6.3(a-c).

back into the bulk solution increases. As a result the saturated concentration in the interface approaches the bulk concentration relatively faster. This manifests itself in a thinner boundary layer as compared to the situation in the

beginning. Thus, the solutal boundary layer is thicker in the initial stages of growth and becomes thinner during later stages of growth. This variation is ~ 50-75 μm. In other words, under fast growth kinetics the boundary layer is thinner whereas the opposite is true for slow growth kinetics. Minor variations in the thickness of the boundary layer are observed over different faces of the crystal for the same supersaturation value. It is an indicator of the relative growth kinetics of the faces. The thickness of the *solutal boundary layer* (SBL) is clearly visible in the shadowgraph images as compared to the wedge interferograms. It is estimated to be between 175 - 200 μm.

The crystal grows to dimensions of 2×5×20 mm^3 ($a \times b \times c$ mm^3) at the end of the experiment. The average growth rate of the KDP crystal along <001> and <100> directions are 2.48 and zero mm/day respectively. It is observed that the crystal does not grow along *a*- and *b*- directions. This is attributed to the hanging geometry growth conditions during which only *c*-axis growth is observed. Additionally, it is observed that throughout the duration of the experiment, only edge plumes are observed. These are signature of growth of pyramidal faces and hence elongation of the crystal along *c*-axis. The crystal quality at the end of the experiment is good (Figure 6.4). It is the result of optimum cooling rate (0.03°C/hr) adopted during the experiment. The value of optimum cooling rate range was found from the results of shadowgraph imaging.

6.1.2. Crystal growth in top hanging geometry imaged in infinite fringe setting

In order to compare the results of wedge fringe setting with infinite fringe imaging, an experiment under similar growth conditions is imaged using infinite fringe interferometry. The KDP seed crystal of dimension 1×3×2 mm^3 having similar morphology and hanging geometry as in the preceding experiment (Figures 6.5) was used. The saturation temperature of the solution is 40°C. The cooling rate is steadily increased during the experiment from 0.01°C/hr for first 96 hours to 0.02°C/hr and 0.03°C/hr for the next 24 and 168 hours respectively. The temperature at the end of the experiment is 33.5°C resulting in total supercooling of 6.5°C in 288 hours. As a result an average cooling rate of 0.02°C/hr is achieved during the experiment.

The infinite fringe interferograms recorded at different stages of the experiment are shown in Figure 6.6(a-c) and the corresponding shadowgraph images are shown in Figure 6.7(a-c). The visibility of edge plumes is comparable in the two techniques. However, the solutal boundary layer has better visibility in shadowgraph images than in infinite fringe interferograms.

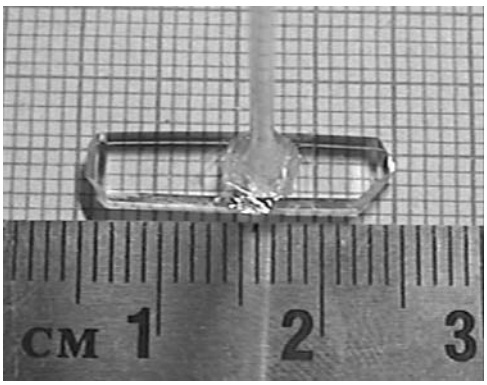

Figure 6.4. Size and quality of the crystal grown in top hanging geometry under free convection conditions.

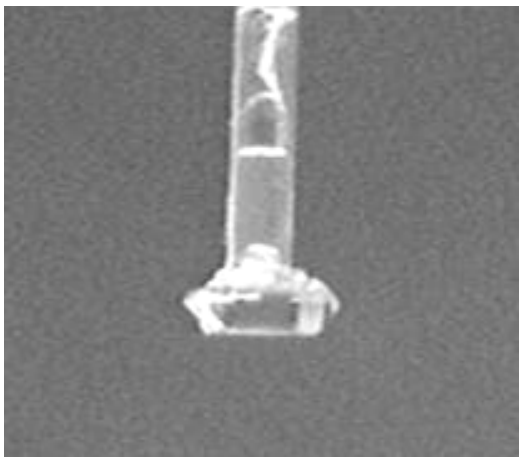

Figure 6.5. Crystal hanging from a glass rod.

The crystal grows to dimensions of 1×3×21 mm^3 ($a \times b \times c$ mm^3) at the end of the experiment (Figure 6.8). The average growth rate of the KDP crystal along <001> and <100> directions are 1.58 and zero mm/day respectively. Again, the result of the preceding experiment is repeated. The crystal does not grow along *a*- and *b*- directions. Only *c*-axis growth is observed. This is attributed to the growth geometry adopted during the experiment. Decrease of growth rate along <001> as compared to the preceding experiment (Section 6.1.1) is attributable to the slow cooling rate of 0.02°C/hr as compared to that of 0.03°C/hr in the previous experiment. Again, it is observed that throughout the duration of the experiment, only edge plumes are observed, confirming that these are the signatures of the growth of KDP crystal along *c*-axis. The crystal quality at the end of the experiment is good (Figure 6.9). This is the result of optimum cooling rate (0.02°C/hr) adopted during the experiment.

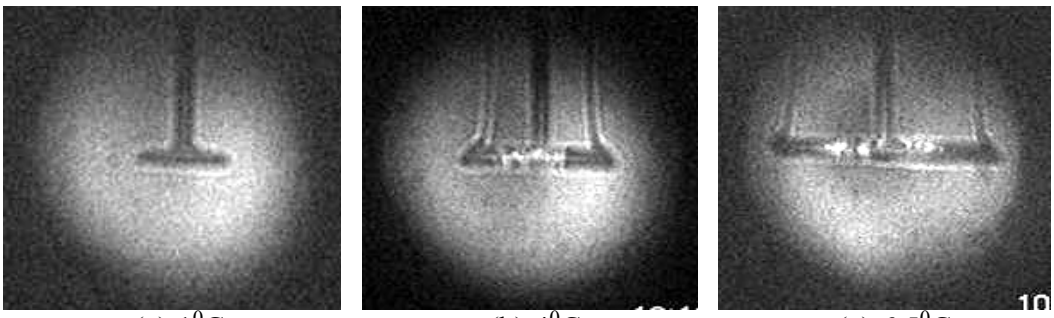

(a) 1^0C (b) 4^0C (c) 6.5^0C

Figure 6.6. (a-c). Infinite fringe interferograms of a crystal growing under free convection conditions in top hanging geometry. The interferograms show the edge plumes at different stages of the growth. The value of supercooling is given under respective image.

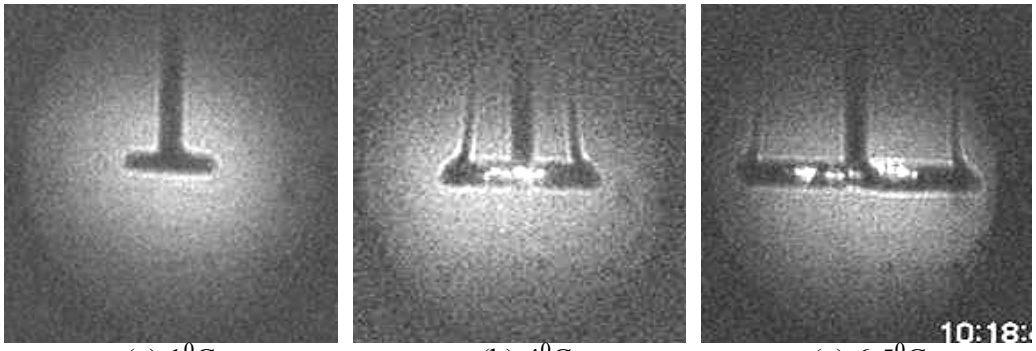

(a) 1^0C (b) 4^0C (c) 6.5^0C

Figure 6.7. (a-c). Shadowgraph images of KDP crystal growing under free convection conditions in top hanging geometry. These images have one-to-one correspondence with the infinite fringe interferograms shown in Figures 6.6(a-c).

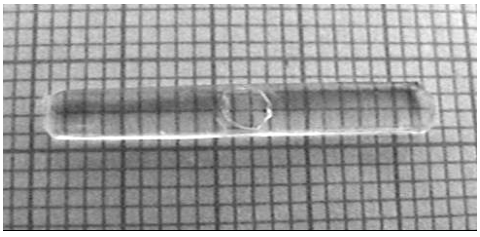

Figure 6.8. Size and quality of the crystal grown in top hanging geometry under free convection conditions.

6.1.3. Crystal growth in platform geometry imaged in wedge fringe setting

The crystal growth described in this section is performed in platform geometry under free convection conditions and is imaged using a Mach-Zehnder interferometer in the wedge fringe setting. A KDP seed crystal of

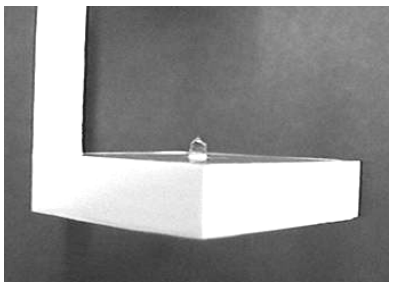

Figure 6.9. Seed crystal placed on a platform.

dimensions 1.5×1.5×1.5 mm^3 having pyramidal morphology and its *c*-axis vertical is placed on a Plexiglas platform (Figures 6.9). The saturation temperature of the solution is 44°C; the cooling rate is steadily increased during the experiment from 0.02°C/hr for first 24 hours to 0.04, 0.05 and 0.06°C/hr for the next 36, 24 and 70 hours respectively. The temperature at the end of the experiment is 36.7°C resulting in total supercooling of 7.3°C in 154 hours. As a result an average cooling rate of 0.05°C/hr is achieved during the experiment.

The infinite fringe interferograms recorded at different stages of the experiment are shown in Figures 6.10(a-c) and the corresponding shadowgraph images are shown in Figures 6.11(a-c). The visibility of plumes observed in shadowgraph images is better than those observed in wedge setting interferometry but comparable to infinite fringe interferograms. The solutal boundary layer has better visibility in shadowgraph images than in the wedge fringe interferograms. The SBL has an intermediate visibility in the infinite fringe interferograms. The extent of SBL is ~ 200 microns.

The crystal grows to dimensions of 5×5×15 mm^3 ($a \times b \times c$ mm^3) at the end of the experiment (Figure 6.12). The average growth rate of the KDP crystal along <001> and <100> directions are 2.1 and 0.55 mm/day respectively. The growth rate of the crystal along c-axis is several times that along *a*- and *b*- axis. In case of top hanging geometry, no growth is observed along *a*- and *b*- directions at moderate levels of supercooling (< 2.5°C) achieved by application of optimized cooling rate (~ 0.02°C/hr). Thus platform geometry growth is preferable for achieving growth along both the directions, though growth rates along the two directions are very different. Throughout the duration of the experiment plumes from the top of the crystal are seen. This is because the solute-depleted solution creeps along the prismatic and pyramidal facets of the crystal, and reaches the top of the crystal where it leaves in the form of a plume. Distinct flow regimes (laminar, irregular, chaotic and turbulent) are observed at various stages of growth, plume formation being prominent in the intermediate stages. The crystal was found to

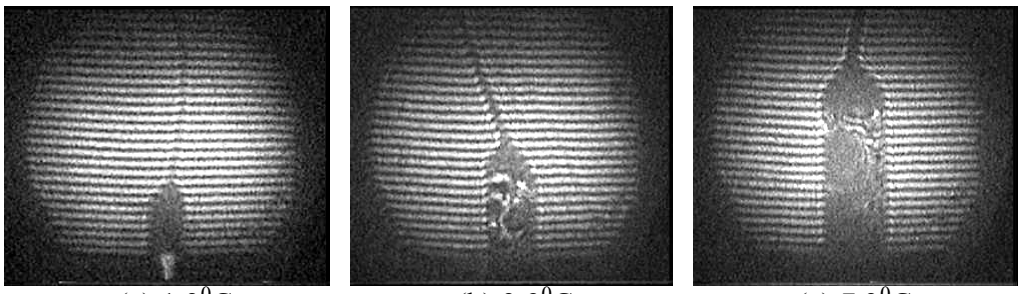

(a) 1.3^{0}C (b) 3.9^{0}C (c) 7.3^{0}C

Figure 6.10. (a-c). Wedge fringe interferograms of crystal growing under free convection conditions in platform geometry. The free convection plume and the diffusion boundary layers are visible in the interferograms.

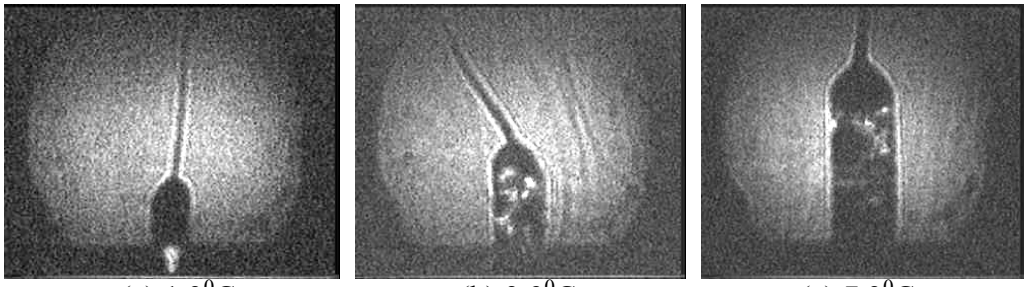

(a) 1.3^{0}C (b) 3.9^{0}C (c) 7.3^{0}C

Figure 6.11. (a-c). Shadowgraph images recorded along with the wedge interferograms shown in Figures 6.10(a-c).

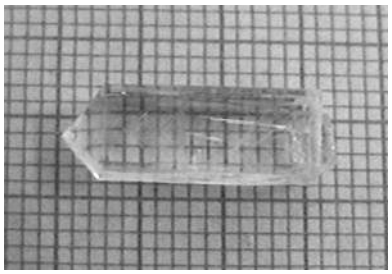

Figure 6.12. Size and quality of the crystal grown in platform geometry under free convection conditions.

have a few inclusions in it (Figure 6.12). This is attributed to the high cooling rate (0.05°C/hr) adopted in the present experiment as compared to an optimum value of 0.02°C/hr found in the earlier experiments.

6.1.4. Crystal growth in platform geometry imaged in infinite fringe setting

In order to compare the results of wedge fringe imaging (Section 6.1.3) with infinite fringe imaging, crystal growth on a platform is imaged using

infinite fringe interferometry. A KDP seed crystal of dimensions 2×2×2 mm^3 having pyramidal morphology is placed on a Plexiglas platform inside the crystallizer (Figure 6.13). The saturation temperature of the solution is 42.5°C. The cooling rate is steadily increased during the experiment from 0.02 to 0.05°C/hr in steps of 0.01°C/hr at regular intervals of time. The temperature at the end of the experiment is 36°C resulting in total supercooling of 6.5°C in 180 hours. An average cooling rate of 0.035°C/hr is achieved during the experiment.

The infinite fringe interferograms recorded at different stages of the experiment are shown in Figures 6.14(a-c) and the corresponding shadowgraph images are shown in Figures 6.15(a-c). In both the type of images the plumes are seen to rise continuously from the top of the crystal. In the infinite fringe interferograms, the contrast of the plumes is the locus of constant phase, hence constant concentration of the solution. The quality of the crystal is good up to a supercooling of 3.0°C. Beyond this the crystal transparency reduces due to defects getting incorporated inside the crystal. The defects are inclusions that are observed at high supercooling under free convection conditions.

The reason for the generation of the inclusions becomes clear when the process is monitored further using the interferometer. It is observed that the

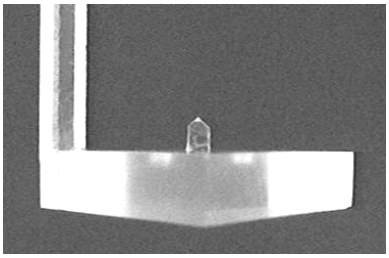

Figure 6.13. The crystal placed on a platform.

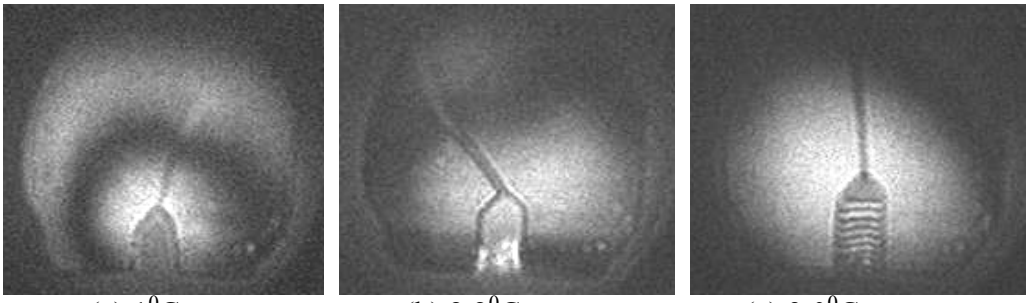

(a) 1^0C (b) 2.2^0C (c) 3.0^0C

Figure 6.14. (a-c). Infinite fringe interferograms of the crystal growing on a platform under free convection conditions.

infinite fringe interferograms had a single bright or dark fringe in the entire field up till a supercooling of 4.1°C. Subsequently, the interferograms show a few horizontal fringes in the top half (Figure 6.16a). This is the first visible indication of the development of a gravity-induced concentration gradient inside the crystallizer. This happens due to accumulation of the low concentration solution in the upper region of the crystallizer due to continuous rising of low density solution in the form of a growth plume from the crystal top. The concentration gradient continues to build with the growth of the crystal. As a result the thickness of the low concentration solution layer increases. This manifests itself in the form of increase in the thickness of the bright and dark bands of fringes. After a few hours of growth, the concentration gradient fills the entire crystallizer (Figure 6.16b). At this stage the fringes in the upper and lower half of the field of view have different thickness in the two regions. Also the population density of fringes is different in the two regions. This shows that the concentration gradient is not constant, and varies in the vertical direction. It is smoother in the upper half, where the fringes are widely separated, as compared to the lower half, where the fringes are relatively densely packed. This brings out the fact that infinite fringe Mach-Zehnder interferometry is ideally suited for visualizing concentration field as well as its gradients. The corresponding shadowgraph images, Figures 6.16(c-d), also show this process, though not as dramatically as seen in the interferograms. A bright horizontal line is observed in the Figure 6.16c, which is the horizontal plane through the crystallizer demarcating the regions having different concentration gradients. The shadowgraph images do not reveal any information about the steepness of the two gradients. This brings out the fact that shadowgraph technique is inadequate for visualizing constant concentration gradient inside the growth chamber. Thus interferometry has a definite advantage over shadowgraphy in this regard. It not only makes the concentration gradient visible in its initial stages but also is capable of showing its gradual build up with time. This phenomenon of solution stratification is observed only during growth under free convection conditions. The reason is improper mixing of the solution under free convection conditions. The increase in the free convection plumes is observed as the number of plumes increases from one in the beginning to 7 in the end. This is visible in the interferograms as well as shadowgraphs.

The crystal grows to dimensions of 16×16×18 mm^3 ($a \times b \times c$ mm^3) at the end of the experiment. The average growth rate of the KDP crystal along <001> and <100> directions are 2.13 and 1.87 mm/day respectively. It is observed that at low levels of supercooling the crystal grows more along *c*-axis. As the supercooling increases beyond a reasonable value (> 2.5°C) the crystal grows more along *a*- and *b*- directions. Throughout the duration of the

(a) 1^0C (b) 2.2^0C (c) 3.0^0C

Figure 6.15(a-c). Shadowgraph images of growth on a platform under free convection conditions. These have one-to-one correspondence with the wedge interferograms shown in Figures 6.13(a-c).

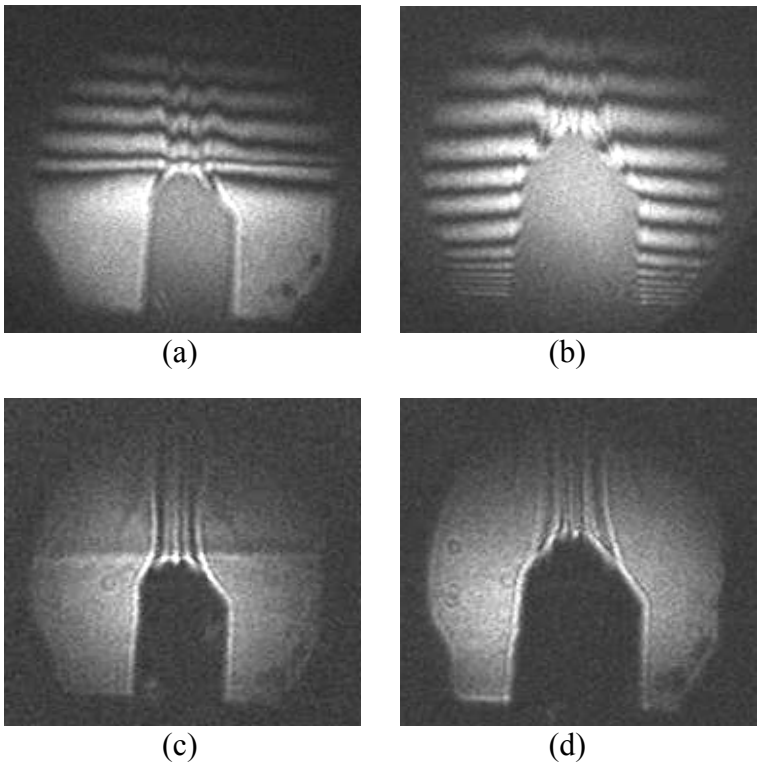

(a) (b)

(c) (d)

Figure 6.16. (a-b). Infinite fringe interferogram of the concentration gradient inside the growth cell during free convection conditions; (c-b) Shadowgraph images of the concentration gradient inside the growth cell. These images have one-to-one correspondence with the interferograms shown in (a-b).

experiment, plumes rise from the crystal top. This process has strong effect on the growth rate of prismatic as well as pyramidal faces of KDP crystal. As the solution having lesser concentration reaches the top of crystal, lesser nutrient is available for the pyramidal faces to grow. As a result growth rate

along <001> direction decreases. At the same time the solution surrounding prismatic faces has higher concentration leading to faster growth along <100> direction. If growth is continued in such a gradient it leads to a tapered morphology. Owing to the development of a concentration gradient inside the crystallizer, the crystal deteriorates in quality. It developed inclusions resulting in loss of transparency. This suggests that the cooling rate of 0.035°C/hr is beyond the safe limit applicable during free convection growth in the platform geometry. Similar result was obtained in the preceding experiment (Section 6.1.3) as well. Since the process of solution stratification is detrimental to the quality of the growing crystal, its early detection and corrective measures to avoid its spread inside the growth chamber are extremely important.

6.2. Crystal growth under forced convection

The crystal growth results described in Section 6.1 are obtained under free convection conditions. In order to compare the results with forced convection, several experiments are performed under forced flow conditions. Except the flow behavior, all other parameters are identical with the corresponding experiment of Section 6.1. Forced convection is achieved through ACRT. The clockwise and anticlockwise rotations taken together constitutes one cycle of ACRT.

6.2.1. Parametric study of forced convection parameters

Before performing the growth experiments under forced convection conditions, a parametric study is undertaken in order to find out the optimum parameters of the ACRT cycle. The parameters varied during the study are the time period of the different phases of the ACRT and the rotation rate used during steady rotation phase of the ACRT cycle. For this purpose, growth in conventional hanging geometry is imaged under six different combinations of the ACRT time periods and rotation rates (Table 6.1). The imaging technique adopted is the Mach-Zehnder interferometry in the infinite fringe mode and the solution parameter that is monitored is the concentration of the solution. A single snap shot of the concentration field during the six experiments is shown in Figures 6.17(a-f). Those values of ACRT parameters are accepted that result in uniform concentration of the solution around the growing crystal.

The above parametric study yield the following optimum values of the ACRT parameters: Spin up time = 40 s, Steady rotation = 40 s, spin down time = 40 s, stationary period = 40 s and maximum rotation rate = 32 rpm. The same cycle is repeated in reverse direction. It is observed that among the process parameters, the most important is the maximum rotation rate. Additionally, it is found that the solution concentration uniformity does not

Table 6.1. Different combinations of ACRT parameters.

Experimen Number	Spin up time (sec)	Steady time (sec)	Spin down (sec)	Stationary time (sec)	Maximum rotation rate (rpm)
Expt-1	20	80	20	20	48
Expt-2	40	60	40	40	48
Expt-3	40	40	40	40	48
Expt-4	60	Zero	60	60	48
Expt-5	40	Zero	40	40	32
Expt-6	40	40	40	40	32

depend as sensitively on the time period of the different phases of the ACRT cycle. Therefore the duration of time periods for the spin up, steady rotation, spin down and stationary phases of the ACRT cycle can be used with minor variations (± 10 %) in the above values. This optimum rotation rate correspond to *Reynolds* number of ~ 1627 for top hanging growth geometry, and ~ 7100 for growth under platform geometry. The forced convection crystal growth experiments reported later in this Section employ the above ACRT parameters. It may be added here that the shadowgraph experiments in Section 5 also use these ACRT parameters.

6.2.2. Crystal growth in platform geometry imaged in wedge fringe setting

In the present experiment growth is performed in platform geometry under forced convection conditions using ACRT parameters found in the Section 6.2.1. The process is imaged using Mach-Zehnder interferometry in the wedge fringe setting. A KDP seed crystal of dimensions $2\times2\times2$ mm^3 having its *c*-axis vertical is placed on a Plexiglass platform. The saturation temperature of the solution is 42.5°C; the cooling rate is steadily increased during the experiment from 0.02°C/hr to 0.06°C/hr in steps of 0.01°C/hr at regular intervals of time. The temperature at the end of the experiment is 38.2°C resulting in total supercooling of 4.3°C in 135 hours. An average cooling rate of 0.03°C/hr is achieved during the experiment.

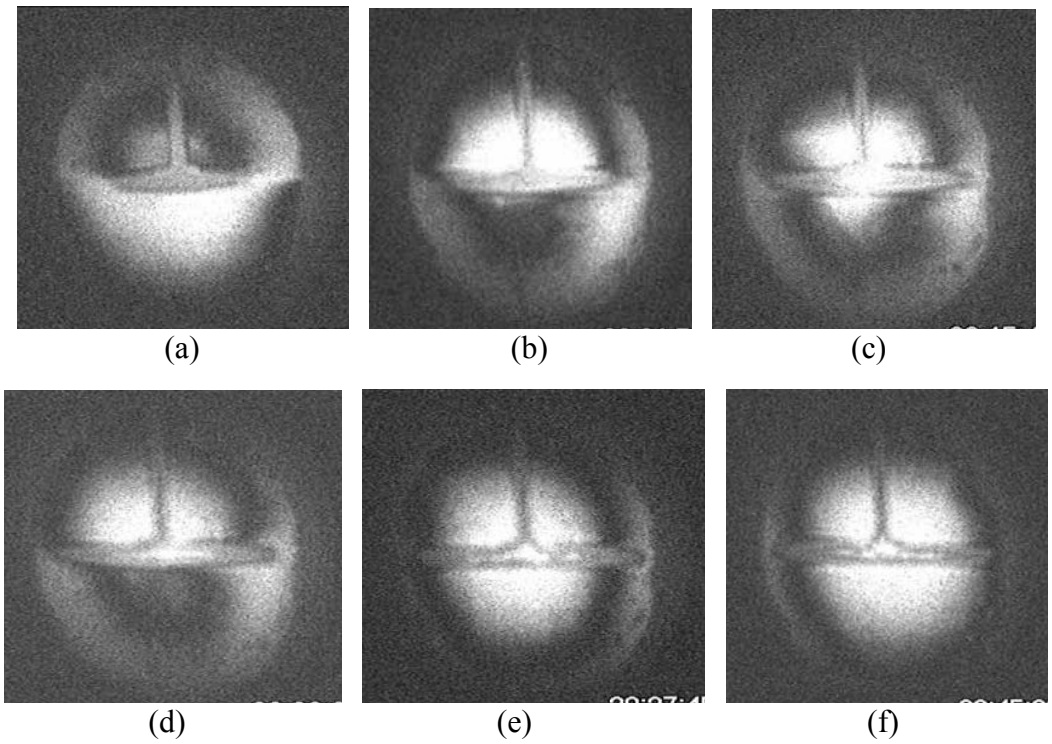

Figure 6.17 (a-f). The infinite fringe Mach-Zehnder interferograms of the concentration field during six different combinations of the ACRT parameters (Table 6.1). The uniform intensity in the last image indicates uniform concentration field.

The wedge fringe interferogram and corresponding shadowgraph image recorded during steady rotation of the ACRT cycle (32 rpm) are shown in Figures 6.18(a-b). Due to forced convection conditions inside the crystallizer, the gravity driven convective plumes are absent. Additionally, no distortion of the wedge fringes is seen, implying uniform concentration around the crystal. The uniformity of the intensity field in the shadowgraph images implies uniformity of solution concentration gradients around the crystal. The wedge interferogram and shadowgraph image recorded during stationary phase of the ACRT cycle are shown in Figures 6.19(a-b). As the swirls in the solution decay, the gravity driven free convection plumes appear. Also with the increases in crystal size, the free convection plume behavior makes transition from being laminar and stable to irregular, which affects the crystal quality adversely.

The crystal grows to dimensions of $10\times10\times19$ mm^3 ($a\times b\times c$ mm^3) at the end of the experiment. The average growth rate of the KDP crystal along <001> and <100> directions are 3.02 and 1.42 mm/day respectively. Due to irregular behavior of the plumes with an increase in crystal size, the crystal is affected by inclusions.

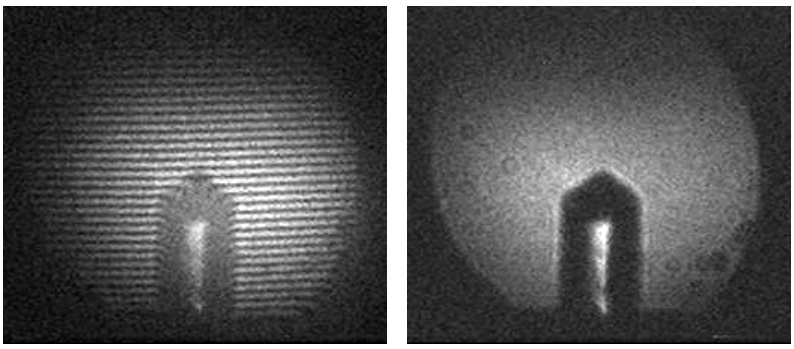

(a) Interferogram (b) Shadowgraph

Figure 6.18 (a-b). Wedge fringe interferogram and shadowgraph image of the growth process when the platform is rotated at 32 RPM of the ACRT cycle.

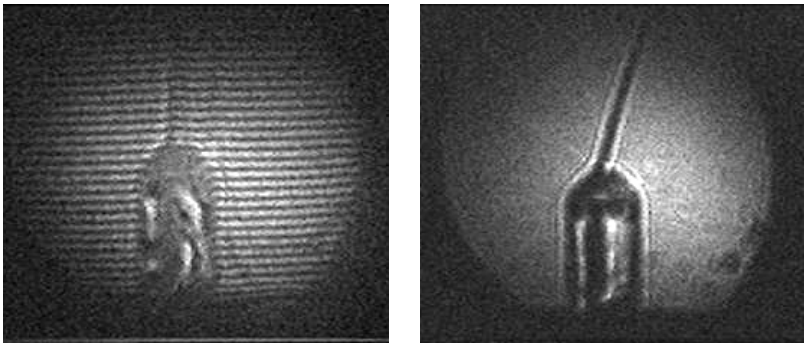

(a) Interferogram (b) Shadowgraph

Figure 6.19 (a-b). Wedge fringe interferogram and shadowgraph image of the growth process during stationary phase of ACRT cycle.

6.2.3. Crystal growth in platform geometry imaged in infinite fringe setting

In order to compare the results of wedge fringe imaging of growth in platform geometry under forced convection conditions (Section 6.2.2), a new experiment using infinite fringe interferometry is performed under identical conditions. A KDP seed crystal ($2\times2\times2$ mm^3) having its *c*-axis vertical is placed on Plexiglas platform and hung inside the crystallizer (Figures 6.20). The saturation temperature of the solution is 41.5°C. The cooling rate is slowly increased during the experiment from 0.02°C/hr to 0.05°C/hr in steps of 0.01°C/hr at regular time intervals. The temperature at the end of the experiment is 35.5°C resulting in a supercooling of 6°C in 177 hours. An average cooling rate of 0.035°C/hr is achieved during the experiment.

The infinite fringe interferograms at 2.2°C and 4.9°C supercooling recorded during steady rotation phase (32 RPM) of the ACRT cycle are shown in Figures 6.21(a-b). A single bright fringe covering the full field of

view around the crystal is a signature of uniform solution concentration. Simultaneously, shadowgraph images are also recorded by blocking the reference beam of the Mach-Zehnder interferometer Figures 6.21(c-d). Due to the forced convection conditions, no gravity driven convective plumes are observed. Since the shadowgraph images do not have sharp contrast variations, so it implies that the solution concentration gradient is uniform around the crystal.

Figures 6.22(a-b) are interferograms arising from free convection conditions for the stationary phase of the ACRT cycle. The plumes are seen rising from the crystal top at each stage of the growth process. In the initial stages of growth, when the crystal dimension is small, the interferograms reveal that there are two separate regions of solution concentration. A low concentration region is formed in the immediate vicinity of the crystal and another, away from it. With the increase of the crystal dimension, the solute diffusion towards the crystal increases leading to creation of uniform concentration. The increase of characteristic length of the crystal increases the Grashof number, which leads to stronger free convection. This allows faster intermixing of the solution leading to further uniformity of the solution concentration. However, in order to avoid the phenomena of solution stratification under free convection conditions, an optimum cooling rate has to be adopted. This helps in achieving the optimum level of supercooling required for desired growth rate and crystal quality. It is observed that the thickness of the diffusion boundary layer is a maximum during free convection growth, and decreases gradually as the crystal moves through mixed convection regime and finally to forced convection. This is attributable to the degree of fluid motion around the crystal. Since it is minimal under free convection and maximum under forced convection, it gets reflected in thickness of the solute depleted solution layer (SBL) adjacent to the crystal. Figures 6.22(c-d) show shadowgraph images of the growth in free convection conditions achieved during the stationary phase of the ACRT cycle. These images have one-to-one correspondence with the infinite fringe interferograms

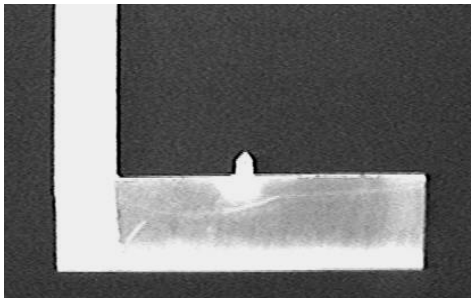

Figure 6.20. Seed crystal placed on a platform.

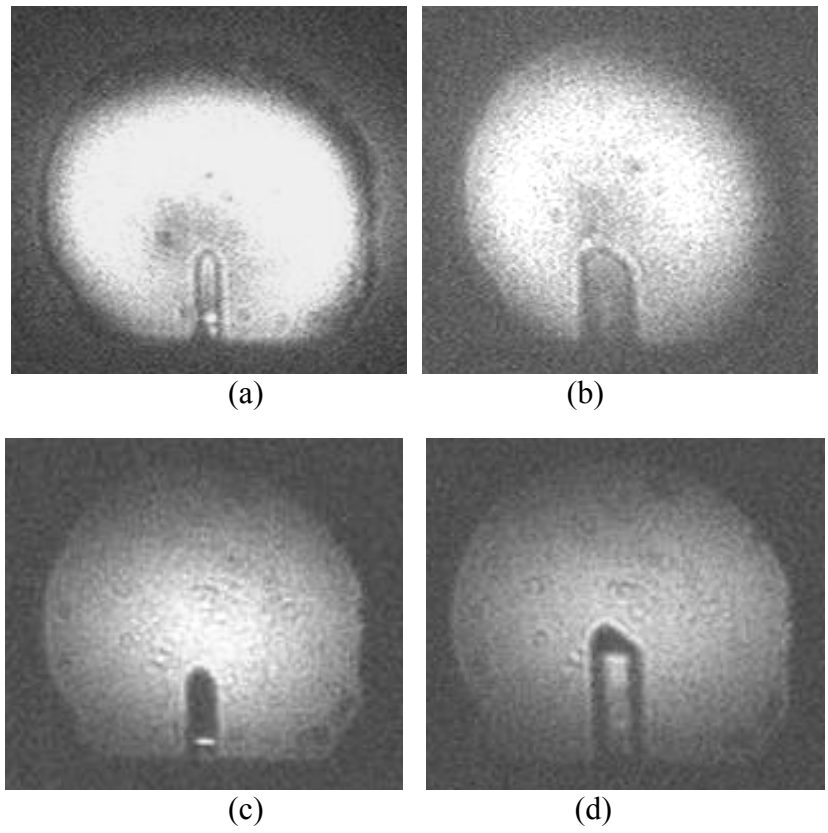

Figure 6.21. Infinite fringe interferograms (a-b) and corresponding shadowgraph images (c-d) of the growth process during steady rotation (32 RPM) of the crystal platform.

shown in Figures 6.22(a-b). Here the free convective activity is seen to increase with the growth of the crystal. Single plume is observed continuously which is laminar, stable and strong till the end of the experiment. This is reflected in the final quality of the crystal, which does not have any visible defect in it. The visibility of plumes is comparable to those observed in infinite fringe interferometry. However, the diffusion boundary layer has somewhat better visibility in shadowgraph images than in the infinite fringe interferograms. The local variations in the concentration can be quantified easily in case of infinite fringe interferograms as compared to the shadowgraph images.

6.2.4. Crystal growth in top hanging geometry imaged in wedge and infinite fringe setting simultaneously

Crystal growth described in Section 6.2.3 is performed in platform geometry under forced convection conditions. In order to compare the results with top hanging growth, an experiment is performed under forced convection. The forced

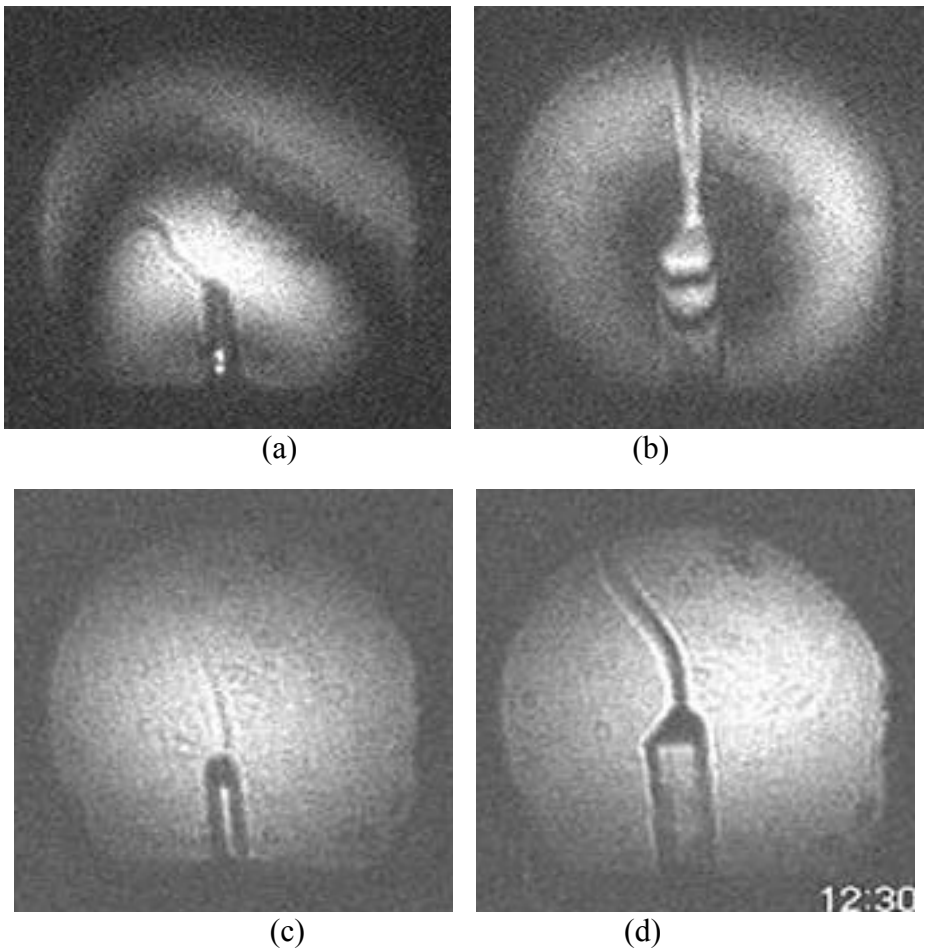

Figure 6.22. Infinite fringe interferograms (a-b) and corresponding shadowgraph images (c-d) at 2.2 and 4.9°C supercooling of the growth process recorded during stationary phase of the ACRT cycle respectively.

convection parameters are identical to the preceding experiments. Here the wedge fringes of the interferometer are vertically aligned. The reason for choosing vertical alignment of wedge fringes is to be able to visualize the solution concentration on the top and bottom faces of the crystal. This information cannot be obtained if the fringes are aligned in the horizontal direction because the fringes do not intercept the crystal surface in the desired manner. A KDP seed crystal of dimensions $1\times4\times4$ mm^3 having bi-pyramidal morphology is glued to one end of a glass rod and hung inside the crystallizer (Figure 6.23).

The saturation temperature of the solution is 40°C. The cooling rate is steadily increased during the experiment from 0.02°C/hr to 0.04°C/hr in steps of 0.01°C/hr at regular time intervals. The temperature at the end of the experiment is 36.7°C resulting in total supercooling of 3.3°C in 150 hours. As a result an average cooling rate of 0.02°C/hr is achieved during the experiment.

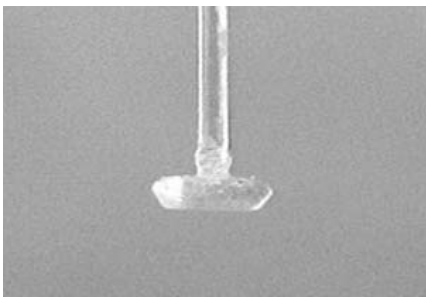

Figure 6.23. Crystal hanging from a glass rod.

The images shown in Figures 6.24(a-b) are the wedge interferograms at two different stages of the growth process corresponding to supercooling of 2.3 and 3^{o}C respectively. These have been recorded under forced convection conditions during steady rotation (32 rpm) phase of the ACRT cycle. No free convection plumes are observable here. The wedge fringes are uniform in the bulk of the crystallizer indicating that the concentration is uniform in that region. However, they are distorted near the crystal surface, which is a signature of a change in concentration in that region as compared to the bulk. The diffusion boundary layer thickness can be computed from the wedge interferograms. It is taken as the point from where the curvature starts all the way to the crystal surface. This is also referred to as the solid-liquid interface region and is the region of intense inter-atomic interactions and hence growth kinetics. The slope of the wedge fringes intercepting the crystal is used to obtain the solution concentration in the solutal boundary layer around the crystal.

The images shown in Figures 6.24(c-d) are the infinite fringe interferograms recorded under steady rotation phase of the ACRT rotation cycle. These have one to one correspondence with the wedge interferograms discussed in the preceding paragraph. It is observed that the bulk region away from the crystal-solution interface has only one bright fringe, indicating uniform concentration of the solution in that region. However, the solution-crystal interface is clearly demarcated by bright and dark fringes. The results of infinite fringe interferometry match with the wedge fringe interferometry for the bulk as well as interface region. However the interface region is mapped more precisely by the infinite fringe interferometry than by wedge fringes.

The images shown in Figures 6.24(e-f) are the shadowgraph images taken at supercooling of 2.3 and 3^{o}C respectively during the steady rotation phase of ACRT cycle. The images do not show sharp contrast variations indicating uniform concentration in the bulk of the crystallizer. The diffusion boundary layer is explicitly visible in the shadowgraph images. However, the local variations in the concentration can be quantified easily in case of infinite

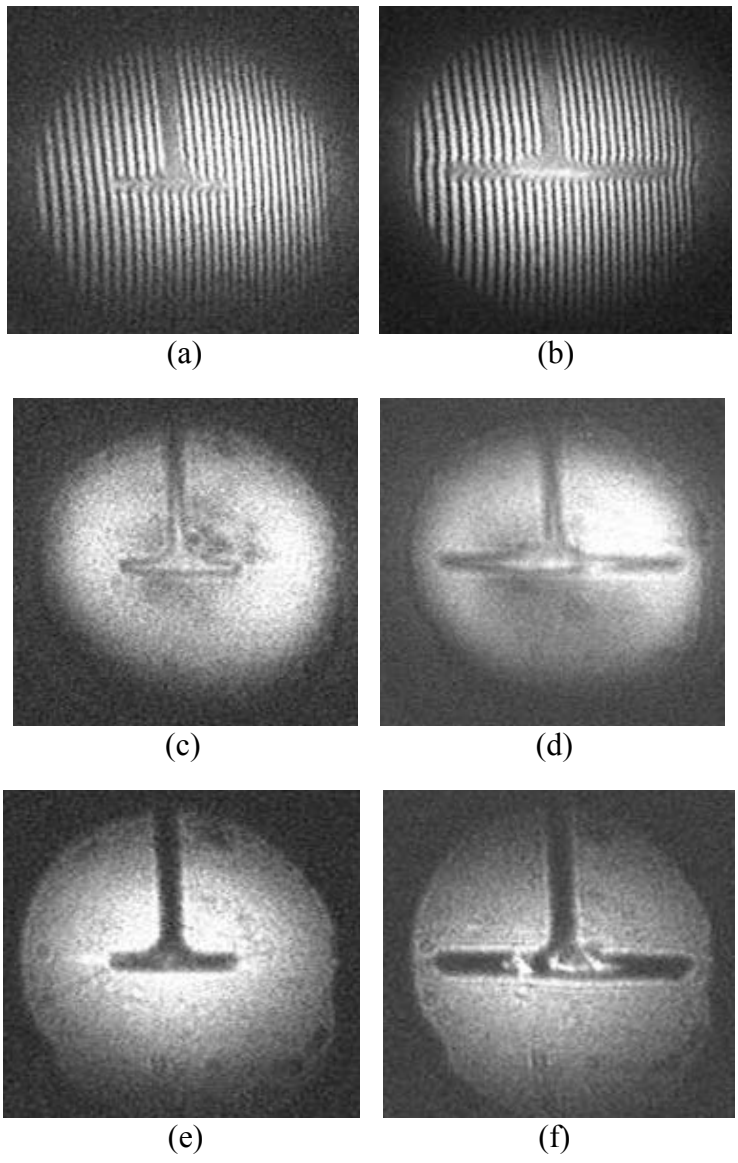

Figure 6.24. (a-b). Wedge fringe interferograms; (c-d) Infinite fringe interferograms; (e-f) shadowgraph images under steady rotation phase (rotation of 32 RPM) of the ACRT cycle at two different stages of growth corresponding to a supercooling of 2.3 and 3ºC respectively.

fringe interferograms as compared to the shadowgraph images. These images have one-to-one correspondence with the wedge and infinite fringe interferograms discussed above.

The images in Figures 6.25(a-b) are the wedge fringe interferograms recorded during stationary phase of the ACRT cycle. These images appear similar to those captured during the forced convection case, except that the fringes in the immediate vicinity of the crystal surface are slight distorted. However the distortion is not as prominent as that required for quantitative

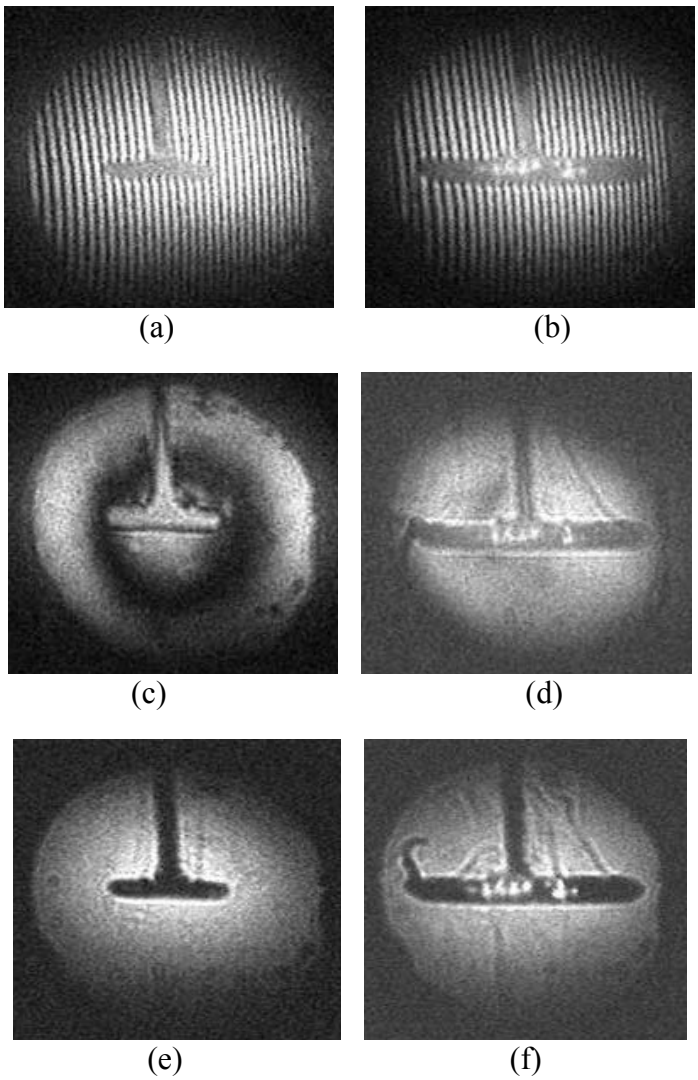

Figure 6.25. (a-b). Wedge fringe interferograms; (c-d) Infinite fringe interferograms; (e-f) shadowgraph images under stationary phase of the ACRT cycle at two different stages of growth corresponding to a supercooling of 2.3 and 3ºC respectively.

analysis. The images shown in Figures 6.25(c-d) are the infinite fringe interferograms recorded during stationary phase of the ACRT cycle. Here also the interferograms have patches of dark and bright fringe representing the non-uniformity of the solution concentration. The crystal boundaries are clearly marked by either dark or a bright fringe. Since the images have been recorded under free convection, the gravity driven plumes are visible rising form the crystal edges. These represent the locus of constant phase in an infinite fringe interferogram. The solutal boundary layer is clearly visible as a bright fringe enveloping the crystal. The images shown in Figures 6.25(e-f) are the shadowgraph images taken at supercooling of 2.3 and 3^{o}C

respectively during the stationary phase of the ACRT cycle. The solutal boundary layer is explicitly visible in these images. The gravity driven convective plumes are visible rising from the edges of the crystal. The solutal boundary layer has better visibility in shadowgraph images than in the infinite fringe interferograms.

The crystal grows to dimensions of 6×2.5×25 mm^3 ($a \times b \times c$ mm^3) at the end of the experiment (Figure 6.27). The average growth rate of the KDP crystal along <001> and <100> directions are 3.36 and 0.32 mm/day respectively. We observe that crystal has very high growth rate along *c*-axis and several times lower along *a*- and *b*- directions. This is attributable to the hanging growth geometry used. Throughout the duration of the experiment, only edge plumes are observed, which are the signatures of the growth of KDP crystal along the *c*-axis. The crystal quality at the end of the experiment is good (Figures 6.26). This is the result of optimum cooling rate (0.02°C/hr) adopted during the experiment.

6.3. Qualitative analysis of the interferograms and shadow-graph images

Different aspects of the growth process are made visible by the three techniques used. While a given technique may be suitable for visualization of a particular growth feature, some other technique may be more suitable for the quantitative data analysis. Therefore, the availability of three techniques to simultaneously visualize the growth process helps in choosing the most appropriate of them to visualize and quantify the process parameter under study. However, not all the techniques provide the dual feature of the ease-of-experimentation as well as simple data-analysis procedure. One has to choose between the two features depending upon the problem at hand. For example, it is sometimes more important to detect onset of a particular phenomenon during growth rather than to monitor its progress after detection. Therefore a technique with better visualization capability is more appropriate for the detection

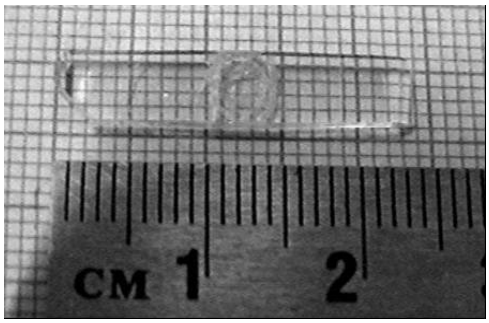

Figure 6.26. Size and quality of the crystal grown in the top hanging geometry.

whereas a technique which is simple to implement and less prone to error propagation is preferred for subsequent quantitative analysis. The procedure for qualitative and quantitative data analysis for the three techniques is described in detail in the Section 4. Here the qualitative data analysis to extract information about the growth parameters such as the solutal boundary layer, the uniformity of concentration field, the concentration gradients, the mass-flux towards the crystal, and the variation of the concentration along horizontal and vertical directions is described.

6.3.1. Solutal boundary layer

The solutal boundary layer (SBL) is most clearly visualized in shadowgraph images, though it is visible in the infinite as well as wedge fringe interferograms in an indirect manner. In case of shadowgraphy, the SBL is seen as a bright band surrounding the edges of the crystal. The principle of shadowgraphy explains the origin of the bright band to be due to the bending of rays from one region to another. The infinite fringe interferograms represent the SBL as a thin bright fringe around the crystal against a broad dark fringe. The dark and bright fringes are seen to switch sometimes depending upon the reference beam phase fluctuations. The wedge fringe interferograms represent the SBL in an indirect manner. The wedge fringes near to the crystal become curved during growth or dissolution. The SBL is taken to extend from the point where the fringe curvature starts and up to the crystal surface.

6.3.2. Concentration field, growth rate and crystal quality

If the fringes in the wedge interferograms show no curvature then it implies uniformity of concentration all around the crystal. This corresponds to the saturation point of the solution and represents no-growth and no-dissolution condition. During growth or dissolution, the concentration adjacent to the crystal changes resulting in the curvature of the wedges fringes. The extent of the curvature of fringes is a measure of the difference in the concentration between regions adjacent to the crystal and far away from it. If the extent of the curvature of the fringes along the crystal edges is constant, it represents uniform concentration along the surface, and hence a constant thickness solutal boundary layer. At the same time a varying curvature of the fringes along the crystal surface points towards a varying concentration along the surface and hence a solutal boundary layer of varying thickness. Additionally, the slope of the fringes intercepting the crystal surface is a measure of the gradient of the concentration field. This, in turn, is a measure of the mass flux towards the crystal, i.e. the amount of solute moving towards the crystal. It is desired that the mass flux towards the crystal

from all direction be equal as far as possible. This has implications for the growth rate of the habit faces of the crystal. The design of the growth crystallizer and associated flow driving apparatus is driven by this condition of achieving the uniformity of the mass flux.

In case of the infinite fringe interferogram, the growing crystal is bound by two regions of different concentration. One is just adjacent to the crystal and another far away from it into the bulk of the crystallizer. If the concentration is uniform around the crystal, then a broad fringe of constant thickness is observed to envelope the crystal in a manner so as to take the shape of the crystal. However, if the concentration is sharply varying in the vicinity of the crystal, a large number of thin fringes are observed enveloping the crystal. The number of fringes per unit distance from the crystal and their thickness are two parameters which are measures of the gradient of concentration. A large number of fringes in the immediate vicinity of the crystal is a signature of high mass flux towards the crystal, which is a desirable feature as it leads to high growth rate. Also the thickness of the fringes around the crystal is an indirect measure of the growth kinetics of the habit faces. The face which grows faster will have large number of thin fringes near it as compared to others. So although the mass flux is desired to be as uniform as possible for constant growth rate of all the habit faces of the crystal, but at the same time it is desired to be as high as possible so that the growth rate is maximum. Therefore these two factors act opposite to each other during crystal growth process. Beyond a particular value of supersaturation (or concentration) these two factors start to act opposite to each other and affect the crystal quality adversely.

In case of shadowgraph images, the intensity field does not provide direct information of the concentration field or its gradient. The reason is that the shadowgraph process relates the intensity field to the Laplacian of the concentration (or refractive index) distribution. As a special case of a solutal boundary layer we can approximate

$$\frac{\Delta I}{I_o} \approx 1$$

Using the shadowgraph governing equation

$$\nabla^2(\ln n) = 1$$

Assuming one dimensional dependence of refractive index and integrating the above equation

$$\ln n = C_1 + C_2 y + C_3 y^2$$

Thus a quadratic dependence of the refractive index is obtained by processing the intensity based shadowgraph image. Thus indirect information about the concentration field is obtained from the shadowgraph images. This has been explained in detail in Section 4. From the shadowgraph images, we can obtain whether the concentration field varies along both *x* and *y* directions or only along *x* direction. If it has uniform thickness as we move along *y* (height), this implies that it varies only along *x* (horizontal direction). It can be interpreted from the thickness of the solutal boundary layer and the convective plume.

6.4. Closure

A novel constant-deviation Mach-Zehnder interferometer has been developed for imaging the concentration field during KDP growth under free and forced convection conditions. The design of the interferometer is such that it is immune to frequent misalignments due to external vibrations and ambient temperature fluctuations (Verma, 2005A). It has been used for imaging the concentration field during KDP growth under free and forced convection conditions in two different geometries. The following results have been obtained:

i) Parametric study of forced convection has been performed by imaging the concentration field during growth in the top hanging geometry for various forced convection conditions. These are achieved by varying the rotation rate and the time periods of the acceleration and deceleration phases of an ACRT (accelerated crucible rotation technique). Results indicate that a uniform concentration is achieved only for selected values of these parameters. These correspond to an average Reynolds number of 1627 for top hanging geometry and 7100 for platform growth geometry.

ii) Infinite fringe M-Z interferometry is demonstrated to be a highly sensitive diagnostic tool to measure concentration gradients inside growth chamber (Verma, 2005B).

iii) The thickness of the solutal boundary layer (SBL), which is the region of large mass fluxes of solute towards the crystal, has been quantified. It lies in the range 150-300 μm. Thinner boundary layer are associated with higher concentration gradients, higher mass fluxes and hence, faster growth kinetics.

iv) Shadowgraph technique is best suited to visualize the solutal boundary layer whereas infinite fringe interferometry is ideal for detecting and measuring concentration gradients inside the growth chamber. Wedge fringe interferometry provides information of the local concentration variation around the crystal.

7. Tomographic reconstruction of shadowgraph data

7.1. Need for three-dimensional imaging

Since conventional optical shadowgraphy and interferometry techniques can only measure the average absorptivity or refractive index along the optical path, quantitatively meaningful results are possible only if: (a) The experiment configuration is two-dimensionalized so that all parameters are constant along the optical path, or (b) The experiment is truly three-dimensional and the optical technique permits either direct three-dimensional imaging or 3-D image reconstruction from a set of two-dimensional images. The former is exemplified by holography and the latter (adopted in the present work) by various forms of tomography.

7.2. Preliminary definitions

Terms used in three-dimensional imaging are first defined here. It is necessary to distinguish between the data defining a spatial arrangement and its derivative pictorial representations.

3-D Digital map: A *map* is a mathematical representation of spatial data in which space is divided into volume elements called *voxels*.

Voxel: The unit element of a 3-D digital map. It contains either (a) one or more visual properties, such as brightness or hue, or (b) one or more numerical values corresponding to physical properties, such as amplitude, phase, or velocity (described by a set of magnitudes and directions). Each voxel has an *address* of three numbers defining its location in the digital map, and three lengths (not necessarily equal) which are related to but not necessarily equal to the spacing between voxels and the resolution of the image.

Image: A visual representation of a map, such as a photograph, is called an *image*. An image is usually two-dimensional, in which case its elements, as shown on a monitor or photograph, are called *pixels*.

Slices: A *slice* is a planar array of voxels of a three-dimensional digital map. Thus a *z-slice* of a 3-D map is a one-voxel-thick layer of all the voxels having the same *z*-axis address. The term *slice* is also used for a 2-D image wherein each pixel corresponds to a voxel of the slice. Slices may be taken at any angle (usually defined as normal to a specified axis) and at any *layer* normal to that axis (defined as a position along that axis); however, great care must be taken to define which voxels belong to a given slice.

Projections: In contrast, a *projection* is a 2-D digital map or image wherein the properties of each pixel are the sum (or average) of the values of that property for all the voxels of the 3-D map along the *projection line* that pass through the pixel in question. In virtually all of the optical techniques described in the previous chapters, the *images* (or *maps*) are parallel projections, with the projection lines normal to the image plane. In a few cases, the images correspond to *conical projections* where all the projection lines, when extended, have a common point of convergence or focus.

In the following discussion, it is important to distinguish between *slices* and *projections*.

7.3. Tomography

The word *tomos* means *slices* and *graphy* implies a type of imaging. Therefore the word *tomography* properly means the sectioning of a 3-D map into a set of (usually parallel) 2-D images, each corresponding to a slice of the 3-D map. More recently, it has come to mean the reconstruction of a 3-D map from a set of 2-D maps or images.

Parallel slice construction: The construction of a 3-D digital map from a set of parallel slices is fairly obvious. Here the slices are taken at incremental values along the axis normal to the 3-D map. The data is obtained directly as a *stack* of parallel 2-D maps, all perpendicular to a common axis and spaced closely enough to provide a detailed 3-D map. One has to take the precaution that the spacing between slices is small enough to preclude the omission of essential details.

Computerized axial tomography (CAT): This is the only non-obvious method of 3-D digital map construction. CAT has been formally defined and discussed in great detail in Section 4. A brief introduction will be provided here. CAT techniques usually start with a set of 2-D projections formed at different angles and parallel to a common axis. Figure 7.1 shows a simple

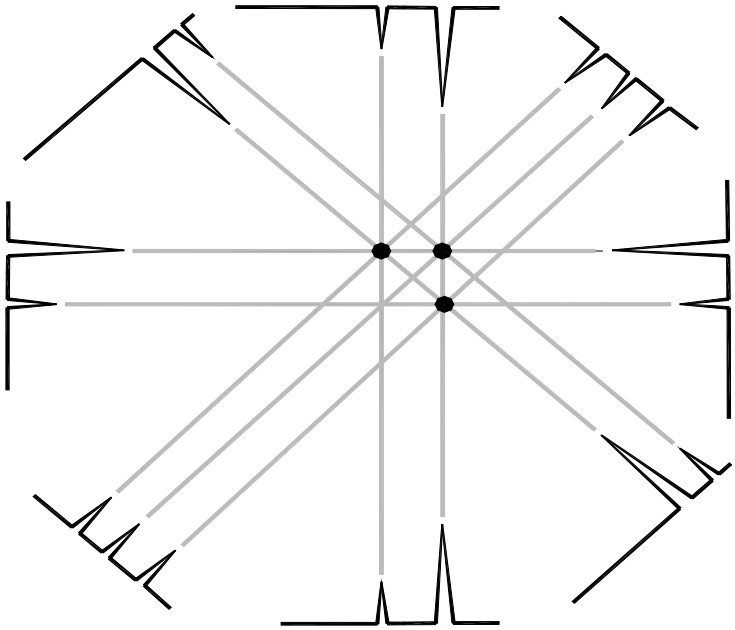

Figure 7.1. Inference of the arrangement of three dots by axial tomographic reconstruction from four 1-D projections (after Hornak, 2001).

example that demonstrates intuitively how the structure of a two-dimensional arrangement of three dots can be inferred from a series of one-dimensional projections from four different directions. It is important to note that slices are used in parallel layer image construction, but projections are necessary for axial tomographic construction.

Optical CAT (OCAT): Optical techniques have seen resurgence in engineering research because of the availability of lasers as sources of light, high-resolution cameras for image acquisition, and high-performance computers for data processing. The only limitation of optical techniques is that information about the three-dimensional processes is available as two-dimensional images. However this limitation can be overcome by using the principles of computerized tomography. Tomography is essentially a two-step process: first, collection of the projection data and, second, reconstructing the field parameter using numerical algorithms. Reconstruction algorithms referred to as convolution back projection (CBP) and algebraic reconstruction technique (ART) are described in Section 4. Optical tomography has numerous applications in many diverse fields of science and engineering. A new approach based on optical tomography, namely shadowgraphic tomography is discussed in the present Section. The first crystal growth experiments to make use of this technique are reported here.

7.4. Why perform tomographic imaging of crystal growth processes?

Most crystal growth processes such as crystal pulling or the growth of suspended crystals in a solution have variables that are distributed in all three dimensions. For example, transport phenomena including heat and mass transfer and fluid flow have three-dimensional character, and strongly influence the crystal quality and the growth rate. In order to study the relationship between convection and the growing crystal, the two-dimensional imaging techniques of shadowgraphy and interferometry are used in the present work. The results of flow visualization were presented in Sections 5 and 6 respectively. Detailed understanding of the growth process requires three-dimensional data. For the detection of convective instabilities, a qualitative 3-D image will suffice. In other contexts, such as determining the mechanism of growth or comparison with theory, 3-D grids of numerical data related to convection velocity, concentration, temperature, and interface motion are necessary.

7.5. Shadowgraphic tomography

In the presence of the immersed crystal, the KDP solution develops a three-dimensional pattern of varying refractive index. Light rays passing through the solution are refracted out of their original path. This causes a spatial modulation of the intensity distribution with respect to the original intensity, and produces a shadowgraph pattern on the screen. The development of buoyancy-driven convection is recorded in the form of shadowgraph images at regular intervals for the entire duration of the experiment. The growth apparatus and instrumentation used for performing the optical tomography experiments were discussed in Section 3. The theoretical formalism of the analysis techniques was presented in Section 4. The steps used to construct consistent projection data from the shadowgraph images that would serve as input for tomographic reconstruction and subsequent reconstruction procedure are described below:

Step 1. Record experimental projection data

Record a finite number of shadowgraph images (I_s) of the process along a few angular directions between 0 to 180 degrees. These are referred to as *views*, and constitute the experimental projection data required for tomographic reconstruction. We record 18 images between 0 to 170 degrees at 10 degrees interval. A shadowgraph image when no process is occurring in the chamber is also recorded as a reference images (I_o).

Step 2. Obtain gray value matrix for each image

Using appropriate *image-processing* software, gray value of each pixel of the above shadowgraph images are obtained. In our case, we obtained 18 gray value matrices of size 350×350.

Step 3. Obtain projection data matrices

Using above gray value matrices different types of projection data can be obtained. The following three types of projection data is generated:

a) Intensity values
b) Contrast $[(I_o\text{-}I)/I_s]$ values
c) Refractive index values

The refractive index projection data is obtained by solving the governing equation of the shadowgraph process. We obtained 3 different sets of 18 data matrices having 350×350 elements. Suitable computer codes have been written for the purpose.

Step 4. Select a few planes above crystal for reconstruction

Depending upon the type of data chosen out of the three types given above for further processing, a few rows are selected from each of the matrix. These rows represent planes above the crystal for reconstructing the field parameter over them. For example, following three planes were selected at a height of *0.25H, 0.5H* and *0.75H* from the crystal top face. *H* is the height difference between image top boundary and the crystal top surface.

Step 5. Obtain matrices having equal number of views and rays

For a given height above the crystal, 18 row matrices are obtained from the 18 shadowgraph images. Each row matrix represents a different *view*. It has 350 elements, where each element constitutes a *ray*. We reduce the number of rays from 350 to 18. For this, 18 elements of the row matrix are selected that are spread symmetrically along the row matrix. Thus, 18 views are obtained, wherein each view has 18 rays.

Step 6. Interpolate to increase the number of views

Due to experimental limitation, only 18 projections were captured between 0 to 180 degrees. However, for faithful reconstruction of the field parameter, it is desirable to have as many projections as possible. Due to this a suitable linear interpolation scheme is adopted to increase the projections to 90. As a result, a view at every 2 degree interval is obtained. This results in increase of matrix size from 18×18 (18 views × 18 rays) to 90×18 (90 views × 18 rays) for each of the planes selected above the crystal.

Step 7. Extrapolate to increase the number of rays in each view

The region mapped by the probe laser beam is only about 20% of the process chamber dimension. Therefore each view contains partial projection data of the process chamber. However, tomography requires complete projection data. For this reason the number of rays was increased in each view from 18 to 90 using linear extrapolation. After extrapolation, the (90×18) matrices become (90×90) matrices. We obtain three such matrices, one each for the plane selected.

Step 8. Consistency check of the generated data

Since all the views (projections) are recorded simultaneously, therefore the cumulative sum of physical quantity (concentration) over a given plane has to be constant. This condition was enforced to ensure the consistency of the data obtained from each view. Average of the 90 views was compared with the individual total of each view. The difference in the values was distributed equally among all the elements of the view. In this way all the views are made consistent to get a complete set of consistent data.

Step 9. Normalization of consistent data

The tomography reconstruction codes demand normalized data (either 0 to 1, or 0 – 255). The above consistent data is therefore normalized. This results in normalized matrix of size 90×90, wherein each row is a view and each column is a ray in that view. This matrix can be considered as a stack of 90 views or projections.

Step 10. Obtain experimental sinogram

Since the normalized matrix obtained in the previous step is a stack of 90 projections, therefore it is used to obtain the experimental sinogram. This is referred to as *direct sinogram*. Such sinograms are obtained for each of the three planes selected above the growing crystal.

Step 11. Perform tomographic reconstruction

The normalized projection data is used as input to the tomography reconstruction codes. It is done either through *Divyadrishti* under *Windows* or *c*-language codes under *Linux*. Two different algorithms are used.

a) *Convolution back projection* (CBP) using a *Hamming filter (H54)* function.
b) *Algebraic reconstruction technique* (ART) using a relaxation factor of 0.01 with error criteria of 0.001%.

The output of the codes is the reconstructed field parameter over the considered plane.

Step 12. Normalization of the reconstructed object

The reconstructed object field parameters are normalized between the minimum and maximum boundary conditions of concentration. The field parameter over a plane is then viewed either as an image file (using MATLAB) or as contour plots (using *Tecplot*).

Step 13. Cross-checks on solution obtained by tomography

After obtaining the reconstructed field over a given plane, a few cross-checks are enforced to confirm the correctness of the solution obtained. These are described below:

i) Cross-check 1: Sinogram of the reconstructed object field is obtained by collecting the projections of the reconstructed object field and stacking them. For our case 90 views between 0 to 180° at 2° interval are obtained. This is accomplished using *Divyadrishti* software. This check is applied to CBP as well as ART based reconstructed objects. These are referred here as *reverse sinograms*. A close match between these and experimental sinogram proves that the procedure adopted for tomographic reconstruction is correct. In other words it means that the 18 reverse projections of the reconstructed object obtained between 0 to 180° are matched with the experimentally recorded projections. A match between the two established the correctness of the solution obtained.

ii) Cross-check 2: Two projections are dropped from the set of 18 experimental projections. In our case, we drop projections corresponding to 30° (view number 4) and 120° (view number 14). The remaining 16 projections are subjected to interpolation and extrapolation and other steps described above to get the 90 views and 90 rays projection matrix. This is used for tomographic reconstruction of the object using CBP and ART. The reconstructed object is then used to generate the originally dropped projections. These generated projections are compared with the dropped projections. A close match between the two established the correctness of the solution obtained through tomography.

7.5.1. Tomography experiment

A crystal growth experiment was performed in which the crystal was placed on top of a glass rod for unhindered visualization of the convection pattern. The shadowgraph projection images were recorded for a KDP crystal 15 mm in size. The experimental parameters during recording of projection data were: supercooling of 4°C, saturation temperature of the solution, 56°C,

and the cooling rate adopted, 0.02°C/hour. The shadowgraph images of the convection process were captured at regular intervals during the growth experiment. The plume activity gradually builds up as the crystal dimension increases. The plume evolves from the laminar stage reaching finally the chaotic, intermediated by irregular behavior. The details of plume dynamics were presented in Section 5. After a few days of growth, the buoyancy-driven convection activity became strong, and plumes of broad width were seen rising continuously from the top surface of the growing crystal. At this stage, two-dimensional shadowgraph images (projections) of the growth process were recorded from 18 viewing directions between 0 to 180° by slowly turning the crystal in steps of 10°. The shadowgraph projection images that contain the three-dimensional character of the free convection plumes over the crystal surface are shown in Figures 7.2(a-d). Since the contribution of the concentration field is much higher (~95%) than the thermal field (~5%) in driving the convection process, temperature is taken to be spatially constant. Three-dimensional concentration maps are reconstructed above the surface of the growing crystal using shadowgraphic tomography. The finite time taken in capturing the projection data is not expected to yield any appreciable error in estimating the 3D structure of the convective field because we are looking at a process which does not involve very fast changing transients.

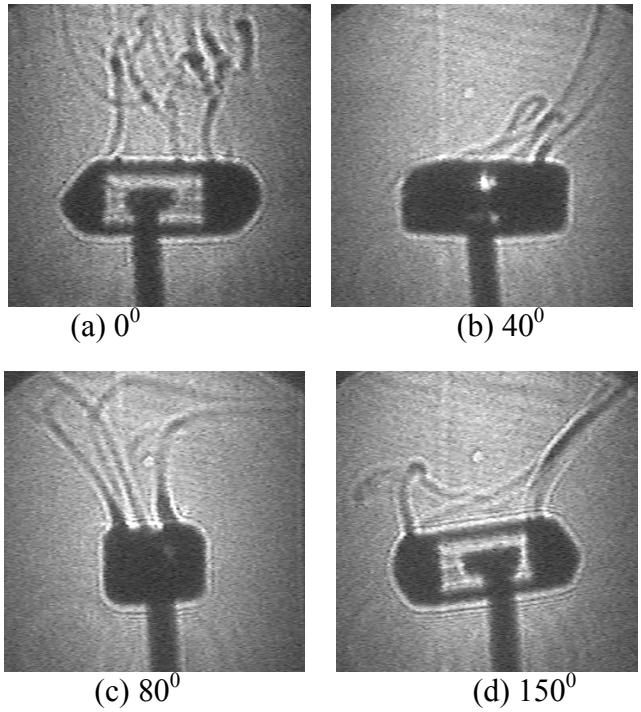

Figure 7.2(a-d). Shadowgraph projection data showing the buoyancy driven convection plumes above the top surface of a growing KDP crystal.

7.6. Shadowgraphic tomography: Influence of the number of views and the type of projection data

The intensity field at each pixel of the 18 shadowgraph images was used as the projection data for the tomographic reconstruction using CBP and ART algorithms. Figures 7.3(a-c) show reconstruction contours obtained using the intensity field over three different planes at normalized heights of 0.25, 0.50 and 0.75 respectively. These have been obtained using the CBP algorithm. Similar results using the ART algorithm are shown in Figures 7.3(d-f). In order to understand the influence of number of views, reconstruction was performed again using 90 views. These were generated from the 18 experimental images using linear interpolation. Linear extrapolation was used to increase the number of rays from 18 to 90 in order to span the entire growth chamber. The results of CBP and ART reconstruction over planes 1, 2 and 3 are shown in Figures 7.4(a-c) and 7.4(d-f) respectively. Results indicate that the ART algorithm recovers the broad features present in the shadowgraph images with the 18 view data set. The finer features appear when a data set of 90 views is used. On the other hand CBP generates several spurious features with the 18 view data-set. These reduce when 90 views are used. Several cross-checks have been applied to verify the correctness of the obtained reconstruction. Error estimates based on a pair of reconstructed solutions show deviations to be small. For the 90-view reconstruction, errors are found to be uniformly negligible.

The influence of the choice of the dependent variable of the projection data is additionally studied. Three different variables namely, intensity values (Fig. 7.2(a-d)), contrast $(I_o-I_s)/I_s$ (Fig. 7.5(a-d)), and refractive index (Fig. 7.6(a-d)) corresponding to the shadowgraph projection images are used. The tomographic contour plots using light intensity as the projection data show that the rising plumes spread horizontally in a dumbbell shaped manner (Fig. 7.3(a-f) and 7.4(a-f)). The shape of the plume has bearing on the stability of convection and hence on the quality of the growing crystal. The gradients in the field parameter (namely, concentration) are high just above the crystal. In the bulk of the solution they are smaller and the changes are gradual. This is because under free convection, the growth process is restricted to a boundary layer adjacent to the crystal. The reconstruction based on contrast (Fig. 7.7(a-b)) also reveal similar information, however several features get lost because of relatively small variations in the adjacent pixels. This fact becomes more pronounced when refractive index data is used for tomographic reconstruction. Due to extremely small variations in the projection values of the adjacent pixels (10^{-5} - 10^{-6}), the refractive index based reconstruction (Fig. 7.7(c-d)) does not provide meaningful values.

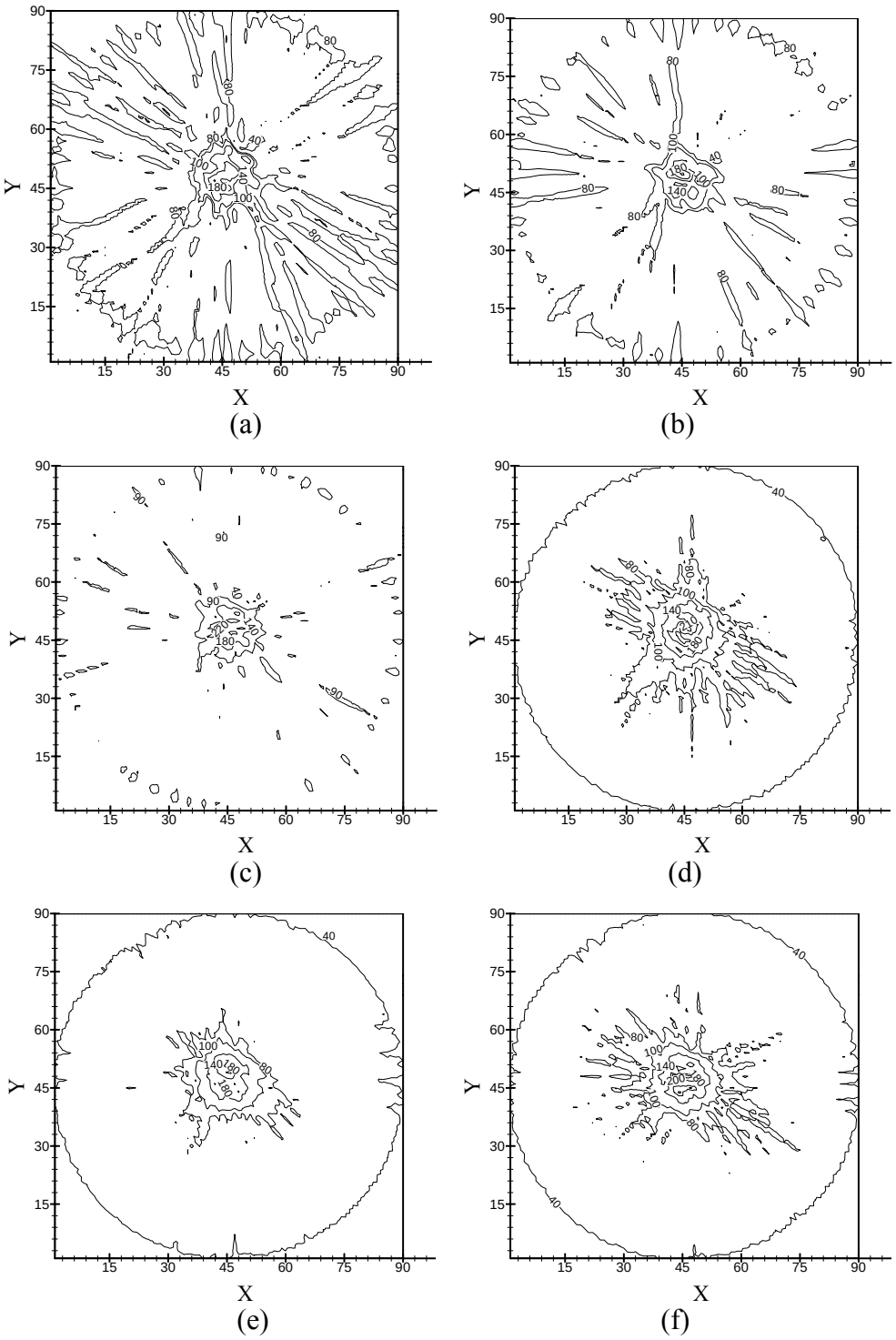

Figure. 7.3 (a-f). Reconstruction of the intensity field over planes 1, 2 and 3 using 18 views and 90 rays projection data. (a-c) Reconstruction using CBP; (d-f) Reconstruction using ART.

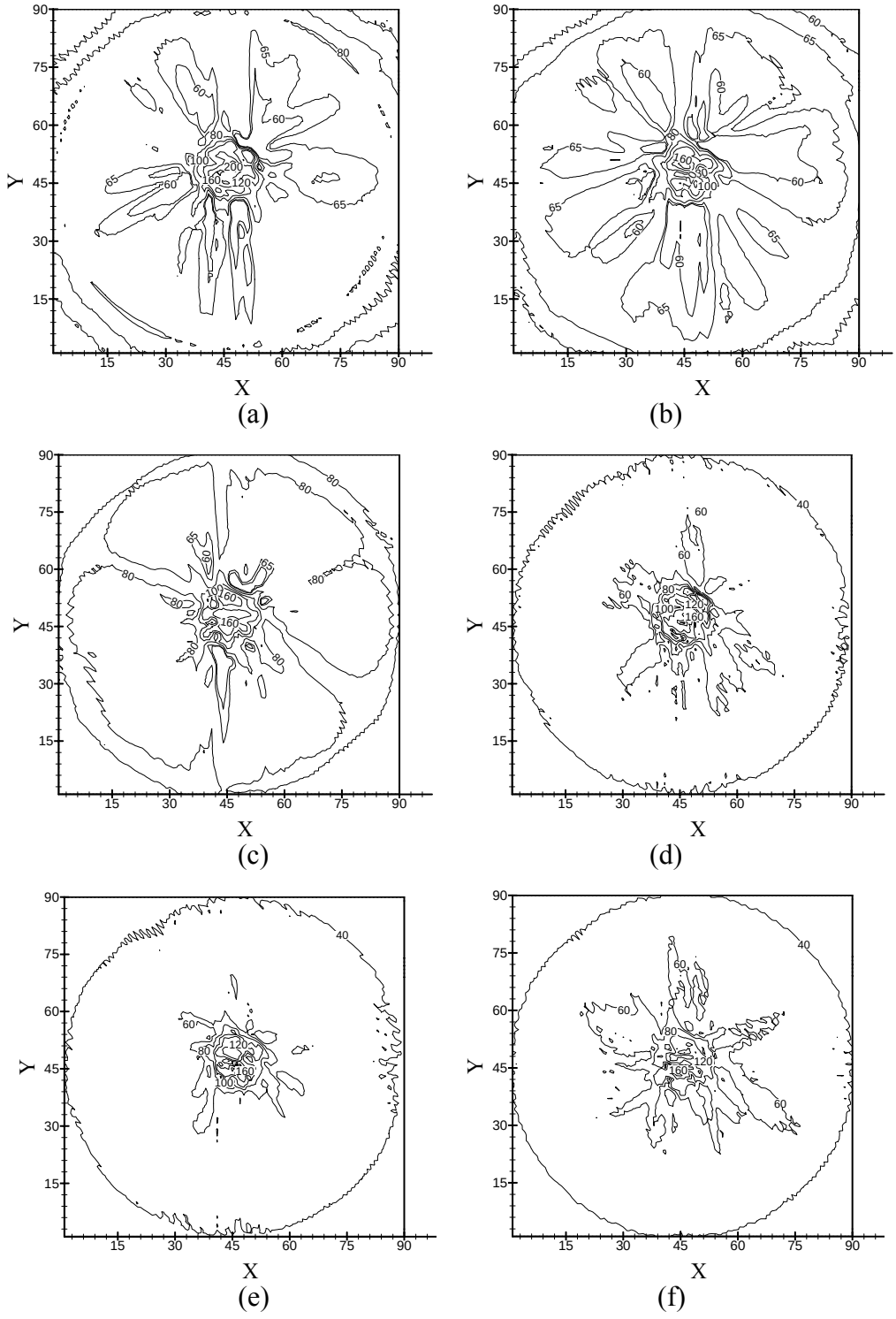

Figure. 7.4 (a-f). Reconstruction of the intensity field over planes 1, 2 and 3 using 90 views and 90 rays projection data. (a-c) Reconstruction using CBP; (d-f) Reconstruction using ART.

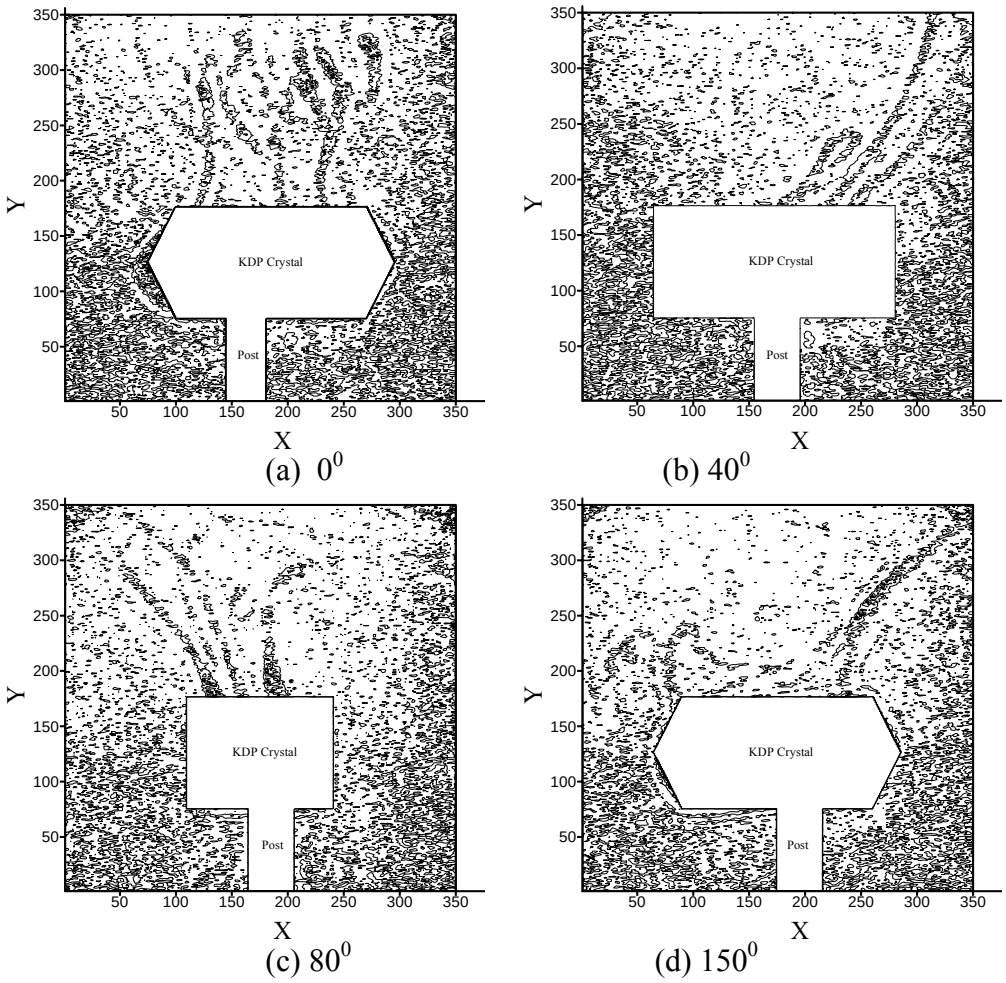

Figure. 7.5 (a-d). The projection maps of contrast *(Io-Is)/Is* corresponding to shadowgraph images in Figures 7.2(a-d) respectively. The contrast is the driving term in the Poisson governing equation.

7.7. Closure

Distribution of solute concentration and mass fluxes during growth of KDP (potassium dihydrogen phosphate) crystal under free convection conditions is imaged using shadowgraph technique and analyzed using principles of computerized tomography (Verma, 2006). Two types of reconstruction algorithms, namely convolution back projection (CBP) and algebraic reconstruction technique (ART) have been employed for the purpose. Inferences about the shape of the convection plume, its three dimensional character and plume stability have been drawn from the results of tomographic reconstruction (Verma, 2008A). The flow details are found to have bearing on the crystal quality. The effect of the number of views

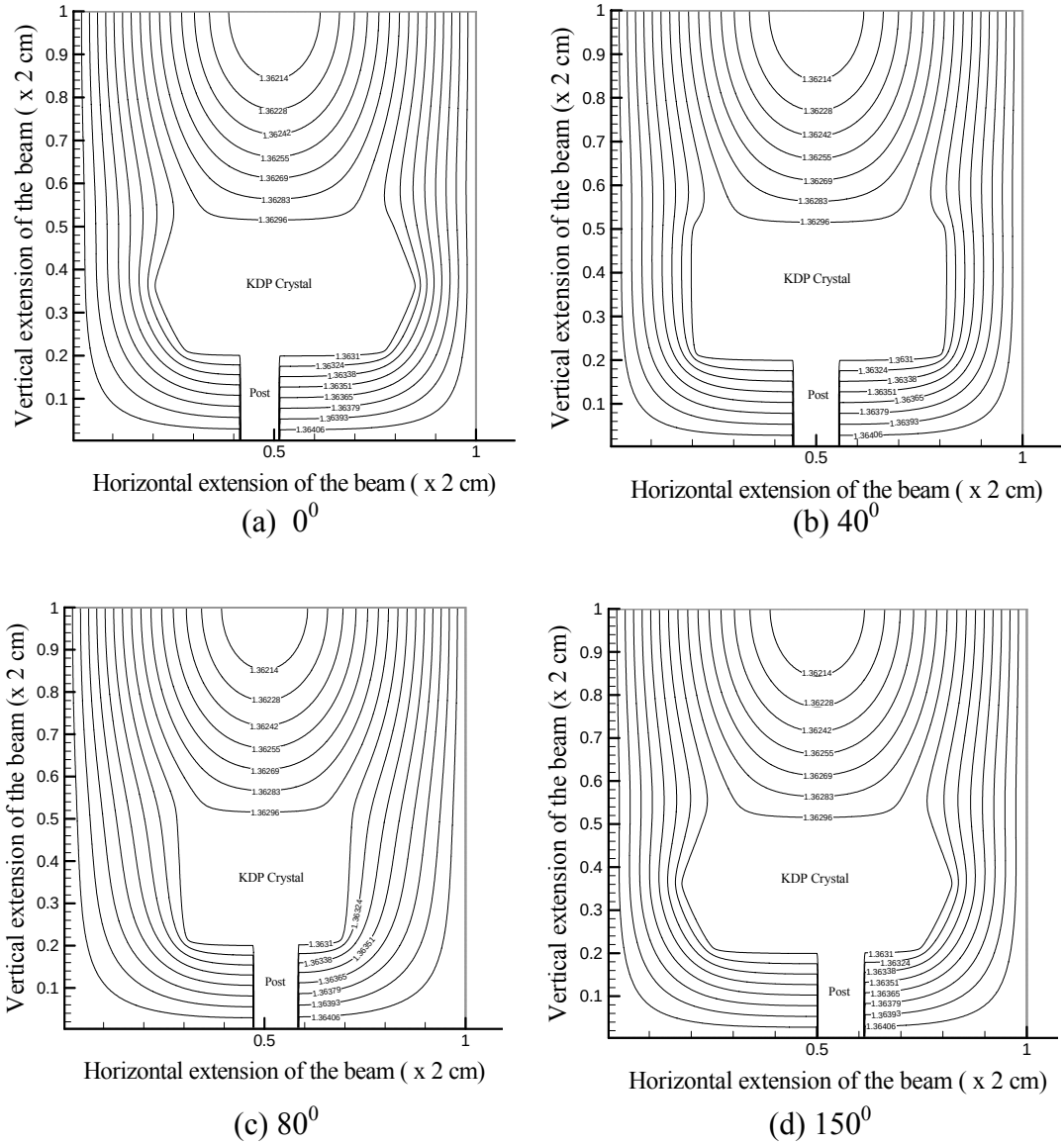

Figure 7.6(a-d). Refractive index contours corresponding to the shadowgraph images shown in Figures 7.2(a-d). They are obtained by solving the Poisson equation governing the process.

available for reconstruction has been studied using two different projection data consisting of 18 and 90 views respectively. Error estimates are obtained for a pair of reconstructed solutions from 18 and 90 projections. The influence of the choice of the dependent variable in the projection data is additionally studied. Two different types of variables, namely, intensity and contrast *[(Io-Is)/Is*] of the shadowgraph images are considered. Results show that the latter affords an improved interpretation of the reconstruction obtained (Verma, 2008C).

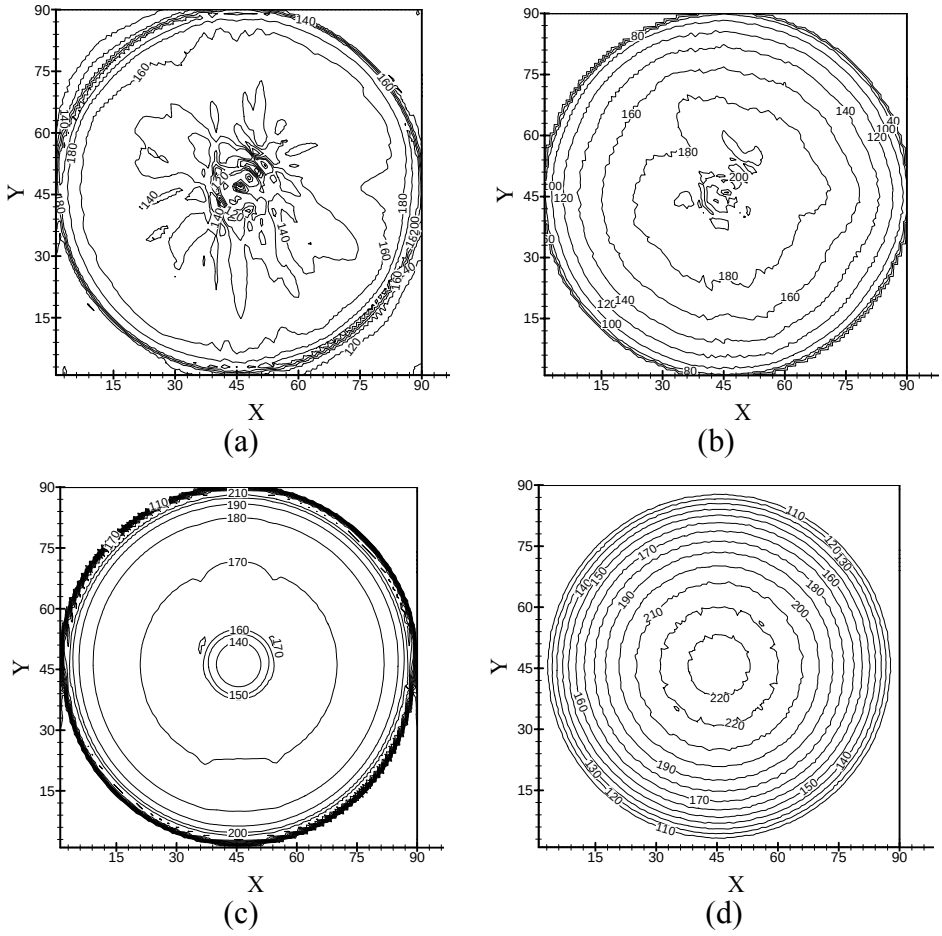

Figure. 7.7. (a-b). Reconstruction of contrast field using 90 views and 90 rays projection data using CBP and ART algorithms respectively over plane 1. (c-d) Reconstruction of refractive index fields using CBP and ART using same number of views and rays.

8. Crystal surface micromorphology imaging

Study of growth kinetics and mapping of micromorphology of habit faces of a growing crystal are indispensable to any comparison of theory with experiment. A few optical techniques used for this purpose are cathetometry, microscopic techniques, single- dual- and multiple-beam interferometry, holography, atomic force microscopy, and synchrotron based imaging. In this chapter, the results of online and *in situ* imaging of the solution refractive index (hence concentration) during growth and the surface microstructure developing over (100) and (101) habit faces of the KDP crystal are reported. The technique employed is two-beam interferometry in the Michelson geometry.

8.1. Measurement of solution refractive index using Michelson interferometry

Michelson interferometry is used here for online and *in situ* quantitative measurements of the refractive index of the aqueous solution. For this purpose a prismatic (or pyramidal) face in the form of a plate is hung inside the crystallizer and a laser beam is incident normal to it. The beam reflected from the crystal face is made to interfere with a beam reflected from a mirror placed in air. The crystal plate and the reference mirror constitute the two mirrors of the Michelson interferometer; and the resulting interference pattern consists of *Hadinger fringes* (Figure 8.1). Since the reflectivity of the crystal-solution interface is very feeble, a mirror is glued with a transparent optical adhesive at the back of the crystal plate (Figure 8.2) to increase the intensity of the reflected beam. This helps in improving the contrast of the interference fringes.

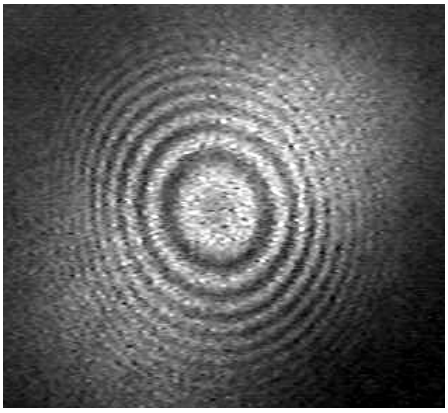

Figure 8.1. Haidinger fringe pattern obtained in Michelson interferometry.

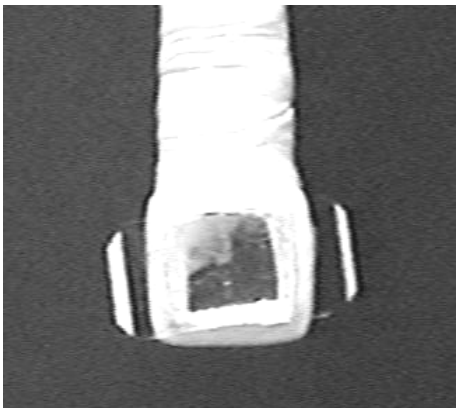

Figure 8.2. Mirror glued behind crystal plate to increase the intensity of the reflected beam.

When the temperature of the KDP solution is changed, it results in a change of the concentration of the solution. The refractive index of the KDP solution is a stronger function of the concentration as compared to thermal changes. Thus it is justifiable to assume that the concentration changes are proportional to the refractive index changes arising from the slow cooling of the solution in the whole temperature range. Since the refractive index of the solution affects the phase of the beam traversing through it, a changing refractive index manifests itself in a changing Haidinger fringe pattern.

In order to demonstrate the potential of the Michelson interferometer to monitor instantaneous changes in the refractive index, the temperature of the solution is first increased by 0.1ºC from its saturation value, followed by a corresponding reduction. When the temperature is increased the Haidinger fringes are observed to move inwards. Figures 8.3(a-d) are the interferograms showing successive stages of the movement of one Hadinger fringe from the field of view. On increasing the temperature by 0.1ºC a total of 8 fringes are observed to cross the field of view. The time taken for the movement of 8 fringes was 20 seconds thus representing the capability of the technique in recording instantaneous fractional changes in the solution concentration. The sensitivity of the refractive index measurement is estimated as follows: On heating the solution by 0.1ºC, 8 fringes cross the field of view. Therefore, the optical path difference is

$$8 \times \lambda = 2 \times L \times \Delta n$$

where L = distance of the crystal face from the entrance window of the chamber (0.1 m);

Δn = change in the solution refractive index;

λ = wavelength of the He-Ne laser.

Substituting the values in the above equation

$$\Delta n = \frac{8 \times 6328 \times 10^{-10}}{2 \times 10 \times 10^{-2}} = 2.5312 \times 10^{-5}$$ for 8 fringes crossing the field of view.

Therefore, Δn / fringe shift = 3.164×10^{-6}.

As shown in Figures 8.3(a-d), the fractional changes in the solution concentration are revealed by the interferometer. This experimental capability, when combined with suitable image processing operations, can further enhance the sensitivity of the measurements by about an order of magnitude. Thus refractive index changes of the order of $10^{-7} - 10^{-8}$ can be detected using Michelson interferometry, demonstrating the extreme sensitivity

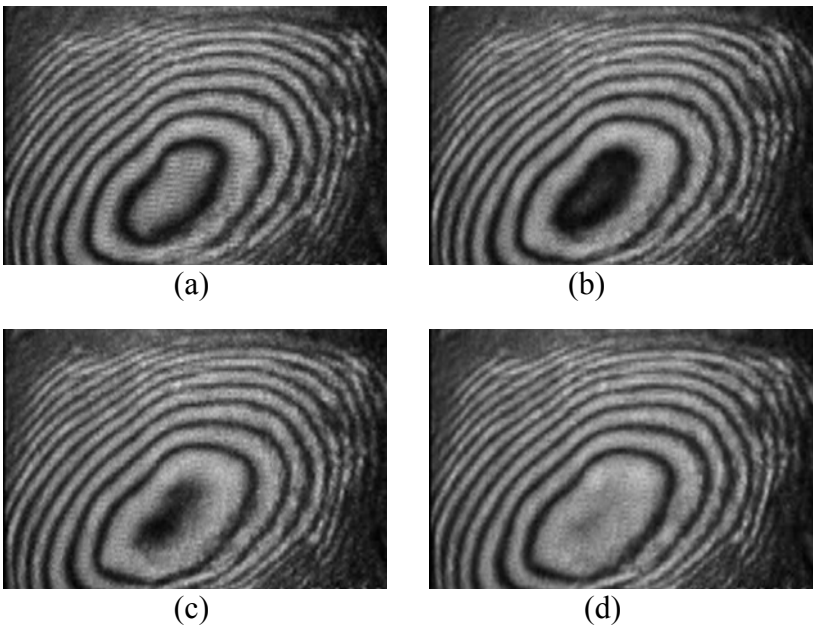

Figure 8.3(a-d). Time sequence of Michelson interferograms showing fractional movement (inwards) of a fringe during heating of the KDP solution.

of this technique for measurements during the crystal growth process. Figures 8.4(a-d) show the Michelson interferograms when the temperature of the solution is decreased by 0.1ºC from its saturation point. Here the fringes are found to move outward. When the solution is maintained at saturation point, no change in the Michelson interferograms is observed (Figures 8.5(a-d). Here the interferograms are identical to each other, indicating that the solution refractive index and hence the concentration is constant.

8.2. Crystal growth kinetics

In order to perform *in situ* and online mapping of the microstructure of the growing crystal face, the Michelson interferometer is used. The optical arrangement of a Michelson interferometer for such studies is described in Section 3. The basic principle of the Michelson interferometry and the quantitative data analysis procedure has been explained in Section 4. With every change in the crystal thickness by $\lambda/2n$, one fringe shift takes place. Here λ is the wavelength of the laser used, and n is the refractive index of the solution. Quantitative analysis of the interferogram yields the growth-kinetic parameters such as normal growth rate R, slope of the dislocation growth hillock p, and tangential growth velocity V of the steps.

A plate of 1 mm thickness is cut parallel to either a prismatic or a pyramidal face of the KDP crystal, and is subsequently polished to improve

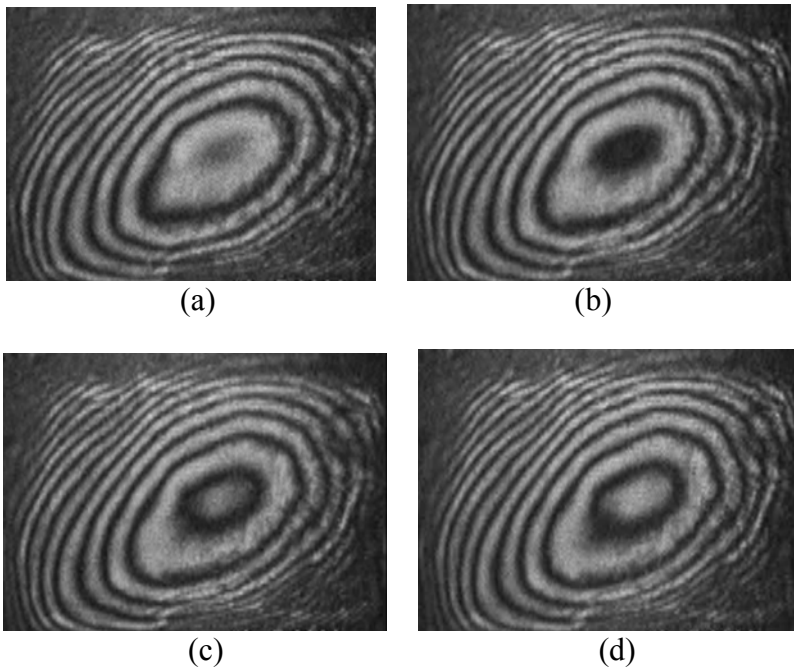

Figure 8.4(a-d). Time sequence of Michelson interferograms showing fractional movement (outwards) of a fringe during cooling of the KDP solution.

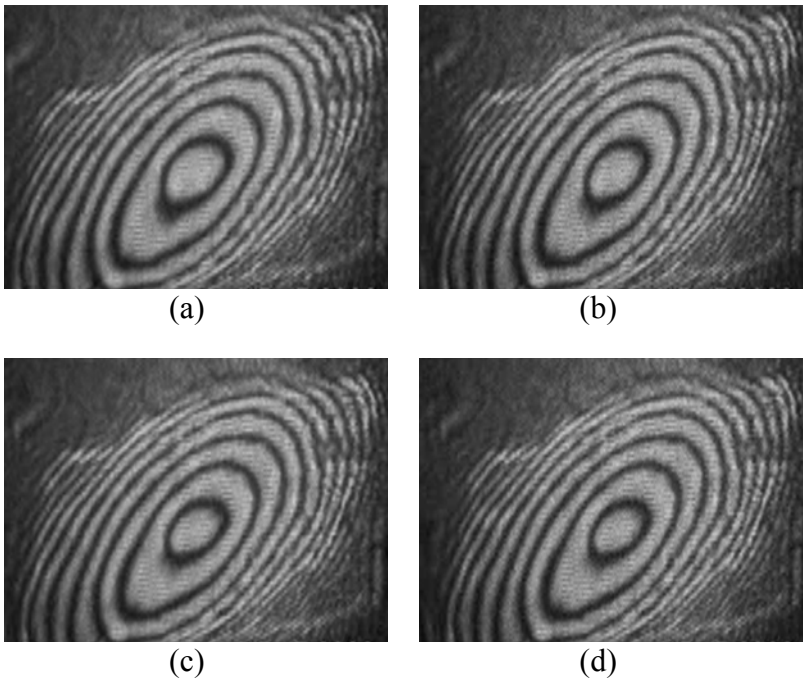

Figure 8.5(a-d). Time sequence of Michelson interferograms recorded during the saturation stage of the KDP solution. The interferograms are identical, though they are recorded at different instants of time.

its reflectivity. The polished plate is hung inside a growth chamber so that one of the interfering beams is reflected from the surface of the growing crystal plate. This reflected beam is made to interfere with a reference beam to obtain an interference pattern. The fringes carry surface-microtopographic details of the growing face. Since interferometry through solution requires reflection of the light beam from the solution-crystal interface of extremely low reflectivity (~ 0.02), it necessitates matching of the intensity of the interfering beams to get a reasonable contrast in the interference pattern. For this purpose a neutral density filter is used in the reference arm of the interferometer. Even after elaborate precautions, the procedure to obtain a stable and good contrast interference pattern is a difficult and tedious task, except when the difference in refractive index between the solution and the crystal is sufficiently large to enable higher reflectivity. A few crystal plates cut and polished from a KDP crystal are shown in Figures 8.6(a-d).

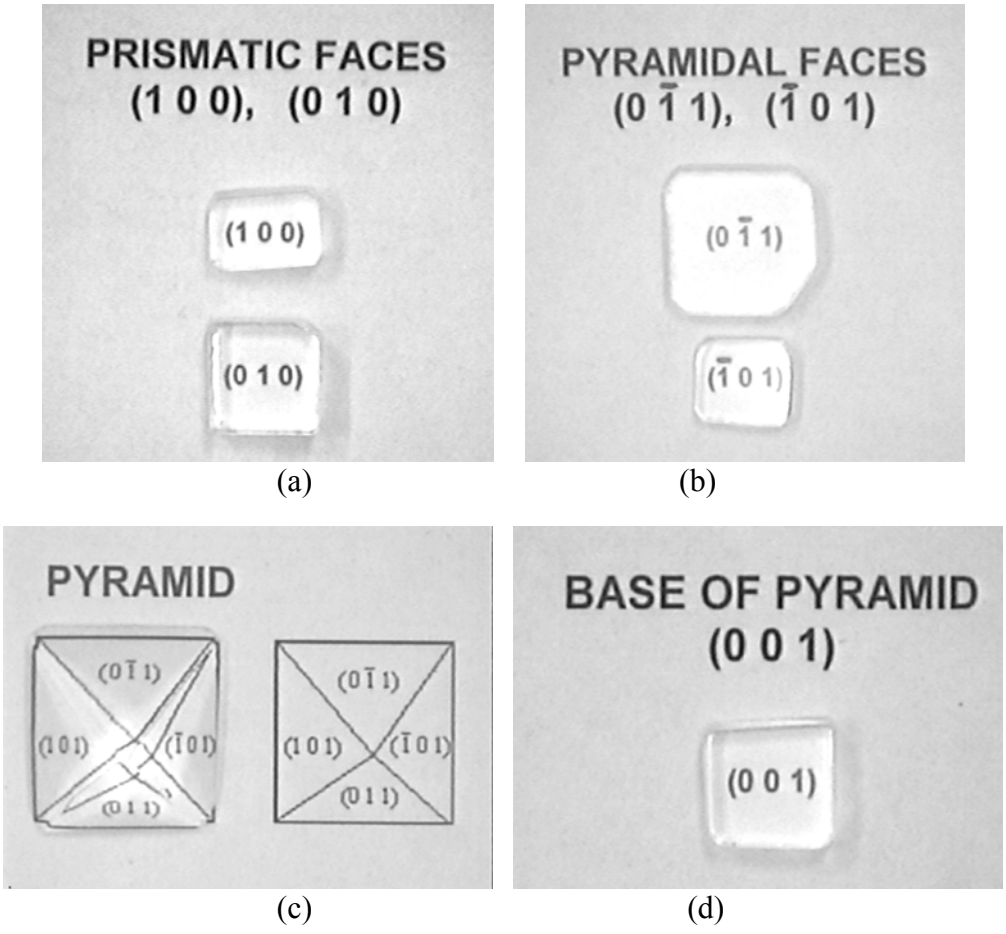

Figure 8.6(a-d). Cut and polished plates from prismatic and pyramidal facets of KDP crystal.

8.2.1. Surface micro-morphology of the prismatic face of KDP crystal

The growth of the (100) prismatic face of the crystal was investigated at a temperature of 51°C. In order to perform surface micromorphology studies, the interferometer is first aligned in the finite-fringe setting. It is done by creating a wedge between the interfering wavefronts. Figure 8.7 shows the wedge interferogram. In the initial stages of growth the (100) face reveals a rough surface, as seen in the irregular fringe pattern (Figure 8.8a). It is indicative of the morphological instability of the growing crystal face. The solution was subjected to slow cooling for 10 hours at a rate of 0.01°C/h to increase the solution supersaturation. With the increase of supersaturation the surface regenerates itself to become smooth, which manifests itself in parallel and equi-spaced fringes (Figure 8.8b).

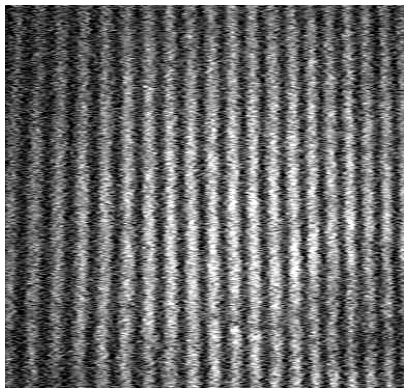

Figure 8.7. Finite fringe interferogram obtained by creating a wedge between the two interfering wavefronts of the Michelson interferometer. The interferograms shown in Figures 8.8(a-b) are captured in this setting.

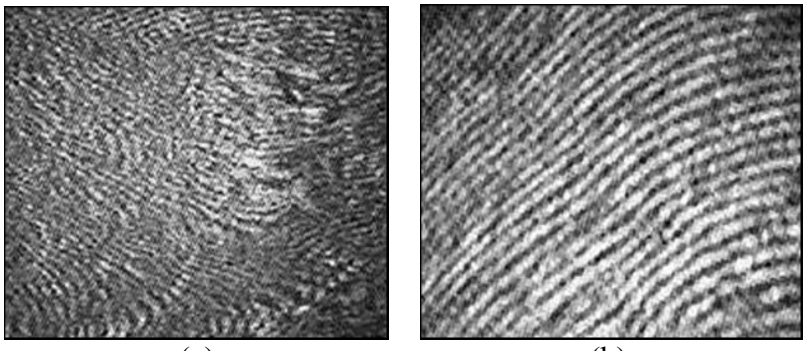

(a) (b)

Figure 8.8. (a) Michelson interferograms showing irregular surface relief in the initial stages of growth, and (b) a smooth crystal face after a few hours of growth.

The next step in imaging the micro-morphological features is to realign the Michelson interferometer to obtain the infinite-fringe interferogram. This is achieved by separating the wedge fringes to infinity by carefully eliminating the wedge angle between the interfering wavefronts. In the case of an atomically flat surface devoid of microstructural features, the infinite-fringe interferogram consists of either a bright or dark fringe in the field of view. However, under practical conditions a crystal face is always covered with micro-morphological features. This manifests itself in interference fringes of different shapes and thickness that are indicative of the mechanism by which the face is growing.

Figures 8.9(a-d) are four such interferograms recorded at 15-minute intervals. The positions of dislocation on the surface have been marked by a "+". The concentric fringes around the point of dislocation are due to the growth hillock originating from a dislocation, implying that the prismatic face is growing by the spiral-growth mechanism. The normal growth rate R, the slope of the dislocation hillock p, and the tangential step velocity V are computed from the above interferograms as described below.

The difference of heights between two points on adjacent fringes in Figure 8.9(a) is

$$d = \frac{\lambda}{2n}$$
$$= \frac{0.6328 \times 10^{-3}}{2 \times 1.36289} \text{ mm}$$

Here λ is the wavelength of the *He-Ne* laser and n is the refractive index of the KDP solution at 50°C. The relationship used here to calculate the refractive index of the KDP solution is

$$n = 1.3486 + (0.0002858 \times T)$$

In 60 minutes, four fringes were observed to cross the point of observation in the interferogram. Therefore the normal average growth rate of the face is

$$R = \frac{\Delta h}{\Delta t} = \frac{N \times d}{\Delta t}$$
$$= \frac{N \times \lambda}{2 \times n \times \Delta t}$$
$$= \frac{4 \times 0.6328 \times 10^{-3}}{2 \times 1.36289 \times 60} = 1.5477 \times 10^{-5} \ mm/\min$$

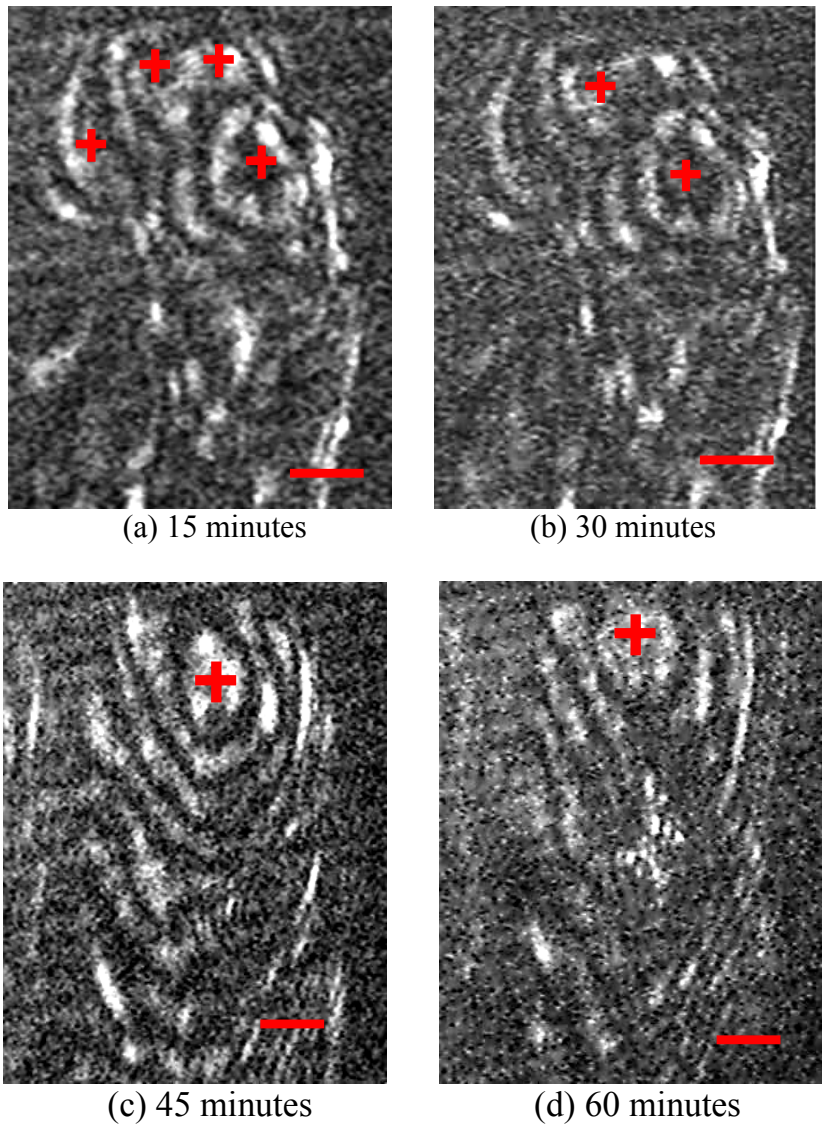

(a) 15 minutes (b) 30 minutes

(c) 45 minutes (d) 60 minutes

Figure 8.9(a-d). Michelson interference fringes showing the micro-morphological features over a growing prismatic face of KDP crystal. The locations of the dislocations have been marked by a cross. A few concentric fringes are seen around the point of dislocation. Marker line on the figure represents 1 mm.

The physical distance between the two points lying on adjacent fringe in Figure 8.9(a) is 0.5 mm. Therefore the slope of the hillock is

$$p = \tan\theta = \frac{d}{D}$$

$$= \frac{0.6328\times10^{-3}}{2\times1.36289\times0.5} = 4.643\times10^{-4}$$

The normal growth rate and the slope of the dislocation hillock are related to the tangential step velocity V as

$$R = p \times V$$

Thus the tangential step velocity is

$$V = R / p$$
$$= \frac{1.5477 \times 10^{-5}}{4.643 \times 10^{-4}} = 3.3334 \times 10^{-2}\ mm/\min$$

8.2.2. Competition between dislocation hillocks

The interferogram in Figure 8.9(a) has four dislocation hillocks (marked by dots). Out of these, the one at the lowest point is the strongest and active, while the other three are relatively weak in character. This is inferred from the shape and broadness of the fringes surrounding the location of the hillocks. This is confirmed by subsequent interferograms where the weak dislocations are found to merge with the active one. After one hour of growth the face is covered by only one dislocation. Such a competition between dislocations is a favorable growth feature as it suggests that the face is growing at uniform rate in the lateral direction. Also a face with a lesser number of dislocations is smoother.

8.2.3. Surface micro-morphology of a pyramidal face of KDP crystal

Figures 8.10(a-f) are Michelson interferograms of surface micro-morphological features developing over a pyramidal face of a growing KDP crystal. They have been recorded in the infinite setting mode and at every 30 minutes interval from the beginning of the experiment. A slow cooling of 0.01°C/h was applied to increase the supersaturation to allow the crystal to grow. It was observed that the hillock morphology changed with increase of supersaturation. Initially it covered only about 40% of the face and the hillock was irregular in shape. The length of the hillock at the base was double its width. This is inferred from the major and minor axis of the elliptical concentric fringes in Figure 8.10a. This changed with supersaturation, as is visible in the subsequently recorded interferogram (Figure 8.10b). It has 16 semicircular concentric fringes that cover 90% of the face. The semicircular shape of the fringes is due to the reason that the laser beam maps only one side of the hillock. The elliptical nature of fringes has changed to circular, implying that the hillock shape is becoming regular. This is a desired growth kinetic feature as the hillock is gradually occupying

the entire face, and the regularity of the shape suggests that the growth rate in lateral directions is uniform. The subsequent interferograms in Figures 8.10(c-f)

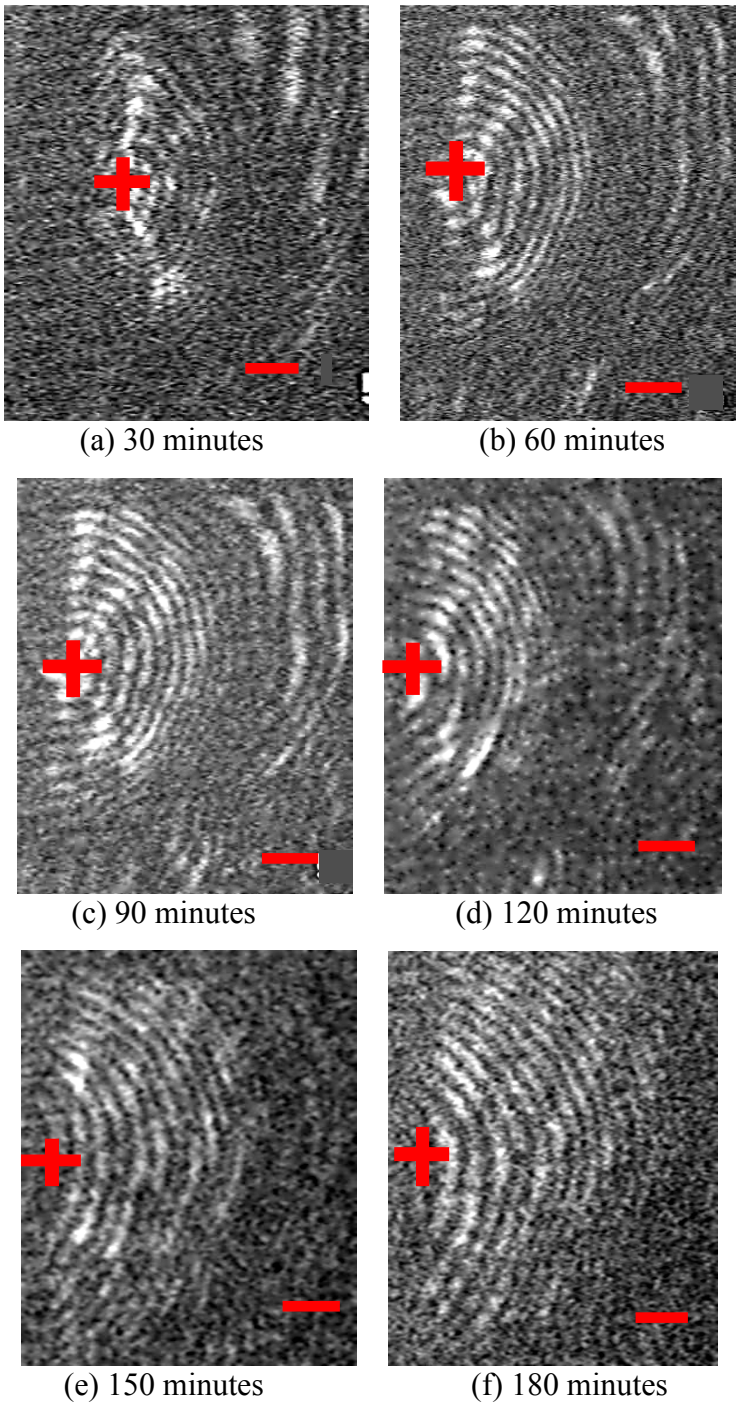

(a) 30 minutes (b) 60 minutes

(c) 90 minutes (d) 120 minutes

(e) 150 minutes (f) 180 minutes

Figure 8.10 (a-f). Michelson interference fringes showing the change in the micromorphology of the growth hillock with time. The location of the dislocation has been marked by a cross. The marker line on the figures represents 1 mm.

show that the hillock covers the entire face and the slope of the hillock is uniform in all directions.

The normal growth rate R, the slope of the hillock, and the effective step velocity for the interferograms shown in Figures 8.10(f) are computed below. The difference of heights between two points on adjacent fringes in Figure 8.10(f) is

$$d = \frac{\lambda}{2n}$$
$$= \frac{0.6328 \times 10^{-3}}{2 \times 1.36289} \text{ mm}$$

Here λ is the wavelength of the *He-Ne* laser and n is the refractive index of the KDP solution at 50°C. Eighteen fringes are observed to cross the point of observation in 3 hours. Therefore the normal average growth rate of face is

$$R = \frac{N \times \lambda}{2 \times n \times \Delta t}$$
$$= \frac{18 \times 0.6328 \times 10^{-3}}{2 \times 1.36289 \times 180} = 2.32 \times 10^{-5} \text{ mm/min}$$

The physical distance between the two points lying on adjacent fringes in Figure 8.10(f) is 0.25 mm. Therefore, the slope of the hillock is

$$p = \tan\theta = \frac{d}{D}$$
$$= \frac{0.6328 \times 10^{-3}}{2 \times 1.36289 \times 0.25} = 9.28 \times 10^{-4}$$

The normal growth rate and the slope of the dislocation hillock are related to the tangential step velocity V as follows

$$R = p \times V$$

Thus the tangential step velocity must be

$$V = R / p$$
$$= \frac{2.32 \times 10^{-5}}{9.28 \times 10^{-4}} = 2.5 \times 10^{-2} \text{ mm/min}$$

Figures 8.11(a-b) show the prismatic seed plate and the plate grown over it during the Michelson studies. Similarly Figures 8.11(c-d) show the pyramidal face grown during the experiment.

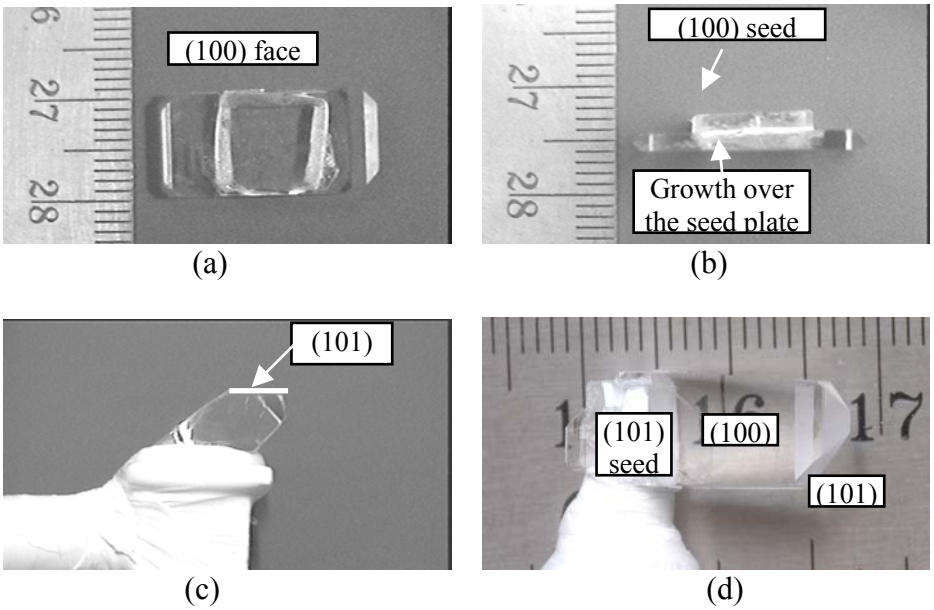

Figure 8.11. (a-b). Prismatic seed plate and the growth over it during the microstructure mapping experiment; (c-d) Pyramidal face and the crystal grown during the surface structure studies using Michelson interferometry.

8.3. Closure

Michelson interferometry has been used to make measurements of the refractive index variations of the KDP solution with a resolution of 10^{-7}. Growth kinetics of the prismatic and pyramidal faces of KDP crystal has been measured. At moderate supersaturation, the faces are found to grow by screw dislocation mediated spiral growth mechanism (Verma, 2008A). The growth hillocks are imaged as concentric fringes of equal thickness.

9. Conclusions and scope for future work

9.1. Conclusions

The present review is concerned with the study of the crystal growth process using optical diagnostics. We have imaged convection, concentration and surface features during the growth of KDP (Potassium Dihydrogen Phosphate) crystal. The relationships of the process parameters, such as cooling rates and convection modes, to the growth rate, crystal quality, and growth mechanism are explored. Shadowgraphy is used for mapping the convective field, Mach-Zehnder interferometry for the concentration field, computerized tomography for obtaining three-dimensional information, and Michelson interferometry for surface features. The main conclusions arrived at in this work are summarized below.

9.1.1. Shadowgraph imaging of KDP crystal growth

The laser shadowgraph technique was configured for mapping free convection phenomena during crystal growth in different geometries. It was found to be a highly sensitive imaging tool for mapping minute changes in the refractive index field, which appear as high-contrast features in the images. The evolution of the averaged refractive index (concentration) field along the line-of-sight was obtained by solving a linearized governing equation of the shadowgraph process at different stages of growth. Results show the following overall trends:

i) In the initial stages of growth, the crystal dimension is small and the growth chamber has isolated regions of high and low concentration that do not mix with each other. With the growth of the crystal, free convection is established. It helps in breaking regional non-uniformity in the concentration field. Once a plume is established, concentration gradients are higher in the vicinity of the crystal as compared to in the bulk of the chamber. This is favorable for fast growth kinetics because high gradients signify high mass fluxes of solute towards the crystal faces. Plume formation also explains preferential growth of one face with respect to the other.

ii) In order to estimate higher-order optical effects such as scattering and interference, the path of the optical rays was traced through the growth chamber, and the deflections in the x- and y-planes (normal to the propagation direction of the optical ray) were quantified. Various stages of the experiment were considered. Ray deflections were found to be consistently small in all experiments, suggesting that higher-order effects are not relevant to the present work.

iii) There is a tradeoff between growth rate and the quality of the crystal. Only at optimum values of process parameters, such as cooling rates and convection strength, are best results obtained. The strength of free convection is quantified in terms of Grashof number. Beyond a certain supercooling, the Grashof number rises exponentially, and the crystal quality becomes sensitive to temporal fluctuations in the concentration field. Inclusions and striations get incorporated beyond this stage of growth. The critical Grashof (Rayleigh) number in the present set of experiments falls in the range of 60 to 85 (3×10^4).

iv) Time-lapsed shadowgraph images are used to quantify the growth rate as a function of supercooling. Based on growth rate results and convection imaging, a cooling rate in the range 0.02 - 0.03°C/h is found to be optimum for growing crystals with high growth rate and good quality.

v) The nature of the free-convection plumes in the shadowgraph images is correlated with the growth mechanism. Signatures of two-dimensional nucleation and birth and spread mechanism have been observed.

9.1.2. Mach-Zehnder interferograms

A Mach-Zehnder interferometer has been used for imaging the concentration field during KDP growth under free and forced convection conditions. The design of the interferometer is such that it is immune to frequent misalignments due to external vibrations and ambient temperature fluctuations. Infinite-fringe M-Z interferometry is demonstrated to be a highly sensitive diagnostic tool to measure concentration gradients inside the growth chamber. The following results were obtained and conclusions drawn:

i) Imaging the concentration field during growth in the top-hanging geometry was carried out for various forced-convection conditions. These were achieved by varying the rotation rate and the time periods of the acceleration and deceleration phases of an ACRT (accelerated crucible rotation technique) unit. Results indicate that a uniform concentration is achieved only for selected values of these parameters. These correspond to an average Reynolds number of around 1627 for top hanging geometry and around 7100 for platform growth.
ii) Solution stratification is a limiting factor for growth under free convection at high cooling rates and for long durations.
iii) The thickness of the solutal boundary layer (SBL), which is the region of large mass fluxes of solute towards the crystal, has been quantified. It lies in the range 150-300 μm. Thinner boundary layer are associated with higher concentration gradients, higher mass fluxes and hence, faster growth kinetics.

9.1.3. Tomographic reconstruction of shadowgraph data

Implementation of the tomographic reconstruction of shadowgraph projection data in an engineering process is reported. Two different algorithms, namely *convolution back projection* (CBP) and *algebraic reconstruction technique* (ART) have been employed for the purpose. Convective features, as seen in the shadowgraph images, have been reconstructed over three horizontal surfaces at different heights above the crystal. The following inferences about the three-dimensional character of the convection and its stability have been drawn:

i) The contour plots of light intensity show that the rising plumes spread horizontally in the shape of a dumbbell. The shape of the plume has bearing on the stability of convection and hence on the quality of the growing crystal.

ii) The gradients in the field parameter (namely concentration) are high just above the crystal. In the bulk of the solution they are smaller and the changes are gradual. This is because, under free convection, the growth process is restricted to a boundary layer adjacent to the crystal.

iii) The effect of the number of views available for reconstruction has been studied using projection data consisting of 18 and 90 views respectively. Results indicate that the ART algorithm recovers the broad features present in the shadowgraph images with the 18-view data set. The finer features appear when a data set of 90 views is used. On the other hand, CBP generates several spurious features with the 18-view data set. These reduce when 90 views are used.

iv) The influence of the choice of the dependent variable of the projection data is additionally studied. Three different variables, namely intensity values, contrast $(I_o-I_s)/I_s$, and refractive index corresponding to the shadowgraph projections are used. The refractive index distribution over a cross-section does not reveal meaningful reconstruction, as the total variation of n in the growth chamber is extremely small ($\sim 10^{-5}$ - 10^{-6}).

v) Several cross-checks have been applied to verify the correctness of the obtained reconstruction. Error estimates based on a pair of reconstructed solutions show the deviations to be small. For the 90-view reconstruction, errors are found to be uniformly negligible.

9.1.4. Surface microtopography

Michelson interferometry is a highly sensitive tool for measuring solution concentration changes due to thermal fluctuations. The double Mach-Zehnder interferometer enables simultaneous studies of the flow features as well as surface kinetics. Benchmark results obtained using the interferometer show its potential. In addition:

i) Refractive index variations as small as $\Delta n \sim 10^{-7}$ in the solution could be measured.

ii) Screw-dislocation-generated growth hillocks were imaged using the interferometer. Growth hillocks appear as concentric fringes of equal thickness.

9.2. Scope for future work

The work reported in the present review can be extended in the following directions:

i) Joint imaging of concentration and temperature in the aqueous solution.
ii) Whole field measurements of the refractive index field as an improvement over partial-field data.
iii) Real-time holographic measurements to capture three dimensional fields that change with time.
iv) Extension of the approach adopted to magnetic resonance imaging of the crystal growth process.
v) X-ray topographic imaging of a crystal grown under different convection conditions to understand the history of defect-generation and subsequent propagation inside the crystal.

Acknowledgements

SV is grateful to Dr. P.K. Gupta, Prof. Prabhat Munshi, Dr. P.J. Shlichta and Dr. V.K. Wadhawan for advise, encouragement and continuous support. KM gratefully acknowledges association with Professors Prabhat Munshi and P.K. Panigrahi as well as his previous graduate students, Debasish Mishra, Sunil Punjabi and Atul Srivastava.

Nomenclature

$T_{supersat}$	Supersaturated (or growth) temperature, ^{o}C
T_{sat}	Saturation temperature, ^{o}C
$\Delta T = T_{supersat} - T_{sat}$	Supercooling, ^{o}C
$C_{supersat}$	Supersaturated concentration, ^{o}C
C_{sat}	Saturated concentration
$\Delta C = C_{supersat} - C_{sat}$	Driving force for crystal growth (The concentration is expressed in units of x gm of solute per 1000 gm of solvent)
$\sigma = \frac{C_{supersat} - C_{sat}}{C_{sat}}$	Relative supersaturation
NLO	Non-Linear Optics
KDP	Potassium Dihydrogen Phosphate
I_s	Intensity on screen in the presence of disturbance (on a scale of 0-255)
I_o	Intensity on screen in the absence of disturbance

SD	Source to Detector distance
R_c	Fourier cutoff frequency (spatial)
$W(R)$	Filter function
W	Value of weight function
n	Refractive index of the solution
λ	Wavelength of the laser light, nm
t	Thickness of film, μm
θ	Angle of incidence
r	Radius of the cluster, mm
ΔG_s	Free energy change per unit surface area, J/m^2
ΔG_v	Free energy change per unit volume, J/m^2
$\theta_{sol}, \theta_{qtz}, \theta_{air}$	Angle of incidence of the light at the quartz window, the angle of refraction of the light ray into the quartz window, the angle of refraction of the light ray in the air, respectively.
$n_{sol}, n_{qtz}, n_{air}$	Refractive index of the KDP solution, the refractive index of the quartz window, and the refractive index of the quartz window
$Gr = \rho \frac{\partial \rho}{\partial C} \frac{(C_o - C_i)}{\mu^2} g L^3$	Grashof number
$\mathrm{Re} = \frac{\omega L^2}{\nu}$	Reynolds number
$Sc = \frac{\mu}{\rho D}$	Schmidt number
ρ	Density of the solution at a certain temperature in kg/m^3,
$\partial\rho/\partial C$	Gradient of density with concentration
C_o	Bulk solute concentration in mole/m^3,
C_i	Interface concentration near to the crystal
g	Acceleration due to gravity in m/s^2
L	Characteristic length in meter
μ	Dynamic viscosity in kg/(m.s)
ν	Kinematics viscosity in m^2/s
ω	Rotation velocity in rad / s,
D	Diffusion coefficient of solute in the solution in m^2/s

k	Gladstone-Dale constant
ΔC_E	Concentration change per fringe shift
$R = \frac{\Delta h}{\Delta t}$	Normal growth rate, m/s
Δh	Thickness normal to the crystal face in time Δt
p	Slope of the dislocation hillock
V	Tangential step velocity, m/s, J/m^2

References

1. [Adrian, 1983] R. J. Adrian, Laser velocimetry, in: "Fluid Mechanics Measurements", R. J. Goldstein (Ed.), (Hemisphere, Washington D.C., 1983), pp. 177-240.
2. [Adrian, 1991] R. J. Adrian, Particle-imaging techniques for experimental fluid mechanics, Annu. Rev. Fluid Mech., 23 (1991) 261-304.
3. [Bedarida, 1983] F. Bedarida, L. Zefiro, P. Boccacci and C. Pontiggia, Reconstruction by multidirectional holographic interferometry of the concentration field in a supersaturated solution near a growing $NaClO_3$ crystal, J. Cryst. Growth, 61 (1983) 641-644.
4. [Bedarida, 1986] F. Bedarida, Developments of holographic interferometry applied to crystal growth from solution, J. Cryst. Growth, 79 (1986) 43-49.
5. [Braslavsky, 1998B] I. Braslavsky and S.G. Lipson, Interferometric tomography measurement of the temperature field in the vicinity of a dendritic crystal growing from a supercooled melt, Trans. of optical methods and data processing in heat and fluid flow, IMeChE, London, (1998) 423-432.
6. [Born, 1980] M. Born and E. Wolf, “Principles of Optics”, Pergamon Press, Oxford, U.K., 1980, 808 pp.
7. [Bunn, 1949] C. W. Bunn, Crystal growth from solution. II. Concentration gradients and the rates of growth of crystals, Discuss. Faraday Society, 5 (1949) 132-144.
8. [Burton, 1951] W. K. Burton, N. Cabrera, and F. C. Frank, Growth of crystals and the equilibrium structure of their surfaces, Phil. Trans. Roy. Soc. London, A 243 (1951) 299-358.
9. [Censor, 1983] Y. Censor, Finite series-expansion reconstruction methods, Proc. IEEE, 71 (3) (1983) 409-419.
10. [Cha, 1981] S. Cha and C. M. Vest, Tomographic reconstruction of strongly refracting fields and its application to interferometric measurement of boundary layers, Appl. Opt., 20 (16) (1981) 2787-2794.
11. [Cha, 1990] S. S. Cha and H. Sun, Tomography for reconstructing continuous fields from ill-posed multidirectional interferometric data, Appl. Opt., 29 (1990) 251-258.

12. [Chen, 1977] P. S. Chen, Convection Irregularities during Solution Growth and Relation to Crystal-Defect Formation, Ph.D. Thesis, Univ. of Southern California, Los Angeles, CA, USA, (1977), 213 pp.
13. [Chen, P, 1979A] P. S. Chen, W. R. Wilcox and P. J. Shlichta, Free convection about a rectangular prismatic crystal growing from a solution, Int. J. Heat Mass Transfer, 22 (1979) 1669-79.
14. [Chen, P, 1979B] P. S. Chen, P. J. Shlichta, W. R. Wilcox and R. A. Lefever, Convection phenomena during the growth of sodium chlorate crystals from solution, J. Cryst. Growth, 47 (1979) 43-60.
15. [Chen, W, 2002] W. C. Chen, D. D. Liu, W. Y. Ma, A. Y. Xie and J. Fang, The determination of solute distribution during growth and dissolution of NaClO3 crystals: the growth of large crystals, J. Cryst. Growth, 236 (2002) 413-419.
16. [Chernov, 1984] A.A. Chernov, L.N. Rashkovich, I.L. Smol'skii, Yu. G. Kuznetsov, A.A. Mkrtchyan and A.I. Malkin, Growth of KDP-group crystals from solution, in "Growth of Crystals", 12 (1984) 43-91, E. I. Givargizov, S.A. Grinberg (Eds.), (Consultants Bureau, New York).
17. [Chernov, 1986] A.A. Chernnov, L.N. Rashkovich and A.A. Mkrtchan, Solution growth kinetics and mechanism: Prismatic face of ADP, J. Cryst. Growth, 74 (1986) 101-112.
18. [Chernov, 1988] A.A. Chernnov and A.I. Malkin, Regular and irregular growth and dissolution of (101) ADP faces under low supersaturations, J. Cryst. Growth, 92 (1988) 432-444.
19. [Duan, 2001] L. Duan and J. Z. Shu, The convection during NaClO3 crystal growth observed by the phase shift interferometer, J. Cryst. Growth, 223 (2001) 181-188.
20. [Durst, 1981] Franz Durst, A. Melling and J. H. Whitelaw, "Principles and Practice of Laser Doppler Anemometry", 2nd ed., (Academic press, New York, 1981).
21. [Faris, 1986] G.W. Faris and R.L. Byer, Quantitative optical tomographic imaging of a supersonic jet, Opt. Lett., 11 (7) (1986) 413-415.
22. [Faris, 1988] G.W. Faris and R.L. Byer, Three-dimensional beam-deflection optical tomography of a supersonic jet, Appl. Opt., 27 (24) (1988) 5202-5212.
23. [Goldstein, 1996] Richard J. Goldstein and T. H. Kuehn, Optical Systems for flow measurement: Shadowgraph, schlieren, and interferometric techniques, in "Fluid Mechanics Measurements", R. J. Goldstein (Ed.), (Taylor & Francis, New York, 1996), pp. 451-508.
24. [Hariharan, 1986] P. Hariharan, "Optical Holography: Principles, Techniques and Applications", (Cambridge University Press, Cambridge, 1986), 319 pp.
25. [Hariharan, 2002] P. Hariharan, "Basics of Holography", (Cambridge University Press, Cambridge, 2002), 161 pp.
26. [Herman, 1980] G. T. Herman, "Image Reconstruction from Projections: The Fundamentals of Computerized Tomography", (Academic Press, New York, 1980), 316 pp.
27. [Jain, 2001] A. K. Jain, "Fundamentals of Digital Image Processing" (Prentice-Hall of India, New Delhi, 2001) 569 pp.

28. [Gebhart, 1988] B. Gebhart, Y. Jaluria, R.L. Mahajan & B. Sammakia, "Buoyancy Induced Flows and Transport", (Hemisphere Publishing, New York, 1988) 971 pp.
29. [Kang, 2001] Q. Kang, L. Duan and W. R. Hu, Mass transfer process during the $NaClO_3$ crystal growth process, Int. J. Heat and Mass Transfer, 44 (2001) 3213-3222.
30. [Kim, 1998A] Y. K. Kim, B.R. Reddy, R.B. Lal, Laser and Mach-Zehnder interferometer for in-situ monitoring of crystal growth and concentration variation, SPIE 3479 (1998) 172-180.
31. [Kim, 1998B] Yong Kee Kim, J. D. Trolinger, B. R. Reddy and R. B. Lal, Refractive index measurements of fluids using common-path zeeman interferometry, J. Mod. Optics, 45 (8) (1998) 1637-1643.
32. [Lewitt, 1983] R. M. Lewitt, Reconstruction algorithms: Transform methods, Proc. IEEE, 71 (3) (1983) 390-408.
33. [Macovski, 1983] Albert Macovski, Physical problems of computerized tomography, Proc. IEEE, 71 (3) (1983) 373-378.
34. [Maiwa, 1990] K. Maiwa, K. Tsukamoto and I. Sunagawa, Activities of spiral growth hillocks on the (111) faces of barium nitrate crystals growing in an aqueous solution, J. Cryst. Growth, 102 (1990) 43-53.
35. [Mayinger, 1994] Franz Mayinger (Ed.), "Optical Measurements: Techniques and Applications", (Springer-Verlag, Berlin, 1994) 463 pp.
36. [Merzkirch, 1987] W. F. Merzkirch, "Flow Visualization", 2nd Edition, (Academic Press, New York, 1987), 260 pp.
37. [Mishra, 1999A] Debasish Mishra, K. Muralidhar and P. Munshi, Interferometric study of Rayleigh-Benard convection using tomography with limited projection data, Numerical Heat Transfer, 12 (1999) 117-136.
38. [Mishra, 1999B] Debasish Mishra, K. Muralidhar and P. Munshi, A robust MART algorithm for tomographic applications, Numerical Heat Transfer, Part-B, 35 (1999) 465-506.
39. [Mishra, 2004] Debasish Mishra, Jon P. Longtin, Raman P. Singh and Vishwanath Prasad, Performance evaluation of iterative tomography algorithms for incomplete projection data, Appl. Opt., 43 (7) (2004) 1522-1532.
40. [Mullin, 2001] J.W. Mullin, "Crystallization", 4th ed., (Butterworth-Heinemann, Oxford, 2001).
41. [Muralidhar, 2001] K. Muralidhar, Temperature field measurement in buoyancy-driven flows using interferometric tomography, Annual Reviews of Heat Transfer, 12 (2001) 265-375.
42. [Nakadate, 1990] S. Nakadate and I. Yamaguchi, Japanese patent describing the technique of real-time phase shifting interferometry, Patent # H02-287107 (1990).
43. [Natterer, 2001] F. Natterer, "The Mathematics of Computerized Tomography", (Philadelphia, PA, SIAM 2001), 222 pp.
44. [Onuma, 1988] K. Onuma, K. Tuskamoto and I. Sunagawa, Role of buoyancy driven convection in aqueous soultion; A case study of $Ba(NO_3)_2$ crystal, J. Cryst. Growth, 89 (1988) 177-188.

45. [Onuma, 1989A] K. Onuma, K. Tuskamoto and I. Sunagawa, Measurement of surface supersaturations around a growing K-alum crystal in aqueous solution, J. Cryst. Growth, 98 (3) (1989) 377-383.
46. [Onuma, 1989B] K. Onuma, K. Tuskamoto and I. Sunagawa, Effect of buoyancy-driven convection upon the surface microtopographs of $Ba(NO_3)_2$ & CdI_2 Crystals, J. Cryst. Growth, 98 (3) (1989) 384-390.
47. [Onuma, 1990] K. Onuma, K. Tuskamoto and I. Sunagawa, Growth kinetics of K-alum crystals in relation to the surface supersaturations, J. Cryst. Growth, 100 (1990) 125-132.
48. [Onuma, 1991] K. Onuma, K. Tuskamoto and I. Sunagawa, Dissolution kinetics of K-alum crystals as judged from the measurements of surface undersaturations, J. Cryst. Growth, 110 (1991) 724-732.
49. [Onuma, 1993] K. Onuma, K. Tsukamoto and S. Nakadate, Application of real time phase shift interferometer to the measurement of concentration field, J. Cryst. Growth, 129 (1993) 706-718.
50. [Onuma, 1994] K. Onuma, T. Kameyama and K. Tsukamoto, In-situ study of surface phenomena by real time phase shift interferometry, JCG, 137 (1994) 610-622.
51. [Raffel, 1998] M. Raffel, C. Willert and J. Kompenhans, "Particle Image Velocimetry: A Practical Guide", (Springer Verlag, Berlin Heidelberg, 1998), 253 pp.
52. [Rangayyan, 1985] R. Rangayyan, A. P. Dhawan and R. Gordon, Algorithms for limited-view computed tomography: An annotated bibliography and a challenge, Appl. Opt., 24 (23) (1985) 4000-4012.
53. [Rashkovich, 1982] L. N. Rashkovich, V. T. Leshchenko and N. M. Sadykov, Growth kinetics of TGS, Sov. Phys. Crystallogr., 27 (2) (1982) 580-585.
54. [Rashkovich, 1985] L. N. Rashkovich, A. A. Mkrtchan and A. A. Chernov, Optical interference investigation of growth morphology and kinetics of (100) face of ADP growing from aqueous solution, Soviet Phys. Crystallogr., 30 (2) (1985) 219-223.
55. [Rashkovich, 1987] L. N. Rashkovich and O. A. Shustin, New optical interference methods for studying the kinetics of crystallization in solution, Soviet Phys. Usp., 30 (3) (1987) 280-283.
56. [Rashkovich, 1990A] L.N. Rashkovich and B.Yu. Shekunov, Hydrodynamic effects in growth of ADP and KDP crystals in solution. I. Growth kinetics, Sov. Phys. Crystallogr., 35 (1) (1990) 96-99.
57. [Rashkovich, 1990B] L.N. Rashkovich, B.Yu. Sheknunov and Yu.G. Kuznetsov, Hydrodynamic effects in growth of ADP and KDP crystals in solution. II-Morphological stability of faces, Soviet Phys. Crystallogr., 35 (1) (1990) 99-102.
58. [Rashkovich, 1990C] L. N. Rashkovich and B. Yu. Shekunov, Morphology of growing vicinal surface; Prismatic faces of ADP and KDP crystals in solutions, J. Cryst. Growth, 100 (1990) 133-144.
59. [Rashkovich, 1991] L.N. Rashkovich, “KDP-Family Single Crystals”, The Adam Hilger Series on Optics and Optoelectronics, (Adam-Hilger, New York), 1991, 202 pp.

60. [Rashkovich, 1995] L.N. Rashkovich and G.T. Moldazhanova, Growth kinetics and morphology of KDP crystal faces in solutions of varying acidity, J. Cryst. Growth, 151 (1995) 145-152.
61. [Rashkovich, 1996A] L.N. Rashkovich and G.T. Moldazhanova, Growth kinetics and bipyramid-face morphology of KDP crystals, in "Growth of Crystals", 20 (1996) 69-78, E.I. Givargizov and A.M. Melnikova (Eds.), (Consultants Bureau, New York).
62. [Rashkovich, 1996B] L.N. Rashkovich and B. Yu. Shekunov, Influence of impurities on growth kinetics and morphology of prismatic faces of ADP and KDP crystals, in "Growth of Crystals", 20 (1996) 107-119, E.I. Givargizov and A.M. Melnikova (Eds.), (Consultants Bureau, New York).
63. [Rosmalen, 1978] R. Janssen-van Rosmalen, W. H. van der Linden, E. Dobbinga and D. Visser, The influence of the hydrodynamic environment on the growth and the formation of liquid inclusions in large KDP crystals, Kristall and Technik, 13(1) (1978) 17-28.
64. [Schneberk, 1990] D. J. Schneberk, S. G. Azevedo, H. E. Martz and M. F. Skeate, Sources of error in industrial tomographic reconstructions, Materials Evaluation, 48 (1990) 608-617.
65. [Schopf, 1996] W. Schopf, J. C. Patterson and A. M. H. Brooker, Evaluation of the shadowgraph method for the convective flow in a side-heated cavity, Expts in Fluids, 21 (1996) 331-340.
66. [Settles, 2001] G. S. Settles, "Schlieren and Shadowgraph Techniques" (Springer, Berlin, 2001) 376 pp.
67. [Sharma, 2002] S. K. Sharma, Sunil Verma, B. B. Shrivastava and V. K. Wadhawan, In-situ measurements of pH and supersaturation dependent growth kinetics of the prismatic and pyramidal facets of KDP crystals, J. Cryst. Growth, 244 (2002) 342-348.
68. [Shlichta, 1985] P. J. Shlichta, Crystal growth in a spaceflight environment: final report, Materials processing in space environment, Experiment # 770100, (September 1985), pp. 1-123, (Jet Propulsion Laboratory, Pasadena, CA 91109).
69. [Shlichta, 1986] P. J. Shlichta, Feasibility of mapping solution properties during the growth of protein crystals, J. Cryst. Growth, 76 (1986) 656-662.
70. [Snyder, 1984] Ray Snyder and L. Hesselink, Optical tomography for flow visualization of the density field around a revolving helicopter rotor blade, Appl. Opt., 23 (20) (1984) 3650-3656.
71. [Snyder, 1988] Ray Snyder and L. Hesselink, Measurement of mixing fluid flows with optical tomography, Opt. Lett., 13 (2) (1988) 87-89.
72. [Solitro, 1989] Filomena Solitro, Laura Gatti, Federico Bedarida, Gian Antonio Dall'Aglio and Leonardo Michetti, Multidirectional holographic interferometer (MHOI) with fiber optics for study of crystal growth in microgravity, SPIE 1162 (1989) 62-65.
73. [Srivastava, 2004] A. Srivastava, K. Muralidhar and P.K. Panigrahi, Comparison of interferometry, schlieren and shadowgraph for visualizing convection around a KDP crystal, J. Cryst. Growth, 267 (2004) 348-361.

74. [Srivastava, 2005] Atul Srivastava, K. Muralidhar and P. K. Panigrahi, Reconstruction of the concentration field around a growing KDP crystal with schlieren tomography, Appl. Opt., 44 (26) (2005) 5381-5392.
75. [Subbarao, 1997] P. M. V. Subbarao, P. Munshi and K. Muralidhar, Performance evaluation of iterative tomographic algorithms applied to reconstruction of a three-dimensional temperature field, Numerical Heat Transfer, Part B, 31 (1997) 347-372.
76. [Sunagawa, 1995] I. Sunagawa, K. Tsukamoto, K. Maiwa and K. Onuma, Growth and perfection of crystals from aqueous solution: Case studies on barium nitrate and K-alum, Prog. Crystal Growth and Charact., 30 (2-3) (1995) 153-190.
77. [Sweeney, 1973] D. W. Sweeney and C. M. Vest, Reconstruction of three-dimensional refractive index field from multidirectional interferometric data, Appl. Opt., 12 (11) (1973) 2649-2664.
78. [Sweeney, 1974] D. W. Sweeney and C. M. Vest, Measurement of three-dimensional temperature field above heated surfaces by holographic interferometry, Int. J. Heat Mass Transfer, 17 (1974) 1443-1454.
79. [Szurgot, 1991] M. Szurgot, Effect of Buoyancy-driven convection on surface morphology and macromorphology of potassium bichromate crystals, Cryst. Res. Technol. 26(1) (1991) 43-52.
80. [Trolinger, 1991A] J. D. Trolinger, R. B. Lal and A. K. Batra, Holographic instrumentation for monitoring crystal growth in space, Opt. Engg., 30 (10) (1991) 1608-1614.
81. [Vartak, 2000] Bhushan Vartak, Yong-Il Kwon, Andrew Yeckel and Jeffery J. Derby, An analysis of flow and mass transfer during the solution growth of potassium titanyl phosphate, JCG, 210 (2000) 704-718.
82. [Vartak, 2005] Bhushan Vartak, Andrew Yeckel and Jeffery J. Derby, Time-dependent, three-dimensional flow and mass transport during solution growth of potassium titanyl phosphate, JCG, 281 (2005) 391-406.
83. [Vekilov, 1990] P. G. Vekilov, Yu G. Kuznetsov and A.A. Chernov, Dissolution morphology and kinetics of (101) ADP face: Mild etching of possible surface defects, J. Cryst. Growth, 102 (1990) 706-716.
84. [Vekilov, 1992A] P. G. Vekilov and Yu G. Kuznetsov, Growth kinetic irregularities due to changed dislocation source activity: (101) ADP face, J. Cryst. Growth, 119 (1992) 248-260.
85. [Vekilov, 1992B] P. G. Vekilov, Yu G. Kuznetsov and A.A. Chernov, The effect of temperature on step motion: (101) ADP face, J. Cryst. Growth, 121 (1992) 44-52.
86. [Vekilov, 1992C] P. G. Vekilov, Yu G. Kuznetsov and A.A. Chernov, Interstep interaction in solution growth: (101) ADP face, J. Cryst. Growth, 121 (1992) 643-655.
87. [Vekilov, 1993A] P. G. Vekilov, M. Ataka and T. Katsura, Laser Michelson interferometry investigation of protein crystal growth, J. Cryst. Growth, 130 (1993) 317-320.
88. [Vekilov, 1993B] P. G. Vekilov, Elementary processes of protein crystal growth, Prog. Crystal Growth Charact., 26 (1993) 25-49.

89. [Vekilov, 1995A] P. G. Vekilov, M. Ataka and T. Katsura, Growth processes of protein crystals revealed by laser Michelson interferometry investigation, Acta. Cryst., D51 (1995) 207-219.
90. [Vekilov, 1995B] P. G. Vekilov, L. A. Monaco and F. Rosenberger, High resolution interferometric technique for in-situ studies of crystal growth morphologies and kinetics, J. Cryst. Growth, 148 (1995) 289-296.
91. [Vekilov, 1998A] P. G. Vekilov and F. Rosenberger, Increased stability in crystal growth kinetics in response to bulk transport enhancement, Phys. Rev. Lett., 80 (12) (1998) 2654-2656.
92. [Vekilov, 1998B] P. G. Vekilov and F. Rosenberger, Protein crystal growth under forced solution flow: experimental setup and general response of lysozyme, J. Cryst. Growth, 186 (1998) 251-261.
93. [Verma, 2005A] Sunil Verma, S. Dhawale, V. Bande, K. Muralidhar and V. K. Wadhawan, Novel optical instrumentation and apparatus for studying crystal growth from solution, Proc. 3rd Asian Conference on Crystal Growth & Crystal Technology (CGCT-3), Oct. 16-19, 2005, Beijing, China.
94. [Verma, 2005B] Sunil Verma, K. Muralidhar and V. K. Wadhawan, Convection and concentration mapping during crystal growth from solution using Mach-Zehnder interferometry and computerized tomography, Proc. 3rd Asian Conference on Crystal Growth & Crystal Technology (CGCT-3), Oct. 16-19, 2005, Beijing, China.
95. [Verma, 2005C] Sunil Verma, K. Muralidhar and V. K. Wadhawan, Flow visualization and modeling of convection during the growth of K.D.P. crystals, Ferroelectrics, 323 (2005) 25-37.
96. [Verma, 2005D] Sunil Verma, Atul Srivastava, Vivek Prabhakar, K. Muralidhar and V. K. Wadhawan, Simulation and experimental verification of solutal convection in the initial stages of crystal growth from an aqueous solution, Ind. J. Pure & Appl. Phys., 43 (2005) 24-33.
97. [Verma, 2006] Sunil Verma, K. Muralidhar and V. K. Wadhawan, Determination of concentration field around a growing crystal using shadowgraphic tomography, Chapter 14, in "Computerized Tomography for Scientists and Engineers", P. Munshi (Ed.), (CRC Press, New York & Anamaya Publishers, New Delhi), 2006, 158-174.
98. [Verma, 2007] Sunil Verma, Eglon Depty and P.K. Gupta, Strength of free convection during KDP growth and its relation to crystal quality, Proc. 52nd Solid State Physics Symposium, 27-31 Dec. 2007, University of Mysore, Mysore.
99. [Verma, 2008A] Sunil Verma, Convection, concentration and surface feature analysis during crystal growth from solution using shadowgraphy, interferometry and tomography, Ph.D. thesis, IIT Kanpur (2008), India.
100. [Verma, 2008B] Sunil Verma and P.J. Shlichta, Imaging techniques for mapping of solution parameters, growth rate, and surface features during the growth of crystals from solution, Prog. Cryst. Growth & Charact. Materials, 54 (2008) 1-120.
101. [Verma, 2008C] Sunil Verma and K. Muralidhar, Three-dimensional reconstruction of convective features during crystal growth from solution using computerized tomography, in "CT2008: TOMOGRAPHY CONFLUENCE",

P. Munshi (Ed.), American Institute of Physics (AIP) Proceedings Vol. 1050, Melville, New York, 2008, 103-114.

102. [Vest, 1984] C. M. Vest and I. Prikryl, Tomography by iterative convolution: empirical study and application to interferometry, Appl. Opt., 23 (14) (1984) 2433-2440.
103. [Volmer, 1939] Max Volmer, "Kinetik der Phasenbildung", (Steinkopf Verlag, Dresden and Leipzig, 1939).
104. [Wilcox, 1983] W. R. Wilcox, Influence of convection on the growth of crystals from solution, J. Cryst. Growth, 65 (1983) 133-142.
105. [Wilcox, 1993] W. R. Wilcox, Transport phenomena in crystal growth from solution, Prog. Crystal Growth Charact., 26 (1993) 153-194.
106. [Yeckel, 1998] Andrew Yeckel, Yuming Zhou, Michael Dennis and Jeffery J. Derby, Three dimensional computations of solution hydrodynamics during the growth of potassium dihydrogen phosphate II. Spin down, J. Cryst. Growth, 191 (1998) 206-224.
107. [Yu, 1994] Xiling Yu, Youchen Liu, Xuefeng Yue and Yi Sun, Mass Transport Effect Within the Boundary Layers in Solution Crystal Growth: Holographic Study of KTP and KDP Crystal Growth, Cryst. Res. Tech., 29(2) (1994) 229-236.
108. [Zhou, 1997] Yuming Zhou and Jeffery J. Derby, Three-dimensional computations of solution hydrodynamics during the growth of potassium dihydrogen phosphate I. Spin up and steady rotation, J. Cryst. Growth, 180 (1997) 497-509.